Edge turbulence self-organization in fusion plasmas

Olivier Panico

INSTITUT POLYTECHNIQUE DE PARIS

NNT : 2024IPPAX133

Thèse de doctorat

Edge turbulence self-organization in fusion plasmas

Thèse de doctorat de l'Institut Polytechnique de Paris
préparée à l'Ecole polytechnique et IRFM Cadarache

École doctorale n°626 Institut Polytechnique de Paris (IPP)
Spécialité de doctorat : Physique

Thèse présentée et soutenue à Saint-Paul-Lez-Durance, le 18 Décembre 2024, par

OLIVIER PANICO

Composition du Jury :

Steven TOBIAS Professeur, Université de Leeds	Président
Yann CAMENEN Directeur de Recherche, CNRS (PIIM)	Rapporteur
Benoit LABIT Directeur de Recherche, EPFL (SPC)	Rapporteur
Özgür D. GÜRCAN Chargé de recherche, CNRS (LPP)	Examinateur
Peter MANZ Professeur, Université de Greifswald (IPP)	Examinateur
Pascale HENNEQUIN Directrice de Recherche, CNRS (LPP)	Directrice de thèse
Yanick SARAZIN Directeur de Recherche, CEA (IRFM)	Directeur de thèse
Xavier GARBET Professeur, Université de technologie de Nanyang et CEA (IRFM)	Invité

Laboratoire de Physique des Plasmas (LPP), CNRS, Observatoire de Paris, Sorbonne Université, Université Paris Saclay, Ecole polytechnique, Institut Polytechnique de Paris, 91120 Palaiseau, France

CEA, IRFM, F-13108 Saint-Paul-lez-Durance, France

Ecole Polytechnique Fédérale de Lausanne (EPFL), Swiss Plasma Center (SPC), CH-1015 Lausanne, Switzerland

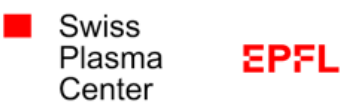

Contents

Remerciements

Ces trois années ont été pour moi enrichissantes et passionnantes. Cela est dû à de nombreuses personnes que je tiens à remercier chaleureusement ici.

Pour commencer j'aimerais remercier l'ensemble de mon jury de thèse. En particulier, merci à Steven Tobias d'avoir accepté le rôle de président de ce jury. Je tiens également à remercier les rapporteurs de ce manuscrit, Yann Camenen et Benoit Labit pour leur relecture attentive et leurs propositions d'amélioration. Enfin, j'aimerais remercier les examinateurs Özgür D. Gürcan et Peter Manz pour leur déplacement jusqu'à Cadarache ainsi que pour les discussions intéressantes qu'ils ont apportées. Finalement, je tiens à remercier Xavier Garbet, qui n'a malheureusement pas pu être présent le jour de la soutenance. Merci tout d'abord de ton suivi au cours de ma thèse mais également de m'avoir ouvert la porte d'un stage en physique théorique au CEA en 2020 en pleine pandémie, alors que toutes les autres semblaient se fermer. Ton enthousiasme et ton expertise m'ont convaincu d'entreprendre un doctorat dans ce domaine.

Ensuite, j'aimerais remercier mes directeurs de thèse : Pascale Hennequin et Yanick Sarazin. Merci à tous les deux de m'avoir donné les clés pour comprendre ce sujet. J'ai gardé une note d'environ 120 réunions hebdomadaires, parfois (très!) longues. Ces heures à débattre de tous les aspects de mon sujet sont pour moi extrêmement précieuses. Merci de m'avoir toujours poussé à faire plus, à faire mieux, en me laissant libre d'explorer les voies qui me plaisaient. Je me sens véritablement chanceux d'avoir pu travailler à vos côtés. Yanick, merci d'avoir accueilli toutes mes idées avec enthousiasme. Tu sembles toujours pouvoir relancer et proposer de nouvelles choses sur n'importe quel domaine. Pascale, merci pour ton enseignement et pour m'avoir soutenu et encouragé à réaliser ces expériences et sortir de mon cocon de théoricien.

J'aimerais aussi remercier chaleureusement Guilhem Dif-Pradalier et Özgür Gürcan. Vous avez suivi mon travail de près, merci d'avoir toujours pris le temps de répondre à mes questions. Je tiens à remercier également Emily Bourne, Hugo Bufferand, Guido Ciraolo, Peter Donnel, Philippe Ghendrih, Virginie Grandgirard, Kévin Obrejean, Cyrille Honoré, Pierre Morel, Laure Vermare et plus généralement toutes les personnes affiliées de près ou de loin au GTSN et au groupe fusion du LPP. Merci pour votre disponibilité et votre amitié.

Je remercie également mes collègues thésards. En particulier la promotion du 513 : Virginia Quadri, Mattia Dicoratto, Raffaël Düll et Yann Munschy. Nous avons affronté ces années ensemble, entre discussions de physique et boissons de toutes sorte. Mention spéciale à Yann qui a réussi à me convaincre d'aller à Cadarache en vélo. Le Sambuc c'est joli pour les yeux, moins pour les jambes. Sascha Rienäcker, merci pour ton soutien aussi bien dans les expériences sur TCV et l'utilisation du DBS que sur les blocs de Vitrolles. Une pensée pour tous les nouveaux docteurs Samy, Alexis, James, Quentin x2, Mathieu et plus généralement tous les compagnons

de Plasmapéros : Riccardo, Luigi, Maylis, Theo, Louis, Antoine, Timothée, Ludovica, Naren, David et tous les autres qui se reconnaitront. Merci à mes amis postdocs et jeunes embauchés, Eleonore Geulin, Samuele Mazzi, Mathieu Peret, Nicolas Rivals et Robin Varennes, grâce à vous – en particulier l'encadrement de Robin – je ne suis enfin plus un stagiaire-thésard !

Enfin j'aimerais remercier mes amis d'enfance. Même si vous ne savez pas trop ce que je fais de mes journées (non Ninon je ne vais pas devenir astronaute), votre soutien est inégalable. Maeva merci d'avoir partagé le fardeau de la thèse avec moi pendant ces trois années, en vrai t'es sympa. Entre les parties de Rami endiablées avec Noémie, les films étranges et pas toujours compréhensible avec Val, les repas chez Ninon, toutes les activités partagées avec vous tous ont été des bouffées d'oxygène bienvenues. Seb merci d'être toujours au premier rang de mon spectacle, mes blagues n'auraient pas la même saveur si tu n'y rigolais pas. Adrien, Sim, Tim et Bin, merci d'être mes potes à perf, grâce à vous j'atteins des nouveaux niveaux de conscience et je fais de mon corps un temple. Merci à Kim de me montrer que la fracture n'est pas une fin en soi, et à Blan de prouver qu'il y a des choses plus essentielles que le travail. Merci à Louis qui arrive à suivre de l'autre bout de la France. Merci également à Joachim, Mattia, Laps, Thomas, Celio.

Plus généralement, merci à tous les amis qui m'ont suivi ces trois années. A mes amis des Mines, trop nombreux pour tous les citer, de me retrouver à chaque fois comme si on ne s'était jamais quittés. Merci à Charles et Rachel, Romain, Albane, Iman, Jeanne et Shanon. Merci également à mes nombreux colocs aux cours de ces trois années et en particulier à Constance, Guillaume, Bénédict, Juliette, Stanislas, Antoine, Maoh, Made, Julie, Nico, Louis, Camille, Ambre et Isilie.

Pour finir, j'aimerais remercier ma famille, mes parents Anne et Thierry. Merci de m'avoir poussé à faire ces études. Merci également de toujours m'accueillir comme un roi lorsque je rentre à Claix, et de faire que cet endroit soit toujours mon chez moi. Merci à mes frères Pierre et François. Merci pour ces innombrables débats, parfois perdus d'avance pour moi, qui m'ont donné la curiosité de faire de la recherche en physique.

Evidemment, un incommensurable merci à Alizé. Tu as suivi ce travail avec une telle attention que tu aurais sans doute pu faire la soutenance à ma place. Merci d'avoir relu en nombre mes abstracts, articles et autres contributions. Merci également d'avoir été à mes côtés et de m'avoir supporté durant les moments de doutes, de difficultés et de joie.

Résumé étendu

La fusion de l'hydrogène

La fusion de l'hydrogène représente, depuis les années 1930, l'espoir d'une source d'énergie abondante et peu dangereuse. Lors des premières grandes expériences de fusion comme Scylla I aux Etats-Unis ou Zeta au Royaume-Uni la réussite de la fusion paraissait accessible. Pourtant, d'importantes difficultés se sont présentées, dont certaines ne sont toujours pas résolues à ce jour. Maintenir un plasma stable à des températures très élevées, tout en protégeant les parois, représente un défi considérable. Les enjeux liés au changement climatique ont remis la production d'énergie au centre des préoccupations. A ce titre, la fusion bénéficie d'un regain d'intérêt notable.

Aujourd'hui, la réaction de fusion privilégiée est la fusion d'un atome de deutérium et de tritium afin de former un atome d'hélium et un neutron. Cette réaction permet, en principe, de libérer une très grande quantité d'énergie ($\approx 17.5\ MeV$). Pour cela, il est nécessaire de franchir la barrière de potentiel produite par répulsion électrostatique. Cette réaction se produit essentiellement dans des milieux très denses, comme le Soleil, ou à des températures très élevées, de l'ordre de 150 millions de degrés. À ces températures, les électrons et les noyaux légers sont entièrement séparés dans un état appelé "plasma". Le plasma réagit aux champs magnétique, ce qui présente un avantage important pour son confinement dans des machines appelées "tokamaks".

Les conditions extrêmes du plasma ainsi que la qualité du confinement par la machine sont directement responsables de l'efficacité d'un réacteur et de son bilan énergétique. Le critère de Lawson, donne la valeur minimale pour que ce bilan énergétique soit positif, autrement dit pour que la production d'énergie soit supérieure à celle introduite effectivement pour la génération du plasma. Il dépend de la densité, température et du temps de confinement de l'énergie.

$$nT\tau_E \geq 3 \times 10^{21} m^{-3}.keV.s \tag{1}$$

La réaction de fusion est plus efficace dans une certaine plage de température, ce qui contraint T. Ainsi, il reste deux paramètres sur lesquels jouer pour atteindre le critère de Lawson. Ou bien augmenter la densité, c'est le principe du *confinement inertiel*. Ou bien augmenter le temps de confinement, c'est le principe du *confinement magnétique* dans des tokamaks ou des stellarators notamment. Nous nous intéressons dans cette thèse au confinement dans les tokamaks.

Le confinement dans les tokamaks

Le tokamak est une machine en forme de donut comportant un important champ magnétique dans la direction dite toroïdale c'est-à-dire le long du grand rayon du donut. Les particules

chargées du plasma suivent les lignes du champ magnétique de telle sorte qu'elles sont amenées à effectuer des tours dans la direction toroïdale. Cependant, les propriétés du plasma impliquent des effets de dérive. C'est le cas de la dérive électrique $\mathbf{v}_E = \mathbf{E} \times \mathbf{B}/B^2$. Le champ magnétique étant courbé par la géométrie du tokamak, les particules proches du cœur ne sont pas sujettes au même champ magnétique que celles du bord. Il en résulte une dérive dite "verticale" qui crée une séparation des charges dans la direction verticale, produisant ensuite un déplacement radial du plasma par la dérive électrique. Ce phénomène conduit à la perte très rapide du plasma. Afin de résoudre ce problème, un deuxième champ magnétique plus faible est ajouté dans la direction poloïdale, créant des lignes de champ torsadées. Ainsi, les particules explorent à la fois les régions internes et externes de la machine : leur dérive verticale est compensée.

Dans un tokamak, nous pouvons définir trois régions principales. D'abord, la zone de confinement du plasma, où les surfaces magnétiques sont fermées. Ensuite, la zone externe où le plasma interagit avec les matériaux. Enfin, une zone de transition, dite « de bord », entre la zone confinée et la zone externe.

Transport radial

En principe une machine parfaitement axisymétrique dont les champs d'équilibre ne varient pas dans le temps permet le confinement du plasma. Pourtant, plusieurs phénomènes physiques viennent perturber cette configuration d'équilibre. C'est le cas des collisions entre les particules qui génèrent un transport radial à travers les surfaces du champ magnétique. C'est également le cas de la turbulence, qui produit la majorité du transport radial.

La turbulence est générée par les forts gradients thermodynamiques présents entre le cœur chaud et dense du plasma et le bord froid. Ces gradients, qui stockent une importante quantité d'énergie, peuvent atteindre un seuil d'instabilité. Ils commencent alors à donner une partie de leur énergie aux fluctuations. Lorsque ces fluctuations deviennent importantes, elles commencent à interagir entre elles et atteignent en général une saturation non-linéaire. C'est ce que l'on considère comme le régime turbulent.

Turbulence

Mieux comprendre la turbulence et sa saturation est essentiel pour le développement de futurs réacteurs. Il s'agit aussi d'un sujet fondamental, partagé avec de nombreux domaines physiques. La turbulence est caractérisée par une dynamique complexe et chaotique dans laquelle de nombreuses échelles sont couplées. On considère souvent la turbulence sous la forme de «vortex » qui représentent une partie du fluide se comportant de façon cohérente. La turbulence implique l'interaction de multiples vortex à des échelles de tailles variées. Dans l'espace de Fourier, on considère ces échelles sous la forme de leurs nombre d'onde k, où $k = 2\pi/\lambda$ et λ représente la taille du vortex.

La turbulence s'auto-organise également en structures complexes. Tout d'abord elle génère du transport sous forme d'évènements balistiques. Ces évènements de transport peuvent être assimilés à une avalanche dans un tas de sable : un évènement de transport aplati le profil de pression localement, ce qui engendre deux zones de plus fort gradient de chaque côté. Dans chacune de ces zones, le fort gradient produit un important transport et amène à un aplatissement

du profil local. Ainsi, l'avalanche se déplace dans les deux sens : une anomalie négative vers le haut du profil, une anomalie positive vers le bas. De plus, la turbulence génère des écoulements à travers le tenseur de Reynolds qui consiste en un couplage des fluctuations de vitesses radiale et poloïdale. Plusieurs vitesses peuvent ainsi participer au tenseur de Reynolds. Historiquement, on a principalement considéré la dérive électrique. Plus récemment, il a été démontré que la dérive diamagnétique est également importante dans certains régimes de turbulence. Les écoulements poloïdaux ainsi générés sont appelés « écoulements zonaux (ZF) » car ils sont symétriques dans la direction toroïdale et poloïdale. Les ZF sont considérés comme des facteurs clés dans la saturation de la turbulence dans la mesure où ils permettent de stocker l'énergie de la turbulence sans générer eux-mêmes du transport. De plus, leur structure radiale permet de participer au cisaillement généré par les écoulements dans la direction poloïdale : les structures turbulentes sont allongées et parfois même déstructurées par l'effet de cisaillement.

Il est prédit dans certaines simulations que les zones de cisaillement provoquées par les écoulements pourraient amener à une réduction du transport turbulent local et donc à une augmentation locale du gradient de pression. Le profil prend ainsi une forme en marches d'escalier où les zones de fort gradient correspondent aux écoulements et les zones de faible gradient aux avalanches. Cette structure globale est appelée *staircase*.

Contexte et objectifs de la thèse

Les paramètres du plasma dans la zone de bord sont considérés comme des facteurs clés dans la compréhension de la turbulence et du transport. Ils permettent d'identifier des zones de fonctionnement du tokamak : certaines sont des limites et ne permettent pas l'opération, d'autres permettent l'accès à des modes de « haut confinement » (mode-H). Un exemple de limite est donné par une trop forte densité dans laquelle le plasma atteint un régime de très fort transport turbulent, ne permettant pas de continuer l'opération. Si cette limite est bien prédite, les mécanismes physiques sous-jacents sont encore débattus. Certaines contributions mettent en avant le rôle des ZF puisque lorsque la densité augmente, des simulations observent l'écroulement de l'activité zonale et un transport, en conséquence, très important. De plus, des questions demeurent quant aux mécanismes physiques de l'auto-organisation de la turbulence. La génération des *staircases* ainsi que l'interaction entre les ZF et les avalanches sont encore discutées.

Dans cette thèse, nous proposons de revenir sur le domaine de fonctionnement du tokamak en se focalisant sur les effets d'auto-organisation du plasma. Ce travail demande une formulation du modèle dite “conduite par le flux": il n'y a pas de séparation d'échelle supposée *a priori* entre les quantités moyennes (profil de pression, écoulements moyen) et les fluctuations. Le système évolue librement à l'aide d'une source et en fonction de la turbulence générée. Pour cela, et dans l'objectif de cartographier le comportement du plasma dans l'espace des paramètres, nous développons un modèle réduit en description fluide pour l'étude de la turbulence et des écoulements. Ce modèle doit comporter des éléments essentiels : être conduit par le flux, ne pas supposer de séparation d'échelle, inclure plusieurs instabilités du plasma de bord et pouvoir réaliser des simulations dans des temps raisonnables tout en atteignant le temps de confinement des particules et l'équilibre statistique des profils moyens.

De plus, les observations expérimentales de l'auto-organisation du plasma sont très peu nombreuses dans les grandes machines. Il est, en effet, difficile de mesurer ces quantités dans la

zone confinée d'un plasma chaud de tokamak. Pour identifier un ZF, il faudrait pouvoir mesurer le potentiel électrique (ou à défaut la vitesse), et vérifier la structure symétrique du mode : $m = n = 0$ avec m le nombre d'onde poloïdale et n le nombre d'onde toroïdal. Une solution consiste à faire des mesures de corrélation à longue distance séparées poloïdalement et toroïdalement. Cependant, les sondes permettant de mesurer le potentiel ne peuvent pas atteindre la zone confinée du plasma car celle-ci est trop chaude. A la place, nous utilisons des systèmes de réflectométrie comme la réflectométrie Doppler (DBS) qui permet de mesurer les fluctuations de densité du plasma à un nombre d'onde k donné. Un DBS permet également d'obtenir la vitesse d'advection de ces fluctuations par le décalage en fréquence Doppler. De même, les avalanches nécessitent une très bonne résolution spatiale et temporelle, pour pouvoir suivre le déplacement de la structure. Récemment, il a été démontré, à l'aide d'un DBS, que les avalanches peuvent être observées sous la forme d'une deuxième pente dans la fonction de corrélation radiale de la turbulence. Ainsi, dans cette thèse nous nous intéressons à trois questions principales :

- Quels sont les paramètres plasma permettant l'auto-organisation du plasma en écoulements zonaux, avalanches et *staircases* ?
- Quels en sont les mécanismes d'interaction et de génération sous-jacent ?
- Pouvons-nous mieux observer ces structures à l'aide de la réflectométrie Doppler ?

Tokam1D : un modèle réduit pour l'étude de l'interaction entre la turbulence et les écoulements

Tout d'abord un modèle, nommé « Tokam1D » est développé. Celui-ci inclut plusieurs paramètres jugés importants. Il est conduit par le flux et ne suppose pas de séparation d'échelles entre les quantités dites « d'équilibre », i.e. moyennées dans la direction toroïdale et poloïdale et les quantités fluctuantes. Ensuite, deux instabilités considérées dominantes dans les plasmas de bord sont incluses : les ondes de dérive collisionnelles et l'interchange. La première instabilité dépend d'un déphasage parallèle fini entre les fluctuations de densité, contrôlé par le paramètre C. La deuxième est liée à l'inhomogénéité du champ magnétique. Le modèle est considéré dans une géométrie simple, dans l'optique de le réduire à une seule dimension ensuite. L'inhomogénéité du champ magnétique est donc seulement considérée sous la forme d'un paramètre scalaire : g. Le modèle est isotherme avec une température ionique finie afin que la composante diamagnétique du tenseur de Reynolds soit incluse. Enfin, le modèle est réduit à une seule dimension en considérant un unique mode pour les fluctuations dans la direction parallèle au champ magnétique et dans la direction poloïdale. Avec cette hypothèse, le modèle repose sur le transport turbulent (relaxation des profils) et sur le stockage dans les écoulements zonaux pour saturer l'énergie turbulente. La saturation sous la forme de cascades, n'est ainsi pas prise en compte *per se*, mais celle-ci peut être considérée par l'ajout d'un terme heuristique de saturation non-linéaire.

La dérivation du modèle est d'abord effectuée dans le cadre d'un plasma en mode L (« de faible confinement »), pour lesquelles l'approche électrostatique est envisagée. Le modèle est constitué de deux équations : la continuité de la densité et la continuité de la charge. Il décrit ainsi deux variables : la densité et la vorticité. L'inversion de la vorticité permet d'obtenir le potentiel électrique. Le modèle est fermé en considérant une loi d'Ohm collisionnelle qui

permet de relier le courant parallèle à la densité et au potentiel électrique.

L'analyse linéaire est réalisée à la fois pour la version à trois dimensions et pour la version à un seul mode correspondant aux simulations de Tokam1D. Il est montré que le paramètre d'adiabaticité C, stabilise l'instabilité d'interchange. Lorsque C est très grand, les deux instabilités sont stables et aucun transport n'est attendu. Pour des paramètres plasmas similaires, lorsque les deux instabilités sont présentes, l'interchange montre un taux de croissance et un sinus de déphasage plus élevé. Le déphasage est important pour le transport turbulent : $\Gamma_{turb} = |\widetilde{n}||\widetilde{\phi}|\sin\Delta\varphi$, avec $\widetilde{n}$ les fluctuations de densité, $\widetilde{\phi}$ celles du potentiel électrique et φ le déphasage entre les fluctuations.

Des ajouts au modèle sont réalisés pour inclure une physique plus riche. Tout d'abord, le rôle des écoulements moyens provenant de l'équilibre général du plasma est ajouté. Ces écoulements, ajoutés aux ZFs, permettent une description plus générale de la rotation dans le plasma de bord. Ils sont globalement négatifs dans la zone confinée, et les ZF apparaissent comme des ondulations par-dessus ces écoulements. Ils participent également à l'effet de cisaillement énoncé plus haut. De plus, le modèle est étendu pour décrire à la fois la partie confinée et la partie externe. Ainsi, le modèle décrit toute la zone de transition considérée comme cruciale. Dans la zone externe, les écoulements sont globalement positifs, de sorte que le changement de signe dans la zone de la transition implique un cisaillement qui peut être important. Cet effet de cisaillement à la transition est considéré comme clé dans l'atteinte de régimes à haut confinement. Enfin, des effets électromagnétiques sont ajoutés. Ceux-ci dépendent du paramètre β (ratio de la pression plasma par la pression magnétique). Dans les régimes à forts gradients, tel que le mode H, il est montré que les effets électromagnétiques peuvent jouer un rôle crucial pour la turbulence et le transport. Dans le cas du modèle électromagnétique, une troisième équation est ajoutée au modèle : la loi d'Ohm généralisée. Cette fois-ci, le potentiel vecteur est obtenu, en considérant les effets d'inertie des électrons, de variation parallèle des lignes de champ magnétique (« flutter ») et d'induction : le champ électrique ne dérive plus seulement du gradient du potentiel électrique mais également de la variation temporelle du potentiel vecteur. L'analyse linéaire du modèle électromagnétique montre une augmentation du taux de croissance avec β pour l'instabilité d'interchange et une stabilisation de l'instabilité de dérive. A très grand β, l'instabilité électromagnétique idéale est retrouvée, comme attendue. Son développement non-linéaire permettra une description du plasma et de son auto-organisation dans des régimes plus étendus.

Génération des écoulements zonaux selon les regimes de turbulence

Le modèle électrostatique décrivant la zone confinée sans l'équilibre des forces est ensuite utilisé pour étudier l'espace des paramètres en régime non-linéaire. Un total de 120 simulations ayant atteint le temps de confinement des particules et l'équilibre statistique du système est étudié. Les simulations sont faites à source constante ainsi qu'à distance constante au seuil d'instabilité. Cinq résultats principaux peuvent être mis en lumière.

Tout d'abord, en étudiant la répartition d'énergie entre les écoulements et la turbulence, il est montré que ceux-ci sont importants lorsque le paramètre C est grand. Lorsque C décroît,

les écoulements stockent moins d'énergie et la turbulence devient plus importante. Cependant, l'effondrement de l'activité zonale, observée dans d'autres contributions, n'est pas retrouvée ici. Une explication est que les simulations sont contrôlées par le flux : le profil de densité peut ainsi s'adapter plus librement à la turbulence. Un second régime dominé par les écoulements est trouvé à fort g. Dans celui-ci, dominé par l'instabilité d'interchange, les écoulements apparaissent radialement structurés et stables dans le temps. Si les simulations proches du seuil amènent toujours à un certain degré de structuration radiale, les simulations loin du seuil (forçage très important) sont les plus structurées et les plus stables.

Une compréhension plus fine de ces deux régimes est apportée par l'analyse des tenseurs de Reynolds. Le régime à fort g faible C, dominé par l'interchange, montre les contributions électrique et diamagnétique en opposition de phase mais avec la première largement dominante. Lorsque C augmente, la contribution diamagnétique devient de plus en plus importante, jusqu'à être dominante. Enfin à très fort C, les deux contributions sont en phase et de la même amplitude. Le comportement du tenseur de Reynolds est directement lié aux propriétés sous-jacentes de la turbulence. Le rapport d'amplitude entre les contributions au tenseur dépend du rapport d'amplitude entre fluctuations de densité et de potentiel électrique. Leur corrélation, en phase ou en opposition, dépend de l'alignement des fluctuations de densité et de potentiel électrique.

Lorsqu'ils sont structurés, les écoulements conduisent toujours à l'apparition de marches dans le profil de densité. Les avalanches apparaissent également principalement en régime d'interchange, lorsque les ZF sont structurés. Cependant, il est montré que la formulation par le flux est essentielle à la dynamique des *staircases*. Lorsque les profils ne sont plus autorisés à fluctuer sur de petites échelles, alors toute la structure se perd. Autrement dit, il apparaît essentiel pour les *staircases* de pouvoir stocker de l'énergie dans le profil de densité et dans les écoulements. La disparition de l'un de ces deux mécanismes amène à la disparition de la structure.

Finalement, le rôle des écoulements sur le confinement est étudié. Il est montré que ceux-ci permettent une réduction du transport turbulent, d'autant plus importante lorsqu'ils sont structurés radialement. Ainsi, dans les simulations réalisées, les *staircases* permettent un meilleur confinement du plasma.

Pour terminer, l'objectif est également de mesurer expérimentalement ces structures. A l'aide du modèle, leurs régimes d'existence ont été mieux identifiés. De plus, certaines signatures pouvant être observées à l'aide d'un DBS sont mises en lumière. En particulier, les avalanches sont caractérisées par une fonction de corrélation radiale à deux pentes : la première pente est attribuée à la taille des structures turbulentes à petite échelle, la seconde pente est liée à la longueur typique des avalanches.

Mesures expérimentales de l'auto-organisation de la turbulence

Enfin, le dernier objectif de la thèse est de chercher des signatures de l'auto-organisation de la turbulence dans les plasmas de tokamak. Pour cela nous utilisons un double système de réflectométrie Doppler (DBS) sous deux configurations différentes.

Premièrement, nous utilisons des données expérimentales ayant été récoltées précédemment sur le tokamak Tore Supra lorsque le double système DBS était installé. Comme les deux sys-

tèmes sont séparés poloïdalement et toroïdalement, il est possible de réaliser des corrélations à longue distance. Initialement, ce système a été utilisé pour l'étude des modes géodésiques acoustiques (GAM), une branche à plus haute fréquence des écoulements zonaux. Dans notre cas, nous l'utilisons pour observer les ZF à basse fréquence. Pour ce faire, le signal est tout d'abord décomposé à l'aide d'une méthode temps-fréquence appelée MUSIC qui permet d'estimer la fréquence Doppler instantanée. Ainsi, la vitesse des écoulements, liée à la fréquence Doppler, peut être obtenue avec une importante résolution temporelle. En corrélant les deux signaux de vitesse instantanée, une importante corrélation à longue distance est observée à la fréquence attendue pour le GAM. Afin de mieux observer les basses fréquences, nous isolons le GAM à l'aide d'une « décomposition en mode empirique » (EMD). Cette méthode permet d'identifier et d'isoler des signaux dont la fréquence et l'amplitude varient dans le temps. En isolant les GAM et les hautes fréquences, il est possible de corréler uniquement les signaux à basses fréquences. Ainsi, une corrélation à longue distance bien supérieure au bruit est obtenue pour les basses fréquences indiquant une possible activité zonale. Le nombre de données expérimentales disponibles avec cette configuration ne permet pas de caractériser la méthode en détail. Celle-ci reste cependant prometteuse pour de futures applications ou expériences.

Deuxièmement, des expériences sont réalisées sur le tokamak TCV à l'EPFL. Dans cette configuration, les deux systèmes DBS sont à la même position. Ainsi, il est possible de mesurer des fonctions de corrélation radiale de la turbulence. Un grand nombre d'expériences est réalisé avec différents chauffages (par résonance cyclotronique électronique et par injection de neutre) pour tenter de modifier les profils et les régimes de turbulence sous-jacents. Dans la configuration choisie, une forme en point-X haute à bas confinement, les différents types de chauffage n'ont pas permis de modifier les instabilités. Le plasma est dominé par une instabilité dite « d'électrons piégés ». Dans la majorité des régimes observés, une double pente est observée sur la fonction de corrélation radiale de la turbulence. Par analogie avec les travaux précédents et avec les simulations, la deuxième pente est attribuée à l'extension spatiale des avalanches. Les longueurs de la turbulence et des avalanches sont caractérisées avec les différents chauffages. Une comparaison est réalisée avec le réflectomètre à impulsion rapide (SPR) et montre un très bon accord pour la mesure de la taille des structures turbulentes. De plus, des expériences ont été réalisées en accordant les profils de densité, température et vitesse toroïdale en hydrogène et en deutérium. Celles-ci permettront dans un futur proche, de caractériser les variations des longueurs de turbulence et d'avalanche en fonction du paramètre normalisé $\rho_\star$.

Chapter 1

Introduction

Contents

Subject of many promises, nuclear fusion has long offered the potential for clean and abundant energy. The journey began about a century ago in the stars, when Jean Perrin and Arthur Eddington first suggested that the Sun's power came from the fusion of hydrogen into helium. With the experimental demonstration of nuclear fusion reactions in a particle accelerator by Rutherford and Oliphant, it rapidly followed that this reaction could be sustained to produce energy. A quest then began to reproduce this energy on Earth. As it happens sometimes with science, the first progress came with the development of a weapon: the Hydrogen-bomb in the early 50s. The first machines claiming to achieve controlled thermonuclear fusion were pinch devices in the late 50's: Scylla I in the US, Zeta in the UK. When these projects were made public, it was believed that the completion of fusion was near, and that a new and free energy source would soon be at our disposal. This is evidenced by British newspapers headlines from 1958, illustrated in Figure 1.1.
"Britain unveils her Sun", "the good side of the H-bomb", "Too cheap to charge", no superlative is strong enough to capture the potential of fusion. It turned out a little later, that Zeta had not achieved fusion. And, 66 years later, as this thesis is being written, commercially viable fusion is still under development.

The research did move forward during all these years. First with the concept of tokamak: "**To**roidal'naya **ka**mera s **ma**gnitnymi **k**atushkami" (toroidal chamber with magnetic coils) developed by Sakharov and Tamm and the concept of Stellarator by Spitzer in the early 50's. Then with the many machines developed in the 80s and the ITER project now under construction. Many time throughout this century of research, fusion seemed within reach, only for a new challenge to emerge that needed solving - each time bringing us closer to the realisation of fusion.


THE CHRONICLE, SATURDAY, FEBRUARY 1, 1958.

ZETA REVEALS THE GOOD SIDE OF THE H-BOMB

SIR John Cockcroft said on Friday night that he is 90 per cent. certain that British atomic scientists have already controlled the hydrogen bomb reaction.

He was speaking at a Press conference shortly after the British Atomic Energy Authority had released from Harwell an account of the research, of Zeta (the apparatus in which the fusion reaction is controlled), and the possible benefits of the process.

Two years' work

Ahead of U.S.

How far ahead is Britain? The experiments show that the bigger the fusion machine the better, and Zeta is much larger than any of the American machines. Although the American scientists claim comparable temperatures (several million degrees) their evidence is not as good as Dr. Thonemann's. And in any case they were able to hold the temperatures only for a few millionths of a second, against Harwell's few thousandths.

Rapid progress is now predicted at Harwell—much higher temperatures and the chance of holding them for a whole second, within the next few months.

There is no sign that the Americans will be able in the next few years to get even as far as we have already. The Soviet scientists were somewhat deterred by early difficulties which they encountered, and the rumour is that they are still having trouble.

Zeta spells H-power everlasting

By HUGH McLEAVE

BRITAIN last night became—officially—the first country to prove that the H-bomb can be tamed to feed power-hungry nations. Harwell unveiled Zeta, its mad-made sun, to show that we lead the world in Project H-Power Unlimited.

The atom men who have won the first round against their scientific big brothers, Russia and America, have already planned the second stage. It will end in building a prototype H-power station which will pay its own way.

TOO CHEAP TO CHARGE

It is this machine which will be the prototype of the new monster power stations which would farm the sun's energy and make power too cheap to charge for it—except to the biggest consumers.

Another member of the staff said he thought they might have an experimental model of a power station in ten years although it might take longer.

Harwell rolled back the steel doors of the hangar where Zeta sits to let scientists and journalists look at the Wellsian machine. Two other man-made suns sit beside it.

There is another "sun"—the second largest in the world—but it is 20 miles away, at Aldermaston. This is Scepire, which scientists have

MEN OF HARWELL SHOW THE WORLD HOW H-BOMB WAS TAMED

Now it's money galore to keep our lead in atoms for peace

BRITAIN UNVEILS HER SUN

The Birmingham Post

Birmingham Gazette

SATURDAY, JANUARY 25, 1958

What the New Source of Power Could Mean

THE TRIUMPH OF ZETA

SIR JOHN COCKCROFT said last night that he is 90 per cent certain that British atomic scientists have already controlled the hydrogen bomb reaction.

By Our Scientific Correspondent

What does it mean? Behind the British Atomic Energy Authority's muted announcement is one of the greatest achievements of all time: the development, on earth, in safety, of the kind of atomic behaviour which occurs in the heart of the sun.

Lightweight atoms raised to a very high temperature fuse together and give off heat. Although Dr. Peter Thonemann and the 50 members of his Zeta team are reluctant to affirm that they have really "done it," this scientific reticence need not distract us from the simple conclusion: success.

How will it affect our lives? One ton of ordinary sea-water can be made to yield as much heat and power as 200 tons of coal. The fuel for Zeta is the heavy hydrogen gas which can be extracted from water, in the fraction of about one ounce per ton.

Free as Water

The oceans of the world will meet all mankind's power needs for a million generations, and we need never be deterred from any venture for lack of fuel. Indeed, electricity from fusion may come to be used almost as freely as water itself.

How soon will this happen? The first fusion power station should be working within 20 years, possibly much sooner. Zeta is consuming more power than it provides; the scientists will be trying from now on to preserve the baby sun in Zeta for more than the split second

Raising the Temperature

Another Harwell table gave the estimated reserves of coal and oil as lasting for another 100 years; reserves of uranium and thorium to supply power for 200 to 300 million years. A power station on the seashore would literally have oceans of fuel before it.

Sir John, after referring to being 90 per cent sure that it was the hydrogen bomb reaction that was being controlled, said: "I would certainly be surprised if they were not thermonuclear neutrons. They are produced in about the right numbers; they increase at about the right rate."

Speaking of high temperatures, officially described as one of the most important results of the research, Sir John Cockcroft said: "To have achieved temperatures a third of those at the centre of the sun (5 million degrees centigrade) and to hold them for so long is a remarkable scientific achievement, and I have no doubt that, within a year, Zeta will far surpass the sun's central temperature."

Dr. R. Carruthers, a principal scientific officer at Harwell, inspecting Zeta.

PROMISE OF

Figure 1.1 – Selection of articles from *The Birmingham Post*, *The Chronicle* and *News Chronicle*. Dated from January and February 1958.

With the energy crisis and climatic change the world faces as of 2024, fusion energy research sees a growing interest. The production of energy is one of the main sources of released greenhouse gases, leading to a warming of the Earth's atmosphere. Among other effects this induces an increase in the frequency of extreme weather events as well as the loss of biodiversity[1]. It is one of the major challenges faced by Humanity in the 21st century. The research activity on climate is compiled by the intergovernmental panel on climate change (IPCC) from which the most recent report can be found here: IPCC reports. For some, fusion energy appears as a solution to meet growing energy demands, while being carbon free, less dangerous than fission and generating less long-lived nuclear waste. However, everything suggests that the development of fusion will take too long to have a real impact on climate change. Its contribution will still be valuable, in the longer term.

Fusion research also represents a ground for scientific and technological developments, pushing the boundaries of our understanding in areas such as materials, superconducting magnets, and high temperature plasmas. As such, it represents a fantastic playground for physicists. Hot plasmas involve complex and nonlinear physics. Fusion devices represent one of the only place on Earth where fundamental and experimental studies can be carried out together on hot plasmas. Among them, turbulence and spontaneous structure formations are of particular interest. They will be the focus of this thesis.

[1]Multiple causes can be identified for the loss of biodiversity, with Earth's warming and extreme events being just one facet of a much broader issue that encompasses the destruction of ecosystems, pollution, spread of invasive species etc.

1.1 Towards a D-T fusion power plant

1.1.1 The fusion reaction

There are two ways to produce energy – more exactly to convert mass energy into kinetic energy – from a nuclei: fission and fusion. The first consists in splitting a heavy nucleus into two lighter elements. The second is the opposite, it consists in fusing two light elements to get a heavier one.

The nucleus of an atom is composed of nucleons that are held close by the strong interaction. This force manifests as a binding potential energy between nucleons: $B(A,Z)$ for a nucleus composed of Z protons, N neutrons and $A = N + Z$. This binding energy translates into a mass defect: the mass of the nucleus is not equal to the sum of the individual masses of its nucleons. From Einstein's relation, there is a direct equivalence between mass and energy:

$$B(A,Z) = \Delta m\, c^2 = (Zm_p + Nm_n)c^2 - M(A,Z)c^2$$

Where c is the speed of light, m_p, m_n and $M(A,Z)$ are the rest mass of proton, neutron and the nucleus composed of Z protons and $A - Z$ neutrons, respectively. Stable nuclei have a positive $B(A,Z)$. The ratio of binding energy per nucleons B/A is illustrated with the Aston curve, displayed in Figure 1.2.

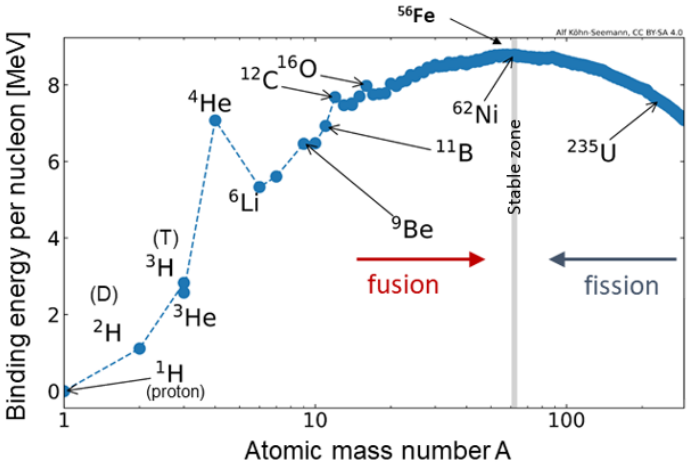

Figure 1.2 – Binding energy per nucleus as a function of the number of nucleons in the nucleus.

Any reaction leading to a higher binding energy per nucleons can release energy. Then, there are two ways to get to the top of the curve: by fusing small elements and by splitting heavy ones. The maximum is given by iron, F_e^{56}, the most stable element. Fission reactors mainly use the fission of Uranium 235 (right of Figure 1.2) with an energy release of the order of 1 MeV per nucleon. At the other end of the Aston curve, the fusion reactions of light materials can reach $4-5$ MeV per nucleon. An example is the fusion of deuterium and tritium into an Helium and a neutron:

$$^2_1D + ^3_1T \longrightarrow\ ^4_2H_e\ (3.52\ MeV) + ^1_0n\ (14.1\ MeV)$$

Which has the potential to free $\approx 17.5\ MeV$ of energy. Fusion energy then appears more *dense* than fission and other chemical energy sources. To give an order of magnitude, the combustion of one ton of coal releases the same energy as the fission of ≈ 0.4 gram of Uranium 235 or the fusion of ≈ 0.1 gram of deuterium and tritium.

However, the energy yield is not the only parameter to look at. The reaction rate is also important. Indeed, during the fusion of two nuclei, two forces are competing: the repulsive electrostatic force and the attractive strong interaction. Conversely to fission, fusion is only accessible by providing enough energy to cross the electrostatic barrier. The cross-section is representative of the interaction probability. It is defined as the ratio of the number of reacting nuclei per time unit on the number of impacting nuclei per time unit and surface unit. It is expressed in barns (1 barn $10^{-28}\ m^2$) and depends on the sole relative velocity of the interacting nuclei. Typical values for fission and fusion reactions are shown in Figure 1.3.

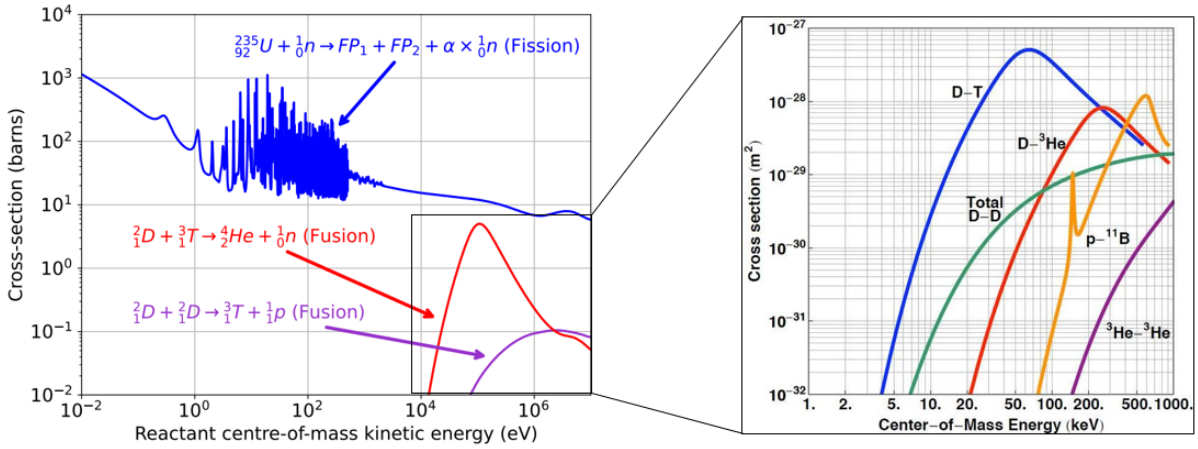

Figure 1.3 – Cross-section for some fission and fusion reactions. On the right are indicated the 'easiest' fusion reactions to achieve.

Fusion reactions peak at about 5 barns while fission is two orders of magnitude above. This ratio accounts for the larger size of the fission nuclei, typically composed of about 100 times more nucleons than deuterium. Also, fission probability is maximum with thermal neutrons at around $\sim 10^{-2}\ eV$ or lower, while fusion is more likely to occur above $\sim 10^{4}\ eV$. Note here and in the following of the thesis that the temperature T is to be understood as a thermal energy E_{th}. Usually expressed in electron-Volt, the correspondence is the following: $E_{th} = k_B T/e$ with $k_B \approx 1.38 \times 10^{-23}$ the Boltzmann constant, T the temperature in Kelvin and $e \approx 1.6 \times 10^{-19}$ C the elementary Coulomb charge. One electron-volt then corresponds to about 11600 K and required temperatures for fusion are of the order of $>$ 100 million degrees. On the right hand side of Figure 1.3 are plotted the cross-sections for some of the easiest fusion reactions to achieve. Deuterium-Tritium is the easiest in the sense that it features the largest cross-section at the smallest temperature. In Figure 1.3, the D-T reaction peaks at 65 keV. In practice, the goal is to have the minimum T/σ_v, where σ_v is the reaction cross-section (see the Lawson criterion in the next section). This minimum is obtained for $T \approx 26\ keV$. Additionally, one aims at maximizing the fusion power that is proportional to σ_v/T^2 and peaks at 13 keV. One way to estimate the maximal energy gain is to calculate the ratio between the fusion energy E_{DT} and

the thermal energy $E_{th,DT}$, the latter being the minimum energy required to maintain the fuel at the optimum temperature. One finds $E_{DT}/E_{th,DT} \sim 17.5 \times 10^3/6T_{[keV]} \approx 3 \times 10^3/T_{[keV]}$, so a maximum gain of about 300 for a 10 *keV* D-T plasma[2]. This leaves, *a priori*, a comfortable margin to achieve economic viability in a DT fusion reactor.

At such temperatures, electrons and light nuclei are totally separated, forming a gas of charged particles called a *plasma*. Plasma is relatively rare on Earth where its natural occurrences can be seen for example in fires and auroras. However, it is the most common state of matter in the universe accounting for more than 99 % of its constituents.
The plasma states yields interesting properties. It is composed of charged particles, such that we can use a magnetic field to confine it, for example in a tokamak (cf. Section 1.2). It is also quasi-neutral at distance larger than the Debye length. This length is the characteristic distance at which the electric charge e_s of a given particle of species 's' can be considered screened by the charges of its neighbours. It is defined as:

$$\lambda_{D,s} = \sqrt{\frac{\varepsilon_0 T_s}{e_s^2 n_s}}$$

With, ε_0 the permeability of free space, T_s and n_s the temperature and particle density of the species 's'. It ranges typically from $10^{-5}m$ for a density and temperature equal to $(n,T) = (10^{19}\ m^{-3}, 300\ eV)$ to $10^{-4}m$ for $(n,T) = (10^{20}\ m^{-3}, 15\ keV)$ in a confined plasma. Above the Debye length, the plasma can be considered as quasi-neutral. Note that quasi-neutrality does not preclude the development of an electric potential and electric field in the plasma. It simply states that such a field exhibits large scale variations only.

1.1.2 Amplification factor and Lawson criterion

Ultimately, the objective is to produce energy: the energy balance of the plasma has to be positive. We briefly introduce the notion of the amplification factor Q – ratio of fusion energy to the auxiliary energy coupled to the plasma – and the Lawson criterion, derived in 1957 [1], which gives an estimation of $Q \sim 1$.

The time evolution of the Plasma internal energy W is governed by the heating P_{heat} and loss P_{loss} powers. In a reactor, heating comes from *alpha* particles produced by the nuclear reactions and auxiliary heating systems (radio frequency waves, energetic neutral beams, ohmic heating): $P_{heat} = P_\alpha + P_{aux}$. Losses come from radiation P_{rad} and cross-field transport P_{transp} due to collisions and – mainly – turbulence. At this level of description, assuming P_{rad} is small, we account for all the losses via the so-called energy confinement time τ_E such that $P_{transp} = W/\tau_E$. The confinement time relates to the reactor efficiency to confine the energy: it measures the characteristic e-folding time of the stored energy in the absence of an external heating.
Additionally, one can define the *Lawson time* τ_L: it represents the confinement time needed to reach ignition – when the entire plasma heating is provided by α-particles – in the absence of additional heating: $\tau_L = W/P_\alpha$.

[2]The thermal energy is $3T_s/2$ per species (electrons and ions), so $3T$ assuming the same electron and ion temperature.

The fusion gain of the D-T reaction is defined as the ratio of the fusion power, $P_{fus} \approx 5P_\alpha$[3] to the auxiliary power. The amplification factor Q is defined as follows:

$$Q = \frac{P_{fus}}{P_{aux}} = \frac{5}{\frac{\tau_L}{\tau_E} - 1} \tag{1.1}$$

Where we have assumed steady-state and negligible radiation. *Break-even* is reached for $Q = 1$ when the fusion power compensates the auxiliary power. It corresponds to a state where the reaction – not the power plant – achieve a net energy gain. Q diverges when the entire plasma heating is provided by α-particles: $\tau_E = \tau_L$, the *ignition*. Such plasmas are also called burning plasmas, or self-heated plasmas. However, it should be highlighted that Q corresponds to the energy balance of the plasma itself. If one wants to estimate the energy production of a nuclear reactor, it is necessary to take into account the energy required to power the rest of the systems. This includes the energy to cool the superconducting magnets, to pump the coolant which circulates in the blankets etc. This global Q is sometimes called $Q_{engineering}$ and is much smaller than Q. For a fusion reactor to be economically viable, it is generally admitted that a Q-factor of the order of $30-40$ needs to be achieved. As a comparison, target values for ITER plasmas are $Q = 5$ for long duration discharges and $Q = 10$ for the most performing ones.

The break-even is estimated with the Lawson criterion. It is often recast in the form of a triple product[4]:

$$nT\tau_E \geq 3 \times 10^{21}\ m^{-3}\ keV\ s \tag{1.2}$$

Exceeding this criterion is a necessary but insufficient condition to produce energy. For how long this criterion can be sustained or having large repetition rates matters as well. For the D-T reaction, it appears that the minimal threshold for $n\tau_E$ is found for $T \sim 26\ keV$. One is then left with two solutions to reach break-even:

- Maximizing the density: for example by compressing a target of fuel with lasers. This method is called *inertial confinement fusion* and holds the record for the largest Q ever achieved. However, the engineering constraint are huge and the currently achieved repetition rates are very low.
- Maximizing the energy confinement time: this is done by confining the plasma with magnetic fields. This is called *magnetic confinement fusion* and is the basis of many designs: Z-pinch, tokamak, stellarator etc.

As stated in the introduction, fusion devices have made progress from the early days of the Zeta pinch device to the most recent experiments. In Figure 1.4 is shown the product $n\tau_E$ as a function of the ion temperature for various inertial and magnetic confinement experiments. On the right hand side is indicated the amplification factor Q.
Note that only the national ignition facility (NIF) based on inertial confinement, has achieved $Q \gtrsim 1$ [3]. Despite the achievement, inertial confinement programs are far from being viable fusion reactors. Currently, the most advanced projects are tokamaks, with ITER and SPARC

[3]The 5 comes from the neutrons energy being about 4 times the α-particle energy.

[4]this expression is valid for plasma temperatures in between 10 and 18 keV, for which the reactivity $\langle\sigma_v\rangle$ of D-T fusion reactions scales like T^2

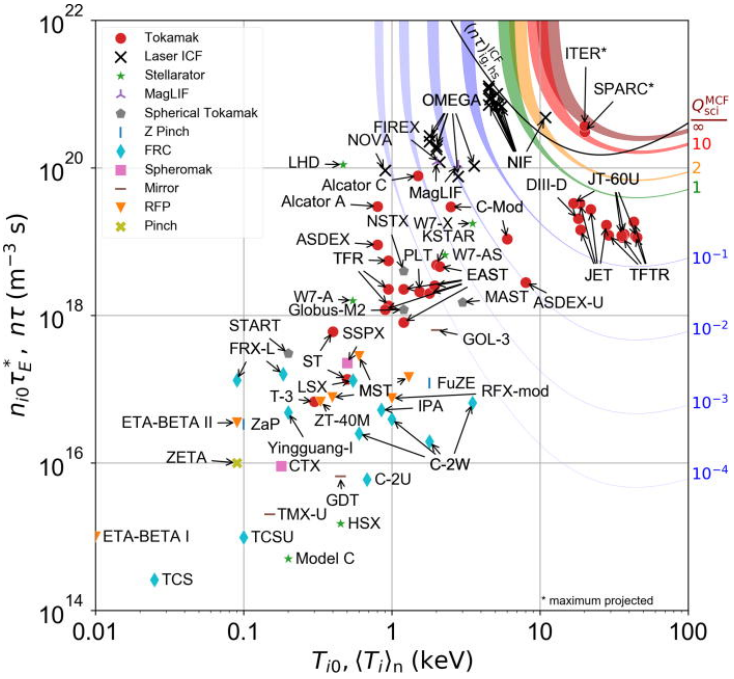

Figure 1.4 – Double product $n\tau_E$ as a function of the ion temperature T_i for many different fusion experiments. The amplification factor Q is indicated on the right hand side. Figure taken from [2].

expecting to reach $Q \sim 10$. The tokamak that reached the largest amplification factor as of 2024 is JET with a peak $Q = 0.64$ achieved in 1997 and $Q = 0.25$ for a $5s$ discharge in 2021 leading to a record released energy of $\sim 60\ MJ$. Comparatively, the inertial confinement experiments leading to $Q \gtrsim 1$ were of the order of $0.2\ MJ$ of released fusion energy.

1.1.3 Challenges faced for the achievement of fusion

The challenges to be addressed in moving from the above principle to energy production are many. Here, we briefly outline some of the main obstacles to achieving a DT-fusion reactor, in no particular order:

- Producing the deuterium and tritium fuel.
- Handling the heat flux and energetic neutrons.
- Prevent or mitigate disruptions and runaway electrons.
- Confine the hot plasma well-enough for the energy gain to be positive.

A fusion reactor plant delivering 1 GW of electric power is expected to require about 100 kg of deuterium and 150 kg of tritium per year. Deuterium is present in sea water (about 32 mg of deuterium per kg of sea water) and is abundant on Earth. Conversely, tritium is a radioactive element with a half-life of 12.3 years. As such, it does not exist in nature and needs to be produced. As of 2024 a few dozens of kg of Tritium are produced annually, mainly through CANDU-type nuclear reactors that use heavy water D_2O as the neutron moderator such that neutron captures can lead to the formation of tritiated water T_2O. For the longer term, the plan is to use the neutrons created by the D-T reaction to trigger reactions with Lithium 6 and

Lithium 7 in the *tritium breeding blankets*:

$$
\begin{aligned}
{}^{6}_{3}L_i + {}^{1}_{0}n &\longrightarrow {}^{4}_{2}H_e + {}^{3}_{1}T + \ (4.78\ MeV) \\
{}^{7}_{3}L_i + {}^{1}_{0}n &\longrightarrow {}^{4}_{2}H_e + {}^{3}_{1}T + {}^{1}_{0}n - \ (2.47\ MeV)
\end{aligned}
$$

The first reaction, with the low abundant ($\approx 7\%$) light isotope, is exo-energetic and exhibits a large cross-section for thermal neutrons. The second reaction requires energy and is characterized by a much smaller cross-section. As of now, it appears essential to rely on ${}^{6}_{3}L_i$ to produce the required Tritium. The technologies behind the breeding of tritium represent an important field of research for fusion, and commercially viable solutions are yet to be tested.

The second point is linked to the high temperatures involved with fusion reactions. One needs to protect the walls of the tokamak from the important heat flux coming from the reactions. The confinement is obtained with the help of strong magnetic fields. Since the development of diverted shapes for the plasma, the heat flux is mainly located on the *divertor* that needs to resist heat fluxes a few times more than the one faced by a space shuttle entering back into the atmosphere, although for much longer periods of time. Additionally, a fusion machine needs to resist energetic neutrons that, being neutral, are not confined by the magnetic field. First because they cause damage to the wall of the tokamak. Second, because they activate the materials. Dedicated efforts are undertaken to develop materials capable of resisting those hard conditions and neutron irradiation.

The third point corresponds to a sudden loss of the magnetic confinement that can occur as a result of large scale instabilities: *the disruption*. The energy stored inside the plasma is violently released which stops the fusion reaction and can damage the divertor and walls of the confinement vessel. The runaway electrons – highly energetic beams – can be generated as a result of a disruption and create irremediable damages to wall elements. To avoid the deleterious effect of disruptions and runaway electrons, plasma scenario are developed to remain in the stable zones of those instabilities. This defines the so-called operational regime. More details on the large scale MHD instabilities are given in Section 1.4.1.

The last point, which is the focus of this thesis, is the confinement of the plasma energy. As stated, the plasma is confined with the help of strong magnetic fields. The behaviour of charged particles and the specific magnetic configuration of a tokamak are detailed in the following section.

1.2 Magnetic configuration of a tokamak

1.2.1 Motion of charged particles in a magnetic field

A charged particle in a uniform and constant magnetic field follows a cyclotron motion, represented in Figure 1.5. It corresponds to a helical trajectory along magnetic field lines of characteristic width and frequency defined by the Larmor radius ρ_s and the gyro-frequency frequency

$\omega_{c,s}$:

$$\omega_{c,s} = \frac{eB}{m_s} \tag{1.3}$$

$$\rho_s = \frac{v_{th,s}}{\omega_{c,s}} = \frac{\sqrt{m_s T_s}}{eB} \tag{1.4}$$

Where B is the magnetic field strength, e is the absolute charge of the particle and $v_{th,s} = \sqrt{T_s/m_s}$ is the thermal speed of species "s" with a temperature T_s and a mass m_s.

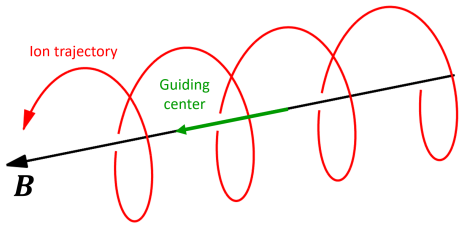

Figure 1.5 – Helical trajectory of an ion along a uniform and constant magnetic field. Adapted from [4].

If the magnetic field $\mathbf{B} = B\mathbf{b}$ is not constant - either in magnitude, direction or time - particle trajectories deviate from magnetic field lines. In tokamaks, the electromagnetic fields vary on small timescales as compared to the cyclotron frequency: $\omega = |\partial_t \log B| \sim |\partial_t \log E| \ll \omega_c$[5]. Additionally, the magnetic field is considered to vary on large scales as compared to the Larmor radius: $\rho_s \ll |\partial_r \log B|$. As a result, one can approach this problem with a perturbative treatment, known as the *adiabatic theory*, by ordering with $\varepsilon = \omega/\omega_c \ll 1$. Within the framework of the adiabatic theory, the particle motion can be decomposed in a slow and fast dynamics as follows:

$$\mathbf{v} = \langle \mathbf{v} \rangle + \widetilde{\mathbf{v}}$$

The equilibrium quantity is obtained by averaging over a cyclotron motion: $\langle \mathbf{v} \rangle = \int \mathbf{v}\, d\varphi_c/2\pi$, where φ_c stands for the cyclotron phase. Consistently, as we shall see in the following, fast variables represent only the cyclotron motion and have zero mean. The equilibrium magnetic field is approximated by its value at the guiding center: $\langle \mathbf{B} \rangle \approx B_G \mathbf{b}$. The cyclotron average of a charged particle dynamics immersed in an electromagnetic field then obeys Newton's equation:

$$m_s \frac{d\langle \mathbf{v} \rangle}{dt} = e_s \left[\langle \mathbf{E} \rangle + \langle \mathbf{v} \rangle \times \mathbf{B}_G + \langle \widetilde{v} \times \widetilde{B} \rangle \right] \tag{1.5}$$

The last term on the right hand side can be recast in the form of:

$$\langle \widetilde{v} \times \widetilde{B} \rangle = -\frac{\mu_s}{e_s} \nabla B_G$$

[5]This assumption can be challenged when cyclotron heating is used. However, it can be shown that the change in the frequency stays relatively small as compared to the wave frequency.

Where, $\mu_s \equiv e_s \omega_c \rho_c^2/2$ is the adiabatic invariant that depends on the charge e_s, the cyclotron frequency ω_c and the Larmor radius ρ_c. Equation 1.5 then depends on averaged quantities only:

$$m_s \frac{d\langle \mathbf{v} \rangle}{dt} = e_s \left(\langle \mathbf{E} \rangle + \langle \mathbf{v} \rangle \times \mathbf{B}_G \right) - \mu_s \boldsymbol{\nabla} B_G \tag{1.6}$$

The last term on the right hand side represents the drag force felt by the guiding center in response to the inhomogeneity of the magnetic field at the Larmor radius scale. Considering that the cyclotron-averaged velocity represents the guiding-center velocity, we can decompose it into two components: parallel and perpendicular to the magnetic field: $\langle \mathbf{v} \rangle \sim \mathbf{v}_G \equiv v_\parallel \mathbf{b} + \mathbf{v}_{G\perp}$. The transverse drift is then obtained by projecting Equation 1.6 on the perpendicular direction. The projection of the parallel velocity onto the perpendicular direction generates a centrifugal force which lead to the so-called *curvature drift*, the gradient of $\mathbf{B}$ leads to the *grad-B drift* and the electric field to the *electric drift*. The transverse drifts can be recast as follows:

$$\mathbf{v}_{G_\perp} = \mathbf{v}_E + \mathbf{v}_{g,s}$$

With $\mathbf{v}_E$ the electric drift and $\mathbf{v}_{g,s}$ the sum of the grad-B and curvature drifts. They read,

$$\mathbf{v}_E = \frac{\langle E \rangle \times B}{B^2} \tag{1.7}$$

$$\mathbf{v}_{g,s} = \frac{m_s v_\parallel^2 + \mu_s B}{e_s B^3} \mathbf{B} \times \boldsymbol{\nabla} B + \frac{m_s v_\parallel^2}{e_s B^2} \boldsymbol{\nabla} \times B|_\perp \, . \tag{1.8}$$

The second term on the right hand side of $\mathbf{v}_g$ is negligible in the low-β limit, $\beta = 2\mu_0 p/B^2$ being the ratio of plasma to magnetic pressure. The electric drift is weakly dependent (through the gyro-average operator) on the particle species. The second drift, $\mathbf{v}_g$ is essentially along the vertical direction in tokamaks, because the equilibrium magnetic field is mainly toroidal and because ∇B points horizontally towards the symmetry axis, this drift leads to a vertical charge separation. It is also called *vertical drift*. For a tokamak to properly confine the charged particles, this drift has to be compensated, as detailed in the next section.

Another set of drifts can be derived, this time using the fluid description of the plasma. This second approach recovers the electric drift, and also defines the diamagnetic and polarization drifts. They are also derived here as they will be important in the derivation of the fluid model in chapter 3. The plasma is described by the conservation of its momentum:

$$n_s m_s \left(\frac{\partial}{\partial t} + \mathbf{u}_s \cdot \boldsymbol{\nabla} \right) \mathbf{u}_s = n_s e_s (\mathbf{E} + \mathbf{u}_s \times \mathbf{B}) - \boldsymbol{\nabla} p_s - \boldsymbol{\nabla} \cdot \overline{\overline{\pi}}_s \tag{1.9}$$

With n_s and m_s the density and mass of the species 's'. The pressure is split between the scalar pressure p_s and $\overline{\overline{\pi}}_s$ which contains the anisotropic part of the pressure tensor and the gyro-viscous tensor (that derives from finite Larmor radius effects). Still proceeding within the adiabatic theory, we expand the perpendicular fluid velocity $\mathbf{u}_\perp$ according to the same small

parameter $\varepsilon = \omega/\omega_c$: $\mathbf{u}_\perp = \varepsilon \mathbf{u}_\perp^{(1)} + \varepsilon^2 \mathbf{u}_\perp^{(2)} + O(\varepsilon^3)$. At the first order, one finds:

$$\mathbf{u}_\perp^{(1)} \equiv \mathbf{u}_E + \mathbf{u}_{\star,s} = \frac{\mathbf{E}\times\mathbf{B}}{B^2} + \frac{\mathbf{B}\times\boldsymbol{\nabla} p_s}{n_e e_s B^2} \,. \tag{1.10}$$

The first component corresponds to the electric drift, already derived in the particle-based approach. The second is a fluid quantity only and is known as the *diamagnetic drift*. Since it depends on the charge, it also leads to a transverse current. The drift is sketched in Figure 1.6, it results from the gyromotions and pressure gradient. Consider the particle motion transverse to the magnetic field. In the left column, there are more particles than in the right column due to the density gradient. It follows that in a fluid picture where one integrates over several individual particles (statistical approach) as illustrated by the black rectangle, the gyro-motion of the ions (resp. electrons) lead to a collective downwards (resp. upwards) motion.

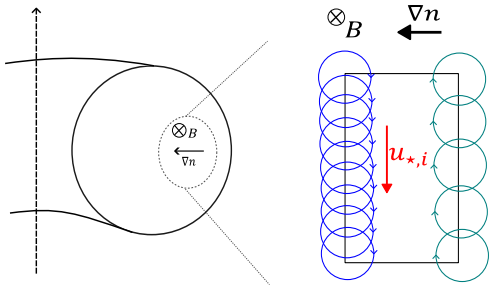

Figure 1.6 – Illustration of the diamagnetic drift.

The second order drift results from the incomplete balance between $d\mathbf{u}_\perp^{(1)}/dt$ and the divergence of the stress tensor. Its derivation can be found in [5]. It is called the *polarization drift* and reads,

$$\mathbf{u}_\perp^{(2)} \equiv \mathbf{u}_{pol,s} = -\frac{m_s}{e_s B^2}\left[\partial_t + (\mathbf{u}_E + \mathbf{u}_\parallel)\cdot\boldsymbol{\nabla}\right]\left(\boldsymbol{\nabla}_\perp \phi + \frac{\boldsymbol{\nabla} p_s}{e_s n_s}\right) \tag{1.11}$$

In this drift, the advection by the diamagnetic flow cancels with the gyro-viscous pressure tensor in a process known as the *diamagnetic cancellation* [5, 6].

The particle-based and fluid approaches are complementary. In the first approach, one is interested in the motion of the guiding center while in the second approach, collective fluid effects are retained. One can reconcile the two approaches and in particular the vertical and diamagnetic drifts by considering their induced current. It can be shown that the same current arise from both drifts when one includes the magnetic moment of the gyromotion in the vertical drift.

The drifts have to be considered when designing a magnetic confinement device. If only a toroidal field is present, a vertical charge separation will inevitably appear as a result of the field curvature, leading to a vertical electric field and an outward radial electric drift of the entire plasma. The tokamak configuration, described in the following section, provides a solution to this issue.

1.2.2 Tokamak magnetic geometry

The principle of a magnetic confinement device is to confine the plasma with strong magnetic fields in a donut-shaped vessel. The principal magnetic field is the toroidal magnetic field B_ξ. Since the field lines are curved, a vertical drift develops leading to a charge separation and a quick loss of the magnetic confinement. So as to compensate the vertical drift, the idea is to add a second field in the poloidal direction: B_θ. The sum of the two fields produces a helical field such that, in first approximation, particles following the field lines travel on the inner and outer side of the magnetic surface during a toroidal turn. The tokamak magnetic configuration is presented in Figure 1.7, for the simplified case of a circular geometry.

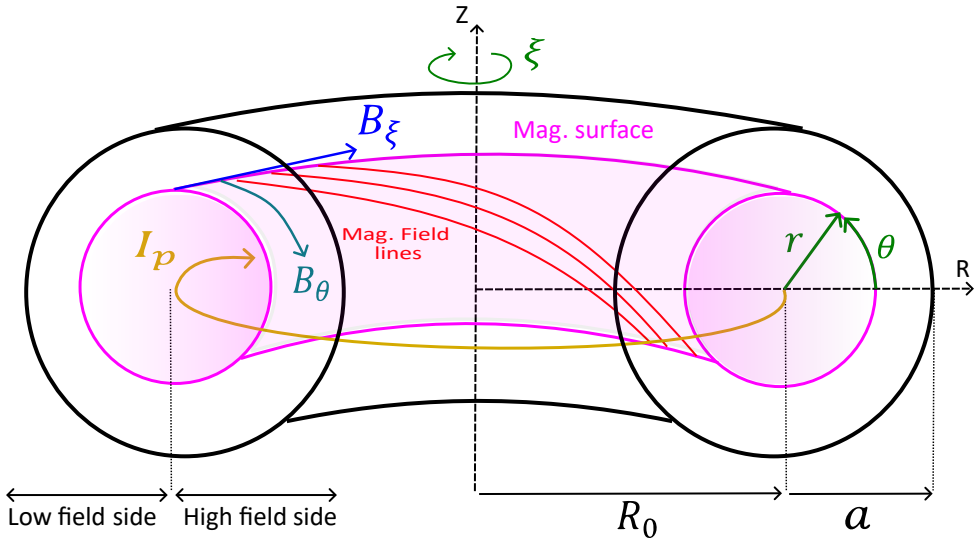

Figure 1.7 – Circular tokamak magnetic configuration.

On this figure, the machine geometry is defined by its major radius R_0, its minor radius a. We define the inverse aspect ratio as $\varepsilon = a/R_0$. By solving the Grad-Shafranov equation, one can resolve the location and the shape of the magnetic *flux surfaces* that delimit surfaces of constant magnetic flux. An example of a circular magnetic surface is shown in pink in Figure 1.7. The poloidal – or toroidal – magnetic flux can be used to label the magnetic surfaces. The normalized radius is then defined with the help of the magnetic flux,

$$\rho = \sqrt{\frac{\psi - \psi_a}{\psi_0 - \psi_a}}\,. \tag{1.12}$$

With, ψ_a the value at the separatrix - last closed flux-surface (i.e. not touching the wall) - and ψ_0 the value on the magnetic axis. The coordinates of the magnetic surfaces in circular geometry can be written as $R = R(\rho) + r(\rho)\cos\theta$, $Z = r(\rho)\sin\theta$, with (r,θ) the polar coordinate in the poloidal plane, where $\theta = 0$ corresponds to the mid plane.

The toroidal component of the magnetic field, B_ξ, is typically one order of magnitude larger than the poloidal component B_θ. Their sum leads to helical field lines characterized by a dimen-

sionless number called the *safety factor*, written $q(r)$ and defined as follows:

$$q(\psi) = \frac{1}{2\pi}\oint \frac{\mathbf{B}\cdot\nabla\xi}{\mathbf{B}\cdot\nabla\theta}\mathrm{d}\theta \approx \frac{rB_\xi}{R_0 B_\theta} \tag{1.13}$$

Where the last expression assumes a large aspect ratio $\varepsilon \ll 1$. The safety factor measures the number of toroidal turns made by a field line makes while completing a single poloidal turn. The poloidal magnetic field can be produced by a toroidal plasma current I_p, this is the principle of a tokamak, or by additional external coils such as performed in stellarators.

When a particle moves along the field line, it explores the magnetic field $B = B_0R_0/R$. Here the subscript '0' is referring to quantities on the magnetic axis. A certain number of particles can be trapped in magnetic wells and undergo a bouncing motion along the field lines. In the poloidal plane, the trajectories have a *banana* shape. Additionally, the trapped particles undergo a *precessional toroidal drift*. The motion of trapped particles is represented in Figure 1.8.

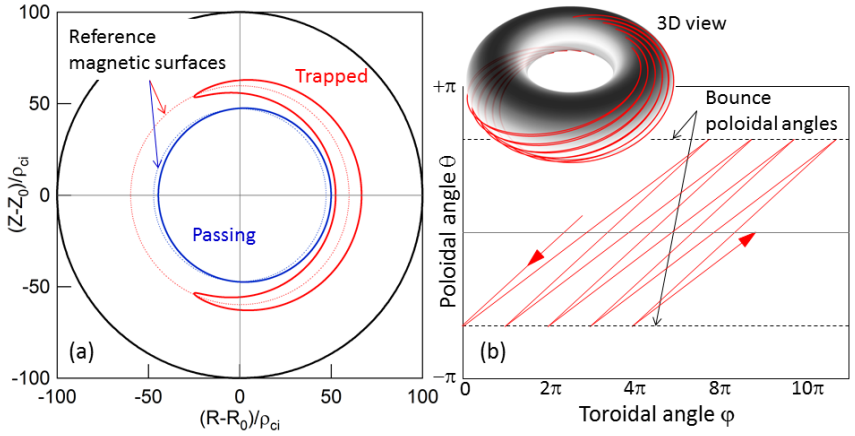

Figure 1.8 – Trajectory of trapped particles in a tokamak magnetic configuration. The particles undergo a bouncing motion along the field lines and a precessional toroidal drift. The projection of the trajectory in the poloidal plane is banana shaped. Courtesy of Y.Sarazin and R.Varennes.

The fraction $f_t \propto \sqrt{2\varepsilon}$ of trapped particles bounce with a bouncing frequency defined as $\omega_b \approx v_T\varepsilon^{1/2}/(qR)$, where $v_T = \sqrt{2T/m}$ is the thermal speed of the particle. A detailed derivation of trapped particles characteristics can be found in refs.[7, 8].

1.2.3 Plasma-wall interaction: Divertor and scrape-off layer

We described above the confined part of a circular plasma. The magnetic configuration is usually diverted, such that the last-closed flux surface forms an X-point close to the *divertor*: the part of the material vessel intersecting the open field lines. The region of the plasma outside of the last-closed flux surface, called the *scrape-off layer* is governed by the plasma-wall interaction.

In this section the SOL is described for the *sheath-limited* regime, where the collisionality is low and the physics is governed by the sheath (interaction with the wall). This regime will be retained for the derivation of the SOL model in chapter 3. In practice, the physics of the SOL is much more complex and involves kinetic effects, plasma-wall interaction and neutrals physics.

Other contributions focused on the SOL physics and neutrals can be found in the form of PhD theses [9, 10, 11], or in books [12, 13].

In the SOL, field lines are connected to the target plates of the divertor. A schematic is shown in Figure 1.9 with a diverted plasma on the left hand side and an unfolded SOL field line on the right hand side. The SOL can be split into two regions: the sheath that governs the plasma-wall interaction itself, typically of a few Debye's lengths ($\sim 10^{-4}$ m). And the pre-sheath of typical length given by the connection between the two divertor plates $L_{\|} = 2\pi qR$ which is of the order of $10 - 100m$. The plasma sheath is a non-neutral layer that forms near surfaces in order to ensure a proper balance between the flux of electrons and ions reaching the material. A large parallel electric field develops in the sheath to accelerate the ions and slow down the electrons due to the species mass ratio: electrons being much lighter than ions, they have low inertia and tend to move much faster.

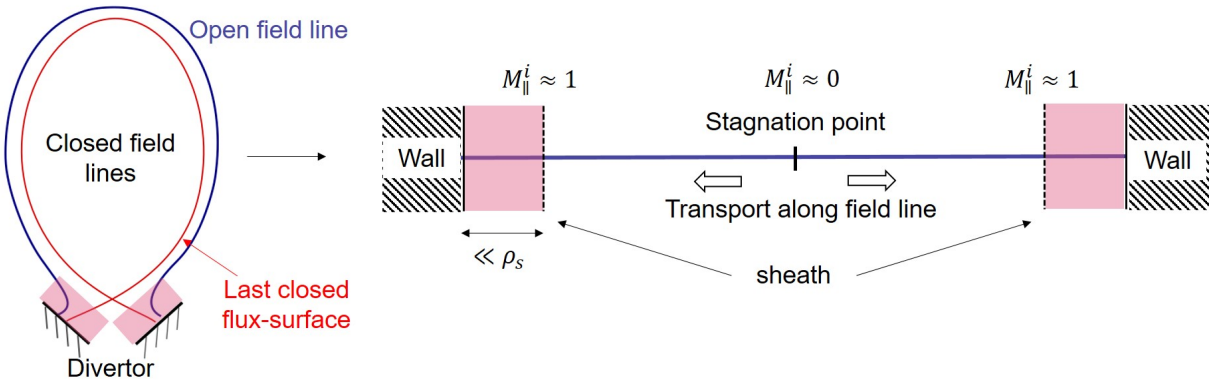

Figure 1.9 – Illustration of a scrape-off layer magnetic field line. (left) On the poloidal plane. (right) Unfolded field line.

In the SOL, the plasma motion along the magnetic field lines is bounded by its interaction with the wall. As it can flow on both target plates (both sides of Figure 1.9 (right)), there is a point where the parallel Mach number $M_{\|} = u_{\|}/c_s$ is equal to zero. This is defined as the *stagnation point*. Here, it is shown at the center of the field line for simplicity, but note that finding its location requires solving the parallel momentum equation. In practice, it is usually closer to the outer mid plane on the low field side [12].

In the following, the transition from pre-sheath to sheath is considered when the ion speed is equal to the sound speed $M_{\|}^i \pm 1$, known as the *Bohm criterion*. It is challenging in practice to define the entry of the sheath with Bohm's criterion because defining the sound speed is difficult in low collisional SOL plasmas. It depends on the assumption made for the closure: isothermal, Maxwellian, polytropic etc. [14]. Additionally, the density at the sheath entrance is assumed to equal half the density at the stagnation point: $n^{sh} = n_s/2$. See [12] (section 1.8) for more details.

1.2.4 Prediction of the potential drop in the sheath

We derive the potential drop $\Delta\phi_{sh}$ in the sheath along with the value of the ion and electron fluxes at the sheath entrance. The derivation is based on [12, 14]. The fluxes then will be used

in the derivation of the SOL model Section 3.3.

The typical profiles of electric potential, ion and electron densities are represented Figure 1.10.

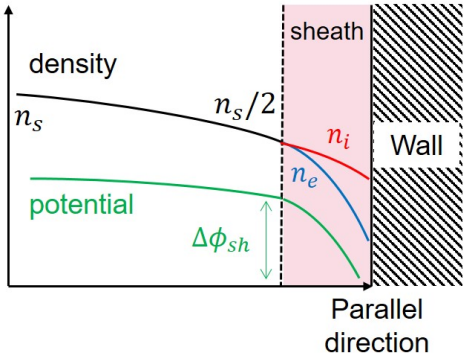

Figure 1.10 – Schematic of electron, ion and electric potential profiles in the pre-sheath and sheath.

We consider a grounded wall, that does not emit any secondary particles. As the Bohm criterion dictates, we consider the entrance of the sheath when the ion parallel Mach number equals 1. Therefore, the flux of ions at the sheath entrance reads,

$$\Gamma_i^{sh} = n_i^{sh} c_s \tag{1.14}$$

With $c_s = \sqrt{\frac{T_e^{sh}+T_i^{sh}}{m_i}}$ the sound speed and $n_i^{sh} = n_e^{sh} = n^{sh}$ the particle density taken at the sheath entrance. Neglecting collisions in the Debye sheath, one can write the Hamiltonian for electrons along the parallel direction (i.e. along a magnetic field line), $H_e = \frac{1}{2}m_e v^2 - e\phi$. Since it does not depend explicitly on time, it is conserved along electrons trajectories. Writing the conservation on a trajectory connecting the sheath entrance to the wall leads to,

$$\frac{1}{2}m_e v(x_{sh})^2 - e\phi(x_{sh}) = \frac{1}{2}m_e v(x_w)^2 - e\phi(x_w)$$

With x_{sh} the sheath entrance and x_w the wall. As a result of the potential drop, only electrons that have a large enough velocity are able to reach the wall. The cut-off velocity v_c discriminates slow electrons that get reflected back into the plasma and fast electrons which cross the barrier of the electric potential and are absorbed in the wall. It reads:

$$v_c = \sqrt{-2e\frac{\Delta\phi_{sh}}{m_e}} \tag{1.15}$$

Since we consider a perfectly absorbing wall with no recycling[6] (emission of neutral particles from the wall as a result of the impact of ions and electrons from the plasma) nor any secondary emission, there are no electrons with velocities $v(x_{sh}) < -v_c$ at the sheath entrance. The electron

[6]This assumption is not fulfilled with present day materials used in tokamaks, where the particle recycling coefficient is larger than 99%.

distribution function at the sheath entrance is then expected to be a truncated Maxwellian of density n_e^{sh} and temperature T_e^{sh},

$$f_e(x_{sh}, v) = n_e^{sh} \sqrt{\frac{m_e}{2\pi T_e^{sh}}} \exp\left(-\frac{m_e v^2}{2T_e^{sh}}\right) \mathscr{H}(v + v_c) \tag{1.16}$$

where $\mathscr{H}(v+v_c)$ is the Heaviside function that is equal to unity when $v \geq -v_c$ and zero otherwise. Note that since the Maxwellian is truncated, n_e^{sh} and T_e^{sh}, does not exactly correspond to the density and temperature at the sheath entrance. Using this, the expression of the electron flux at the sheath entrance is,

$$\begin{aligned}\Gamma_e^{sh} &= n_e^{sh} \sqrt{\frac{m_e}{2\pi T_e^{sh}}} \int_{-v_c}^{+\infty} dv\, v \exp\left(-\frac{m_e v^2}{2T_e^{sh}}\right) \\ &= n_e^{sh} \sqrt{\frac{T_e^{sh}}{2\pi m_e}} \exp\left(\frac{e\Delta\phi_{sh}}{T_e^{sh}}\right)\end{aligned} \tag{1.17}$$

By equating the electron and ion fluxes we retrieve the prediction of the sheath potential drop,

$$\Lambda \equiv \Delta\phi_{sh} = \frac{T_e^{sh}}{e} \log\left(\sqrt{2\pi \frac{m_e}{m_i}\left(1 + \frac{T_i^{sh}}{T_e^{sh}}\right)}\right) \tag{1.18}$$

Note that Λ depends on the radial direction mainly as a result of the electron temperature. Its radial dependence has implications on the radial electric field that arises in the scrape-off layer, see Section 3.3.

1.3 Example of Tokamaks and main dimensionless parameters

In this section, we briefly present the two tokamaks on which experiments have been conducted and used in this work. Then, we summarize the main dimensionless parameters in a tokamak. The Typical length and time scales involved in fusion plasmas are summarized in Section A.2.

To give an idea about what a tokamak looks like, the outside of the WEST tokamak (left) and the inside of the "Tokamak à configuration variable (TCV)" (right) are displayed in Figure 1.11. The first is located at CEA, Cadarache and the second at the SPC in Lausanne.[7]
Tore Supra (TS), now WEST, is a super-conducting tokamak of major radius 2.4 m and minor radius 0.7 m with a nominal on-axis magnetic field of $B_T \approx 4.5\ T$ (usually operated at 3.8 T). It has been designed for long plasma operations in limiter configurations. TCV is a tokamak three times more high than large. It has a large number of magnetic coils enabling large flexibility in terms of shapes and divertor configurations. It has a major radius of $R = 0.88\ m$, a minor radius of $a = 0.25\ m$ and an on-axis toroidal magnetic field of $B_{tor} < 1.4\ T$. In chapter 5, we use data collected in Tore Supra and we perform experiments in TCV.

Several dimensionless numbers can be linked to the plasma geometry and dynamics. Some

[7] A picture of this thesis author in front of TCV can be found in Section A.1.

(a)

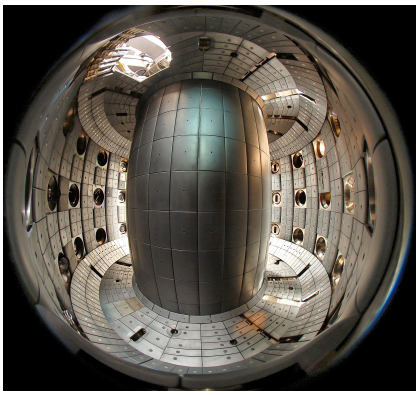

(b)

Figure 1.11 – (a) WEST torus hall, credits: C. Roux. (b) Inside of TCV vessel, credits: A. Herzog.

of them, deemed important for the present work are defined in the following.

- The **inverse aspect ratio**: $\varepsilon = a/R$, ratio of the minor to major radii.
- The **safety factor**: $q = (rB_\xi)/(R_0 B_\theta)$.
- The **plasma beta**: defined by the ratio of the plasma to magnetic pressure: $\beta = 2\mu_0 p/B^2$. This parameter is usually of the order of a few % in a tokamak. For large values of β, electro-magnetic effects greatly influence the behaviour of the plasma.
- The **collisionality**: can be expressed in multiple ways. A popular choice uses the ratio between the detraping and bounce frequencies [8]. It reads,

$$\nu_\star \sim \varepsilon^{-3/2} \frac{qR}{v_T} \nu_i \tag{1.19}$$

  With ν_i the ion collision frequency and $v_{T,i} = \sqrt{2T_i/m_i}$ the thermal speed of the ions. Alternatively, for plasma dominated by electron dynamics (in terms of turbulence, transport), one can define nu-star with the electron-ion collision frequency. The collisionality parameter defines the neoclassical transport regimes briefly described in Section 1.4.2.
- The **normalized Larmor radius**: $\rho_\star = \rho_s/a$, with $\rho_s = \sqrt{m_i T_e}/(eB)$ the sound Larmor radius. Alternatively, rho-star can be defined with the normalized electron or ion Larmor radii.
- The **parallel Mach number**: ratio of the sound speed, $c_s = \sqrt{T_e + T_i} m_i$ to the parallel velocity $M_\parallel = v_\xi/c_s$. Note that the sound speed is a definition, often considered for normalization purposes but does not correspond to the velocity of sound waves in the plasma *per se*.

1.4 Plasma confinement: the key players

In a tokamak, the confinement of the particles is ensured under the triple condition that:

1. The system is axisymmetric, i.e. the Lagrangian associated with the particle motion is independent of the toroidal direction.

2. The scalar and vector potential of the electromagnetic field does not depend explicitly on time.
3. The adiabatic assumption is verified, i.e. the magnetic field evolves slowly (in space and time) in comparison to the cyclotron motion.

Each of the above condition is linked to a motion invariant. Respectively, the toroidal kinetic momentum, the energy and magnetic moment (adiabatic invariant). The invariants are associated to three periodic directions: the toroidal ξ, the poloidal θ and the cyclotronic phase φ_c. In turn, the particles motion are integrable in the confined region. Any phenomenon breaking one of the invariant leads to a cross-field – across the magnetic field – transport. The MHD modes and the turbulence break condition 1 and 2. The Coulomb collisions break the condition 3.

1.4.1 MHD modes

The first fusion devices such as Z-pinch configurations and early tokamaks were prone to the development of large scale modes – of $k_r a \sim 1$ with k_r the radial wavenumber and a the minor radius – leading to a quick confinement loss. In those categories entered principally the current-driven instabilities and magneto-hydrodynamic (MHD) modes. The zoology of MHD modes is wide: tearing, sausage, fishbone, sawtooth etc. [7]. To give an idea we illustrate here one of the most problematic: the kink instability.

The kink is a $m = 1$ mode (m being the poloidal wavenumber), characterized by a transverse displacement of a plasma column from its center of mass. It is illustrated in Figure 1.12. On one side of the plasma column there is an area of large curvature leading to a strong magnetic pressure, while the small curvature region leads to a weak magnetic pressure. As a result, the perturbation continue to grow. Eventually, the plasma column touches the confinement vessel walls giving rise to a violent disruption.

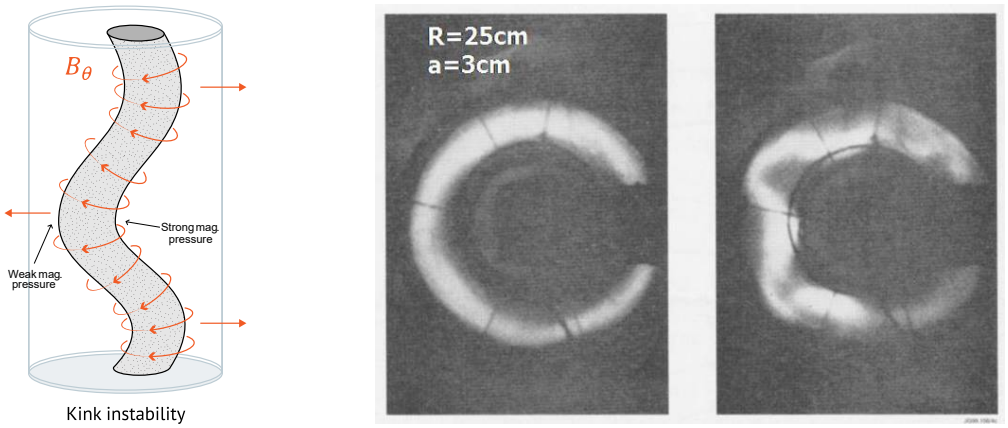

(a) (b)

Figure 1.12 – (a) Illustration of the kink instability on a plasma column, adapted from energyencyclopedia.com . (b) Photo of the kink instability on a Z-pinch device (early 50s), taken from Wikipedia.

It can be shown that the kink instability develops with a characteristic wavelength of $L_{kink} = 2\pi r B_\xi / B_\theta$. If L_{kink} is larger than the perimeter of the machine, $2\pi R$, then the kink cannot form.

This is the so-called *Kruskal-Shafranov limit*, that gives the condition $rB_\xi/(RB_\theta) \equiv q > 1$. It results that in present-day tokamak, the safety factor profile is constrained by the development of these MHD modes. Their thresholds have been largely investigated [15], such that modern-day tokamaks operate mostly free from these large scale MHD modes.

1.4.2 Neoclassical and turbulent transport

Consider now a MHD-stable configuration. Non-vanishing fluxes of particles and energy still exist across the magnetic surfaces. Those fluxes are caused by the collisions, generating the neoclassical transport (enhanced collisional transport due to the effect of particle trajectories in the magnetic configuration of controlled fusion devices), and by turbulence which used to be called "anomalous transport" before its true origin was clarified. The first led to intensive research as soon as machines started to be MHD-stable. However, it rapidly appeared that the fluxes were one order of magnitude above the prediction of neoclassical theory. This discrepancy has been named "anomalous" transport until the difference has been understood as coming from turbulence.

Neoclassical transport

Coulomb collisions, which lead to particle transport in the velocity space, also result in a random-walk in the configuration space with a typical step proportional to the Larmor radius and a typical time of the inverse collision frequency. Since this frequency scales like $n/T^{3/2}$, the collisional transport tends to be very small in the hot core plasma of fusion devices. The effective transport increases when one takes into account the particle trajectories (trapped, passing). This is called the *neoclassical transport*. The details of this theory is out of the scope of this thesis, only some of the main aspects will be discussed here. The interested reader can refer to ref.[8] for a comprehensive review on neoclassical theory.

It has been stated in the previous section that due to the magnetic configuration, some particles were trapped in magnetic wells. Those undergo a bouncing banana motion. Depending on the collisionality, the dynamics of trapped and passing particles is modified. Three regimes of transport can be distinguished as a function of the collisionality $\nu_\star$. They are summarized in Figure 1.13.
The first corresponds to low collisionality regimes $\nu_\star \ll 1$. In this setup, trapped particles have the time to bounce back and forth in between the turning points before getting detrapped. This is called the *banana regime*. The second corresponds to intermediate collisionality regimes $1 < \nu_\star < \varepsilon^{-3/2}$. In this case, the trapped particles do not have the time to explore the entire banana trajectory. The diffusion in this regime is independent of the collisionality, it is called the *Plateau* regime. The third and last regime corresponds to high collisionality $\nu_\star \gg \varepsilon^{-3/2}$. Trapped particles still do not have the time to explore a banana trajectory. Additionally, passing particles also encounter a collision before exploring a full poloidal section. This is called the *Pfirsch-Schlüter* regime.

In practice, many refinements can be considered to this simplified view. For example taking into account nonaxisymmetric equilibria, such as performed in ref.[16].

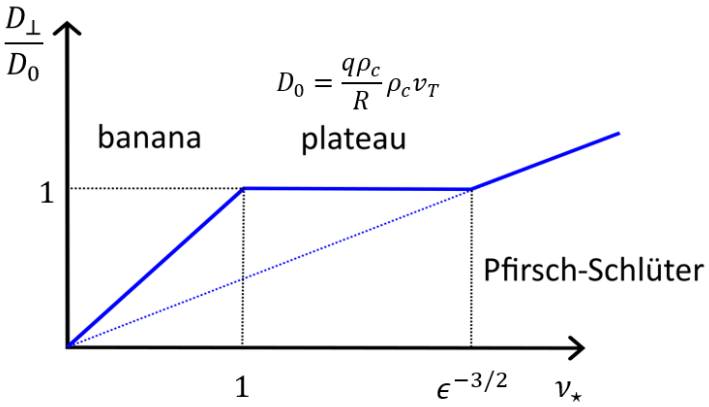

Figure 1.13 – Schematic of the diffusion coefficient as a function of collisionality for the three main neoclassical transport regimes. The diffusion is normalized to $D_0 = q\rho_c^2 v_T/R$ with q the safety factor, R the major radius, v_T the thermal velocity of the particle and ρ_c the Larmor radius. Courtesy of Y. Sarazin.

Turbulent transport

Tokamak plasmas are also subject to a turbulent transport. Turbulence arises due to the strong thermodynamic gradients from the hot and dense core to the cold edge of the plasma. Those gradients, storing an important amount of energy, can reach an instability threshold and will start feeding energy to fluctuations. When those fluctuations become large enough, they interact with each other and usually saturate nonlinearly. This is the onset of *turbulence*, detailed in chapter 2.

Turbulence develops into vortices correlated over a typical size of l_c. An example of electric potential fluctuation is illustrated in Figure 1.14 (left) for a full-tokamak circular simulation performed with the GYSELA code.

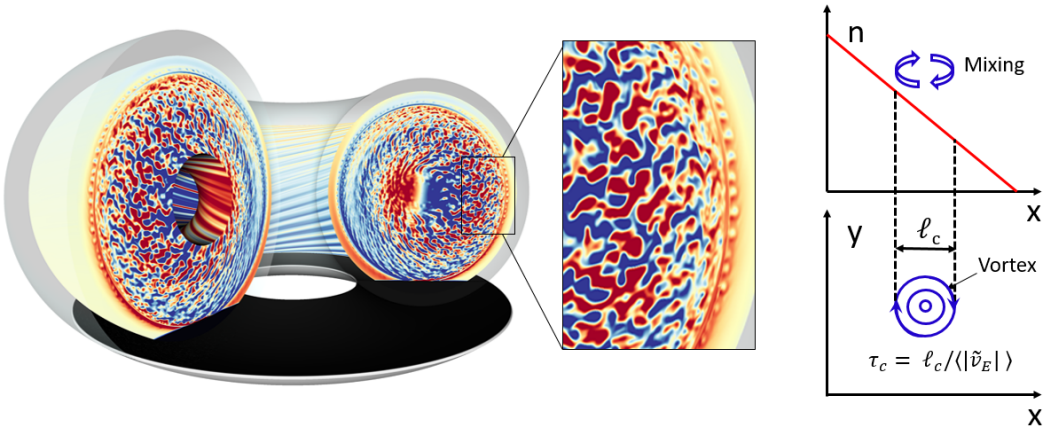

Figure 1.14 – (left) Fluctuation of the electric potential from a GYSELA simulation. Taken from [17]. (b) Physical intuition of the radial diffusion induced by turbulent vortices.

The fluctuations appear as small structures, in red $\widetilde{\phi} > 0$ while $\widetilde{\phi} < 0$ in blue. We can convince ourselves that those fluctuations lead to a transport of heat and particles. Considering the situ-

ation sketched in Figure 1.14 (right), the turbulent vortices mix the plasma on a typical vortex size of l_c with a velocity given by $\widetilde{v}_E = B \times \nabla\widetilde{\phi}/B^2$, akin to the mixing-length considered by Prandtl [18]. The particles undergo a random walk for which the diffusive coefficient reads: $\chi_{turb} \approx \langle|\widetilde{v}_E|\rangle l_c$. In this view, the transport is proportional to the mean velocity fluctuation and to the typical size of the turbulent structure.

In practice, for electrostatic turbulence, one has to consider the phase shift between the density (or temperature) and the electric potential fluctuations. The radial flux of particles is mostly governed by the radial electric drift $\widetilde{u}_{E,r} \approx -\partial_\theta\widetilde{\phi}/(rB)$. The flux surface average of the radial flux reads,

$$\Gamma = \langle\widetilde{n}\widetilde{u}_{E,r}\rangle$$

Consider now the Fourier transform of the density and electric potential in the poloidal direction:

$$\widetilde{n} = \sum_m |\hat{n}_m|\ e^{i(m\theta+\varphi_m^n)}$$
$$\widetilde{\phi} = \sum_m |\hat{\phi}_m|\ e^{i(m\theta+\varphi_m^\phi)}$$

The Fourier coefficients, $\hat{n}_m$, $\hat{\phi}_m$, still depends on time and on the radial and toroidal directions (r,ξ,t). The flux can then be recast as:

$$\Gamma = -\sum_{m>0} 2\frac{m}{rB}\ |\hat{n}_m|\ |\hat{\phi}_m|\ \sin(\varphi_m^n - \varphi_m^\phi) \tag{1.20}$$

Where we have used, $|\hat{n}_{-m}| = |\hat{n}_m|$ and $\varphi_{-m}^n = -\varphi_m^n$ since $\widetilde{n}$ is a real quantity. The same holds for $\widetilde{\phi}$. Hence, for the turbulent particle flux to be non-zero, the density and electric potential fluctuations need to be out of phase.

Turbulence is the main contributor to cross-field transport in tokamaks. It appears crucial to understand and control it, for example by reducing the size of the structures or the fluctuations amplitude. Regimes with a reduced cross-phase between density and electric potential fluctuations also have a reduced transport.

1.4.3 Role of the shear and improved confinement regimes

In this section, we introduce the role of the velocity shear and of the magnetic shear. Both act on the turbulent structures but are generated by very different processes. The magnetic shear arises from the magnetic configuration through the helicity of the field lines. The velocity shear arises mainly through the action of the radial electric field (perpendicular velocity due to the $E \times B$ drift). The radial electric drift itself is generated through several processes. In the core, considering by convention a negative magnetic field, the radial force balance can be recast as:

$$v_\perp = \frac{\langle E_r\rangle}{B} = +\frac{\nabla p_i}{ne} + v_\phi B_\theta - v_\theta B_\phi\ . \tag{1.21}$$

It is typically negative in at the edge of the confined plasma due to the pressure profile, but can become positive further inside. An example is provided in Figure 5.28 for a TCV plasma where the radial electric field becomes positive in the core due to the action of the toroidal velocity. In the scrape-off layer, the radial dependence of Λ can lead to the generation of a positive electric field. An example is displayed in Figure 3.5 using the Tokam1D SOL model derived in Section 3.3. Additionally, turbulence can also generate perpendicular flows through the action of the Reynolds stress, those are detailed in Section 2.3.

Velocity shear

The velocity shear – both induced by the equilibrium and turbulence generated flows – play a role in mitigating turbulence. The role of the velocity shear on plasma turbulence has been elucidated by Biglary, Diamond and Terry (BDT model) in ref.[19]. In the following is provided a brief description of the shear mechanism illustrated in Figure 1.15.

In a tokamak, one is interested in reducing the cross-field transport in the radial direction. Turbulence vortices stir the plasma on a length characteristic of their size (fig at time t_1). Introducing a shear in the poloidal direction elongates the turbulence poloidally (time t_2). In turn, the characteristic mixing length in the radial direction is reduced, and so is the corresponding transport. Provided that the velocity shear is strong enough, it can decorrelate the turbulent vortices, leading to smaller structures (time t_3).

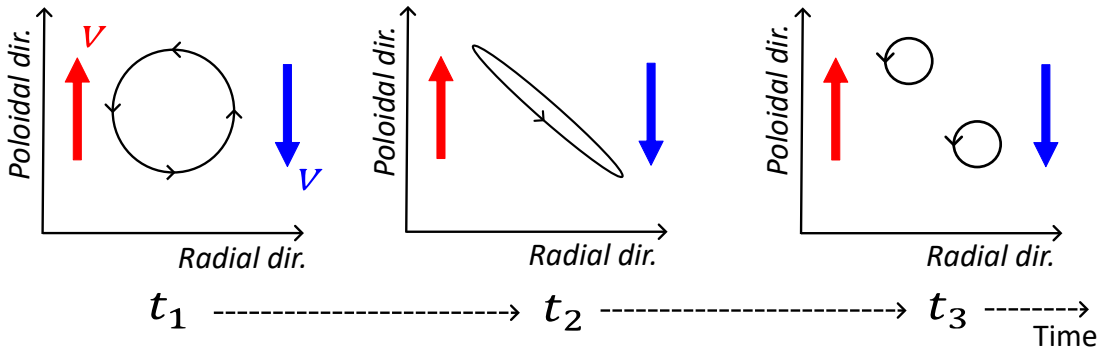

Figure 1.15 – Role of velocity shear on turbulent vortices.

It results from this mechanisms that zones of strong shear lead to *barrier of transport* by greatly reducing the local turbulent transport.

Magnetic shear

In tokamaks, there is also an intrinsic shear imposed by the magnetic field configuration through the helicity of the field lines. The magnetic shear depends on the safety factor profile $q(r)$,

$$s = \frac{r}{q}\frac{dq}{dr} \tag{1.22}$$

The magnetic shear induces a continuous stretching of flux tubes along the parallel direction. Since the turbulent structures are elongated in the parallel direction ($k_{\|} \approx 0$), their transverse cross sections are non-uniform along flux surfaces [20]. The mechanism is illustrated Figure 1.16.

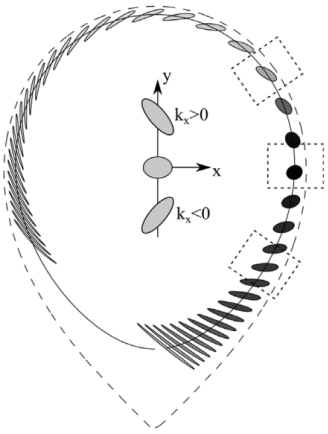

Figure 1.16 – Role of the magnetic shear on a turbulent vortex in the poloidal plane. Extracted from ref.[20].

The magnetic shear is also expected to lead to transport barriers, in particular in the case of magnetic shear reversal. It also plays a role in breaking radially extended streamers [21].

Note that in tokamaks both shears are synergistic. Ref.[22] provides a revue on the two combined effects. In neutral fluids, we could expect the velocity shear to be less effective because it is subject to Kelvin-Helmholtz (KH) instability. In tokamaks, the magnetic shear stabilizes KH instability thus enhancing the role of the velocity shear [23, 19].

Improved confinement regimes: the example of the H-mode

The shear, in particular due to the velocity, is considered crucial to access improved confinement regimes. Several improved confinement regimes have been discovered, with the most emblematic being the high-confinement mode (H-mode), discovered on ASDEX in 1982 [24]. Upon the L-H transition, one observes a large increase of the radial electric field close to the separatrix. This region, labelled the E_r *well*, is considered instrumental in forming an edge transport barrier. The bifurcation of turbulence into a reduced saturated regime leads to the generation of an edge transport barrier. As a result, the plasma builds a steep pressure gradient - a pedestal - to evacuate the particle and heat fluxes. Both the pedestal and E_r well are illustrated in Figure 1.17.

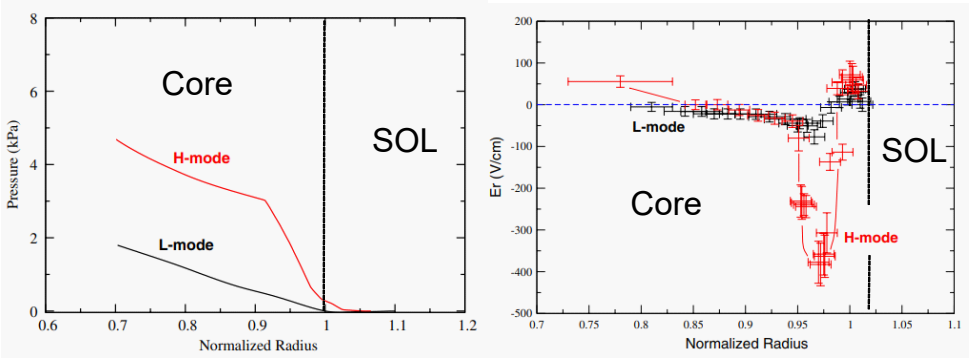

Figure 1.17 – (left) Pressure pedestal in H-mode. (right) Associated radial electric field. Adapted from [25].

The radial electric field well is observed routinely on experimental measurements in tokamaks. However, the reasons for its generation and its dependence regarding various plasma parameters (especially the prediction of its power threshold) are still not clearly understood and remain an active research field. A recent experimental contribution on WEST reviews some of the main results [26]. Gyro-kinetic simulations have also been performed, in particular by looking at the role of the safety factor see ref.[27].

Operating in H-mode leads to a better confinement time of the energy and is one of the solution considered for ITER to reach $Q > 1$. However, H-mode usually comes with the existence of edge localized modes (ELMs): quasi-periodic relaxations of the transport barrier. ELMs are problematic because they release a large fraction (up to 10%) of the energy content of the plasma in a few milliseconds. Their existence can damage the divertor, which is not viable for the long term operation of a fusion power plant. A part of the research has then turned to the mitigation of those modes, for example using resonant magnetic perturbations. Additionally, other improved regimes have been found, some being ELM-free.

Finally, plasma shaping can also greatly increase the confinement. This is the case of negative triangularity, experimentally assessed on TCV in 1997 [28]. Negative triangularity leads to a confinement similar to H-mode, without an edge transport barrier. As such, they may constitute a good alternative to other ELM-free improved confinement regimes.

1.5 Conclusion

With the presentation of the D-T fusion reaction and the tokamak configuration, this chapter has set the scene for the rest of this thesis. The problem of interest is the confinement of the plasma, mainly governed by the turbulent transport. Turbulence being at the heart of the problem, it is introduced in details in the following chapter. The focus will be primarily on turbulence self-organization aspects and on the turbulent regimes.

Chapter 2

Turbulence in fusion plasmas

Contents

Turbulence is crucial for tokamaks as it governs the transport of heat and energy from the core to the walls. It is also a fundamental subject, for which there is still much to discover. In this chapter, a short introduction to turbulence is proposed. The focus is then made on the turbulence self-organization and the current state of the art in simulations and experiments.

2.1 Basics on turbulence: from neutral fluids to fusion plasmas

In the following, the basics on turbulence are provided for the already complex case of an incompressible fluid with constant viscosity. Plasmas can be described as fluids, as such, they are also subject to turbulence. Some of the differences between neutral fluid and fusion plasmas are provided in Section 2.1.3. The incompressible assumption is used here to simplify the description. However, it is frequently acknowledged that fluid with low Mach numbers can be assumed incompressible.

The fluid is described by the conservation of its momentum through Navier-Stokes equation,

$$\boldsymbol{\nabla}\cdot\mathbf{u} = 0 \tag{2.1}$$

$$\partial_t\mathbf{u} + (\mathbf{u}\cdot\boldsymbol{\nabla})\mathbf{u} = -\frac{\boldsymbol{\nabla}p}{\rho} + \nu\nabla^2\mathbf{u} + \mathbf{g} \tag{2.2}$$

Where $\mathbf{u}$ is the velocity of the fluid element in $3d$, p its pressure, ρ its mass, ν its kinetic viscosity and $\mathbf{g}$ the gravity.

2.1.1 What is turbulence?

Turbulence describes a chaotic states of fluids where many temporal and spatial scales are coupled and nonlinearities are important. It usually appears above an instability threshold which depends on thermodynamic gradients.

The first depiction of a turbulent flow, along with the word "turbulence", is attributed to L. Da Vinci in the Codex Atlanticus and in the "Study of water" (c.1510 – 12). In the latter, he represents flows coming out of a dam into a pool as a set of coexisting vortices of different sizes. This concept was formalized mathematically 400 years later by Kolmogorov (see Section 2.1.2) and remains an active area of research. One of his drawings along with a recent simulation trying to reproduce the experiments are displayed in Figure 2.1.

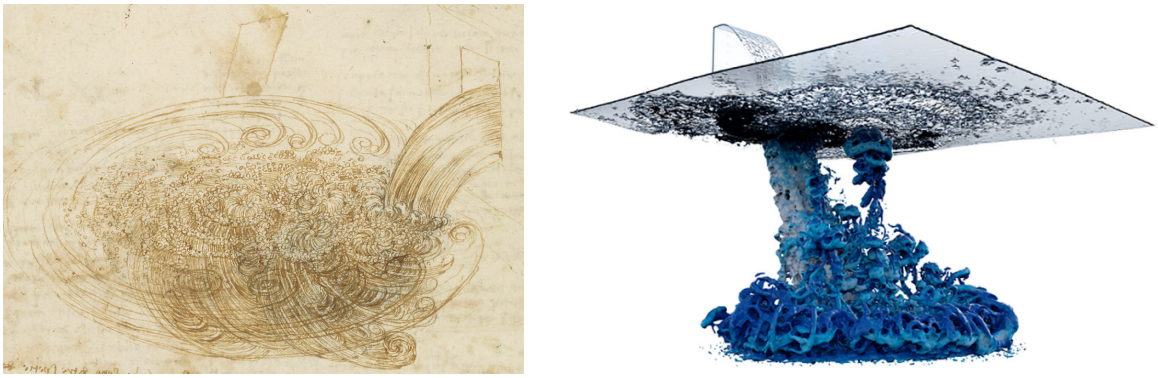

(a) (b)

Figure 2.1 – (a) Leonardo Da Vinci's Studies of water (c.1510 – 12), the fall of a stream of water into a pool. Sheet RCIN 912660. Royal Collection Trust, copyright His Majesty King Charles III 2022. (b) Recent air-water simulation attempting to reproduce the left figure. Adapted from ref.[29].

The "vortices" (or eddies) themselves are not well defined objects. Loosely speaking, they correspond to a region of the fluid behaving coherently. Turbulence have some key aspects that will be detailed in the following sections:

- **Irregularity**. Turbulence flows are often chaotic and difficult to assess with a predictive theory. They have a large number of degrees of freedom and are often treated statistically instead.
- **Mode coupling**. Turbulence is composed of vortices of many sizes interacting together. Their scales can be considered in Fourier space as modes $k = 2\pi/\lambda$ with k the mode number and λ the spatial scale. This notion is usually associated with **Nonlinearities** in the equations. The modes are coupled both with the mean – in time and space – gradients (linear interaction) and between themselves (nonlinearities). Turbulence onset is often considered when the second interaction becomes important.
- **Diffusivity**. Turbulent flows tend to accelerate the mixing of fluids and lead to higher diffusivity. In tokamaks, turbulence leads to a larger transport of heat and particles.

The threshold of turbulence in hydrodynamics, when irregularity becomes important, can be evaluated with the Reynolds number: $\mathscr{R}_e = \rho U L/\eta$, with ρ the fluid density, U its velocity,

L the characteristic length of the system and η the dynamic viscosity. It measures the ratio between inertial and viscous forces. At low $\mathscr{R}_e$ the flow is dominated by viscosity and is described as *laminar*. It means that the fluid moves roughly in the same direction with little lateral mixing. At larger $\mathscr{R}_e$, the flow becomes turbulent. In this case, fluid recirculation occurs with parts going upstream forming vortices and chaotic motions.

2.1.2 Forward and inverse energy cascades

As stated in the previous section, turbulence is a matter of scale coupling. In the classic turbulence picture, there is a transfer of energy from large scales of motion to smaller scales. This is called a direct energy cascade, poetically summarized by L.F. Richardson in 1922,

Big whirls have little whirls that feed on their velocity,
And little whirls have lesser whirls and so on to viscosity.
Lewis Fry Richardson, 1922

This idea has been developed mathematically by A.Kolmogorov in 1941 [30] for the case of incompressible, isotropic, homogeneous $3d$ turbulence. It is schematized in Figure 2.2. Energy is injected at large forcing scales (small k_F). The largest vortices contain most of the kinetic energy. Then, the energy is distributed following a $k^{-5/3}$ law through local-in-k transfers to smaller scales (large k) without dissipation. This represents the inertial subrange. At very small scale, vortices reach the dissipation scale where the energy gets dissipated through heat.

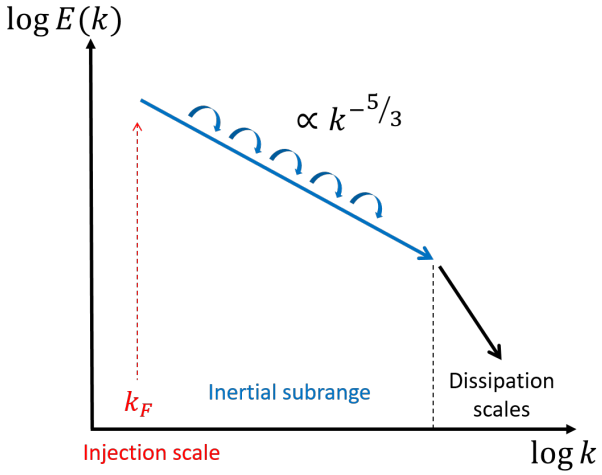

Figure 2.2 – Direct cascade of energy in $3d$ incompressible isotropic homogeneous turbulence as described in K41 theory [30].

The transfer of energy in the inertial subrange can be looked at from a vortex stretching point of view. Let us consider a $3d$ vortex defined by its vorticity $\omega = \nabla \times \mathbf{u}$, the rotational of its velocity. Due to the volume conservation, when this incompressible fluid element gets stretched in one direction, it reduces in the direction perpendicular to the stretching. Stretching different vortices in all sorts of directions, forms a complex figure as represented in Figure 2.3 for a direct numerical simulation of Navier-Stokes equation. Statistically, as there is more vortex stretching

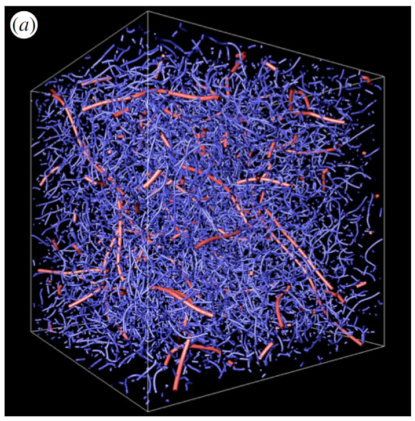

Figure 2.3 – Vortices in an isotropic $3d$ direct numerical simulation of Navier-Stokes. Red curves identify largest scales vortices, from ref.[31].

to vortex squeezing, the energy tends to flow down the cascade to smaller scales.
Vortex stretching works in $3d$ turbulence. Then, the energy can be transferred directly from one mode k_1 to a larger k_2 mode. Even though it requires an incompressible flow, one can speculate that compressible flows with low Mach numbers should behave similarly. Actually, K41 inertial subrange properties have been observed in a large number of simulations and experiments.

In highly anisotropic systems – especially the ones featuring strong stratification – turbulence can be considered as a 2-dimensional problem. This is known for planets atmospheres where turbulence eddies exhibit a small vertical scale as compared to the planetary scale. It is also the case of tokamak plasmas, that have a privileged direction due to the strong toroidal magnetic field. In those systems, vortex stretching cannot occur as the vortices are stuck onto a $2d$ plane. As a result, there is a new conserved quantity in the Navier-Stokes equation: the enstrophy, defined as the square of the vorticity $\Omega \equiv |\omega|^2$. The enstrophy spectrum is linked to the energy spectrum by $\Omega_k \approx k^2 E_k$. The simplification made in $3d$ turbulence where the energy is transferred from one mode to another does not work anymore since it is not possible to transfer both energy and enstrophy in a conservative way using two modes. The transfers now occur between three modes $k_3 = k_1 + k_2$, in a process called a *triad interaction*. The problem of energy and enstrophy transfer has been studied by Fjortoft in ref.[32]. To give an idea of the change of behaviour between $3d$ and $2d$ we give here the simpler demonstration of Lesieur [33].

We consider the following triadic interaction: $k_2 = 2k_1$ and $k_3 = 3k_1$. The conservation of energy implies that between two times t_1 and t_2, the energy variation $\delta E_i \equiv E(k_i, t_2) - E(k_i, t_1)$ satisfies:

$$\delta E_1 + \delta E_2 + \delta E_3 = 0$$

Similarly, the enstrophy conservation reads,

$$k_1^2 \delta E_1 + k_2^2 \delta E_2 + k_3^2 \delta E_3 = 0$$

These two conservation equations lead to the following relationships between the energy and

enstrophy transfers:

$$\delta E_1 = -\frac{5}{8}\delta E_2 \quad ; \quad \delta E_3 = -\frac{3}{8}\delta E_2$$
$$\delta \Omega_1 \equiv k_1^2 \delta E_1 = -\frac{5}{32}k_2^2 \delta E_2 \quad ; \quad \delta \Omega_3 \equiv k_3^2 \delta E_3 = -\frac{27}{32}k_2^2 \delta E_2$$

Hence, if energy is transferred from a central mode k_2 towards k_1 and k_3, the energy received by k_1 is larger than the energy received by k_3. The energy is transferred to lower k (i.e. higher scales). Conversely, the enstrophy received by k_3 is larger than the one obtained by k_1. The enstrophy is transferred to higher k (smaller scales). Note that from the above expression, if the mode k_2 receives energy instead of giving it away, the process reverses. However, from the second law of Thermodynamics we can expect the energy to spread more than concentrate of a single mode so that the system reaches a state of minimum entropy. Then, statistically, the first situation is favoured.
By injecting the energy at scale $1/k_F$, Fjortoft theorem states that more energy is transferred towards larger scales ($k < k_F$) than smaller scales. Similarly, the transfer of enstrophy is performed principally towards smaller scales. This phenomenon is called the dual or inverse cascade of energy and enstrophy. Performing a similar dimensional analysis to Kolmogorov's theory, Kraichnan has established the scaling of the energy and enstrophy transfer in $2d$ [34]. The dual cascade behaviour is shown in Figure 2.4.

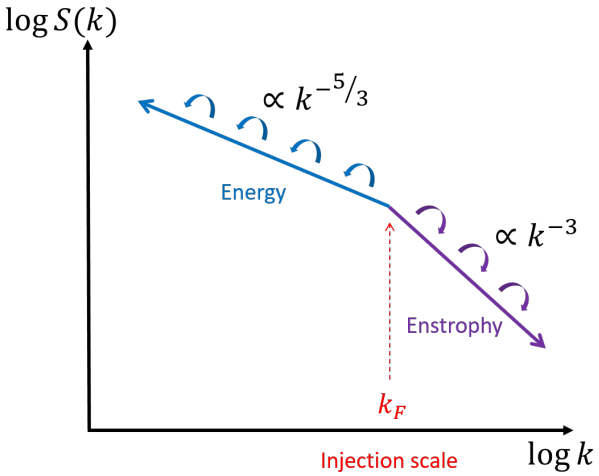

Figure 2.4 – Dual cascade of energy and enstrophy in $2d$ turbulence. $S(k)$ refers to the energy and the enstrophy spectra.

In turn, turbulence in $2d$ tends to present a self-organization at large scales into states of minimum enstrophy. In planetary atmospheres, the generation of those structures impacts the large scale circulation [35].

The transition from $3d$ to $2d$ turbulence, for example increasing the rotation of a fluid disk, is a complex process and represents a research field on its own. In that case, it is possible to decompose the velocity fields into helical modes. Depending on the modes, one can find that some triad interactions lead to a direct energy cascade, while others imply an inverse cascade. The interested reader can refer to ref.[36, 37] for more details about the helical decomposition.

Here we have presented the phenomenology of $3d$ and $2d$ turbulence in a simplified picture where the fluid is forced at a single scale and the transfers of energy and enstrophy are local in Fourier space. Note that the locality of the transfers implies a scale separation since each scale interacts only with its neighbours. It will appear in the following sections that locality and scale separation do not necessarily hold in magnetized plasmas.

2.1.3 Analogies & differences in plasmas

Plasmas can be described as fluid systems that are also subject to turbulence. However, the underlying mechanisms are different than for neutral fluids. In plasmas one needs to take into account magnetic and electric fields together with the behaviour of electrons and ions. The coupled dynamics of the fields with multi-fluid turbulence leads to a more complex situation than the one described previously.

In particular, it is challenging to define the inertial subrange and the dissipation scales. First, there are many instabilities leading to the injection of energy at many separate scales. Second, one needs to take into account Landau resonance that emerges as a result of resonant particle-wave interactions in tokamak plasmas. Finally, non-local interactions also become important. The Reynolds stress, resulting mainly from "non-local in k" interactions of velocity fluctuations that involve disparate scales (anisotropic triadic interactions with e.g. $k_1 \ll k_2, k_3$), is crucial for the self-organization of turbulence. It is detailed along with aspects of self-organization in Section 2.3.

Even though the universality of K41 theory is challenged for plasmas, some attempts have been made at measuring the k-spectrum of energy in tokamak plasmas. First, with microwave [38] and light [39, 40, 41] scattering diagnostics. Then, using Doppler backscattering (DBS) [42, 43]. The latter diagnostic will be detailed in Section 5.1 and used for experiments. An example of a density fluctuations spectrum measured with DBS in the Tore Supra tokamak is given in Figure 2.5.

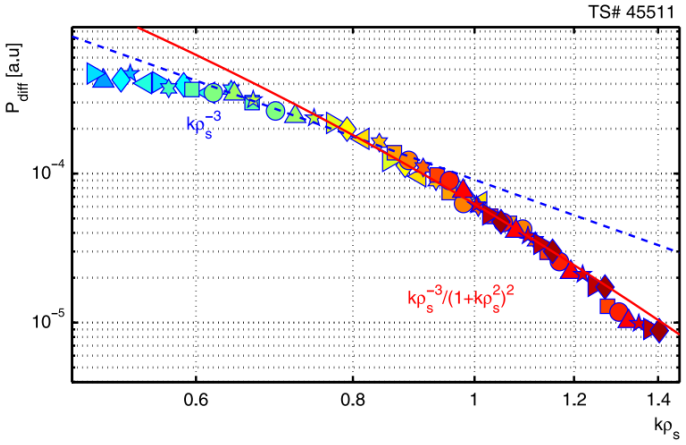

Figure 2.5 – Wavenumber spectra P_{diff} of density fluctuations in discharge #45511 of Tore Supra at $\rho \sim 0.8 \pm 0.08$. The region scaled by k^{-3} corresponds to energy injection while the one scaled by $k^{-3}/(1+k^2)^2$ to corresponds to an energy transfer region. Figure taken from [44].

The behaviour of the spectra in Figure 2.5, has also been investigated using a shell-model applied to drift-wave turbulence, see ref.[45]. The spectrum for density fluctuations is predicted to scale like $k^{-3}/(1+k^2)^2$ when disparate interactions are dominant.

2.2 Main micro-instabilities in tokamak plasmas

A vast number of micro-instabilities has been identified already from the mid 80s, see ref.[46] table III for example. Even though some instabilities have changed names since then, it provides a pretty good overview of the large number of modes considered relevant for tokamaks. Some of the modes and instability relevant for the present work are introduced.

2.2.1 Classes of micro-instabilities: Drift waves & interchange

In the present work, we focus on electrostatic instabilities that belong to two groups, or *classes*. Namely modes originating from the drift wave instability and those originating from an interchange-like instability. The first relies on the particle response to parallel perturbations: it is essentially three dimensional and, as such, depends on a finite parallel wavenumber $k_\parallel$. The second relies on the curvature of the magnetic field.

Drift wave instability

First the stable drift waves are described. Then, by inducing a phase shift between density and electric potential fluctuations, the drift wave instability is detailed. We consider an electric perturbation in an homogeneous magnetic field $\mathbf{B} = B\mathbf{e}_z$ made of a plane wave in the perpendicular direction (y in slab geometry): $\exp[i(k_y y - \omega t)]$, drawn in Figure 2.6 (center). Due to their low inertia, electrons adjust instantaneously to any perturbation whose frequency ω is small with regard to their parallel dynamics, $k_\parallel v_{th,e}$. The electron response in that case is called *adiabatic*. Meaning that the electron follows a Boltzmann response $n_e = n_0 \exp(e\phi/T_e)$ so that,

$$\frac{\delta n_e}{n_{eq}} \approx \frac{e\delta\phi}{T_e} \,. \tag{2.3}$$

In this framework, electron density and electric potential perturbations are in phase. Note that the response of the electron to the electric potential perturbation depends on the parallel direction. Therefore, only modes that exhibit a structure in the parallel direction (i.e. $k_\parallel \neq 0$) are subject to an adiabatic response of the electrons.
The electric potential perturbation leads to an electric field in the perpendicular direction from super-density regions (+) to sub-density regions (-), that reverses sign at the extrema of the potential wave. As a result, the electric drift governs an inward (resp. outward) radial motion of half the super-density (resp. sub-) lobe, and an outward (resp. inward) in the other half. The net result is an oscillation of the wave with a phase velocity along the y-direction, directed upwards.

It is possible to derive the drift wave frequency by considering the continuity equation of the electron density fluctuation: $\partial_t \delta n_e + u_{E,r} dn_{eq}/dr = 0$ with $\widetilde{u}_{E,r}$ the radial component of the

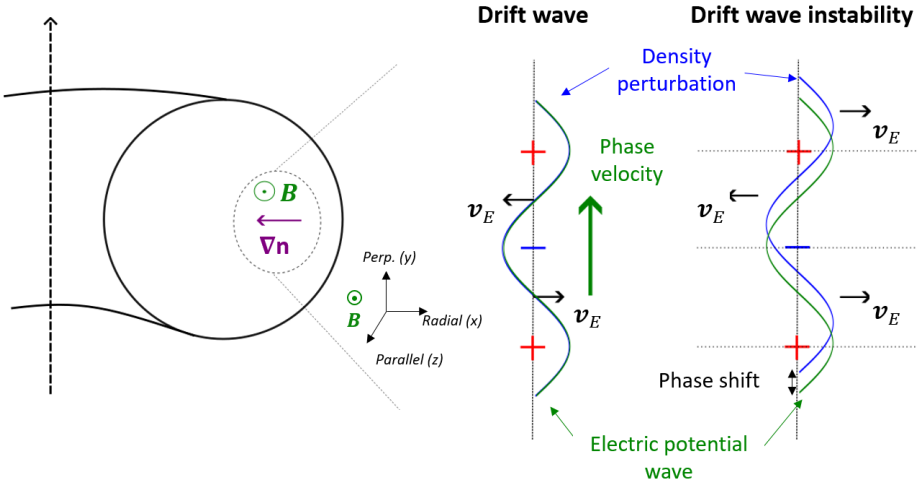

Figure 2.6 – Physical mechanism of the drift wave instability in tokamaks.

fluctuating $E \times B$ drift velocity. Performing the Fourier transform leads to:

$$\omega = -\frac{k_y}{B}\frac{dn_{eq}}{dr}\frac{\delta\phi}{\delta n_e} \,. \tag{2.4}$$

Considering the adiabatic relation Equation 2.3, one is left with the electron drift frequency:

$$\omega = \omega_e^\star = -(k_y\rho_s)c_s\frac{d\log n_{eq}}{dr} \tag{2.5}$$

Where $c_s = \sqrt{T_e/m_i}$ is the sound speed and $\rho_s = \sqrt{m_i T_e}/(eB)$ the sound Larmor radius.

Consider now the case when the electron density and electric potential perturbations are out of phase, drawn on Figure 2.6 (right). The shape of the electric field is still the same as it is governed by the electric potential perturbation. What changes is the location of the super and sub-density regions. Let's focus on the super-density region (on top). This region experiences a net outward motion on average. In other terms, the blue curve is not split in half between the super and sub-density regions. Consequently, the perturbation gets amplified by the electric drift. Applying the same reasoning to the sub-density region leads to a net inward motion of this region. Notice that reversing the sign of the phase shift removes the instability. It turns out that this instability only develops for modes k such that:

$$\frac{\delta n_k}{n_{eq}} = (1 - i\delta_k)\frac{e\delta\phi_k}{T_e} \quad ; \quad \text{with } \delta_k > 0 \tag{2.6}$$

Where k is the wave vector in the direction transverse to the density gradient and the magnetic field (perpendicular direction here). The modes with $\delta_k < 0$ are damped.

The remaining question, then, is what causes the density and electric potential perturbations to become out of phase? Many mechanisms can induce a phase shift, with the two principal being the plasma resistivity and wave-particle resonances. The first breaks up the assumption of an adiabatic response of the electrons (cf.Equation 2.3), it is the mechanism retained for

Tokam1D model derived in chapter 3.

Interchange instability

The interchange instability depends on the relative signs between the pressure gradient and the magnetic field gradient. It is responsible for the "ballooned" form of the turbulence in tokamaks. The idea is illustrated in Figure 2.7.
Let us assume that a perturbation induces a set of vertically aligned charged structures near the equatorial plane, represented as red and blue circles for positive and negative charges respectively. The electric field induced by the cells leads to an outward (resp. inward) radial electric drift v_E (in black) for the upper (resp. lower) dipole. Additionally, the particles undergo the vertical magnetic drift (Equation 1.8): $\mathbf{v}_D \propto \mathbf{B} \times \boldsymbol{\nabla} B/e$ which depends on the particle charge. The vertical drift is indicated as red and blue arrows for the ions and electrons respectively. Let's first focus on the upper dipole. The sum of the electric and vertical drifts implies that ions (resp. electrons) coming from the left (i.e. up-gradient) are channeled towards the positively (resp. negatively) charged cell. Doing the same reasoning for the bottom cell leads to ions (resp. electrons) coming from the right (i.e. down-gradient) channeled into the negative (resp. positive) cell. The two dipoles tend to oppose each other. However, the upper-dipole takes particles from a high pressure region, whereas the bottom dipole finds its source in a low pressure region. It results that there is an imbalance of charges: the positive cell receives more ions than electrons and grows over time.

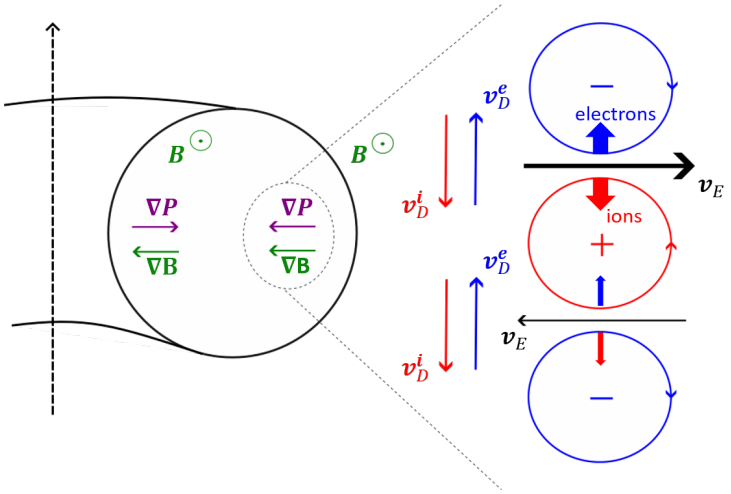

Figure 2.7 – Physical mechanism of the interchange instability in tokamaks.

This instability mechanism works when the pressure and magnetic field gradients are pointing in the same direction. Performing the same analysis on the high field side region leads to a stable situation.

In tokamaks, due to the helicity of the magnetic field lines, particles explore both of these regions. Thus, the plasma parallel current, which carries electric charges between stable and unstable regions has a stabilizing effect. It will appear later on when performing the linear analysis of the drift-waves - interchange Tokam1D system (Section 3.4), that a low resistivity leads to the stabilization of the interchange instability.

Note also that the instability ultimately depends on both the inhomogeneity and curvature of the magnetic field through the vertical drift. The *curvature parameter*, controlling the instability, is further detailed in the next chapter (Section 3.1).

2.2.2 More specific modes: CDW, ITG/RBM, TEM

In practice, the literature involves modes that describe more specifically the physics at hand. In the following is described the classification used in the rest of this thesis. Note that this view is not shared by every authors. The term 'drift waves' stems from the adiabatic framework characterised by transverse drifts. As such, in some contributions, drift waves instabilities represent any micro-instability leading to a net outward transport and interchange as the MHD global scale mode. Here we separate micro-instabilities between interchange-like and drift-waves-like as it will come in handy in the following chapters. Most of the following instabilities are better detailed in review papers [46], or in books [47]. Note that two things have to be distinguished. First, the class of instability to which the mode belongs. Second, the class of particles from which the instability draws its energy. The latter defines turbulence that is ion or electron driven. Typically, ion (resp. electron) driven turbulence has a phase velocity of the sign of the ion (resp. electron) diamagnetic frequency. Usually, drift-wave instabilities are understood to be electron driven, while interchange can be ion or electron driven.

Let us first focus on the drift wave instability class. In this work we are mostly interested with the *collisional drift waves (CDW)*. It corresponds to a phase shift induced by the parallel collisions (resistivity) of the plasma. This mode has been made popular by Hasegawa and Wakatani in 1983 [48]. The resulting model, which bears their name, consists of an equation on the electric potential - sufficient to describe stable drift waves, see Hasegawa-Mima model [49] - and an added equation for density. The phase shift between density and electric potential is induced by a collisional closure using Ohm's law. CDW have been used extensively in simulations owing to the simplicity of their numerical treatment and to the relevance of their governing nonlinearities for magnetized plasma turbulence. They can be expected in tokamaks for some plasma parameters, see for example ref.[50]. One can also note the existence of *slab ITG / ETG*, which has a different drive from toroidal ITG although sharing the same energy source. In this case the phase shift is induced by parallel Landau damping.

As interchange-like instability, one can note the *toroidal ion temperature gradient mode (ITG)* [51, 52, 53], linked to the ion scales $k_\perp \rho_i \sim 0.1 - 1$. It involves specifically the ion temperature as the source of its energy. It was first named η_i-mode, $\eta_i = d\log T_i / d\log n$ being the ratio of the ion temperature gradient to density gradient, because it is destabilized by the temperature gradient and stabilized by the density gradient [54]. An identical mode exists for electrons, labelled ETG, but is involved with electron scales: $k_\perp \rho_i > 10$. Using a similar interchange drive is the *resistive ballooning mode (RBM)*. It is similar to ITG although mostly considered in the pedestal [55, 56, 57]. RBM is usually considered as the resistive analogue of the global interchange MHD mode, sometimes called the *ideal ballooning mode*.

Finally, one can consider *trapped electron modes (TEM)*. They can also be considered interchange-type, as their existence relies on the presence of a curved magnetic field. TEM are waves that can become unstable due to the resonant interaction between an electrostatic perturbation and the toroidal precessional drift of trapped electrons. They were first described by Kadomtsev and

Pogutse in 1966, for reference we provide their review paper as the original one is in Russian [58]. One considers two groups of particles, passing electrons responding adiabatically to low frequency perturbations ($\omega < k_{\parallel} v_{th,e}$), and trapped electrons. The latter are forced to bounce back and forth in magnetic mirrors induced by the machine's magnetic field. Because of the combination of parallel motion and vertical drifts, they drift in the parallel direction. Conversely to passing electrons, they do not average out the effect of a perturbation but may act resonantly with it, giving rise to an instability. Despite being driven by the electrons, TEM develop at the ion scales and are efficiently stabilized by the collisions.

2.2.3 Mode localization on resonant surfaces

Fluctuations in tokamaks tend to localize on resonant surfaces. One can distinguish the coordinates linked to the machine itself: toroidal $\mathbf{e}_{\xi}$ and poloidal $\mathbf{e}_{\theta}$, and those linked to the helical magnetic field: along the magnetic field $\mathbf{e}_{\parallel}$ and perpendicular to it $\mathbf{e}_{\perp}$.

As stated in the previous sections, turbulence in a tokamak is highly anisotropic due to the strong toroidal magnetic field. As a result a mode tends to be extended in the parallel direction. One can define a perturbation ψ by its poloidal and toroidal mode number m and n such that $\psi = \hat{\psi}(r)\exp(i(m\theta + n\xi))$. Using the definition of the safety factor, the parallel wavenumber then reads[1],

$$k_{\parallel} = \frac{1}{R}\left(n + \frac{m}{q}\right) \tag{2.7}$$

Magnetic surfaces, labelled r_{mn}, characterized by a rational $q = -m/n$ then correspond to a vanishing parallel wavenumber. In a tokamak, an electrostatic wave interact resonantly with particles. It can be shown that at a distance $r - r_{mn}$ from the resonant surface, the wave looses energy to passing particles. The result is that waves tend to localize on so called *resonant surfaces* characterized by a rational $q(r_{mn}) = -m/n$.

2.2.4 Electromagnetic fluctuations & fast particles

Electromagnetic (EM) effects are suspected to play a key role in driving plasma turbulence in the pedestal region, especially when approaching the L-H transition. They lead to drift Alfvén turbulence and greatly influence cross-field transport [59, 60, 61]. It can be shown that the key parameter is an effective beta parameter, with $\beta = 2\mu_0 p/B^2$,

$$\beta_{eff} = \beta\left(\frac{qR}{L_p}\right)^2 \tag{2.8}$$

With q the safety factor, R the major radius and L_p the pressure gradient length [62]. It results that in high gradient zones, such as the pedestal, L_p can reach very small values ($L_p \ll a$) and β_{eff} can become of order unity. In certain regimes of beta, EM effects have also been reported to play some role in the SOL, especially regarding the filamentary structures and blob transport [63]. Finally, they are crucial to describe L-H transition and H mode regimes. First because

[1]The derivation is based on $\nabla_{\parallel} \equiv B^{-1}\mathbf{B}\cdot\boldsymbol{\nabla} \approx R^{-1}(\partial_{\xi} + q^{-1}\partial_{\theta})$

this particular regime leads to large gradients, hence small L_p. Second because, H-mode edge-localized-modes (ELMs) require electromagnetism to be described [64]. Some instabilities are also primarily electromagnetic. Examples of this are the *micro-tearing modes (MTM)* and the large scale MHD *tearing modes* [65, 66]. Also of interest are the *kinetic ballooning modes* and, at very large β, the *ideal ballooning modes*, electromagnetic version of the interchange-like RBM [67].

EM effects are mainly twofold: magnetic flutter and magnetic induction. The first leads to a sort of magnetic inertia for the electrons. Indeed, magnetic flutter corresponds to as small perturbations on a field line in the parallel direction, see schematic in Figure 2.8. As a result, particles following the field line now have to follow the corrugations: their parallel dynamics is slowed by the flutter.

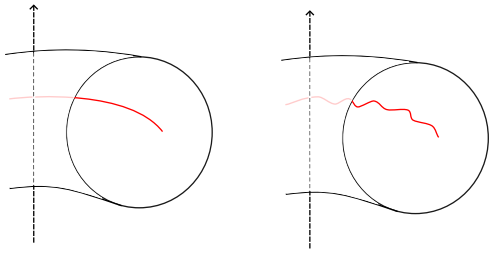

Figure 2.8 – Schematic of a field line magnetic flutter in a tokamak.

In practice, it modifies the parallel gradient operator by adding a component depending on the parallel vector potential. The magnetic induction modifies the electric field which now depends on both the gradient of the electric potential and the time derivative of the vector potential. Details about both effects are given in Section 3.5 in the framework of the Tokam1D model.

Fast particle physics will be crucial in next generation D-T operation machines where heating will primarily come from fast particles. Fast particles also trigger instabilities: some of them are linked to the pressure gradient of the fast particle population. Others are linked to a gradient in the velocity phase space – similarly to a thermodynamic gradient in real space – reaching an instability threshold. This is the case of the bump on tail instability. Considering an equilibrium distribution function f_{eq} as a function of velocity, displayed Figure 2.9. Fast particles, of distribution f_{tail}, interact with the bulk plasma at rest. The bump on tail instability develops when the slope of the distribution function is positive with respect to the velocity.
Fast particles lead to a whole zoology of other instabilities that are outside the scope of the present work. Comprehensive topical reviews can be found in refs.[68, 69].

It is important to note that fast ions are also likely to improve the overall confinement. Recently, a study has been conducted where fast ions are shown to excite Alfvénic instabilities which, in turn, lead to the generation of zonal flows and improve confinement [70]. The physics of zonal flows, in the electrostatic framework, is detailed in Section 2.3.

2.3 Turbulence self-organization

Once developed, turbulence can, in turn, give rise to secondary structures. Some of them are beneficial to the overall confinement while others are expected to be detrimental. In this work,

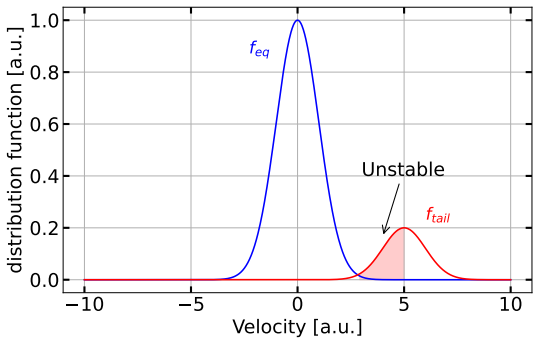

Figure 2.9 – Example of a non-monotonic distribution function in the velocity space leading to a bump on tail instability.

we are interested in avalanches and zonal flows. Both are generated through the underlying turbulence and impact the plasma performance.

2.3.1 From scale separation to scale interplay

In the previous sections, the following simple picture has been laid out. When thermodynamic gradients exceed a certain threshold, an instability is triggered. The fluctuations grow and saturate when mode coupling becomes important. The turbulence now has two ways to evacuate its energy. The first is through the energy cascades described in the previous sections. The second is by producing a transport. This may flatten the gradient below the threshold and stabilize the instability. It follows that the overall confinement is largely dependent on the threshold - linear and nonlinear - loosely defined as *marginality*. The larger the threshold is, the larger the confinement will be [71, 72]. The confinement also depends on the system's *stiffness*: i.e. the instability growth rate as a function of the local driving gradient. If stiffness is important, a small departure from marginality will lead to a large transport. The characteristic time associated with transport is of the order of the confinement time, τ_E. The one associated to cascades is typically of the order of the vortex turnover time $\tau \ll \tau_E$. In the above description, the interaction between turbulence and profiles through cascades and transport is considered as *local*: respectively in terms of scale and space.

Based on these premises, most transport codes also used to be local. Meaning that the transport properties only depend on local thermodynamic gradients. This inherently assumes a scale separation between large scale gradients evolving on long timescales and small scales fluctuations. In this framework, turbulence roughly evolves in a frozen-equilibrium, such that non-linear simulations can be performed at "fixed gradient", namely without considering the back-reaction of turbulent transport on the equilibrium profile. Such simulations are called *gradient-driven (GD)*.

However, it was argued that the scale separation could break down. Non-locality has been tested experimentally by sending carbon impurities in the plasma of the TEXT tokamak. The large variation of temperatures in the machine could not be explained by transport coefficients being functions only of local thermodynamic variables [73][2]. As a matter of fact, the local

[2]This view has been challenged by refs [74, 75]. However, while the temperature variation is explained through

assumption is challenged in tokamaks where the gradient lengths of flux-surface averaged profiles may become commensurable to the fluctuations lengths. Additionally, tokamaks are open systems where fluxes (heat, particles) are prescribed, not gradients. The system then self-consistently finds the balance between gradients and turbulence to overcome the imposed driving fluxes. New models, labelled *flux-driven (FD)*, then appeared to deal with this issue. First for fluids [76, 77, 78, 21], then for gyro-kinetics [79, 80, 81, 82]. Those models have shown the existence of intermittent and large scale transport events, called avalanches. They are described in the following section.
Finally, another secondary structure, called zonal flows can also be generated. This time non locally in Fourier space: small scale turbulence can generate large scale flows, in a way by-passing the turbulent cascades. They are detailed in Section 2.3.3.

2.3.2 Streamers and avalanches

In tokamaks, most of the instabilities tend to develop for the lowest value of radial wavenumber k_r accessible to the system. As a result, turbulence develops into radially-extended vortices, called *streamers*. Those are deemed problematic because they tend to mix large portions of the plasma. They have been extensively studied using GD simulations. When, FD simulations started to emerge, avalanches have been identified. *Avalanches* are a form of turbulence and transport self-organization. They consist in ballistic transport events of heat and particles that propagate over long distances as compared to the correlation length of turbulent eddies. Conversely to a streamer, an avalanche does not necessarily result from a radially extended vortex. It can be composed of several small size cells. The important point is that the avalanche causes the means of its own propagation.

A comparison of GD and FD simulations is displayed in Figure 2.10 taken from [83]. Avalanche-like events are shown to appear in the FD turbulence. This provides one of the first evidence for avalanche-like transport in simulations relevant for fusion plasmas.

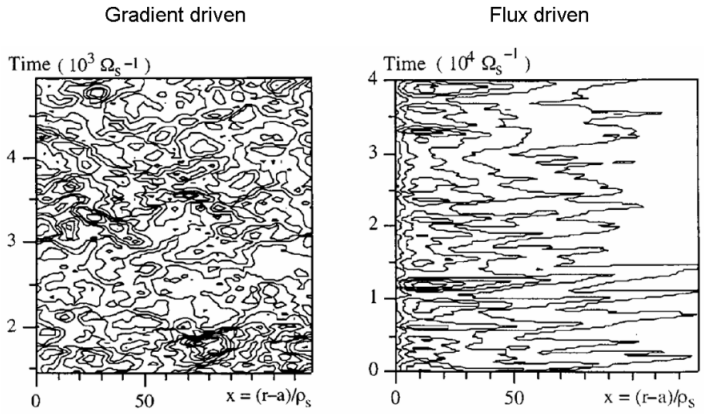

Figure 2.10 – Contour plot of the particle flux in the gradient-driven case (left) and in the flux-driven case (right). Simulations of 2*d* interchange in the scrape-off layer. Taken from ref.[83].

local parameters, the authors do not provide an explanation for the fast modification of the density at the edge, which could in principle be nonlocal.

They are often understood, by analogy with a sand pile, as resulting from a domino-like effect [72], illustrated in Figure 2.11. A local relaxation flattens the profile locally and steepens it on both sides due to conservation laws. The strong gradients on both sides then lead to local strong fluxes, further leading to local flattening. The process can repeat over long distances, resulting in the formation of voids and bumps that propagate radially up and down hill, respectively. Actually, we show in the present work that avalanches can exist even when this mechanism is artificially removed, see Section 4.4.3.

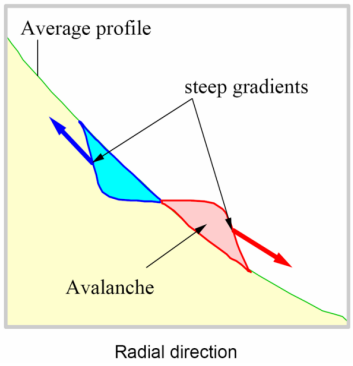

Figure 2.11 – Schematic view of an avalanche-like event. Taken from ref.[84].

Local profile relaxation then appears to be key to the whole dynamics. In that situation, scale separation can no longer be assumed.

Some evidence of avalanches has also been found experimentally using electron cyclotron emission (ECE) diagnostic [85] and more recently with correlation Doppler backscattering (CDBS) [86]. In chapter 5, we study avalanche-like events in TCV using CDBS.

2.3.3 Generation of zonal flows and geodesic acoustic modes

Zonal flows (ZFs) are large scale symmetric flows generated by turbulence. They have been known for a long time in atmospheric sciences where they are contributors to the large scale atmospheric circulation [35]. They also appear in the solar tachocline were they have implications for angular momentum transport [87]. In the case of spherically symmetric systems, they form longitudinally symmetric band like flows. A few examples consist of jet streams on Earth or band-like flows in the atmosphere of Jupiter. In magnetic confinement devices, a ZF corresponds to an electric field perturbation which is constant on a magnetic surface but varies in the radial direction.
One can distinguish several classes of such flows discriminated on the basis of their frequency: a high frequency branch called *geodesic acoustic modes* and a low frequency residual zonal flow, sometimes called "low frequency zonal flow (LFZF)". This latter branch LFZF is sometimes split itself in two sub-categories by comparing with the turbulence broad-band frequency, one with finite frequency $\omega_{ZF} < \omega_{turb}$, the other with almost vanishing frequency $\omega_{ZF} \ll \omega_{turb}$ – sometimes called mean flows in this case (cf. e.g. [88]). In this work, we refer to low frequency zonal flows by 'zonal flows' (ZFs) and call the high frequency component GAM. The denomination 'low frequency zonal flows' (LFZF) is only used in Section 5.2 to avoid any confusion.

ZFs are of significant interest as they provide an additional mechanism for turbulence to saturate in addition to cascades and transport. For magnetic fusion devices, the more energy is stored into flows, the less is available for turbulence to produce transport. In this section, we introduce the physics of ZFs, their generation through Reynolds stress, saturation and impact on turbulence. The GAMs are also briefly introduced.

Zonal flow structure

Consider the situation of an axisymmetric tokamak with a toroidal magnetic field $\mathbf{B} = -B\mathbf{e}_\xi$. The ZF electric potential ϕ_{zf} verifies vanishing toroidal and poloidal wavenumbers: $k_\xi = k_\theta = 0$ and a finite radial wavenumber k_r. The flow symmetries are illustrated in Figure 2.12 in poloidal, toroidal and bird's eye views.

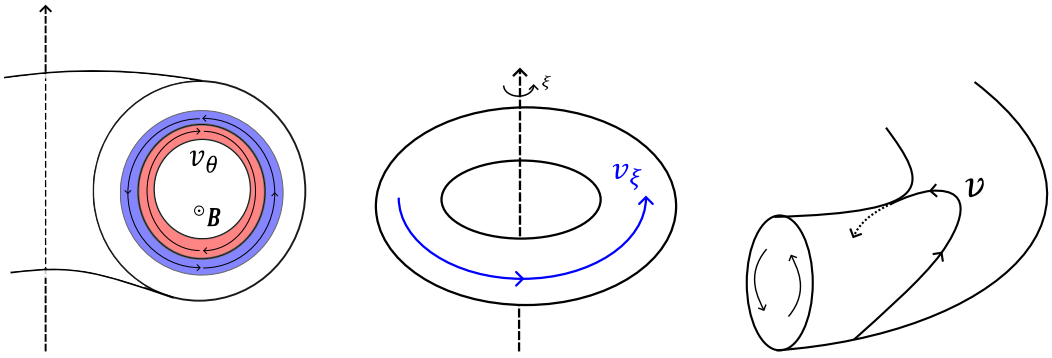

Figure 2.12 – Schematic representation of the zonal flows. (a) Poloidal plane. (b) Toroidal plane. (c) Bird's eye view. (b) and (c) are inspired from 2005 P.Diamond's review on ZF [89].

The flow induces a poloidal rotation through the action of the electric drift: $v_{zf} = \partial_r \phi_{zf}/B$. There is also a return toroidal flow associated with the zonal flows. Indeed, the magnetic field lines are curved due to toroidicity. As a result of geodesic curvature, plasma volume elements on the high field side are less spaced apart than on the low field side. In turn, when a flow arises in the poloidal direction, it induces a plasma compression. To maintain incompressibility, the flow in the poloidal direction is compensated by a return flow along the field lines [89].

Founding contributions on ZFs have been made in the late 70s by Hasegawa [90]. ZF generation theory in fusion plasmas has then been extensively developed by Diamond [91], who also authored a review on the subject [89].

Generation mechanism of ZFs: Reynolds stress

To give an idea of the generation of zonal flows by the Reynolds stress we perform a simple demonstration of the Reynolds decomposition in a neutral fluid. A more complete derivation of the Reynolds stress, using current conservation is performed in chapter 3.

Let us consider an incompressible fluid characterized by the velocity $\mathbf{u}$ in a Cartesian geometry (x, y, z). For simplicity, y and z are assumed as periodic directions, reminiscent of poloidal and toroidal directions in a tokamak. The flow $\mathbf{u} = (u_x, u_y, u_z)$ is described with its momentum

equation:

$$\partial_t \mathbf{u} + (\mathbf{u}\cdot\boldsymbol{\nabla})\mathbf{u} = RHS \tag{2.9}$$

Where *RHS* stands for the right-hand side of the equation, not described. The flow is split between a "flux-surface average" (understood here as an average over y and z) and fluctuating components following a Reynolds decomposition:

$$\mathbf{u} = \langle \mathbf{u} \rangle + \widetilde{\mathbf{u}} \tag{2.10}$$

With $\langle u \rangle = (1/2\pi)^2 \int u \, \mathrm{d}y\mathrm{d}z$ the flux-surface average. Injecting this and projecting the momentum equation on the y direction leads to,

$$\partial_t(\langle u_y \rangle + \widetilde{u}_y) + \boldsymbol{\nabla}\cdot((\langle \mathbf{u} \rangle + \widetilde{\mathbf{u}})(\langle u_y \rangle + \widetilde{u}_y)) = RHS_y \tag{2.11}$$

Taking the flux-surface average of the above equation and noticing that $\langle \widetilde{\mathbf{u}} \rangle = 0$ by construction,

$$\partial_t \langle u_y \rangle + \boldsymbol{\nabla}\cdot(\langle \mathbf{u} \rangle \langle u_y \rangle) + \langle \boldsymbol{\nabla}\cdot(\widetilde{\mathbf{u}}\widetilde{u}_y) \rangle = \langle RHS_y \rangle \tag{2.12}$$

Since, y and z are periodic directions, the average of any derivative along their direction vanishes. The last term on the left-hand side then reduces to,

$$\langle \boldsymbol{\nabla}\cdot(\widetilde{\mathbf{u}}\widetilde{u}_y) \rangle = \partial_x(\langle \widetilde{u}_x \widetilde{u}_y \rangle) \tag{2.13}$$

This force corresponds to the divergence of the Reynolds stress: $\Pi_{xy} = \langle \widetilde{u}_x \widetilde{u}_y \rangle$. The Reynolds stress consists in the cross-correlation of the fluctuations of the poloidal and radial components of the plasma velocity. Now remains the question of what the velocity u consists of. The electric component, $\Pi_E = \langle \widetilde{u}_{E,x} \widetilde{u}_{E,y} \rangle$, generated with the $E \times B$ velocity (Equation 1.7), has long been deemed central in the generation process [91]. Often overlooked at, the diamagnetic component $\Pi_\star = \langle \widetilde{u}_{\star,x} \widetilde{u}_{E,y} \rangle$ through the diamagnetic velocity (Equation 1.10) now also appears as an important mechanism for the poloidal flow generation [92, 93, 94, 95].
Note also that symmetric terms of the form of $\langle u_{\star,y}(u_{E,x} + u_{\star x}) \rangle$ do not exists. They are compensated by terms of the RHS that originate from the gyro-viscous tensor. This process is called the *diamagnetic cancellation* [5], it has already been introduced for the polarization drift (Equation 1.11).

Taking into account the decomposition of the electric potential and the pressure into Fourier modes along the z and y directions, the electric and diamagnetic components of the Reynolds stress read [95],

$$\Pi_E = -2 \sum_n \sum_{m>0} m \Im(\phi^*_{mn} \partial_x \phi_{mn}) \tag{2.14}$$

$$\Pi_\star = -2 \sum_n \sum_{m>0} m \Im(p^*_{mn} \partial_x \phi_{mn}) \tag{2.15}$$

With m and n the y and z modes respectively such that $\phi = \sum_{m,n} \phi_{mn} \exp(i(my + nz))$. A derivation of the Reynolds stress in a more complete geometry can be found in ref.[95]. From this

decomposition, it appears that the Reynolds stress can be both local or non-local. It can possible couple small scales to produce a large scale zonal flow.

It is difficult to have a physical understanding of the Reynolds stress as it is defined as a non-zero statistical average of velocity fluctuations. Note that the Reynolds force can be recast as a vorticity flux, this is called the Taylor identity. The equivalence is derived considering the velocity in the form of stream functions, $\mathbf{u} = \boldsymbol{\nabla} \times (\psi \mathbf{e}_z)$. We perform the demonstration in the simplified case where $u_z = 0$, such that $\mathbf{u} = (\partial_y \psi, -\partial_x \psi, 0)$. The vorticity reads, $\omega = -\nabla_\perp^2 \psi$, with $\nabla_\perp = (\partial_x^2 + \partial_y^2)$. Then, the Reynolds force reads,

$$\langle \partial_x (u_x u_y) \rangle = \langle \partial_x (-\partial_y \psi \partial_x \psi) \rangle = -\langle \frac{1}{2} \partial_y (\partial_x \psi)^2 + \partial_y \psi \partial_x^2 \psi \rangle$$

Noticing that the average of the first term on the right hand side is zero, one can recast the Reynolds force as a radial vorticity flux:

$$\langle \partial_x (u_x u_y) \rangle = \langle u_x \omega_x \rangle$$

Damping mechanisms

Naively, three principal mechanisms can be considered for the damping of ZFs: Landau damping, tertiary instabilities such as Kelvin-Helmholtz (KH) and collisions. Landau damping requires a non-zero $k_\parallel$ and therefore does not affect the low frequency zonal flows. Kelvin-Helmholtz is stabilized by the magnetic shear in tokamaks. Therefore, the KH instability is not expected to strongly limit the extension of ZFs. Finally, only collisional friction remains [96].

Hence, in its simplest form the governing equation of ZF can be written as the balance of the turbulent drive and frictional damping,

$$\partial_t v_{zf} = -\partial_x \Pi_{RS} - \mu v_{zf} \tag{2.16}$$

Geodesic acoustic modes

GAMs represent the high frequency branch of zonal flows. Based on ref.[97], we provide a very short introduction to their rationale. Let us consider a poloidal flow. Due to the compressibility, the poloidal pressure disturbance $\widetilde{p}_\theta$ is compensated by the return toroidal flow v_ξ. This is the situation for the classic zero-frequency ZF which takes an $m = n = 0$ flow structure, m being the poloidal and n the toroidal mode numbers. When the variation of the perturbation v_{zf} is too fast, the parallel flow is not sufficient to compensate the pressure disturbance. It results in an $m = \pm 1$, $n = 0$ pressure mode, called a side band. It is linearly coupled to the $m = 0$ flow. In that situation, the pressure buildup eventually leads to the inversion of the flow which then becomes oscillatory. In the limit of circular flux-surfaces, the compression is maximum at the top and bottom of the plasma, resulting in a $\sin\theta$ pressure sideband.

GAMs have been identified in the late 60s by Winsor [98] who derived the GAM frequency

using an MHD model:

$$\omega_{GAM} = \frac{c_s}{R_0}\sqrt{2\gamma\left(1+\frac{1}{2q^2}\right)} \tag{2.17}$$

With, c_s the sound speed, R_0 the major radius, γ the adiabatic index and q the safety factor. Since then, many contributions focused on their characterization in terms of frequency, amplitude and damping in a variety of magnetic systems and configurations. In contrast to zonal flows, because they are oscillatory, GAMs are linearly damped through Landau resonance. As such, they exist in tokamaks only by being continuously forced.

Back-reaction on turbulence

ZFs being linearly stable, they efficiently feed on turbulence and deplete it from its energy. In turn, the turbulent drive decreases and so does the generation mechanism. The turbulence-ZF coupling is often seen in the form of a predator-prey mechanism, ZF being the predator [99, 100, 101]. An example of the predator-prey behaviour is provided in the next chapter, see Figure 3.3. Note that ZFs can, in principle, also exchange energy with GAM. The predator-prey relation then occurs between three components: background turbulence, GAMs and ZFs [102]. In practice, it can be even more complex as there are possibly interactions with pressure profiles and with avalanche dynamics.

Second, ZFs can also develop extremely low frequency components (already mentioned earlier) that contribute to the mean velocity shear. Accounting for them in numerical simulations reduces the size of turbulent structures. See for example Figure 2.13 adapted from ref.[103].

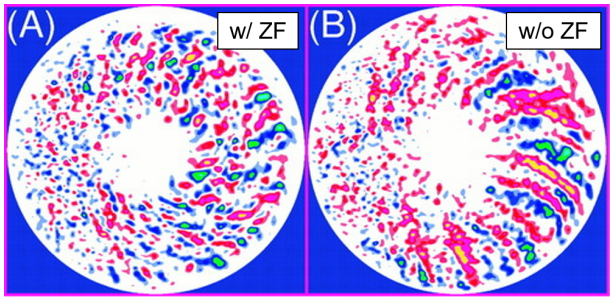

Figure 2.13 – Poloidal contour plots of fluctuation potential. (A) With $\mathbf{E}\times\mathbf{B}$ flows. (B) Without flows. Adapted from ref.[103].

The structures are extended in the radial direction for the case without flows. That is reminiscent of streamers that develop in the absence of velocity shear. Additionally, the turbulence is shown to be ballooned, as expected from the interchange drive detailed in the previous sections. The same trial has been performed using the Tokam1D code presented in the next chapter. Artificially removing ZFs also lead to a turbulence blow-up, see Section C.1.

2.3.4 The particular case of staircases

The shear associated with ZF structures can also generate small transport barriers in the core of the tokamak. It has been shown, in simulations, that plasmas can naturally evolve towards

a state of spatially separated micro transport barriers and sectors of strong avalanche-like transport. This global pattern has been named the $\mathbf{E} \times \mathbf{B}$ *staircase*. It has been predicted first numerically in in ref.[104], then developed in subsequent papers [105, 106] and indirectly hinted at in experiments [107].

The schematic of staircase's properties is shown in Figure 2.14. Staircases yield the following properties:

- Radially structured zonal mean flows.
- Pressure profile corrugations - steps - co-located with ZF shear regions.
- Avalanches in between pressure corrugations, occurring on a size larger than the steps themselves.

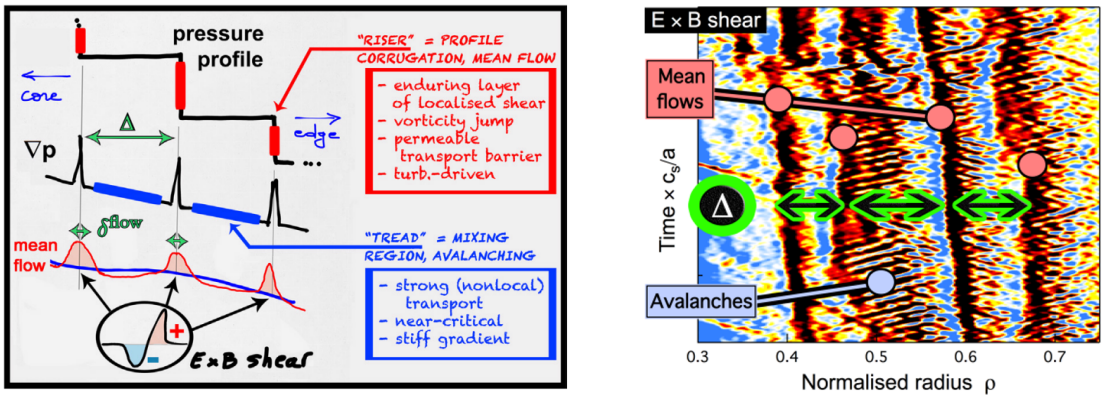

(a) (b)

Figure 2.14 – (a) Schematic view of the $\mathbf{E} \times \mathbf{B}$ staircase. (b) $E \times B$ shear as a function of time and normalised radius. Adapted from ref.[106].

Note that the pressure profile evolves together with the flows. Therefore, scale separation is likely irrelevant to address the physics involved in the generation and possibly sustainment mechanism (this point receives dedicated attention with the Tokam1D code, see Section 4.4.3). In fact, staircases are shown to have a weak amplitude in gradient-driven simulations [106]. The underlying mechanisms leading to the formation of such layered structures is not entirely understood. Additionally, the interplay between zonal flows structures and avalanches is not yet elucidated. Some of these questions will be approached in the present work, they are presented in Section 2.4.3.

The layering is a mechanism shared with many other areas of the physics. In particular when structured zonal flows can be generated, such as the solar tachocline, atmospheres and oceans. In neutral fluids, the staircase step size is often estimated using the Rhines scale [108]. However, the parameter is based on inertial effect which assumes that local interactions are dominant. In fusion plasmas, the phenomena at hand are largely non-local, in particular due to avalanching processes, and such estimation is not necessarily accurate.

2.4 Modelling tools

We review here the hierarchy of models involved in the studies of transport and turbulence. Then, to introduce the work performed in the rest of the thesis, we focus on model reduction and quasi-linear approximation. Some of the current challenges regarding turbulence regimes and self-organization simulations are highlighted.

2.4.1 Hierarchy of models: from first principle to heuristic

A large arsenal of models is available to study turbulence and its self-organization. Each with its own advantages and drawbacks. The different models are discriminated on the basis of their plasma description.

- **The particle description:** consists of solving Newton's equations of motion for each particle in each direction. The equation of motion reads $m_s d_t \mathbf{v}_s = e_s(\mathbf{E} + \mathbf{v}_s \times \mathbf{B}) + \mathbf{F}_{deb}$, with m_s, $\mathbf{v}_s$, e_s the mass, velocity and charge of the ion or electron. Here one needs to take the interaction both with the mean fields (at distances larger than the Debye's length) and with the particles inside the Debye's sphere. Then the fields have to be evolved considering Maxwell's equations. Despite being very precise in terms of information, this description requires a formidable amount of computation. A typical fusion plasma of $\sim 10^{22}$ particles would imply solving as many equations. Even when solving for a very small local part of the machine (hence discarding non local effects), this is too much for current high-performance-computing (HPC) platforms. Additionally, this amount of details is not necessary for the problem at hand where one needs statistical values, such as the mean density, velocity etc.
- **The kinetic description:** consists of a statistical approach. One relies on the distribution function of plasma species, F_s, which gives the probability of finding a particle within a 6-dimensional elementary volume in the vicinity of the position $\mathbf{x}$ and velocity $\mathbf{v}$. The distribution function is evolved using the Fokker-Planck equation:

$$\partial_t F_s + \mathbf{v} \cdot \partial_{\mathbf{x}} F_s + \mathbf{a} \cdot \partial_{\mathbf{v}} F_s = \mathscr{C}(F_s) \tag{2.18}$$

  With $\mathbf{a} = d\mathbf{v}/dt$ the derivative of the velocity $\mathbf{v}$ and $\mathscr{C}(F_s)$ a collision operator. This formalism is tractable for turbulence studies in a fusion plasma environment. However it is time-consuming and resource expensive as one needs to solve the distribution functions in a $6d$ phase-space grid.
- **Gyro-kinetics:** describes a strongly magnetized plasma for which typical frequencies are small in front of the cyclotron frequency. It consists in a phase space reduction from 6-dimensions to 4-dimensions plus the invariant associated to the symmetry of the problem, namely the gyrophase of the cyclotron motion of the particles. This invariant is the magnetic moment $\mu_s = m_s v_\perp^2 / 2B$, ratio of the transverse kinetic energy of the particles divided by the magnetic field. In essence, the gyrokinetic approach is therefore 5-dimensional. The constitutive equation is formed by the gyro-kinetic Fokker-Planck equation. It evolves the gyro-kinetic distribution function, $\bar{F}_s$, in $(\mathbf{x}_G, v_{G\|}, \mu)$, where $\mathbf{x}_G$ is

the gyrocenter position, $v_{G\parallel}$ the gyrocenter parallel velocity and μ the magnetic moment:

$$\partial_t \bar{F}_s + \frac{d\mathbf{x}_G}{dt} \cdot \boldsymbol{\nabla} \hat{F}_s + \frac{dv_{G\parallel}}{dt} \frac{\partial \bar{F}_s}{\partial v_{G\parallel}} = \mathscr{C}(\bar{F}_s) \tag{2.19}$$

Additionally, the quasi-neutrality equation is solved along with the Ampère equation if electromagnetic effects needs to be taken into account. The interested reader is referred to ref.[109] for details on gyro-kinetics.

- **The fluid description:** considers the moments of the distribution function. The moment of order k is computed from the integral of the distribution function as follows: $M_k = \int v^{\otimes k} F_s d^3v$, where $\otimes k$ represents a tensor product of order k. The advantage of this method is that the first moments are related to meaningful quantities. The zero order moment relates to the plasma density, the first to the mean velocity, the trace of the second to the pressure etc. The drawback is that the time evolution of each moment M_k involves the next moment M_{k+1}. That means a closure needs to be considered, such as Braginskii [110] or Zhdanov for multi-species plasmas [111] in the collisional case. In the collisionless – or weakly collisional – case, it is important to capture kinetic effects such as Landau-damping and particles trapping. A few attemps have been done in this direction, which often reveal model dependent, see for example ref.[112, 113] for Landau-damping or [114] for TEM.

5-dimensional gyro-kinetic and 3-dimensional fluid models are the state-of-the-art in terms of plasma turbulence modelling and simulations. The former is principally used in the core. The second is widely used for the edge and the scrape-off layer where the collisionality is larger. See for example gyrokinetic code GYSELA [115] and the Soledge3X fluid code [116]. In both cases however, the simulations are very expensive. They often require months of computation, often without reaching the particle and/or energy confinement time. Additionally, they include so many physics that it is sometimes difficult to infer the underlying mechanisms. In a way, performing those large scale simulations is akin to performing a real tokamak experiment. As complementary tools in this hierarchy of models, reduced models are also widely used. They have the advantage of running much faster, thus allowing large parameter scans. Additionally, by focusing on a reduced number of parameters and by involving dedicated physical cornerstones, they allow one to decipher key nonlinear mechanisms that may be somewhat hidden in more complex simulations. Despite not giving quantitative comparison with experiments and first principle simulations, they help to set up trends and mechanisms that can then be verified using more complex tools.

The reduced models can be separated in two groups. The first group starts from first principle considerations. Assumptions are made allowing to reduce the dimensions of the problem. The game consists in finding the right assumptions to reduce the problem without impacting the physics of interest. The second group consists of heuristic models. The problem is now opposite. One considers a piece of physics of interest. Then, a model is built upon it and compared with first principle simulations or experiments.

In the next chapter, we build a reduced fluid model from first principle considerations. It will be further reduced by considering a single wave vector in the parallel and poloidal directions. It

bears some analogy to a quasi-linear approach, described in the following section.

2.4.2 Basics on the quasi-linear approach

In the Quasi-linear theory (QLT), one is interested in the slow evolution of mean (in a sense to be defined) variables as a result of the fast fluctuation dynamics. By neglecting non-equilibrium mode-mode interactions, all fluctuations are considered as eigenmodes of the system [117]. QLT is usually considered valid in the low Kubo number limit. The idea behind the Kubo number is to compare the amount of time required for a particle to be transported across or between turbulent structures to the duration a particle remains trapped within a turbulent structure. Kubo numbers can have several definitions [118],

$$Ku_1 = \frac{\tau_{jump,\star}}{\tau_{turnover}}$$
$$Ku_2 = \frac{\tau_{lag}}{\tau_{diff,ExB}}$$

The first relates to the ratio of the jumping time due to the diamagnetic velocity to the eddy turnover time. The second stems from the ratio of the Lagrangian correlation time to the particle diffusion time as a result of the $E \times B$ velocity (in radial or poloidal directions). In the low Kubo number limit, a particle cannot sample the totality of the correlated regions it resides in before the landscape – given by the evolutions of the fields – has evolved. Therefore, nonlinearities only result in a modest perturbation of the system. The transport of the particle across the turbulent structures is to some extent comparable to a random walk – diffusive – process.

The following derivation is largely inspired from ref.[119]. Consider a state vector $\mathbf{q}(x,y,t)$ defined on a $2d$ plane (x,y), y being a periodic direction. This can correspond to the poloidal cross-section of a tokamak where x stands for the radial direction and y the poloidal. The evolution of $\mathbf{q}$ is described by a set of partial differential equations (PDE) that can be written as,

$$\partial_t \mathbf{q} = \mathscr{L}[\mathbf{q}] + \mathscr{N}[\mathbf{q},\mathbf{q}] \tag{2.20}$$

Where $\mathscr{L}$ represents a linear operator and $\mathscr{N}$ is a non-linear operator. For simplicity, the non-linear operator includes only quadratic interactions. The state vector is separated between a slow and a fast dynamics following a Reynolds decomposition:

$$\mathbf{q} = \langle \mathbf{q} \rangle + \widetilde{\mathbf{q}} \tag{2.21}$$

In practice, in tokamak plasmas, the brackets usually correspond to a flux-surface average (called a *zonal* average) as well as an average over mesoscopic time durations, intermediate between the energy (or particle) confinement time and the caracteristic time of the fluctuations. Note that performing this decomposition does not imply a scale separation between the two quantities. Injecting the decomposition into Equation 2.20 leads to,

$$\partial_t \langle \mathbf{q} \rangle + \partial_t \widetilde{\mathbf{q}} = \mathscr{L}[\langle \mathbf{q} \rangle] + \mathscr{L}[\widetilde{\mathbf{q}}] + \mathscr{N}[\langle \mathbf{q} \rangle, \langle \mathbf{q} \rangle] + \mathscr{N}[\langle \mathbf{q} \rangle, \widetilde{\mathbf{q}}] + \mathscr{N}[\widetilde{\mathbf{q}}, \langle \mathbf{q} \rangle] + \mathscr{N}[\widetilde{\mathbf{q}}, \widetilde{\mathbf{q}}] \tag{2.22}$$

Taking into account the following relationships:

$$\langle\langle \mathbf{q} \rangle\rangle = \langle \mathbf{q} \rangle \;\; ; \;\; \langle \widetilde{\mathbf{q}} \rangle = 0 \tag{2.23}$$

$$\langle \mathscr{N}[\langle \mathbf{q} \rangle, \widetilde{\mathbf{q}}] \rangle = \langle \mathscr{N}[\widetilde{\mathbf{q}}, \langle \mathbf{q} \rangle \rangle = 0 \tag{2.24}$$

One can separate the equations into equilibrium and fluctuations. The first is obtained by taking the zonal average of the set of PDE. We assume that the zonal average commutes with the time derivative and the various operator, the equation then reads:

$$\partial_t \langle \mathbf{q} \rangle = \mathscr{L}[\langle \mathbf{q} \rangle] + \mathscr{N}[\langle \mathbf{q} \rangle, \langle \mathbf{q} \rangle] + \langle \mathscr{N}[\widetilde{\mathbf{q}}, \widetilde{\mathbf{q}}] \rangle \tag{2.25}$$

Where the last term accounts for every triad interaction resulting in the zonal mode. The remaining equation provides the time evolution of the fluctuations:

$$\partial_t \widetilde{\mathbf{q}} = \mathscr{L}[\widetilde{\mathbf{q}}] + \mathscr{N}[\langle \mathbf{q} \rangle, \widetilde{\mathbf{q}}] + \mathscr{N}[\widetilde{\mathbf{q}}, \langle \mathbf{q} \rangle] + \mathscr{N}[\widetilde{\mathbf{q}}, \widetilde{\mathbf{q}}] - \langle \mathscr{N}[\widetilde{\mathbf{q}}, \widetilde{\mathbf{q}}] \rangle \tag{2.26}$$

Now let us consider the Fourier decomposition of the state vector along the periodic direction:

$$\mathbf{q} = \sum_m \mathbf{q_m} e^{imy} \tag{2.27}$$

One can then project onto each mode $\mathbf{q}_k$:

$$\mathbf{q}_k = \int \mathbf{q} e^{-iky} dy \tag{2.28}$$

This means that one has to solve the triad interactions such that $p + m = k$:

$$\partial_t \mathbf{q}_k = \mathscr{L}[\mathbf{q}_k] + \mathscr{N}[\langle \mathbf{q} \rangle, \mathbf{q}_k] + \mathscr{N}[\mathbf{q}_k, \langle \mathbf{q} \rangle] + (\mathscr{N}[\widetilde{\mathbf{q}}_\mathbf{p}, \widetilde{\mathbf{q}}_\mathbf{m}] - \langle \mathscr{N}[\widetilde{\mathbf{q}}_\mathbf{p}, \widetilde{\mathbf{q}}_\mathbf{m}] \rangle)\big|_k \tag{2.29}$$

The last term on the right hand side can be recast as:

$$(\mathscr{N}[\widetilde{\mathbf{q}}_\mathbf{p}, \widetilde{\mathbf{q}}_\mathbf{m}] - \langle \mathscr{N}[\widetilde{\mathbf{q}}_\mathbf{p}, \widetilde{\mathbf{q}}_\mathbf{m}] \rangle)\big|_k = \sum_{p \neq 0} q_p q_{k-p} \tag{2.30}$$

Excluding $p = 0$ in the sum avoids counting twice the coupling to the mean quantity $\langle q \rangle$. Solving the system then requires to solve the sum for each mode k. This comes with an important computational cost, and involving more dimensions further complicates the system. Quasi-linear approach consists in neglecting the mode-mode interactions, greatly simplifying the resolution. In essence, this amounts to consider that the mode-mode interactions are negligible in comparison to the equilibrium. It works well in small fluctuations amplitude regimes: $\widetilde{\mathbf{q}} \ll \langle \mathbf{q} \rangle$. Alternatively, one could develop a closure to account for some of the effects of the mode-mode interaction without resolving them. One can impose a turbulent cascade, informed from K41 theory for example, to account for those interactions.

A generalization of the QLT consists in retaining NL interactions not only between the fluctuations and the zonal mode (term $\mathscr{N}(\widetilde{\mathbf{q}}, \langle \mathbf{q} \rangle)$ in Equation 2.26) but also between some of the fluctuating modes. This is called the *generalized quasilinear (GQL)* approximation, described

in ref.[119]. Instead of separating between a mean and fluctuating component, one separates the state vector between large and small scales with a spectral filter. It means the equilibrium and fluctuating component now read,

$$\langle \mathbf{q} \rangle = \sum_{|k| \leq \Lambda} \mathbf{q}_k e^{iky} \tag{2.31}$$

$$\widetilde{\mathbf{q}} = \sum_{|k| > \Lambda} \mathbf{q}_k e^{iky} \tag{2.32}$$

The full interactions are retained for the equilibrium modes while the standard quasilinear approach remains for the fluctuating modes. A summary of the conserved triad interaction is illustrated in Figure 2.15.

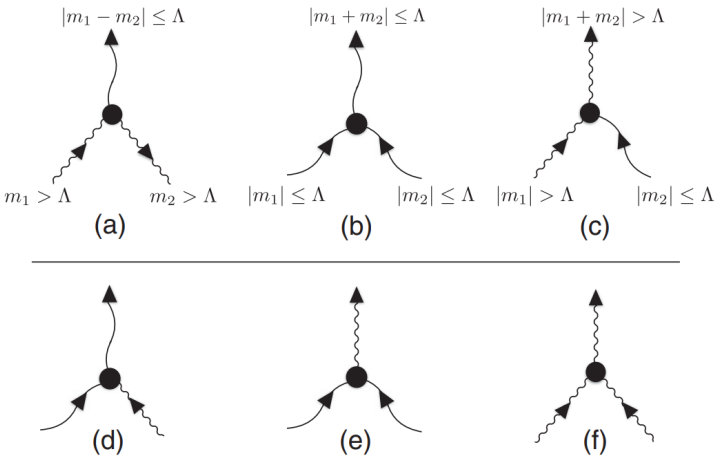

Figure 2.15 – Triad interactions in the generalized quasilinear approximation. Triads (a)-(c) are retained while (d)-(f) are omitted. Taken from [119].

The quasilinear approximation is a particular case of the GQL where $\Lambda = 0$. Conversely, the full non-linear system is obtained when $\Lambda = +\infty$.

To develop the reduced model in the next chapter, the variables are decomposed into an equilibrium and fluctuation equation following a Reynolds decomposition, similarly to QLT. However, in the present case the decomposition is performed with a flux surface average: meaning between zonal and non-zonal modes. *A priori* there is no assumption of timescale separation between zonal and non zonal modes, they are both evolved on an equal footing.

2.4.3 Challenges

Challenges regarding models and simulations are twofold. The first is computational. Performing large scale, first principle simulations is very expensive and time demanding. As a result, a few numbers of simulations are performed. That means we do not have a large knowledge in terms of parameter space. Reduced modelling is less demanding in terms of computation and comes as a possible solution to this. However, it is difficult to account for all the physics, geometry and non-locality in a reduced model. Determining which physics is the most important

then constitutes the second challenge. Below, we detail some key challenges in simulations that are directly relevant to this work.

The first deals with the characterization of turbulence and transport in terms of parameter space. The plasma properties close to the separatrix have been identified as crucial for the overall behaviour of the plasma. It is in this zone that the radial electric field well develops, that the pedestal forms and that the connection with the scrape-off layer is made. The question then is, which density, temperature and magnetic fields favour better confinement? Which parameters lead to operational limits?
On this topic, one can note the early work of Rogers, Drake and Zeiler (RDZ) [60]. In Figure 2.16 is displayed the transport as a function of the "MHD ballooning parameter" $\alpha = Rq^2\beta/L_p$ with L_p the typical pressure gradient length, and as a function of the "diamagnetic parameter" α_d which involves the inverse of the collisionality. Both parameters depend on the density n and temperature T, such that a large range of α and α_d values can be expected in the edge of tokamaks. The resulting phase space illustrated in Figure 2.16 identifies 4 zones of which two are operational limits. At large β, one reaches the electromagnetic ideal ballooning modes. On the left, at high density, the plasma reaches a thermal collapse. The density limit has been acknowledged since the late 80s in tokamaks, it is also called *Greenwald density* in the literature [120]. Both the density and ideal MHD limits lead to a dramatically increased transport such that those regimes are not operable. The two remaining zones are the low (L) and high (H) confinement modes. The latter yields a reduced transport.

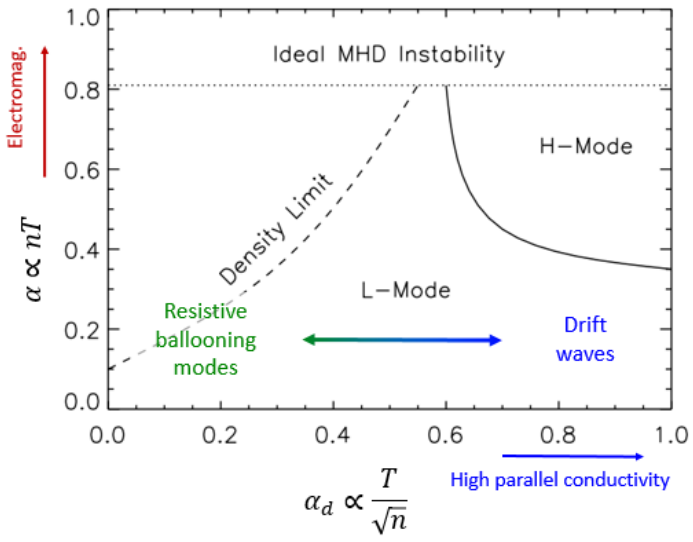

Figure 2.16 – Edge plasma phase space. Adapted from ref.[60].

A complementary work has been performed by Scott [121], where the phase space is considered in terms of competing drift waves and interchange in the electromagnetic regime. The more recent contribution from Eich and Manz [122] manages to close the gap between experiments and simulations. They identify the same 4 regions of the phase space and show remarkable agreement between model prediction and experiments. The phase space is displayed in Figure 2.17. The bottom left (green circles) of the figure corresponds to L-mode discharges, the blue squares

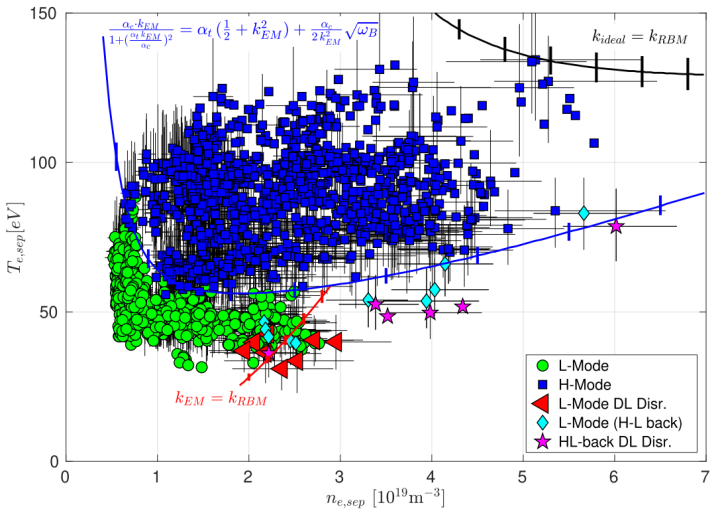

Figure 2.17 – Edge plasma phase space of ASDEX Upgrade in terms of electron density and temperature. Extracted from ref.[122].

in the middle to H-mode shots. The density limit is indicated with the red curve and red triangles, while the ideal ballooning limit is displayed in black. The lines are derived from a set of dimensionless parameters estimated from the complex drift-Alfvén (DALF) model equations.

For both RDZ and Eich/Manz contributions, some parameters are identified as crucial to identify the phase-space. Of particular interest are the electron-ion collisions, leading to the parallel resistivity. The interchange instability develops a charge separation in the vertical direction. Since particles explore both stable and unstable region, the parallel transit, which carries electric charges between the two regions, can be expected to have a stabilizing effect. The parallel conductivity parameter is sometimes recast in form of the *adiabatic parameter* which depends on the inverse of the collision frequency: $C \propto 1/\nu_{ei}$. Naively, we could consider the adiabatic parameter as stabilizing. However it also controls the collisional drift wave instability which can lead to turbulence and transport. The second parameter is linked to the magnetic curvature. Discarding shaping effect it can be estimated as the strength of the magnetic field inhomogeneity. This parameter controls the interchange instability and is often considered as destabilizing: the larger the curvature, the larger the ballooning instabilities. Finally, when electromagnetic effects are included, those add a new control parameter, the plasma β. The electromagnetic parameter has a dual role depending on the other parameters. Above the ideal MHD limit, it leads to ideal ballooning modes which dramatically increase the transport. Below, it modifies the existing instabilities and can be destabilizing (resp. stabilizing) for low (resp. large) values of the adiabatic parameter, see for example the figure 2 of ref.[60]. The authors then choose either some of these parameters or a combination of them. For the two examples above, α_d and α_t describe to some extent the stabilizing effect of parallel conductivity on interchange.

Despite the good agreement with experiments, it is difficult to infer the physical mechanisms at play behind the phase space. The density limit for example is well predicted in terms of the parameter space [123]. However, the mechanisms at play are not entirely elucidated. Refs.[60, 122] put forward the increase of transport due to a turbulent regime transition and nonlinear electromagnetic fluctuations. Other contributions, such as performed by Numata [124],

observe a zonal flow collapse when decreasing the adiabatic parameter at constant density gradient – the critical adiabatic parameter for this collapse increasing strongly with the density gradient. Building on this, a few works propose the density limit to be related to this ZF collapse, see ref.[125]. Since the critical adiabatic parameter depends on the density gradient, one might reasonably ask what would happen if the density gradient were free to adjust and evolve? Approaching this question requires a flux-driven formulation of the problem, so that the profiles (pressure, flows) can be evolved self-consistently with the turbulence.

To further the analysis on the phase space presented in Figure 2.16 and 2.17, we propose to evolve towards a flux-driven formulation of this problem so that the profiles can evolve self-consistently. Relaxing the scale separation assumption enables the study of the flow and profile corrugations along with the generation of avalanches and the generation of staircases. This ultimately requires simulations on the confinement time of the particles – so that the profiles can evolve towards a steady state – while still resolving the small scale turbulence. To this aim, we develop a reduced model in chapter 3. The objective is not to have a quantitative agreement with experiments but to see whether trends exist in the generation of zonal flows, avalanches and staircases depending on the plasma parameters.

Turbulence self-organization itself also bears unanswered question. Previous contribution, in particular by Dif-Pradalier [104, 105] investigated the generation of staircases. The radially organized structures are found mainly in near-marginal ITG turbulence regime and expected beneficial to limit the radial extension of avalanches [106]. Mitigation of avalanches by shear flows has also been hinted at in experiments [126]. In the meantime, some contributions also point out the possible generation of staircases by the avalanches themselves [127]. Staircases and their induced shear could also play a role on the L-H transition itself, as pointed out by ref.[128].

We are convinced that the flux-driven reduced model Tokam1D represents a valuable tool to perform parameter scans and explore which turbulence regime leads to the radial structuring of ZFs and avalanche processes. In a self-consistent manner – thanks to the absence of any implicit scale separation, it can investigate whether radially structured flows always lead to corrugation in the pressure profile. Finally, the interaction between zonal structures and passing avalanches can be approached. Knowing the parameter space leading to the apparition of avalanches and staircases also helps guiding the experiments. Challenges regarding experimental work are presented in the next section.

2.5 Experimental measurements of turbulence self-organization

Plasma self-organization, in particular zonal flow generation, is crucial for simulations. However, those dynamics are difficult to unravel experimentally. In this section, we review some of the past experimental works and challenges regarding the identification of zonal flows, avalanches and staircases. A review on zonal flows experiments by Fujisawa can be found ref.[129]. Additional considerations regarding geodesic acoustic modes (GAM) can be found ref.[97].

2.5.1 Diagnostics and methods

Zonal flows are separated between their low and high frequency branches: low frequency zonal flows (LFZF) and geodesic acoustic modes (GAM). While both are linked to a flow structure $m = n = 0$, with m,n the poloidal and toroidal mode numbers, the GAM is easier to detect because of its pressure sidebands (modes $m = \pm 1$). For zonal flows, one needs to rely on electric potential or velocity measurements. Ideally, the process to clearly identify zonal flows would encompass several of their properties:

1. $m = n = 0$ zonal structure of the velocity or electric potential.
2. Finite radial wavenumber (small k_r) of the fluctuations, thus assess the radial structure.
3. Turbulent drive, i.e. the Reynolds stress.
4. Investigate the coupling between ZF and turbulence: transfer of energy, predator-prey relation.
5. Damping and its dependence on collisionality and other plasma parameters.

In practice, all these points are challenging. Verifying the mode structure requires a multi-point measurement: two measures separated poloidally and toroidally but located at the same exact radial location. This method is called *long range correlation (LRC)*, its principle is sketched in Figure 2.18.

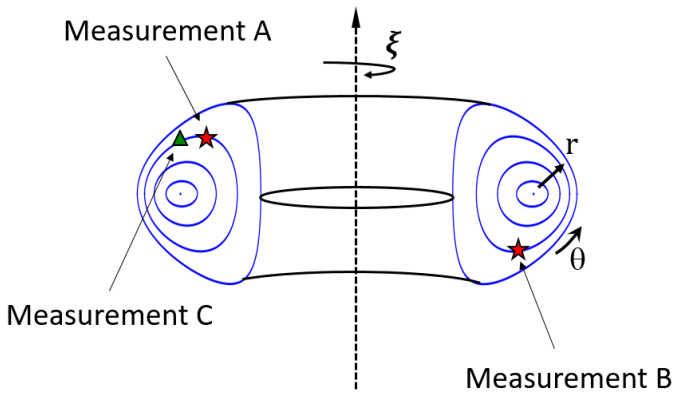

Figure 2.18 – Principle of long range correlation measurement. (A) and (B) are separated poloidally and toroidally but not radially. (A) and (C) are only separated radially.

To verify the zonal structure, one needs to correlate point (A) with point (B). To verify the radial structure, one needs to vary the radial location or add a third measurement point in the radial direction and perform a radial correlation between (A) and (C).
The measure of the Reynolds stress requires an estimation of the radial and poloidal velocity fluctuations and often relies on local multi-point measurements. For example by using a set of Langmuir probes separated radially and poloidally one can infer fluctuating velocities in both directions. Using a probe in a confined plasma requires a low temperature typically not achievable in large scale tokamaks. As such, measurements are mainly performed in small devices, see next section.
Investigating the interaction between low frequency modes such as ZFs and GAMs and the broad-band turbulence requires advanced numerical methods such as spectral, coherence and

bicoherence analysis. Additionally one can rely on signal decomposition methods, such as empirical mode decomposition, detailed in Section 5.2.

To perform those measurements, one needs to rely on the electric potential or on the plasma perpendicular velocity. Not many diagnostics are able to measure those quantities. Langmuir probes have been extensively used, but require relatively cold plasma. Alternatively, imaging techniques and reflectometry methods are able to extract poloidal and/or radial velocities in the confined region. The measurement of the perpendicular velocity is principally made using Doppler backscattering. It consists in sending an electromagnetic wave into the plasma at an angle with the cut-off layer. If the plasma is subject to a finite poloidal mean flow, the backscattered wave is modulated with a Doppler frequency used to infer the perpendicular velocity advecting the underlying density fluctuations. The diagnostic is presented in details Section 5.1. Beam-emission spectroscopy (BES) is also widely used to measure $2d$ maps of the density fluctuations. It consists in measuring the emitted light from the excitation of a probing neutral beam sent into the plasma. Provided that enough channels are present, BES can resolve the radial and poloidal velocity of the density fluctuations.
Alternatively to the plasma velocity one can use the electric potential fluctuations. If cold enough, Langmuir probes can reach the edge of the confined plasma and provide reliable measurements of the plasma electric potential.

Avalanches are ballistic events travelling on large portions of the machine in a short time. Their measurements necessitate a wide spatial coverage and a very good temporal resolution. Interesting results have been obtained using electron cyclotron emission (ECE) and correlation Doppler backscattering (CDBS). They are detailed in the following.

Finally, staircases include both zonal flows and avalanches. Additionally, staircases should be observable directly on the pressure profiles in the form of steps. This can be done using fast-sweep reflectometry to measure density profiles. Ideally, one should verify the step on the pressure profile along with the radially structured perpendicular velocity. If possible, a measurement of the avalanches in between the step would provide a more complete picture of the staircase structure.

2.5.2 Experimental measurements and challenges

The list of references being very long, we cannot be exhaustive on the subject. The references discussed here represent contributions on this topic related to the present work, but the list is inevitably partial.

Zonal flows and geodesic acoustic modes

The GAM are much easier to measure than ZFs: they have a larger frequency and have been studied for decades in all sorts of configurations. Using DBS, GAMs have been measured on many tokamaks such as DIII-D [130], ASDEX Upgrade [131, 132] and Tore Supra [133, 134]. Note that coupling several DBS separated poloidally and/or toroidally can resolve their spatial structure. GAMs are routinely observed in both simulations and experiments. As such, they present a nice ground for testing and to compare codes and diagnostics.

Conversely, zonal flows are much more difficult to assess. They have a vanishing frequency and are not linked to pressure sidebands which make them particularly elusive in experiments.

When the plasma is cold enough, usually on small machines, physical probes can reach the confined part of the plasma. Doing this, LRC have been used to investigate zonal structures. Notably on TJ-II heliac [135, 136]. LRC have also been performed on medium size tokamaks, such as HL-2A [137] and HT-7 [138]. LRC has also been performed with heavy ion beam probes on CHS [139].
However, measurements of ZFs on large machines are scarce. It is not possible to rely on probes due to prohibitive heat loads. One can note the contribution of Gupta ref.[140], who used BES on the DIII-D tokamak. On the left hand side of Figure 2.19 is displayed the BES channel location. The resulting poloidal correlation is shown on the right.

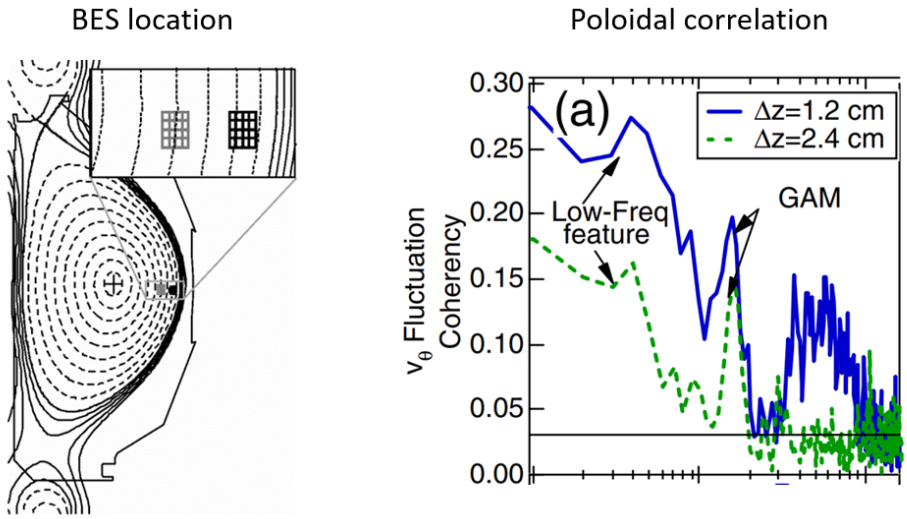

Figure 2.19 – (Left) Beam-emission spectroscopy line of sight location. (Right) Poloidal correlation of velocity fluctuations. Adapted from [140].

The correlation found at low frequency is reminiscent of the expected zonal flow. However, note that the channels here have no toroidal separation and are only separated by a few centimeters poloidally. Even though a few cm is usually larger than the turbulent structures size, it is not a 'long range' correlation *per se*. Recently, three correlated DBS have been used on W7-X stellarator to perform long range correlation [141]. Two of them are separated toroidally and poloidally. The third channel is separated radially, it is used to infer the radial structure.

Reynolds stress measurements are also very scarce. One can note the work of Tynan ref.[142] and collaborators who report measurements of the flows, Reynolds stress and particle flux in a linear device. The Reynolds stress has also been measured on TJ-K stellarator using a poloidal array of Langmuir probes [143].

In chapter 5, using two DBS channels separated poloidally and toroidally, we perform the LRC on a discharge of the Tore Supra tokamak. The signal is shown to be dominated by GAMs which perturbs the low frequency signal. It will appear that removing the GAM helps retrieving a long range correlation at low frequencies.

Avalanches

Ideally, measuring avalanches requires the measure of the turbulent flux of particles or heat. In practice, these fluxes are difficult to measure because it would require the measure of the density / temperature and electric potential fluctuations along with their cross-phase. Alternatively, one can use the temperature or density fluctuations as a proxy for the propagation of the avalanche. In 2000, Politzer [85] observed avalanches in the temperature fluctuations using ECE on the DIII-D tokamak. In Figure 2.20 is shown the avalanche propagation in the electron temperature fluctuations signals.

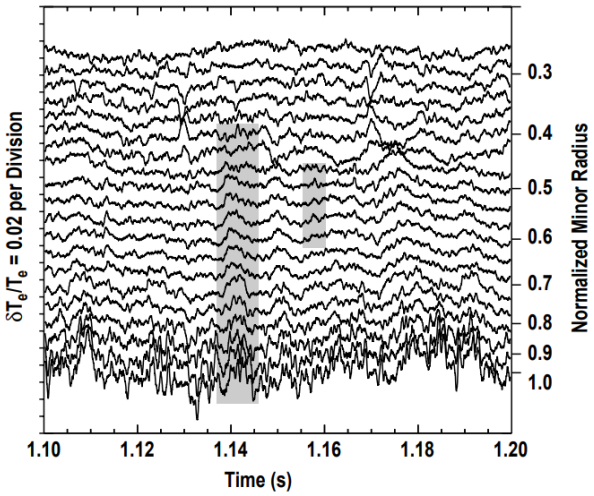

Figure 2.20 – Electron temperature fluctuations for ECE channels between $\rho = 0.25$ and $\rho \approx 1$ as a function of time. The avalanches are indicated in the grey areas. Extracted from [85].

Temperature fluctuations can be tracked when propagating across a large part of the machine. The perturbation moves outwards as the time increases. Indirect evidences of avalanches can also be found by performing the radial correlation using two DBS channels. This time, the density fluctuations are measured. Typically, this setup is used to measure the radial correlation length of turbulence. If events are travelling on large radial parts of the plasma, they should also lead to a correlation of the DBS signals. In ref.[86], the radial correlation is performed on large radial distances, the resulting radial correlation function is displayed in Figure 2.21.
The radial correlation function is not monotonic and displays two slopes. The short scale is expected to be linked to the size of the turbulent structures. The second slope of correlation is a possible sign of avalanches events.

In chapter 4, we report in Tokam1D simulations that the radial correlation of the density fluctuations lead to a second slope of correlation when avalanche transport is present. Then, in chapter 5, we use a double channel DBS on TCV to measure experimentally the radial correlation functions. Two slopes of correlations are found in various configurations and are identified as avalanches signatures by analogy with simulations and ref.[86].

Staircases

At last, the experimental measure of staircases has recently gained interest. Staircases should be observable on the perpendicular velocity signals in the form of radially structured flow. Mea-

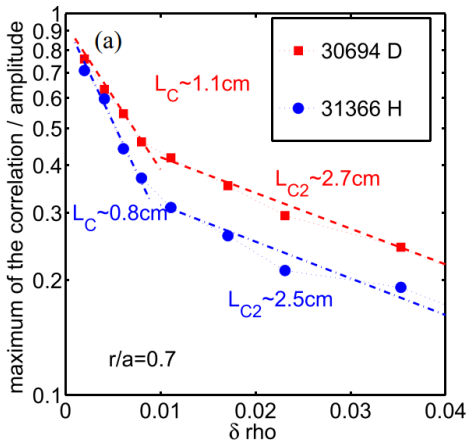

Figure 2.21 – Density fluctuations correlation as a function of the radial separation, from [86].

surements on JET tokamak have shown stable in time corrugations in the radial electric field [128]. Radial electric field profiles are displayed in Figure 2.22. On the left, from [128], six profiles present corrugation in the bottom of the E_r well. On the right, from [144], radial electric field profiles present no corrugations. Both are performed in L-mode discharges.

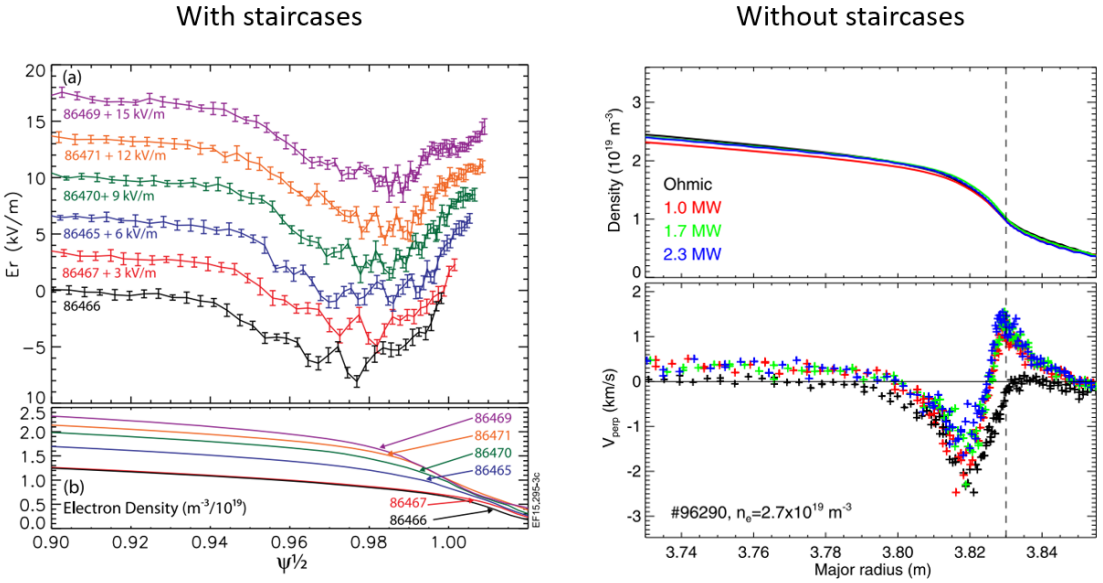

Figure 2.22 – Radial electric field and density profiles from the JET tokamak. (left) With staircases-like corrugations, taken from [128]. (right) Without corrugations, from [144].

The principal issue is that the observations of E_r corrugated profiles have never been reproduced, neither on JET nor on other machines. In most cases, the radial electric field profiles (or $v_\perp$) present no corrugations as exemplified on the right hand side of Figure 2.22. Additionally, the density profile presents no corrugation which could advocate in favour of the staircase presence. Finally, the staircases steps are close to each other, which is different to first principle simulations where staircases are separated by zones mediated by avalanche-like transport (see Figure 2.14).

Another attempt at measuring staircases signatures made use of fast-sweeping reflectometry [107]. The staircases signatures appear in "the local contraction of the coherence of adjacent plasma layers", which indicates a change in the size of the turbulent structures. The modulation of the coherence length is displayed in Figure 2.23.

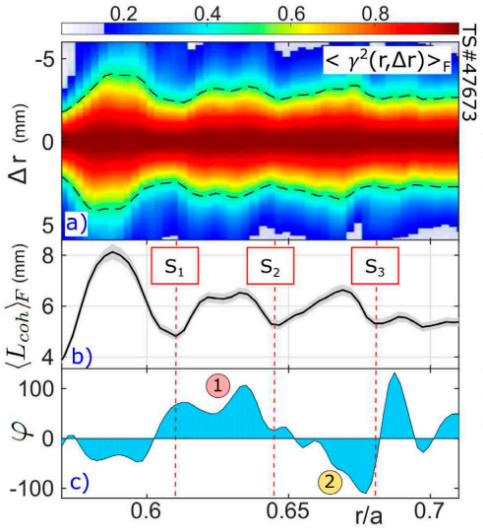

Figure 2.23 – Local contraction of the coherence as a signature of staircases. (a) Spectrally averaged. (b) Displayed as a radial profile. (c) Asymmetry of the cross-correlation functions along the radial profile, indicative of the structures spatial tilt. Adapted from [107].

The results are promising but are difficult to perform and require a certain amount of post-processing. They have to be reproduced in other machines and with different plasma parameters to be reliable.

All in all, staircases such as described by simulations should be observable in experimental signals. DBS and reflectometry systems have the required spatial resolution to observe the corrugations in the velocity and pressure profiles. However, the lifetime of staircase structures might be too short as compared to the required diagnostic measurement time. Also, staircases are sometimes found to be meandering, such that they are moving radially. Their stability – in time and space – might depend on plasma parameters and on the type of turbulence present in the plasma. Some regimes might favour very stable structures while other might favour flows that are moving radially, disappearing, merging and splitting. With the reduced model presented in the following chapter, the type of turbulence (interchange, drift waves) leading to stable radial structures is investigated.

2.6 Conclusion and scope of the thesis

Understanding the properties of turbulence in fusion plasmas is crucial as it governs the turbulent transport. Turbulence can saturate through turbulent cascades, profile relaxation and generation of mesoscale structures such as zonal flows. Turbulence self-organization then appears essential: while generation of zonal flows mitigate turbulent transport, the formation of avalanches can be detrimental for the overall confinement. Staircases, coupling both avalanches and radially structured flows remain largely unexplored and elusive in experiments.

Among the key remaining questions, turbulent regimes leading to the formation of zonal flows, avalanches and staircases have to be better characterized. Doing this will give a better understanding of the mechanisms leading to the formation of such structures. It will also help guiding future experiments. By better understanding the plasma self-organization, some insights regarding turbulent transport and the access to better confinement modes can be obtained. Finally, it is also a fundamental topic that touches on many areas of turbulence and layering physics.

We list here the main questions of interest for the present work:

- What turbulence regimes favour the generation of zonal flows? Of avalanches?
- Which regimes lead to the radial structuring of zonal flows? Do structured flows always lead to staircases?
- Do zonal flows mitigate avalanches? Or do they interact in a more complex way?
- What is the impact of turbulence self-organization on transport?
- Using simulations as a guide, can we better characterize zonal flows and avalanches experimentally?

To approach these questions, we develop a flux-driven reduced model aimed at the study of turbulence and flows. The model includes two fundamental instabilities: collisional drift waves and interchange. It is reduced to one dimension, such that one can perform parameter scans on particle confinement timescales while still resolving small turbulence scales. Using this model, the generation of zonal flows, avalanches and staircases are studied depending on turbulence parameters. The model being flux-driven, it is possible to assess the role of such structures on the turbulent transport and confinement. Finally, using simulations both as a guide for turbulent regimes and as a tool to seek signatures of self-organization, experiments are performed using Doppler backscattering. Having two DBS channels enables long range correlation and radial correlation measurements.

The reduced model is derived chapter 3. Some extensions, by including the physics of the scrape-off layer and electromagnetic effects are included. The characterization of turbulence self-organization and their impact on transport is characterized chapter 4. Finally, experiments on Tore Supra and TCV tokamaks are performed chapter 5. Signatures of zonal flows and avalanches are reported.

Chapter 3

Tokam1D: a reduced flux-driven model for turbulence-flows interaction

Contents

In the previous chapter, we underlined the important role of turbulence in the edge region for the global confinement. It is in this region that the radial electric field well develops and that the transition from close to open field lines is made. As such, the parameters at the last closed flux surface are particularly studied [60, 122]. It is also a region where collisionality, $\nu_\star$ (Equation 1.19), is large. The large collisionality makes a fluid approach relevant and one is not forced to rely on kinetic or gyrokinetics. Additionally, in order to understand the generation of flows and their radial structure together with their impact on turbulent transport, it is necessary to scan different turbulence regimes.

The choice is made to study the turbulence self-organization with a reduced fluid model, so that a large number of simulations can be performed with different parameters. The model needs to include several crucial elements:

- Treat both mean (flux surface averaged) profiles and fluctuations on an equal footing, without any scale separation assumption (in time and in space).
- Self-consistently account for nonlinear terms that govern the dynamics of the mean profiles, namely fluxes (of particles, energy, etc.) and the various components of the Reynolds stress. As will be discussed in Section 4.3.2, the latter point requires a finite ion temperature.

In this framework, the system needs to be flux driven so that an equilibrium can be achieved where sources are balanced by turbulent transport processes.

The model includes two instabilities expected dominant in the edge [50]: collisional drift waves (CDW) and interchange instability (akin to resistive-ballooning or ion temperature gradient modes). The first, detailed in Section 2.2.1, relates to drift-wave class of instabilities that stems from a finite phase shift between density and electric potential fluctuations. The second, introduced in Section 2.2.1, derives from the plasma magnetic inhomogeneity, either caused by curvature or by spatial gradient. Simulations are run until reaching not only the statistical steady-state of turbulence, but also the steady-states of the flux-surface averaged profiles. The latter objective requires runs of several energy and particle confinement times. So as to fasten numerical resolution, the model is reduced to one dimension. This makes possible large confinement time scans on turbulence parameters while still resolving the small turbulence scales.

The model, labelled Tokam1D-ES core, is first derived for an electrostatic plasma in the edge of the confined region. Its derivation along with considerations on the flux-driven regime can be found in a submitted article [145]. Then, additions are performed. First with the transition towards the scrape-off layer (Tokam1D-ES SOL). Second, by adding electromagnetic effects (Tokam1D-EM). For easy access, the different versions of Tokam1D are referenced Table 3.1. The label $-$ES stands for electrostatic and $-$EM for electromagnetic. Note that Tokam1D-ES SOL encompasses both the core and the scrape-off layer.

Model name	$3d$ **version**	$1d$ **reduction**
Tokam1D-ES core	Equations 3.12 – 3.13	Equations 3.32 – 3.35
Tokam1D-ES SOL	Equations 3.55 – 3.56	Equations 3.64 – 3.67
Tokam1D-EM	Equations 3.100 – 3.102	Equations 3.116 – 3.121

Table 3.1 – Easy access for Tokam1D versions

3.1 Considered geometry and magnetic field curvature parameter

The interchange instability depends on the inhomogeneity of the magnetic field through a parameter first named the *effective gravity parameter* by Furth, Killeen and Rosenbluth [15] who derived it in a slab geometry. This effective gravity parameter, also called curvature parameter, is largely dependent on the considered geometry. We can derive it from terms that are linked to the magnetic inhomogeneity such as the divergence of the electric drift and diamagnetic flux:

$$\boldsymbol{\nabla}\cdot\left(\frac{\boldsymbol{B}\times\boldsymbol{\nabla}h}{B^2}\right)=\boldsymbol{\nabla}h\cdot\left(\frac{\boldsymbol{\nabla}\times\boldsymbol{B}}{B^2}+\frac{2\boldsymbol{B}\times\boldsymbol{\nabla}B}{B^3}\right) \tag{3.1}$$

With $h=n$ the density or $h=\Phi$ the electric potential. Note that both the curvature and the amplitude variation lead to the magnetic inhomogeneity. The first term on the right hand side relates to Ampère-Maxwell's law. In tokamaks, at low β, it leads to the current density and

can be neglected. The second term comes from the magnetic field amplitude variation along the major radius of the tokamak and should be kept. Considering a circular geometry where the magnetic field decreases as the inverse of the major radius, $\mathbf{B}(R) = B_0 R_0 / R \mathbf{e}_\parallel$, with B_0, R_0 the magnetic field on axis and R_0 the major radius, it reads at leading order in the inverse aspect ratio $\varepsilon = r/R_0$:

$$\boldsymbol{\nabla} h \cdot \left(\frac{2\boldsymbol{B} \times \boldsymbol{\nabla} B}{B^3} \right) = -\frac{2}{RB} \left(\sin\theta \partial_r h + \frac{\cos\theta}{r} \partial_\theta h \right) + O(\varepsilon)$$

Thereby defining the following operator:

$$\mathscr{G}(\cdot) = -\frac{2}{RB} \left(\sin\theta \partial_r + \frac{\cos\theta}{r} \partial_\theta \right) \tag{3.2}$$

The Tokam1D model is quasi-one dimensional. It retains equilibrium quantities (flux surface average) and one poloidal and parallel mode for fluctuations. As such, the curvature operator is also reduced and does not take into account variations along θ. Doing this simplification removes the following properties from the dynamics:

1. The ballooning structure of the modes. While the interchange instability still occurs only on the low field side, the $2d$ structure in the poloidal plane is not resolved.
2. The physics of geodesic acoustic modes (GAM). Those modes lead to flows that are constant on magnetic surfaces but that oscillate at the GAM frequency $\omega_{GAM} \sim c_s/R$. The inclusion of GAMs can be an interesting addition to the model as those modes could exchange energy with both ZFs and turbulence [89, 102], more details are given in Section 3.6.2.

Considering the reduction of Equation 3.2 in the $1d$ radial direction leads to the following curvature operator:

$$\boldsymbol{\nabla} h \cdot \left(\frac{2\boldsymbol{B} \times \boldsymbol{\nabla} B}{B^3} \right) \approx -\frac{2}{RB} \partial_y h$$

With the corresponding dimensionless curvature parameter:

$$g = 2\frac{\rho_s}{R} \tag{3.3}$$

To give a visual representation, this amounts to consider the torus as a cylinder, with the poloidal direction extended vertically and labelled $\mathbf{e}_y$. The other directions being the toroidal $\mathbf{e}_\phi$ such that $\mathbf{B} = -B\mathbf{e}_\phi$ and $\mathbf{e}_R$ the radial direction. The geometry is illustrated in Figure 3.1.
The modelled region is sketched in blue and is located at the edge of the confined plasma, both sides of the separatrix (indicated in red). The cylindrical coordinates are approximated with cartesian coordinates, such as if the blue section was unwrapped onto a cartesian plane (right side of Figure 3.1). The unit vectors read $(\mathbf{e}_x, \mathbf{e}_y, \mathbf{e}_\parallel)$, where x is the radial, y is the poloidal (now vertical) and z is the parallel (along the field lines) directions. Note that in a tokamak, the toroidal direction is not exactly equal to the parallel direction due to magnetic helicity. Therefore, the coordinates are not exactly orthogonal since the parallel direction is the projection of

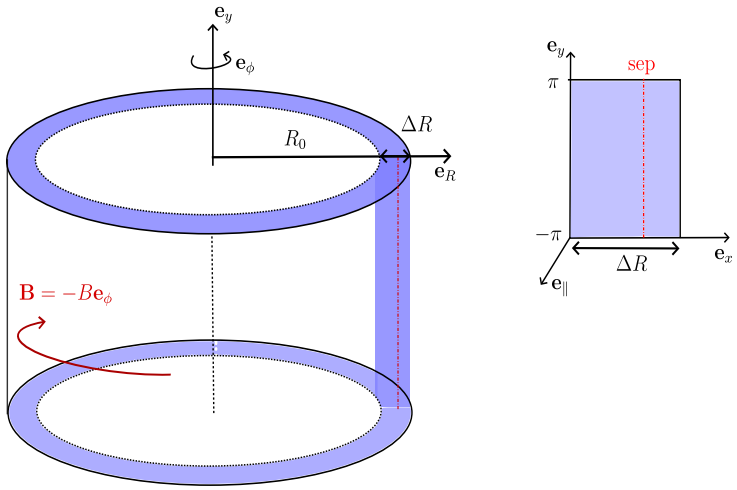

Figure 3.1 – (left) Z-pinch magnetic geometry considered for Tokam1D with the modelled region indicated in blue. (right) Cartesian approximation of the modelled region and its system of coordinates $(\mathbf{e}_x, \mathbf{e}_y, \mathbf{e}_\parallel)$.

the toroidal direction onto the magnetic field line. However, the edge q-factor is large and this effect is deemed small.

3.2 Describing the core: Tokam1D-electrostatic

The model is derived from two continuity equations: the density and charge equations. A generalized Ohm's law closes the system by relating the parallel current to the electric field and the electron pressure gradient. The governing fluid equations rely on a certain number of simplifications that are detailed below. Their derivation proceeds from the adiabatic regime already detailed in Section 1.2.1 and in refs.[62, 21, 146]. The main assumption is to consider that the time and spatial scales of the plasma dynamics are much larger than the ones of the cyclotron motion, namely the gyrofrequency and the sound Larmor radius ρ_s. In this framework, velocity drifts are retained up to the second order in the small expanding parameter, typically the ratio between ρ_s and the gradient length R (also the tokamak major radius) of the magnetic field $\rho_\star \sim \rho_s/R \ll 1$. These velocities are the electric and diamagnetic drifts at first order, and the ion polarization drift at second order. Other finite Larmor radius effects than the polarization drift are not retained.

We consider a magnetized plasma of constant ion (T_i) and electron (T_e) temperatures (with $\tau = T_i/T_e$) in a static magnetic field B. We focus on the tokamak edge, just inside the last closed flux surface (LCFS). The plasma is assumed to be in L-mode so that one can neglect electromagnetic effects. Indeed, when approaching the H-mode, the pressure gradient length L_p decreases strongly, so that the effective beta parameter $\beta_{eff} = (qR/L_p)^2\beta$ - with $\beta = 2\mu_0 p/B^2$ the ratio of plasma pressure to magnetic pressure, q the safety factor and R the major radius - can exceed unity. In this case, as early noticed in [147] and further detailed in [62], magnetic induction can no longer be ignored since it controls the linear response of the parallel current to parallel gradients in the three state variables (electric field, density and electron temperature).

The model for the core (closed flux surfaces) is first derived in $3d$, then is further reduced

to $1d$ by keeping only one fluctuating mode for the poloidal ($\mathbf{e}_y$) and parallel ($\mathbf{e}_\parallel$) directions. An energy principle is calculated and energy channels for the profile, flows and turbulence are clarified. Finally, a heuristic equilibrium velocity is added to the model, to account for the radial force balance equation.

3.2.1 Electron density continuity equation

The particle conservation equation, Eq 3.4, solves the electron density n taking into account the $E \times B$ and diamagnetic drifts, $\mathbf{v}_E$ and $\mathbf{v}_\star$ (defined Equation 1.10), the electron parallel current $\mathbf{j}_{\parallel,e}$ and the source of particle S_n. The polarization drift, $\mathbf{v}_{pol}$ (Equation 1.11), is neglected for the electrons as it scales with the mass of the species.

$$\partial_t n + \mathbf{v}_E \cdot \boldsymbol{\nabla} n + n \boldsymbol{\nabla} \cdot \mathbf{v}_E + \boldsymbol{\nabla} \cdot (n \mathbf{v}_{\star e}) - \nabla_\parallel (j_{\parallel e}/e) = S_n \tag{3.4}$$

Owing to the large inertia of the ions, the total parallel current is approximated by the electron parallel current: $j_{\parallel e} = -env_{\parallel e} \approx j_\parallel$. The compressibility terms, $\boldsymbol{\nabla} \cdot \mathbf{v}_E$ and $\boldsymbol{\nabla} \cdot (n\mathbf{v}_{\star e})$ are kept in the equations. They account for the inhomogeneity of the magnetic field and are crucial in the model. They are necessary to close the energy balance of the system that involves both linear and nonlinear terms, see Section 3.2.7. Additionally, they prove to stabilize the interchange instability at large scale. This is no small effect: at large magnetic inhomogeneity the interchange instability is strongly suppressed, see Section 3.4. The advection of density due to the electric drift can be written in Poisson brackets $\{\Phi, n\} = (\nabla\Phi \times \nabla n) \cdot \mathbf{B}$, or in slab geometry, $\{\Phi, n\} = \partial_x \Phi \, \partial_y n - \partial_y \Phi \, \partial_x n = \partial_y (n \partial_x \Phi) - \partial_x (n \partial_y \Phi)$. Developing the compressibility terms derived in Section 3.1, the above equation reads as follows,

$$\partial_t n + \frac{1}{B}\{\Phi, n\} - \frac{2nT_e}{eRB}\left[\partial_y \left(\frac{e\Phi}{T_e}\right) - \partial_y \ln \frac{n}{n_0}\right] - \frac{1}{e}\nabla_\parallel j_\parallel = S_n \tag{3.5}$$

With n_0 a constant density of normalization and Φ the electric potential.

3.2.2 Charge continuity equation

With the quasi-neutrality assumption, charge conservation reduces to $\boldsymbol{\nabla} \cdot \mathbf{j} = 0$. Taking both the diamagnetic current $\mathbf{j}_\star = (en\mathbf{v}_{\star i} - en\mathbf{v}_{\star e})$ and the polarization current, $\mathbf{j}_{pol} = en\mathbf{v}_{pol}$, into account, it takes the form:

$$\nabla_\perp \cdot \mathbf{j}_\star + \nabla_\perp \cdot \mathbf{j}_{pol} + \nabla_\parallel j_\parallel = 0. \tag{3.6}$$

In the isothermal regime (i.e. constant T_e and T_i), the divergence of the diamagnetic current can be written directly as:

$$\boldsymbol{\nabla}_\perp \cdot \mathbf{j}_\star = \nabla_\perp \cdot (-en\mathbf{v}_{\star e} + en\mathbf{v}_{\star i}) = -(1+\tau)\frac{2T_e}{RB}\partial_y n,$$

with $\tau = T_i/T_e$ the temperature ratio. The polarization current is computed from the ion polarization drift (Equation 1.11). We further neglect the parallel advection assuming that the parallel

gradient length remains small as compared to the transverse ones:

$$\nabla_\perp \cdot \mathbf{j}_{pol} = -\nabla_\perp \cdot \left(\frac{enm_i}{eB^2} \left[\partial_t + \mathbf{v}_E \cdot \nabla \right] \left(\nabla_\perp \Phi + \frac{\tau T_e}{e} \frac{\nabla_\perp n}{n} \right) \right)$$

The above expression is challenging to solve numerically as it leads to two time derivatives: $n\partial_t \nabla ...$ and $\nabla n \partial_t ...$. Instead, the difficulty is often bypassed by considering the Boussinesq approximation. It states that the density can commute with the divergence, thus leading to,

$$\begin{aligned} \boldsymbol{\nabla}_\perp \cdot \mathbf{j}_{pol} \approx & -\frac{n_\Omega m_i}{B^2} \partial_t \nabla_\perp^2 \left(\Phi + \frac{\tau T_e}{e} \ln \frac{n}{n_0} \right) \\ & - \frac{n_\Omega m_i}{B^2} \left[\mathbf{v}_E \cdot \nabla \nabla_\perp^2 \Phi + \nabla \cdot \left(\mathbf{v}_E \cdot \nabla \left[\frac{\tau T_e}{e} \nabla_\perp \ln \frac{n}{n_0} \right] \right) \right]. \end{aligned}$$

Where n_Ω is the commuted density, the subscript $_\Omega$ is added to keep track of its origin in the rest of the derivation.

We take the time here to discuss this assumption and its implications. First of all, Boussinesq assumption is routinely used in many fluid models to simplify computation. It is usually considered valid whenever density gradient length is large with respect to that of the electric potential. Although it is usually considered correct in the core, its validity is debated for simulations including the scrape-off layer as the density fluctuations tend to be larger relatively to the background density, see dedicated contributions [148, 149, 150]. Depending on the model, two variations of the Boussinesq assumption are used. *Weak* Boussinesq where a constant density is commuted $n_\Omega = n_0$ such as in [116, 151, 152]. *Strong* Boussinesq where the choice is made to commute the full density $n_\Omega = n$ [148, 153]. Ultimately, one has to verify that the Boussinesq assumption does not break the conservative form of $\boldsymbol{\nabla} \cdot \mathbf{j} = 0$ and that the model still conserve energy. The breakdown of conservation is discussed for the electromagnetic model derived in Section 3.5. For now, we simply consider that the commuted density is n_Ω, without stating whether this should be n or n_0. The validity of the strong Boussinesq assumption can be checked at the end of the simulation by comparing $\nabla_\perp n \cdot \nabla_\perp (\Phi + \tau \ln(n/n_0))$ and $n\nabla_\perp^2 (\Phi + \tau \ln(n/n_0))$. In the simulations performed, the mismatch proved to be of a few percent.

Additionally, the magnetic field is assumed to commute with the ∇ operator. It is acceptable as the B field decays as $1/R$ which is on much larger scales than the density and electric potential inhomogeneities. Eq. 3.6 then reads as follows,

$$\frac{-n_\Omega m_i T_e}{eB^2} \partial_t \Omega = \frac{n_\Omega m_i}{B^3} \frac{T_e^2}{e^2} \nabla_{\perp,i} \left\{ \frac{e\Phi}{T_e}, \nabla_{\perp,i} \left(\frac{e\Phi}{T_e} + \tau \ln \frac{n}{n_0} \right) \right\} + \frac{2T_e}{RB} (1+\tau) \partial_y n - \nabla_\parallel j_\parallel \qquad (3.7)$$

Where $\nabla_{\perp,i}\{.,\nabla_{\perp,i}(.)\}$ represents Poisson brackets that can be developed using Einstein's notation, $\partial_x\{.,\partial_x(.)\} + \partial_y\{.,\partial_y(.)\}$. Here, the generalized vorticity is defined as follows,

$$\Omega = \nabla_\perp^2 \left(\frac{e\Phi}{T_e} + \tau \ln \frac{n}{n_0} \right). \qquad (3.8)$$

With $\nabla_\perp^2 = (\partial_x^2 + \partial_y^2)$ the perpendicular Laplacian.

3.2.3 System closed through Ohm's law

In order to close the system, one has to evaluate the parallel current present in both Equation 3.5 and 3.7. This is done using Ohm's law, that derives from the electron parallel momentum conservation equation,

$$nm_e[\partial_t + (\mathbf{v}_E + \mathbf{v}_{\star e} + \mathbf{v}_{\|e}) \cdot \nabla] v_{\|e} + T_e \nabla_\| n = en\nabla_\| \Phi + \frac{m_e \nu_{ei}}{e} j_\| \,. \tag{3.9}$$

Due to the small electron inertia, the first term proportional to m_e can be dropped. In this case, the generalized Ohm's law reduces to a balance between parallel current, parallel Coulomb force and parallel pressure. One is left with an explicit relationship between the parallel current on the one hand, and density and electric potential on the other,

$$j_\| = \frac{enT_e}{m_e \nu_{ei}} \nabla_\| \left(\ln \frac{n}{n_0} - \frac{e\Phi}{T_e} \right) \tag{3.10}$$

One has to remember that the parallel current depends on the electron-ion collision frequency, that depends itself on the density and temperature $\nu_{ei} \propto n/T_e^{3/2}$. The temperature is constant in this model, but the density has to be made explicit so that we can treat the pre-factor as a constant. Then, we define $\nu_{ei,0} = \nu_{ei} \frac{n_0}{n_\nu}$, the electron-ion collision frequency taken at reference density n_0. The density is labelled n_ν to keep track of its origin in the following calculations. This density originates from the electron-ion collision frequency. As such it should be understood as a flux-surface averaged density, possibly further coarse grained in time on timescales intermediate between fluctuations and collisions. Also, the energy conservation equation in Section 3.2.7, directly results in the possibility to perform integration by part in the parallel direction. This requires n_ν to be independent of the parallel direction.

$$\nabla_\| j_\| = \frac{en_0 T_e}{m_e \nu_{ei,0}} \frac{n}{n_\nu} \nabla_\|^2 \left(\ln \frac{n}{n_0} - \frac{e\Phi}{T_e} \right) = \frac{\sigma_0}{n_\nu} \frac{n_0 T_e}{B} n \, \nabla_\|^2 \left(\ln \frac{n}{n_0} - \frac{e\Phi}{T_e} \right) \tag{3.11}$$

With, $\sigma_0 = eB/(m_e \nu_{ei,0}) = \omega_{ce}/\nu_{ei,0}$, the parallel conductivity taken at reference density n_0.

3.2.4 3d-model of core Tokam1D-ES

The 3d system of equations is obtained by dividing the density continuity equation by n and the charge continuity equation by n_Ω. It involves the logarithm of the electron density $N = \ln n/n_0$ and the generalized vorticity $\Omega = \nabla_\perp^2 (e\Phi/T_e + \tau N)$. The system reads,

$$\begin{aligned}
\partial_t N + \frac{1}{B}\{\Phi, N\} &= \frac{2T_e}{eRB} \left[\partial_y \left(\frac{e\Phi}{T_e} \right) - \partial_y N \right] + \frac{1}{e} \frac{\nabla_\| j_\|}{n} + \frac{S_n}{n} \\
\frac{-m_i T_e}{eB^2} \partial_t \Omega &= \frac{m_i}{B^3} \frac{T_e^2}{e^2} \nabla_{\perp,i} \left\{ \frac{e\Phi}{T_e}, \nabla_{\perp,i} \left(\frac{e\Phi}{T_e} + \tau N \right) \right\} + \frac{2T_e}{RB} (1+\tau) \frac{n}{n_\Omega} \partial_y N - \frac{\nabla_\| j_\|}{n_\Omega}
\end{aligned}$$

The terms related to the parallel current read,

$$\frac{\nabla_\parallel j_\parallel}{n} = \frac{\sigma_0}{n_\nu}\frac{n_0 T_e}{B}\,\nabla_\parallel^2\left(N - \frac{e\Phi}{T_e}\right)$$
$$\frac{\nabla_\parallel j_\parallel}{n_\Omega} = \frac{\sigma_0}{n_\nu}\frac{n_0 T_e}{B}\frac{n}{n_\Omega}\,\nabla_\parallel^2\left(N - \frac{e\Phi}{T_e}\right)$$

To move forward, we set $n_\nu = 1$ and $n/n_\Omega = 1$. The first amounts to considering a constant collision frequency and adiabatic parameter Equation 3.16 taken at the reference density n_0. The second corresponds to the strong Boussinesq assumption. It is made here for simplicity, one can then deal only with the logarithm of the density in the following. This will be discussed further in Section 3.5.

The dimensionless $3d$ system can then be recast as follows,

$$\partial_t N + \{\phi, N\} = g\partial_y(\phi - N) + \sigma_0\nabla_\parallel^2(N-\phi) + D\nabla_\perp^2 N + S_N \tag{3.12}$$
$$\partial_t \Omega + \nabla_{\perp,i}\left\{\phi, \nabla_{\perp,i}(\phi + \tau N)\right\} = -(1+\tau)g\partial_y N + \sigma_0\nabla_\parallel^2(N-\phi) + \nu\nabla_\perp^2\Omega \tag{3.13}$$

The time is normalized to the ion cyclotron frequency $\omega_{cs} = (eB)/m_i$ and the lengths to the sound larmor radius $\rho_s = (m_i c_s)/(eB)$ with $c_s = \sqrt{T_e/m_i}$. The magnetic curvature parameter is defined as $g = (2\rho_s)/R$, with R the major radius of the tokamak. The parallel conductivity is considered constant and is defined as the electron cyclotron frequency to the electron-ion collision frequency taken at n_0, $\sigma_0 = \omega_{ce}/\nu_{ei,0}$. The system is flux-driven with a source of particles S_N. The damping of small scales is ensured by the diffusive terms D and ν. The normalizations are recalled in Table 3.2.

Dimensionless variables	Dimensionless fields
$(\hat{x},\hat{y}) = \frac{(x,y)}{\rho_s}$	$\hat{n} = n/n_0$
$\hat{t} = \omega_{cs}t$	$\phi = e\Phi/T_e$
$\hat{\nabla} = \rho_s\nabla$	$\hat{v} = v/c_s$
$\{...,...\} = \rho_s^2\{...,...\}$	

Table 3.2 – Tokam1d-ES normalizations

Where the following constants have been introduced,

$$\rho_s = \frac{m_i c_s}{eB} = \frac{c_s}{\omega_{cs}} \;;\; c_s = \sqrt{\frac{T_e}{m_i}} \;;\; \omega_{ci} = \frac{eB}{m_i} \tag{3.14}$$

respectively the sound Larmor radius, the sound speed, and the ion gyro-frequency. Finally, n_0 and $B_0 \approx B$ are constant density and magnetic field.

3.2.5 Semi-spectral formulation: from 3d to 1d

In order to keep track of nonlinear dynamics while dealing with a more tractable system, each field is decomposed into a flux-surface average and a fluctuating component (Eq 3.15). In the spirit of previous similar models [154, 155, 156], the fluctuating components are Fourier transformed and projected onto

- A single parallel wave vector $k_\parallel$, so that $\nabla_\parallel \longrightarrow ik_\parallel$.
- A single poloidal wave vector k_y, so that $\partial_y \longrightarrow ik_y$.

Consequently, each field (N, ϕ) is split into an equilibrium and a fluctuating component as follows,

$$\begin{pmatrix} N \\ \phi \end{pmatrix} = \begin{pmatrix} N_{eq} \\ \phi_{eq} \end{pmatrix}(x,t) + \begin{pmatrix} N_k \\ \phi_k \end{pmatrix}(x,t)\exp[i(k_y y + k_\parallel z)] + \text{ cc} \tag{3.15}$$

where cc stands for the complex conjugate. Notice that (N_{eq}, ϕ_{eq}) are real variables, whereas (N_k, ϕ_k) are complex. The implications of this decomposition call for further discussion. In particular, retaining a single poloidal wavenumber k_y implies that, in the time evolution of the fluctuating modes N_k and ϕ_k, the model cannot consider the nonlinear terms that arise due to mode-mode coupling. Indeed, these terms involve other modes $k'_y \neq k_y$ which are by essence excluded by the model. One of the consequences is that possible energy (and enstrophy) cascade processes cannot be accounted for. Three important remarks can be done at this point:

- A refinement of the model would consist in adding a nonlinear saturation mechanism to the fluctuations of the form $\partial_t N_k = \cdots - D_{NL}|N_k|^2 N_k$ with D_{NL} some positive coefficient [154]. It would account for part of the physics contained in the missing nonlinear interactions, namely nonlinear energy dissipation as one of the routes towards turbulence saturation.
- Even with $D_{NL} = 0$, the model still retains important nonlinearities. The main ones are the turbulent flux and the Reynolds stresses that govern respectively the time evolution of the equilibrium density N_{eq} and poloidal flow V_{eq} profiles (see eqs.(3.32-3.33) and eqs.(3.18-3.25)). Note also that, since these radial profiles enter the time dynamics of fluctuating modes, they result in nonlinear couplings between different radial wave vectors k_x (cf. all terms in eqs.(3.34-3.35) of the form $F(A_{eq})G(B_k)$, where F and G stand for linear operators and $A, B \in \{N, V, \Omega\}$). This latter point is not explicit in the equations since they are not written in the Fourier space in k_x but in the configuration space x.
- In the absence of *ad-hoc* nonlinear term in the dynamics of fluctuating fields (i.e. when taking $D_{NL} = 0$), turbulence saturation in Tokam1D therefore relies on two mechanisms: (i) nonlinear transfer of turbulent energy to large scale flows (ZFs) that do not contribute to transport and (ii) the relaxation of mean profiles - as a result of turbulent fluxes - leading to a reduction of the turbulence drive (lower gradients, i.e. thermodynamical forces). The last one is often overlooked since absent from gradient-driven models. We argue these two mechanisms play a key role close to marginal stability. As a matter of fact, this regime is likely to be relevant in fusion reactor plasmas. Indeed, given the expected large volume of reactor devices, they will likely be weakly driven - low power density - so that the strong efficiency of turbulent transport - as attested by the stiffness of the ex-

perimental temperature profiles in tokamak plasmas (see e.g. [157]) - should maintain the gradients close to marginality [72]. RE Waltz, in ref. [158], also hints that the drift waves (turbulence) to radial (equilibrium) mode coupling "dominates the nonlinear saturation". Which leads to "two-mode" simulations giving close to correct transport provided that the turbulence wavenumber is correctly chosen.

The model bears similarity with the quasi-linear approach of turbulent transport. Yet, it departs from the quasi-linear framework in two ways: no scale separation is *a priori* assumed in the radial direction regarding equilibrium and fluctuations quantities, and fluxes are not assumed to be diffusive in nature. Using the decomposition Equation 3.15, The adiabaticity parameter C is defined as:

$$C = \sigma_0 k_{\parallel}^2 \tag{3.16}$$

It is equivalent to the C_1 parameter initially derived by Hasegawa and Wakatani [48].

The variable associated to the density field is defined as $N = \ln n/n_0$. In the model, we retain N_{eq} and $\widetilde{N}$. It should be noted that the interpretation of the equilibrium and fluctuation parts is quite tricky in this context. Indeed, splitting the density field itself in its equilibrium and fluctuating components, $n = n_{eq} + \widetilde{n}$, leads to: $N_{eq} = \ln n_{eq}$ and $\widetilde{N} = \ln(1 + \widetilde{n}/n_{eq})$. One cannot relate one single Fourier mode $(k_y, k_{\parallel})$ of $\widetilde{n}$ to that of $\widetilde{N}$ because of the logarithmic function. Note that the two definitions can be reconciled if one considers $\widetilde{n}/n_{eq} \ll 1$. Then, the logarithm can then be expanded into $\widetilde{n}/n_{eq}$. An other possibility is to alleviate the Boussinesq approximation. One would then deal directly with the density field instead of its logarithm.

As will appear in the following, one needs to carefully choose the poloidal k_y and parallel $k_{\parallel}$ wavenumber. The first can be estimated using linear analysis, see Section 3.4: we choose k_y for which the growth rate is maximal. It depends slightly on the turbulence parameters and will be fixed to $k_y = 0.3$ in the next chapter. This corresponds to typical ion-scale turbulence measured in experiments. The parallel wavenumber is trickier to estimate experimentally. In ref.[159], an attempt have been made on the torsatron TJ-K. In practice, it can also be estimated considering a connection length, see Section 3.2.6. In the following, the parallel wavenumber is only considered as part of the adiabaticity parameter C.

Density equation

The equilibrium density equation is obtained by taking the flux-surface average of Equation 3.12. The advection term is determined from Equation B.5 derived in Section B.2. Remembering that any exact differential differential operator on y and / or z vanishes when taking the average, one is left with,

$$\partial_t N_{eq} = -\partial_x \Gamma_{turb} + D\partial_x^2 N_{eq} + S_N. \tag{3.17}$$

Where Γ_{turb} is reminiscent of the particle flux that results from the advection of density by the radial electric drift: $\Gamma_{turb} \sim \langle n v_{Ex} \rangle$. It reads,

$$\Gamma_{turb} = -2k_y \Im(N_k \phi_k^*) = -2k_y |\phi_k||N_k| \sin \Delta\varphi_k \tag{3.18}$$

With * denoting the complex conjugate and $\Delta\varphi_k = \varphi_k^N - \varphi_k^\phi$ the cross-phase between density and electric potential fluctuations defined as the difference between the phases of the density, $N_k = |N_k|e^{i\varphi_k^N}$ and of the electric potential. The fluctuation equation is obtained by subtracting the equilibrium to the global equation,

$$\partial_t \widetilde{N} + \{\phi, N\} - \langle\{\phi, N\}\rangle = g\partial_y(\widetilde{\phi} - \widetilde{N}) + \sigma_0 \nabla_\parallel^2(\widetilde{N} - \widetilde{\phi}) + D\nabla_\perp^2 \widetilde{N} \tag{3.19}$$

The Poisson bracket involves both linear and nonlinear terms, it is derived Equation B.7. When taking the Fourier transform and projecting on the single k_y and $k_\parallel$ wave vectors (cf. Equation 3.15), the contribution of the nonlinear Poisson bracket then disappears. As already discussed, this term, which would account for nonlinear couplings between different Fourier modes in y and z, is responsible for energy transfers along these directions. Ultimately, N_k is governed by the following equation:

$$\partial_t N_k = ik_y(\phi_k \partial_x N_{eq} - V_{eq} N_k) + igk_y(\phi_k - N_k) + C(\phi_k - N_k) + D_1 \nabla_\perp^2 N_k - D_{NL} N_k^2 N_k^* \tag{3.20}$$

The terms proportional to g are defined as *compressibility terms* because they originate from the divergence of the electric and diamagnetic drifts.

Vorticity equation

The same method is applied to the charge continuity equation in order to obtain the dynamical equations for the equilibrium and the fluctuations of the vorticity field. Using decomposition Equation 3.15, the general vorticity takes the form $\Omega = \Omega_{eq} + \Omega_k \exp\left[i\left(k_y y + k_\parallel z\right)\right] + \text{cc}$, with:

$$\Omega_{eq}(x,t) = \partial_x^2(\phi_{eq} + \tau N_{eq}) \tag{3.21}$$

$$\Omega_k(x,t) = (\partial_x^2 - k_y^2)(\phi_k + \tau N_k). \tag{3.22}$$

The equation governing Ω_{eq} derives from the flux surface average of Equation 3.13. Using Equation B.6 and integrating once in x leads to,

$$\partial_t(V_{eq} + \tau\partial_x N_{eq}) = \partial_x\langle\partial_y\widetilde{\phi}\,\partial_x(\widetilde{\phi} + \tau\widetilde{N})\rangle + \nu\partial_x^2(V_{eq} + \tau\partial_x N_{eq})$$

Where we have introduced the equilibrium velocity equal, when normalized, to the opposite of the normalized equilibrium radial electric field,

$$V_{eq} \equiv \partial_x \phi_{eq} = -\langle E_r\rangle \tag{3.23}$$

The equation on the mean flow V_{eq} is then derived by subtracting the dynamical equation of $\tau\partial_x N_{eq}$, obtained by taking the radial derivative of Equation 3.17. This leads to,

$$\partial_t V_{eq} = \partial_x\langle\partial_y\widetilde{\phi}\,\partial_x(\widetilde{\phi} + \tau\widetilde{N})\rangle - \tau\partial_x^2\langle\widetilde{N}\partial_y\widetilde{\phi}\rangle + \nu\partial_x^2 V_{eq} + (\nu - D)\tau\partial_x^3 N_{eq} - \tau\partial_x S_N$$

In the following, one considers the case $D = \nu$, so that the term proportional to $\partial_x^3 N_{eq}$ vanishes. The two first terms on the right hand side can be integrated along x and recast in the following

way:

$$\langle \partial_y \widetilde{\phi}\, \partial_x (\widetilde{\phi} + \tau \widetilde{N}) \rangle - \tau \partial_x \langle \widetilde{N} \partial_y \widetilde{\phi} \rangle = \langle \partial_y \widetilde{\phi}\, \partial_x \widetilde{\phi} \rangle + \tau \langle \partial_y \widetilde{N} \partial_x \widetilde{\phi} \rangle = \langle \partial_x \widetilde{\phi}\, \partial_y (\widetilde{\phi} + \tau \widetilde{N}) \rangle$$

where we have used the equivalence $\langle \widetilde{N} \partial_{xy} \widetilde{\phi} \rangle = -\langle \partial_y \widetilde{N} \partial_x \widetilde{\phi} \rangle$. The final equation governing the dynamics of V_{eq} then reads as follows:

$$\partial_t V_{eq} = -\partial_x \Pi_{RS} + \nu \partial_x^2 V_{eq} - \partial_x \Pi_{neo} \tag{3.24}$$

Here, the additional $\partial_x \Pi_{neo}$ accounts for collisions and neoclassical effects. It is discussed in the next section. Also, we have precluded any source of poloidal flow, hence discarding the $\partial_x S_N$ term. This corresponds to assuming that particles are injected into the system without momentum. Finally, the flux surface average of the (x,y) component of the Reynolds stress tensor Π_{RS} is given by:

$$\Pi_{RS} = -\langle \partial_x \widetilde{\phi}\, \partial_y (\widetilde{\phi} + \tau \widetilde{N}) \rangle$$

It corresponds to the cross correlation of the fluctuations of the poloidal component of the $E \times B$ velocity and of the radial component of the $E \times B$ and ion diamagnetic velocities: $\langle \widetilde{v}_{Ey} (\widetilde{v}_{Ex} + \widetilde{v}^{\star}_{ix}) \rangle$. Using Equation B.6, with single k_y and $k_{\parallel}$ wave vectors, it reduces to:

$$\Pi_{RS} = -2 k_y \Im \left[(\phi_k^* + \tau N_k^*)\, \partial_x \phi_k \right] \tag{3.25}$$

The fluctuation dynamics is derived by subtracting the equilibrium from Equation 3.13. Similarly to the analysis done for the density continuity equation, the poisson bracket contains both linear and nonlinear contributions. The latter one, involving products of fluctuating quantities, disappears in the framework of the present model. Using Equation B.8 leads to,

$$\begin{aligned} \partial_t \Omega_k = &- i k_y g (1+\tau) N_k - i k_y V_{eq} \Omega_k + i k_y \partial_x [\phi_k \partial_x (V_{eq} + \tau \partial_x N_{eq})] \\ &- i k_y \partial_x V_{eq} \partial_x (\phi_k + \tau N_k) + C(\phi_k - N_k) + \nu_1 (\partial_x^2 - k_y^2) \Omega_k \end{aligned} \tag{3.26}$$

Accounting for collisions and neoclassical effects on the flow

The equilibrium flow is not only a result of the turbulence induced Reynolds stress. Actually, a substantial part derives from the radial force balance equation. The equilibrium force balance flow is considered crucial in the saturation of turbulence at the edge of tokamaks. It results in an velocity shear important for the turbulence saturation. In particular, it is considered instrumental to access improved confinement modes such as the H-mode [160, 26]. In this section, we show how this additional physics can be accounted for in the framework of the model.

First, a friction μ is added to the equilibrium velocity equation so as to account for neoclassical damping of the flows. Following the work of [161], it can be estimated through neoclassical assumptions. It reads,

$$\mu(x) = \left(\frac{q}{\varepsilon}\right)^2 \frac{0.452 f_T \nu_{i0} n_{eq}}{\left(1 + 1.03\sqrt{\nu_{\star i0} n_{eq}} + 0.31 \nu_{\star i0} n_{eq}\right)\left(1 + 0.66 \nu_{\star i0} n_{eq} \varepsilon^{3/2}\right)} \tag{3.27}$$

With q the safety factor, ε the inverse aspect ratio, $f_T \approx 1.46\sqrt{\varepsilon}$ the trapped particle fraction.

Note that once again, the density dependence has been made explicit from the collision frequency. Following Section 3.2.3, the ion collision frequency reads $\nu_i = \nu_{i0}\frac{n_{eq}}{n_0}$ and the collisionality reads, $\nu_\star = \nu_{\star i0}\frac{n_{eq}}{n_0}$. Remember that for the adiabaticity parameter, the collisionality has been chosen constant. To preserve the consistency of the present version of the model, the friction μ is kept constant whenever C is constant. The above refinement will be considered for tests and future extensions of the model.

Second, the velocity is forced to relax towards the radial force balance equilibrium, $\partial_t V_{eq} = ... - \mu(V_{eq} - V_{eq}^{FB})$ as prescribed in [162]. The force balance velocity can be derived from the radial momentum conservation equation,

$$nm_i\left(\frac{\partial v_x}{\partial_t} + \mathbf{v}\cdot\boldsymbol{\nabla} v_x\right) = -ne\partial_x\phi - \partial_x(nT_i) + ne(v_\theta B_\varphi - v_\varphi B_\theta) \tag{3.28}$$

with v_φ and v_θ the poloidal and toroidal velocities of the plasma ions. In the absence of toroidal momentum injection, v_φ is assumed small and neglected in the following. At equilibrium, the poloidal velocity can be written as,

$$v_\theta = \frac{1}{B}\partial_x\phi + \tau\frac{T_e}{eB}\frac{\partial_x n}{n}. \tag{3.29}$$

The first term on the right hand side is the poloidal component of the $E\times B$ velocity. The second derives from the pressure gradient. It relates to the density gradient for isothermal Tokam1D. Applying the normalization defined in Table 3.2 it reads,

$$V_{eq}^{FB} = v_\theta - \tau\partial_x N \tag{3.30}$$

The poloidal velocity is then considered in the neoclassical theory framework [8],

$$v_\theta = K(\nu_\star,\varepsilon)\frac{\nabla_r T_i}{eB} \tag{3.31}$$

with K a constant that depends on the collisionality $\nu_\star$ and the inverse aspect ratio ε. Due to the isothermal assumption of the present model, this term is equal to zero. As a result, the force-balance velocity only depends on τ and the density gradient: $V_{eq}^{FB} = -\tau\partial_x N$. Provided that the friction μ is large enough, the equilibrium velocity will relax towards V_{eq}^{FB}.

The effect of V_{eq}^{FB} on the equilibrium radial electric field profile $\langle E_r\rangle$ is shown in Figure 3.2. On the left hand side, a test case using $(g,C,\tau) = (5\times10^{-4},\ 10^{-3},\ 1)$ is shown. On the right hand side, the force balance velocity is added with a constant friction $\mu = 10^{-3}$. In both cases the system is driven with a source of particles $S_N = 10^{-4}$ starting from an unstable density profile $L_N = 80$ and constant diffusion coefficients $D_{0,1} = \nu_{0,1} = 10^{-2}$.

In both cases, the system develops spatial corrugations in the equilibrium radial electric field as a result of turbulence-induced Reynolds stress. In Figure 3.2b, the radial electric field remains globally negative due to the contribution from $\partial_x N_{eq}$. Since the density gradient is roughly constant in the radial direction, there is no significant variation in the force balance E_r. Consequently, no strong equilibrium shear is generated, and the impact on the dynamics is limited. However, as will be shown later, this situation changes when SOL physics is taken into account

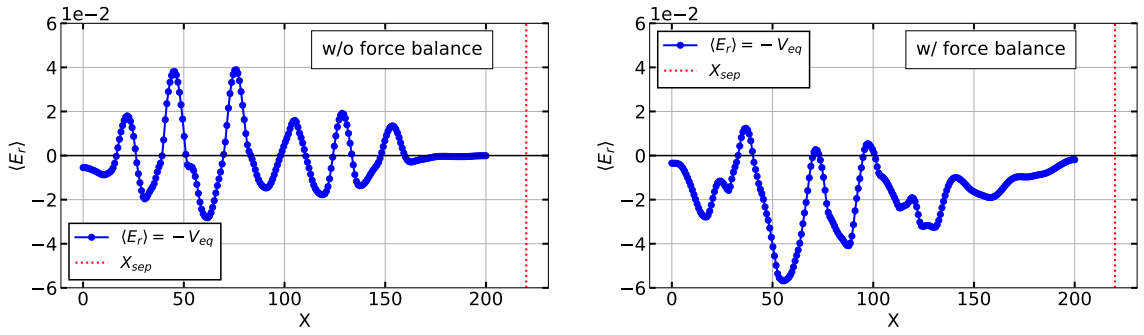

(a) (b)

Figure 3.2 – Equilibrium electric field profile averaged over 200 dt. (a) Without force balance velocity $V_{eq}^{FB} = 0$. (b) With force balance. The vertical red dotted line corresponds to a fictive separatrix location to emphasize the model region of interest. Simulation parameters: $(g, C, \tau) = (5 \times 10^{-4},\ 10^{-3},\ 1)$, $D_{0,1} = \nu_{0,1} = 10^{-2}$, $S_N = 10^{-4}$, $\mu = 10^{-3}$. Initial condition: $L_N = 80$.

(Figure 3.5).

3.2.6 1d semi-spectral model of core Tokam1D

Building on the previous considerations, the 1d semi-spectral system of equations involves 4 fields: two real fields for the equilibrium components (Eq 3.32, 3.33), and two complex fields for the fluctuating parts (Eq 3.34, 3.35). Different values for the diffusion and viscosity can be chosen for the equilibrium (D_0, ν_0) and for the fluctuations $(D_1, \nu_1, D_{NL}, \nu_{NL})$. The nonlinear saturation terms D_{NL} and ν_{NL} have to be chosen after careful comparison with $2D$ similar models to infer the necessary level of saturation. They are included for the sake of completeness but will not be used in the remainder of this work[1].

$$\partial_t N_{eq} = -\partial_x \Gamma_{turb} + D_0 \partial_x^2 N_{eq} + S_N \tag{3.32}$$

$$\partial_t V_{eq} = -\partial_x \Pi_{RS} + \nu_0 \partial_x^2 V_{eq} - \mu (V_{eq} - V_{eq}^{FB}) \tag{3.33}$$

$$\begin{aligned} \partial_t N_k = &+ ik_y(\phi_k \partial_x N_{eq} - V_{eq} N_k) + igk_y(\phi_k - N_k) + C(\phi_k - N_k) \\ &+ D_1 \nabla_\perp^2 N_k - D_{NL} |N_k|^2 N_k \end{aligned} \tag{3.34}$$

$$\begin{aligned} \partial_t \Omega_k = &- ik_y g(1+\tau) N_k - ik_y V_{eq} \Omega_k + ik_y \partial_x [\phi_k \partial_x (V_{eq} + \tau \partial_x N_{eq})] \\ &- ik_y \partial_x V_{eq} \partial_x (\phi_k + \tau N_k) + C(\phi_k - N_k) + \nu_1 \nabla_\perp^2 \Omega_k - \nu_{NL} |\Omega_k|^2 \Omega_k \end{aligned} \tag{3.35}$$

The system of equations includes the logarithm of the density $N = \ln n/n_0$, the equilibrium velocity $V_{eq} \equiv \partial_x \phi_{eq}$ and the fluctuations of the generalized vorticity (Equation 3.22). The particle flux and Reynolds stress can be found in Equation 3.18 and Equation 3.25 respectively. The details of the numerical implementation of the model can be found in Section B.1.

The system is controlled through 4 main physical parameters: the magnetic curvature $g =$

[1]Note that if the nonlinear saturation is considered, the turbulent flux of particles should also be adjusted. Specifically, the present Γ_{turb} is a lower bound, as the $2D$ formulation sums over the whole poloidal spectrum.

$(2\rho_s)/R$, with R the major radius of the tokamak, the adiabatic parameter $C = \sigma_0 k_\parallel^2$, the temperature ratio $\tau = T_i/T_e$ and the source S_N. The Tokam1D system is not well-suited to study the ion to electron temperature ratio, see Section B.4. It is included for the diamagnetic component of the Reynolds stress, but will stay constant at $\tau = 1$ during the analysis. The order of magnitude of the other two parameters can be estimated from plasma parameters. Typically, the parallel wavenumber is estimated considering a connection length, $L_q = 2\pi qR$, which gives $k_\parallel = 2\pi/L_q = 1/(qR)$. Estimations of the main parameters are given for standard edge values of WEST, TCV and MAST-U tokamaks Table 3.3. The values are computed considering a major radius $R = 2.5\ m$ and minor radius $a = 0.5\ m$ for WEST, $(R,a) = (0.87, 0.25)$ m for TCV and $(R,a) = (0.9, 0.6)$ m for MAST-U.

	Model parameters		Plasma parameters			
	$g \equiv 2\frac{\rho_s}{R}$	$C \equiv (k_\parallel \rho_s)^2 \sigma_0$	$n_{sep}\ [10^{19}]$	$T_{sep}\ [eV]$	$B_{sep}\ [T]$	q_{95}
Dependencies	$\propto \frac{T_e^{1/2}}{RB}$	$\propto k_\parallel^2 \frac{T_e^{5/2}}{n_0 B}$				
WEST	$2-3\times10^{-4}$	$1-10\times10^{-4}$	$1-2$	$50-100$	3	5.5
TCV	$8-12\times10^{-4}$	$1.5-15\times10^{-3}$	$0.5-1$	$25-50$	1.4	3.5
MAST-U	3×10^{-3}	3×10^{-3}	1.5	40	0.43	6

Table 3.3 – Main model parameters and their range for typical values of WEST, TCV and MAST-U tokamaks. Parameters are computed assuming $T_e = T_{sep}$, $n_0 = n_{sep}$ and $B = B_{sep}$. The parallel wavenumber is computed assuming a connection length $k_\parallel = 1/(q_{95}R)$.

It appears from the parameter dependencies that the strong variation of density and temperature profiles at the edge of tokamak plasmas translates into a wide range of g and C values. Nevertheless, one has to keep in mind that Eq.3.10 assumes a large electron-ion collision frequency as compared to the electron inertial term. Therefore, the model loses its validity if T_e is too large or n too small. It is interesting to note that C decreases if the density increases. It has implication on the interpretation of the nonlinear simulations: a high density (resp. low C) leads to a decrease in the zonal flows energy, see Section 4.3.1.

3.2.7 Energetics

In this section is considered the energetics of the model. Partitioning the energy into distinct channels gives insight into the energy transfer between turbulence, flows and profiles in the nonlinear regime. Also, it provides a consistency check in order to prevent the appearance of spurious instabilities. As it should, the model obeys an energy conservation principle, which states that energy is conserved in the absence of source (particle source S_N) and sinks (dissipative and viscous terms). The details of the derivation are provided in Section B.3.

To derive an energy balance equation, we multiply Eq. 3.12 and Eq. 3.13 by $(1+\tau)N$ and $(\phi + \tau N)$, respectively. The equations are integrated by parts over the whole domain, leading to surface terms that need to be considered carefully. We neglect the surface terms hereafter, their

form can be found in Section B.3. After integrating by parts, and summing the two equations, the interchange terms, proportional to the g parameter, are found to vanish. Such a cancellation requires to keep the compressibility term originating from the divergence of the electric drift. This compressibility term being of same order as the diamagnetic flux, there is no reason to include divergence of the electric drift and not the divergence of the diamagnetic flux. Therefore, both terms are kept in the equations. The drift wave terms can be reorganized in the form of a parallel current $j_\parallel = \sigma n \nabla_\parallel (N - \phi)$. The conservation of energy then takes the following form,

$$\frac{d\mathscr{E}_{tot}}{dt} = P_{\mathscr{E}} - D_{\mathscr{E}} \tag{3.36}$$

With $\mathscr{E}_{tot}$ the total energy, $P_{\mathscr{E}}$ the production term and $D_{\mathscr{E}}$ the dissipation term.

$$\mathscr{E}_{tot} = \int E_{tot}\, d\mathscr{V} = \int \frac{1}{2}\left\{(1+\tau)N^2 + \left[\nabla_\perp(\phi+\tau N)\right]^2\right\} d\mathscr{V} \tag{3.37}$$

$$P_{\mathscr{E}} = (1+\tau)\int N S_N\, d\mathscr{V} \tag{3.38}$$

$$D_{\mathscr{E}} = \int \frac{j_\parallel^2}{\sigma_0}\, d\mathscr{V} + D(1+\tau)\int (\nabla_\perp N)^2\, d\mathscr{V} + \nu \int \left[\nabla_\perp^2(\phi+\tau N)\right]^2 d\mathscr{V} \tag{3.39}$$

With $\int d\mathscr{V}$ being the integration on the whole volume (x,y,z). It is shown in Section B.3 that the advection terms, linked to Poisson brackets, vanish upon integration. The production term reduces to the source of particles injected in the system. The dissipation terms involve the parallel plasma resistivity, the dissipation and the viscosity.

The total energy E_{tot} is made of two terms. The second one scales like the kinetic energy associated to both electric and diamagnetic drifts, while the first one involves both electron and ion pressures. Notice the somewhat peculiar structure of the latter term, already found in [62], neither proportional to $(1+\tau^2)N^2$ nor to $(1+\tau)^2N^2$ as one may have expected. Note that the final result, ensuring that the first term on the right hand side of Equation 3.39 is positive definite, requires that the conductivity σ only depends on the radial direction and time. Therefore, if one chooses to include a non-constant electron-ion collision frequency in the model, it is necessary to consider a flux-surface averaged quantity.

The energy conservation terms can be decomposed in equilibrium and fluctuating components, following the same method used to derive Eqs.3.32 $-$ 3.35. Noticing that linear terms vanish after the volume integration, the pressure energy turns out to be restricted to:

$$(1+\tau)N^2 \rightarrow (1+\tau)(N_{eq}^2 + 2|N_k|^2). \tag{3.40}$$

The factor 2 in front of $|N_k|^2$ comes from the complex conjugate in (Eq.3.15). The kinetic energy term, associated to the ExB and ion diamagnetic drift velocities, reads:

$$\begin{aligned}(\nabla_\perp(\phi+\tau N))^2 \rightarrow \Big\{ &\left(V_{eq} + \tau\partial_x N_{eq}\right)^2 + 2|\partial_x\phi_k|^2 + 4\tau\Re(\partial_x\phi_k\partial_x N_k^*) \\ &+2|\tau\partial_x N_k|^2 + 2k_y^2\left[|\phi_k|^2 + |\tau N_k|^2 + 2\tau\Re(\phi_k N_k^*)\right] \\ &-2k_y\Im\left[\phi_k\partial_x\phi_k^* + \tau N_k\partial_x\phi_k^* + \tau\phi_k\partial_x N_k^* + \tau^2 N_k\partial_x N_k^*\right]\Big\}\end{aligned} \tag{3.41}$$

The total energy can then be organized into different channels: the equilibrium profiles of density (Eq. 3.42) and velocity (Eq. 3.43) on the one hand, and in between fluctuating components on the other hand. The latter can be split into electron and ion (terms proportional to τ) components but for the sake of simplicity, only a turbulent energy that takes all the fluctuations into account (Eq. 3.44) is considered. Finally, a term corresponding to the interaction between the density and the flows is also obtained (Eq. 3.45). Its role is still unclear; it remains small in all simulations.

$$E_{Neq} = (1+\tau)N_{eq}^2 + \left(\tau\partial_x N_{eq}\right)^2 \tag{3.42}$$

$$E_{Veq} = V_{eq}^2 \tag{3.43}$$

$$\begin{aligned} E_{turb} = {} & 2(1+\tau)|N_k|^2 + 2|\partial_x\phi_k|^2 + 2|\tau\partial_x N_k|^2 + 4\tau\Re(\partial_x\phi_k\partial_x N_k^*) \\ & + 2k_y^2\left[|\phi_k|^2 + |\tau N_k|^2 + 2\tau\Re(\phi_k N_k^*)\right] \\ & - 2k_y\Im\left[(\phi_k\partial_x\phi_k^*) + \tau N_k\partial_x\phi_k^* + \tau\phi_k\partial_x N_k^* + \tau^2 N_k\partial_x N_k^*\right] \end{aligned} \tag{3.44}$$

$$E_{Neq-Veq} = 2\tau V_{eq} N_{eq} \tag{3.45}$$

The total energy E_{tot}, whose volume integral evolves according to Equation 3.36, can then be recast as

$$E_{tot} = E_{Neq} + E_{Veq} + E_{turb} + E_{Neq-Veq}. \tag{3.46}$$

It allows one to study the transfer of energy between the density, flows and turbulence. The dynamics between the flow and turbulence energies typically follows a predator-prey behaviour. First the energy of turbulence increases, until ZFs are created and pump out energy from turbulence. This well-established behaviour – where ZFs behave as a predator for the turbulence-prey – has been studied in specific models such as in [163] and in experiments [99]. An example of this regime is shown in Figure 3.3 for the test case: $(g, C, \tau) = (5\times10^{-4},\ 10^{-3},\ 1)$.

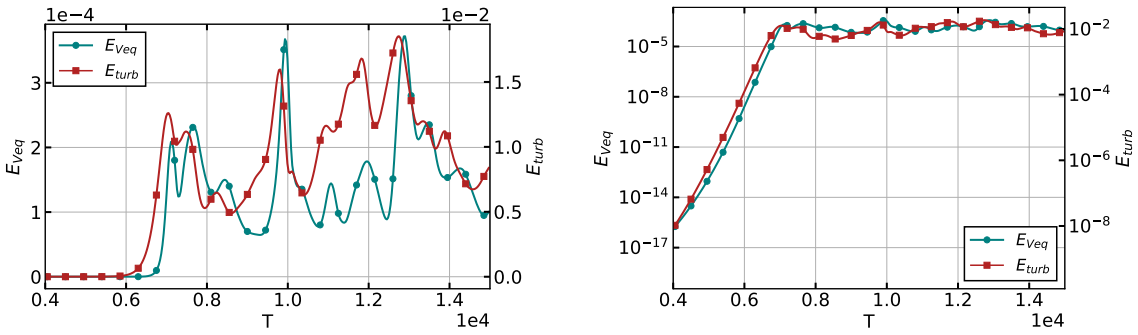

(a) (b)

Figure 3.3 – (a) Example of a predator-prey behaviour on turbulent and flow energies. E_{turb} and E_{Veq} are averaged over the radial axis and plotted as a function of time. (b) Semi-log version of (a): exponential growth of the turbulence and flows. Simulation parameters: $(g, C, \tau) = (5\times10^{-4},\ 10^{-3}, 1)$, $D_{0,1} = \nu_{0,1} = 10^{-2}$, $S_N = 10^{-4}$, $\mu = 10^{-3}$, no force balance. Initial condition: $L_N = 80$.

The presented simulation starts with no fluctuation or flows but with an unstable profile. It follows that fluctuations (E_{turb}) grow exponentially from start to $T = 7 \times 10^3$ during the linear phase. After a small delay, turbulence generated flows (E_{Veq}) start to increase as well. Doing so, they pump out turbulent energy that reaches a maximum at $T = 7 \times 10^3$. The prey-like turbulent source for the predator-like ZFs then decreases and flow energy declines subsequently. This increase-decrease of prey and predator population then leads to quasi-periodic oscillations throughout the simulation.
Note that for these parameters the turbulent energy is about a two order of magnitude larger than the flows energy. It will be shown that the ratio between flows and turbulence energies greatly changes when scanning the (g,C) parameters of the model: some domains in the parameter space are characterized by larger flows to turbulence energy ratio.

3.3 From close to open field lines - describing the SOL

In this section, the model is extended from the core to the Scrape-off layer (SOL hereafter). First, because it enables the core-turbulence to interact with the SOL-turbulence. For example, one can expect SOL conditions to influence the core, or the core turbulence to spread into the SOL. Second, nonlinear dynamics and transport are largely dependent on conditions at the last-closed flux-surface (LCFS) [60, 164, 122]. In particular, the equilibrium radial electric field $\langle E_r \rangle$ is expected to change sign when crossing the LCFS. It results in a velocity shear important for the turbulence saturation. It is considered instrumental to access – or at least to sustain – improved confinement modes such as the H-mode [160, 26]. Therefore, the separatrix region should be incorporated into the model itself, rather than treated as an imposed boundary condition.

The goal here is not to describe in details the dynamics of the scrape-off-layer nor the transition from close to open field lines, but to include some relevant effects such that the boundary condition of the Tokam1D model is outside the separatrix. That way, the inversion of E_r is included and the role of equilibrium shear together with the shear induced by ZFs can be studied. The underlying idea is to couple two models, one for the core and one for the SOL. Then, a mask in a form of a hyperbolic tangent is used to transition from one to the other. As will be shown, the SOL model is very close to the model previously derived in the core. The differences are mainly twofold:

- The system of equations is closed using the Debye sheath condition instead of the Ohm's law.
- The parallel dynamics depends on the parallel connection length instead of the parallel wavenumber: $\nabla_\parallel = ik_\parallel \xrightarrow{SOL} \nabla_\parallel = 1/L_\parallel$.

This results in a different estimation of the adiabatic coefficient and in slight modifications of the equations. Those will lead to linear and nonlinear differences for the two regions. First, the physics retained for the SOL region is described. Then, its implementation into the code is detailed.

3.3.1 Tokam1D-ES SOL

The density and vorticity equations of Tokam1D, Equation 3.4 and Equation 3.6, are similar in the SOL. However, one needs to estimate the parallel current in order to close the system of

equations. A number of assumptions are necessary to complete the derivation. More details can be found in the introduction of the SOL region, in Section 1.2.3.

- *Sheath-limited regime*: the physics of the SOL is governed by the plasma wall interaction and parallel gradients in the quasi-neutral plasma – away from the Debye sheath – assumed to be small.
- We consider the limit of a vanishing width of the Debye sheath. Of the order of a few Debye length, it is indeed very small as compared to the parallel connection length.
- Density at the entry of the sheath is equal to half the density at the stagnation point.

The first assumption implies that the electric potential in the pre-sheath is very close to the potential at the sheath entrance. Since we consider a grounded wall, one has $\phi_{sol} \approx \Lambda$. This stands in contrast to the *conduction-limited regime* where the transport is dominated by collisional processes rather than by direct interaction with the sheath. Typically one can consider the sheath-limited regime at low collisionality, with a low amount of neutrals. Since it is not the objective to describe plasma-neutral interactions we stay in the easiest configuration. Also, the physics of the sheath itself would require a kinetic treatment of the plasma species, out of the scope of the present Tokam1D model. Therefore, even though the physics is determined by the parameter at the sheath entrance, we consider the sheath width to be approximately zero. Finally, we consider the density at the entrance of the sheath to be equal to half the density at the stagnation point [12]. Note that this does not have strong implication on the physics and only enters through the free parameter C_{sol}, Equation 3.54, as a $1/2$ factor.

To estimate the parallel current, we make use of the derivation performed in Section 1.2.3. The equilibrium electron flux is given Equation 1.17, at the sheath entrance it is equal to the equilibrium ion flux Equation 1.14. It is recalled here:

$$\langle \Gamma_e^{sh} \rangle_{eq} = \langle \Gamma_i^{sh} \rangle_{eq} = n_e^{sh} \sqrt{\frac{T_e^{sh}}{2\pi m_e}} \exp\left(\frac{e\Delta\phi_{sh}}{T_e^{sh}}\right) \tag{3.47}$$

On the basis of previous models [78, 165], since the system at hand is turbulent, we allow heuristically the electron flux to move slightly around its equilibrium. This is done in the form of,

$$\Gamma_e^{sh} = \langle \Gamma_e^{sh} \rangle_{eq} \exp\left(e(\Lambda - \phi)/T_e\right) \tag{3.48}$$

Such a formulation ensures that, when the electric potential ϕ is equal to Λ, the parallel fluxes of electrons and ions falling on the wall are equal, consistent with the assumption that the wall is grounded. However, Equation 3.48 allows the potential to deviate from Λ, which relates to the fact that local current loops can develop transiently in the wall. It is important to note that the system is expected to remain close to its steady state, so that $|\Lambda - \phi| \ll 1$, the reason being that these fluctuations around Λ are strongly stabilized. If $\phi > \Lambda$: the electron flux at sheath entrance is larger than the equilibrium. The sheath electric field is then larger than the equilibrium and more electrons are being repelled (v_c increases, Equation 1.15). Consequently, the electron flux decreases towards equilibrium. From this and approximating the ion and electron parallel

current in the pre-sheath to their values at the sheath entrance, we write:

$$j_{\parallel i} \approx j_{sat} \tag{3.49}$$

$$j_{\parallel e} \approx -j_{sat} \exp\left(\frac{e\,(\Lambda-\phi)}{T_e}\right). \tag{3.50}$$

With $j_{sat} = e\frac{n}{2}c_s$, the ion saturation current. When both currents add up, one gets the parallel current at the entry of the sheath,

$$j_{\parallel}^{sheath} = j_{sat}\left(1-\exp\left(\frac{e\,(\Lambda-\phi)}{T_e}\right)\right) \tag{3.51}$$

The parallel gradient is approximated using the parallel connection length $L_{\parallel} = \pi q R$. Therefore, the parallel velocity term of Equation 3.4 reads,

$$\nabla_{\parallel}(nv_{\parallel e}) = -\frac{1}{e}\nabla_{\parallel} j_{\parallel e} = \frac{nc_s}{2L_{\parallel}} \exp\left(\frac{e\,(\Lambda-\phi)}{T_e}\right) \tag{3.52}$$

Using the normalizations from Table 3.2 and with $\hat{\Lambda} = (e\Lambda)/T_e$ one gets,

$$-\frac{1}{e}\hat{\nabla}_{\parallel}\hat{j}_{\parallel e} = \frac{\rho_s}{2L_{\parallel}}\hat{n}\exp(\hat{\Lambda}-\hat{\phi}) \approx \frac{\rho_s}{2L_{\parallel}}\hat{n}(1+\hat{\Lambda}-\hat{\phi}) \tag{3.53}$$

Where the exponential has been developed, thus assuming $\hat{\Lambda}-\hat{\phi}$ small, consistently with the discussion above. Hereafter, the hats are removed for clarity and each quantity must be understood as normalized. One defines the SOL conductivity parameter as,

$$C_{sol} = \frac{\rho_s}{2L_{\parallel}} \tag{3.54}$$

The SOL conductivity parameter plays a similar role as the adiabaticity parameter in the core. Note that C_{sol} shares the plasma parameter dependencies of the interchange dimensionless parameter g but is expected to be smaller: $C_{sol} = \rho_s/2L_{\parallel} = gR/(4L_{\parallel}) \approx g/4\pi q$. With the closure and the definition of the gradient, one can rewrite the system of equations (3.12, 3.13) as,

$$\boxed{\partial_t N + \{\phi, N\} = g\partial_y(\phi - N) - C_{sol}(1+\Lambda-\phi) + D_{sol}\nabla_{\perp}^2 N} \tag{3.55}$$

$$\boxed{\partial_t \Omega + \nabla_{\perp,i}\left\{\phi, \nabla_{\perp,i}(\phi+\tau N)\right\} = -(1+\tau)g\partial_y N - C_{sol}(\Lambda-\phi) + \nu_{sol}\nabla_{\perp}^2\Omega} \tag{3.56}$$

The model is then further reduced from three to one dimension applying the same method as in Section 3.2.5. The steps in the calculations are identical and will not be detailed at the exception of the SOL specific components.

3.3.2 Reduction from 3d to 1d

The SOL model is further reduced from 3 to 1 dimensions applying the same method as in Section 3.2.5. The right hand side of Eq. (3.55, 3.56) is the same as the core version at the exception of terms related to the parallel current. Therefore the derivation details are given only

for terms related to C_{sol}. The equilibrium of Equation 3.55 and Equation 3.56 reads respectively,

$$\partial_t N_{eq} = RHS_{Neq} - C_{sol}\left(1 + \Lambda - \phi_{eq}\right) \tag{3.57}$$
$$\partial_t \Omega_{eq} = RHS_{\Omega eq} - C_{sol}\left(\Lambda - \phi_{eq}\right) \tag{3.58}$$

With RHS_{Neq} the right hand side of Equation 3.17. Similarly, $RHS_{\Omega eq}$ corresponds to the right hand side of the core equilibrium vorticity equation. The fluctuating parts read,

$$\partial_t \widetilde{N} = RHS_{\widetilde{N}} + C_{sol}\widetilde{\phi} \tag{3.59}$$
$$\partial_t \widetilde{\Omega} = RHS_{\widetilde{\Omega}} + C_{sol}\widetilde{\phi} \tag{3.60}$$

Here, $RHS_{\widetilde{N}}$ and $RHS_{\widetilde{\Omega}}$ relate to the right hand side of Equation 3.19 and Equation 3.26, at the exception of terms related to C that are written explicitly in the above expressions.

The difference between the above equations and the core version is first that the divertor acts as a sink of particles. It corresponds to the C_{sol} term for the density equilibrium Equation 3.57 which is new. Note that this term should always be negative (hence act as a sink: the wall is a perfect charge absorber in the model) because ϕ_{eq} should remain close to Λ. Indeed, Equation 3.58 enforces $\phi_{eq} = \Lambda$ in the limit of $C_{sol} \to +\infty$. In any case, this property can be diagnosed when post-processing the simulation data. Second, the parallel current terms in the fluctuation equations now only relate to the electric potential fluctuations instead of being the difference with density fluctuations. It will appear later on during the linear analysis that this leads to the stabilisation of the drift wave instability in the SOL region.

The equilibrium vorticity equation is further integrated resulting in the equilibrium velocity equation,

$$\partial_t V_{eq} = RHS_{Veq} - C_{sol}\left[\int_{x_{sep}}^{x_{max}} (\Lambda - \phi_{eq})dx' + \tau(V_{eq} - \partial_x \Lambda)\right] \tag{3.61}$$

The two terms on the right-hand side have a similar role: they ensure that both the equilibrium potential and velocity tend towards Λ and its derivative respectively. The integration should be performed only in the SOL region from x_{sep} the separatrix to x_{max} the boundary. The outer radial boundary condition on ϕ_{eq} should be adapted accordingly and set to $\Lambda(x_{max})$.

3.3.3 Treatment of the mask and Λ

The mask $\mathscr{M}_{sol}$ is chosen in the form of an hyperbolic tangent that varies from 0 to 1. Defining $\rho_{sep} = x_{sep}/L_x$ the separatrix location and $\rho = x/L_x$ the normalized radius, it reads,

$$\mathscr{M}_{sol}(x) = \frac{1}{2}\left(1 + \tanh\frac{\rho - \rho_{sep}}{\Delta\rho_{\mathscr{M}}}\right) \tag{3.62}$$

One can control the stiffness of the transition with the parameter $\Delta\rho_{\mathscr{M}}$. The separatrix location, ρ_{sep}, is a free input parameter between 0 and 1 such that it corresponds to the middle of the transition mask.

Λ depends on the electron temperature in the radial direction. In Tokam1D-ES, the isothermal

condition would impose a constant Λ and the electric field would not be positive in the SOL. So as to have a non-zero radial electric field in the SOL without alleviating the isothermal condition, the choice is made to impose an exponential decrease of Λ towards the wall. That corresponds to an imposed radial profile of T_e inside the SOL. In this framework, the radial electric field in the SOL tends towards a positive value $E_{x,SOL} = -\partial_x \phi_{eq} \to -d\Lambda/dx > 0$, as expected. Conversely, in the confined region $x < x_{sep}$, the radial force balance tends to force E_x to be negative to balance the radial pressure gradient. In the code, Λ is defined as follows,

$$\Lambda(\rho) = \Lambda_0 \left(1 - \mathscr{M}_{sol}\right) + \Lambda_0 \exp\left(-\frac{\rho - \rho_{sep}}{\Lambda_q}\right) \mathscr{M}_{sol} \tag{3.63}$$

Λ_q corresponds to the steepness of the exponential decay of Λ, the smaller it is, the larger the radial electric field will be. Since the equilibrium velocity depends on the radial derivative of Λ, it is important to ensure that Λ stays C^1 in the transition between the two regions. This is done using the SOL mask, that smooths the transition from the constant Λ_0 in the core to the decreasing Λ in the SOL. If Λ_q is very small, the exponential decrease can be very steep. As a result, there can be a small overshoot of Λ close to ρ_{sep}. To avoid this problem, we slightly slide the SOL mask for Λ such that the transition does not occur at ρ_{sep} but at $\rho_{sep} + 2\Delta\rho_{\mathscr{M}}$. This small adjustment ensures that there is no overshoot for reasonable values of Λ_q.

The mask and Λ are shown in Figure 3.4 for the test case. For this example, the separatrix is located at $\rho = 0.7$, $L_{\mathscr{M}} = \delta = 0.05$. $\Lambda_0 = 3$ and decreases with $\Lambda_q = 0.3$. The corresponding radial electric field is shown in Figure 3.5.

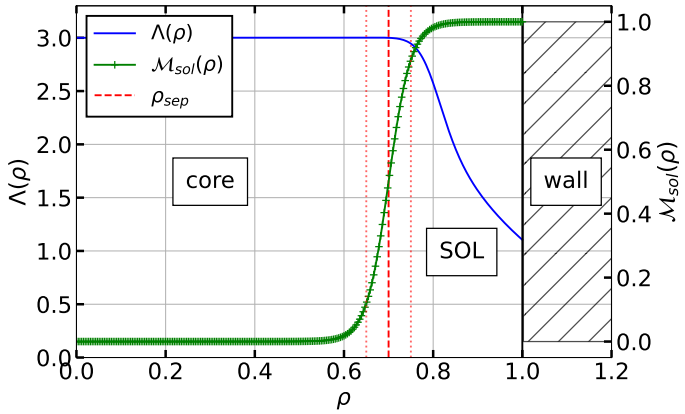

Figure 3.4 – Mask and Λ designed to transition from core to scrape-off layer in Tokam1D.

3.3.4 Semi-spectral formulation of Tokam1D-ES with SOL

Making use of the last developments, one can write the full system of equations for Tokam1D-ES encompassing both the core and the SOL. All in all, the equations are similar for both domains at the exception of terms related to C and C_{sol} that depend on the SOL transition mask

$\mathscr{M}_{sol}$.

$$\partial_t N_{eq} = -\partial_x \Gamma_{turb} - \mathscr{M}_{sol} C_{sol} |1 + \Lambda - \phi_{eq}| + D_0 \partial_x^2 N_{eq} + S_N \tag{3.64}$$

$$\partial_t V_{eq} = -\partial_x \Pi_{RS} + \nu_0 \partial_x^2 V_{eq} - \mathscr{M}_{sol} C_{sol} \left[\int_{x_{sep}}^{x_{max}} |\Lambda - \phi_{eq}| dx' + \tau (V_{eq} - \partial_x \Lambda) \right] - (1 - \mathscr{M}_{sol}) \mu (V_{eq} - V_{eq}^{FB}) \tag{3.65}$$

$$\partial_t N_k = +ik_y(\phi_k \partial_x N_{eq} - V_{eq} N_k) + igk_y(\phi_k - N_k) + \mathscr{M}_{sol} C_{sol} \phi_k + (1 - \mathscr{M}_{sol}) C(\phi_k - N_k) + D_1 \nabla_\perp^2 N_k - D_{NL} N_k^2 N_k^* \tag{3.66}$$

$$\partial_t \Omega_k = -ik_y g(1+\tau) N_k - ik_y V_{eq} \Omega_k + ik_y \partial_x [\phi_k \partial_x (V_{eq} + \tau \partial_x N_{eq})] - ik_y \partial_x V_{eq} \partial_x (\phi_k + \tau N_k) + \mathscr{M}_{sol} C_{sol} \phi_k + (1 - \mathscr{M}_{sol}) C(\phi_k - N_k) + \nu_1 (\partial_x^2 - k_y^2) \Omega_k \tag{3.67}$$

The system of equations includes the logarithm of the density $N = \ln n/n_0$, the equilibrium velocity $V_{eq} \equiv \partial_x \phi_{eq}$ and the fluctuations of the generalized vorticity (Equation 3.22). The particle flux and Reynolds stress can be found in Equation 3.18 and Equation 3.25 respectively.

Using this model on the test case, the equilibrium radial electric field is shown in Figure 3.5. It can be compared to the case without SOL but with force balance velocity presented in Figure 3.2b and without force balance velocity (Figure 3.2a). The simulation parameters are the same, with $(g, C, \tau) = (5 \times 10^{-4},\ 10^{-3},\ 1)$ for the core and $C_{sol} = 10^{-4}$ for the SOL.

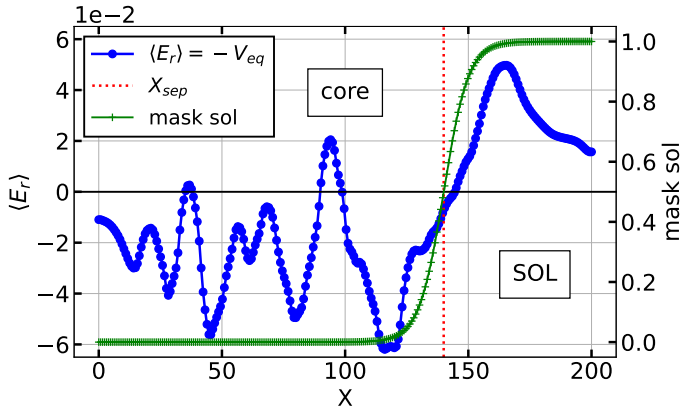

Figure 3.5 – Equilibrium electric field profile averaged over 200 dt with force balance velocity and SOL physics. The vertical red dotted line corresponds to the separatrix location. Simulation parameters: $(g, C, \tau, C_{sol}) = (5 \times 10^{-4},\ 10^{-3},\ 1,\ 10^{-4})$, $D_{0,1} = \nu_{0,1} = 10^{-2}$, $S_N = 10^{-4}$, $\mu = 10^{-3}$, no force balance. Initial condition: $L_N = 80$.

As expected, one observes that the radial electric field ($\langle E_r \rangle \sim -V_{eq}$) changes sign close to the separatrix region. It is globally negative in the confined region as a result of the force balance velocity and becomes positive in the scrape-off layer as a consequence of the Λ radial dependence. The maximum of the radial electric field is located somewhere inside the SOL but its exact location depends on turbulence and equilibrium force balance effect.
Corrugations in the core are caused by the turbulence generated ZFs. Conversely, no such strong

corrugations are observed in the SOL region. In the simulations performed so far, it appeared difficult to destabilize the SOL region. Instead, the turbulence is found to spread from the core into the SOL and to vanish. A first explanation could be that CDW are linearly stable in this region (see Section 3.4.4). It is also possible that the instability threshold for the above set of parameter is above the typical gradient involved in the SOL region.

3.4 Tokam1D-ES linear analysis

The linear analysis serves three main purposes. First, it is used to identify the linear instabilities present in the model. The key parameters governing the instabilities can be identified. Second, it serves as a validation step for the numerical model by checking the agreement between the code and the linear analysis in the linear phase of the fluctuations exponential growth. Third, it guides the nonlinear analysis. Some linear properties, such as the linear cross phase between physical quantities, can be retrieved in the turbulent regime [166]. Also, tokamak plasma turbulence is often considered near-marginal and weakly forced. If follows that, one can often approximate parts of the dynamics with quasi-linear effects [118].

The section is separated in four parts. In the first part the linear analysis of the Tokam1D-ES core model is derived. The second part focuses on the code validation. We will show that the numerical simulation indeed follows the linear prediction during the mode exponential growth part before reaching nonlinear saturation. In the third part the parameter domains of instability existence are studied. The compressibility terms are shown to stabilize the interchange instability at large scales. Finally, the last part takes into account the physics of the SOL. With the assumptions chosen for Tokam1D-ES SOL, the drift waves instability is shown absent in this region.
Additionally, the effect of the ion to electron temperature ratios τ is studied in Section B.4. It is shown that having a single poloidal mode is detrimental to the study of this τ parameter. Therefore, we set $\tau = 1$ in the rest of the thesis.

As an introduction, let us first explain what a linear stability analysis is:

1. We start from a steady-state equilibrium of the system which is then disturbed by infinitesimal perturbations of small amplitude $\varepsilon \ll 1$.
2. In this framework, non-linear terms – quadratic in the present case – can be neglected. The system becomes linear.
3. With a scale separation between large equilibrium and small fluctuations scales, we project the fluctuations on the Fourier space. Each mode then becomes an eigenmode of the linear system.
4. Studying the eigenmodes growth characterizes the instabilities: growth rate, real frequency, instability threshold, cross-phase.

By analysing small disturbances to the equilibrium, two interesting cases can occur. First, if the disturbances decay over time, the system comes back to its original equilibrium state and is considered *linearly stable*. Second, if the disturbances grow over time, the system is considered *linearly unstable*. In this latter case, disturbances will grow exponentially in time up to a point where they will become large enough so that nonlinear effects will not be negligible anymore. If a broad spectrum of unstable modes exist and couple nonlinearly to each other, the system may

then transition to turbulence. In that case, the linear analysis gives information on the growth rate before reaching saturation. By scanning the equilibrium parameters, one can identify those cases where the system is unstable, thus defining a *linear threshold*.

To perform a linear analysis of a dynamical system, it is required to write the equations governing the time evolution of the fluctuations. These are given by Eqs. (3.34-3.35) for Tokam1D. In this case, the linearization step is trivial since we have already discarded mode-mode coupling terms in the model. The only nonlinear terms that remain - and that are neglected in the linear analysis - are the ones proportional to D_{NL} and ν_{NL}. The dynamics of the linearized system is described by the eigenmodes of the linear system. In other words, we consider solutions in the form of plane waves (or Fourier modes). Calculations are performed in Fourier space, taking

$$(N_k, \phi_k) = (\hat{N}_k, \hat{\phi}_k) \exp[i(k_x x - \omega t)]. \tag{3.68}$$

Those solutions are then injected in the system of equations that can be solved numerically. The solutions of the dispersion relation are given in the form of complex frequencies ω that depend on wave-numbers and equilibrium quantities. The imaginary part of the frequency determines the growth (or damping) rate, while the real part gives the wave frequency. The cross-phase between density and electric potential fluctuations is determined by calculating the phase of the complex response function of N_k/ϕ_k.

3.4.1 Derivation of the linear analysis

The linear properties of the Tokam1D-ES core system are obtained by solving Eqs. (3.34-3.35) at prescribed steady state equilibrium fields. In the following, the analysis is restricted to the case $\partial_x^3 N_{eq} = 0$. This amounts to considering that the equilibrium profile is sufficiently smooth so that high order derivatives can be neglected. The velocity terms, V_{eq}, V'_{eq} and V''_{eq} are kept in order to study the possible roles of flow shear and Kelvin-Helmholtz instability in the linear regime, with the prime denoting the derivative along x. The electron diamagnetic frequency is introduced $\omega_{\star e} = -k_y N'_{eq}$ for simplicity. The equilibrium velocity only leads to a Doppler shift on the frequency, therefore we solve for $\overline{\omega} = \omega - k_y V_{eq}$. The determinant then reads

$$D(k,\overline{\omega}) = \begin{vmatrix} \overline{\omega} + \mathscr{A} & \mathscr{B} \\ \overline{\omega} k_\perp^2 \tau + \mathscr{C} & \overline{\omega} k_\perp^2 + \mathscr{D} \end{vmatrix} \tag{3.69}$$

With the following notations:

$$\mathscr{A} = -g k_y + i\left(C + k_\perp^2 D_1\right) \tag{3.70}$$

$$\mathscr{B} = -\omega_{\star e} + g k_y - iC \tag{3.71}$$

$$\mathscr{C} = (1+\tau) g k_y + i\left(-C + k_y k_x \tau V'_{eq} + \nu_1 \tau k_\perp^4\right) \tag{3.72}$$

$$\mathscr{D} = -k_y V''_{eq} + i\left(C - k_y k_x \tau N''_{eq} + \nu_1 k_\perp^4\right) \tag{3.73}$$

The non trivial solutions providing the linear growth rate and frequency are given by the dispersion relation $D(k,\overline{\omega}) = 0$. This leads to the corresponding polynomial equation,

$$\overline{\omega}^2 + \overline{\omega}\left(\frac{\mathscr{D}}{k_\perp^2} + \mathscr{A} - \tau\mathscr{B}\right) + \frac{\mathscr{A}\mathscr{D} - \mathscr{C}\mathscr{B}}{k_\perp^2} = 0 \tag{3.74}$$

The linear phase shift between density and electric potential fluctuations corresponds to the phase of the complex response function $F(k,\overline{\omega}) = N_k/\phi_k$:

$$F(k,\overline{\omega}) = \left|\frac{N_k}{\phi_k}\right| e^{i(\varphi_k^N - \varphi_k^\phi)} = \frac{-\mathscr{B}}{\overline{\omega} + \mathscr{A}} = \frac{\omega_{\star e} - gk_y + iC}{\overline{\omega} - gk_y + i\left(C + k_\perp^2 D_1\right)}. \tag{3.75}$$

The turbulent particle flux scales like the sine of the cross phase $\Delta\varphi_k$. Its linear expression is given by

$$\sin(\Delta\varphi_k) = \sin(\varphi_k^N - \varphi_k^\phi) = \frac{\Im(F(k,\overline{\omega}))}{|F(k,\overline{\omega})|} \tag{3.76}$$

With the determinant and linear cross phase equation, one can study the growth rate, frequency and phase as a function of equilibrium parameters. In particular, we are interested in the role of g, C and τ, as those parameters control the instabilities at play.

3.4.2 Validation of the numerical model using linear analysis

The simulation is initialized with a bath of modes. If some of them are unstable, they will grow linearly and the system might reach turbulence. We expect the system to follow linear prediction in the early stage of the simulation. An example of the growth of different modes is shown in Figure 3.6 for a test simulation. In this case, we launched the mode $k_y = 0.3$ and $k_x = 2\pi\, m/L_x$, with $m = 10$ and L_x the radial size of the simulation, in a gradient driven configuration to measure its evolution in time and compare with the analytically predicted growth rate. Note that due to the boundary conditions, $m = 10$ has no reason to be an eigenmode of the system. Therefore, there is a leakage towards the other modes, such that they do not start from noise level. As an example, we also display modes $m = 1$ and $m = 5$. In any case, the launched mode $m = 10$ is 2 orders of magnitude above the others, which is enough to study its evolution during the linear growth part.
The first part, shaded in green, corresponds to the linear growth of the modes. The logarithmic slope of the modes gives their growth rate. At a certain point, the modes become large enough so that nonlinear interactions cannot be neglected anymore. This saturated regime corresponds to the onset of turbulence. In the case of Tokam1D, there is no interaction between the different modes. Therefore, the saturation is obtained when the modes interact with the equilibrium. In the case of a gradient driven simulation, the equilibrium density profile is imposed constant but the equilibrium velocity can be generated through the action of the Reynolds stress. This equilibrium velocity is crucial to have a transfer of energy between modes of different k_x in the absence of a turbulence cascade.

The linear analysis verification consists in launching several simulations at different mode numbers m. The linear growth rate is compared to the simulation growth rate of the density

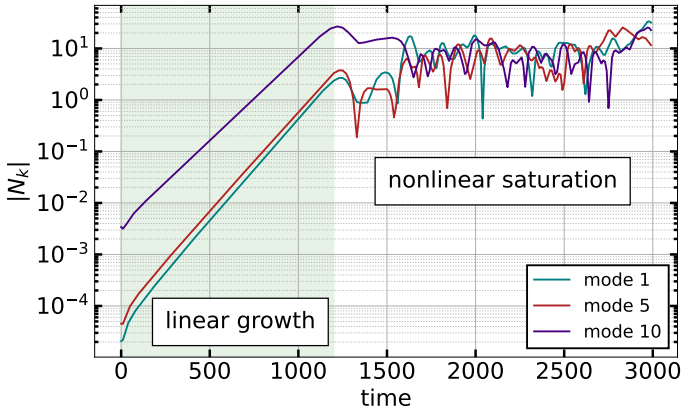

Figure 3.6 – Mode linear growth at the early stage of a test simulation.

fluctuations N_k at the same k_x. The simulation frequency is obtained by performing the time Fourier transform of the density fluctuations. Finally, the sinus of the cross phase $\sin\Delta\varphi = \Im(N_k/\phi_k)/|N_k/\phi_k|$ is computed in the simulation and compared to its linear prediction. The three linear attributes are verified for a test simulation and shown in Figure 3.7. The choice is made to use values that can be quite extreme for the code, in order to check its validity.
For the simulations tested, the agreement between the linear analysis and simulation in the linear regime is very good with relative errors of the order of 0.1 %. One might notice that simulation frequencies at larger k_x are not plotted in Figure 3.7b. In these ranges, ω_{lin} becomes very small. Consequently, one needs a long time window to perform the Fourier analysis. Ultimately, the mode period might exceed the length of the linear part of the simulation and the frequency cannot be estimated. We do not investigate these modes further at this point, considering that the two other plots provide enough comparison.

3.4.3 Core Tokam1D-ES: competition between CDW and interchange instabilities

The model contains two intrinsic instabilities. In this section we first perform the linear analysis of each instability separately. Then, we study the coupled system. Finally, we highlight the role of the compressibility terms. It will appear that the linear behaviour of the system is not a simple linear combination of the two instabilities. Instead, the two instabilities are coupled and their interaction can lead to stabilization or destabilization of the whole system.

Specific cases: interchange or CDW only

Setting $\tau = C = 0$ eliminates the drift instability, leaving only the interchange. Consider $V'_{eq} = V''_{eq} = N''_{eq} = 0$ and no dissipation $D_1 = \nu_1 = 0$ for simplicity. We make explicit the compressibility terms originating from the divergence of the electric velocity and of the diamagnetic flux in the particle balance equation (Equation 3.4). Those terms involve the magnetic curvature through the term: $g\partial_y(\phi - N)$. To distinguish them from the other terms, the interchange parameters originating from the diamagnetic flux and the electric velocity are written $g_\star$ and g_E, respectively. They should both be understood as equal to g as they come from the same

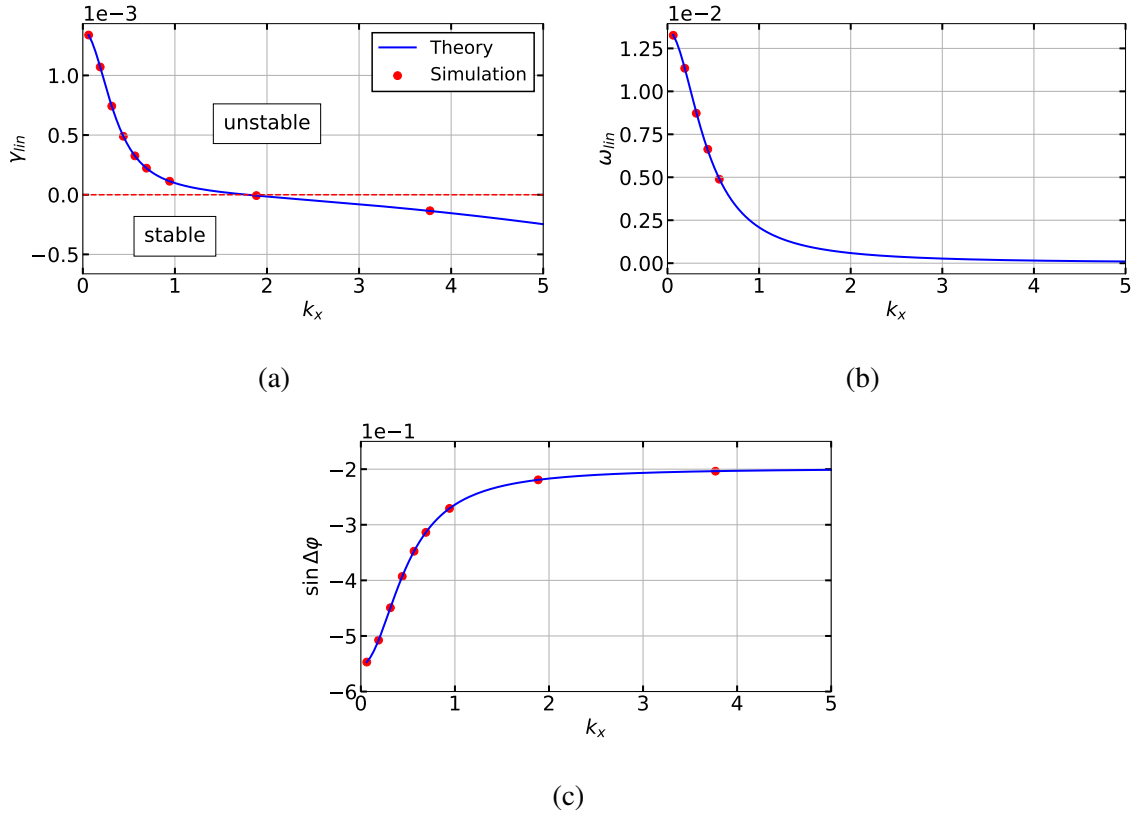

Figure 3.7 – Linear analysis verification of a test simulation. (a) Growth rate γ_{lin}. (b) Frequency ω_{lin}. (c) Sinus of the cross phase $\sin\Delta\varphi$. The gradient driven simulations are performed using a constant density gradient $1/L_N = 50$ and vanishing velocity $V_{eq} = 0$. Other parameters are set to $D_{0,1} = \nu_{0,1} = 10^{-2}$, $L_x = 100$, $C = 3\times10^{-2}$, $g = 10^{-2}$ and $\tau = 10$.

magnetic field inhomogeneity.

With the above assumptions, the dispersion relation, Equation 3.74, reduces to,

$$\overline{\omega}^2 - \overline{\omega} g_\star k_y - \frac{g k_y}{k_\perp^2}\left[g_E k_y - \omega_{\star e}\right] = 0. \tag{3.77}$$

The instability develops above the following critical density gradient that defines the linear threshold:

$$-N_{eq}'^{crit} = g_E\left[1 + \frac{g_\star^2 k_\perp^2}{4 g g_E}\right], \tag{3.78}$$

A few remark can be made at this point. First, the instability disappears if $-N'_{eq}$ changes signs. In Section 2.2, we sketched how the interchange instability was occurring only when the magnetic field and the pressure gradients were of the same sign. This is recovered here in the Tokam1D model. Second, the largest scales (small $k_\perp$) are found to be the most unstable since they have the lowest threshold (lowest critical gradient). Third, the compressibility terms increase the instability linear threshold. The threshold disappears if one removes compressibility by setting $g_E = g_\star = 0$. The stabilization by compressibility will be further discussed in Sec-

tion 3.4.3. Finally, note that when we neglect compressibility, the solution reads,

$$\overline{\omega} = i\left(\frac{gk_y\omega_{\star e}}{k_\perp^2}\right)^{1/2} \tag{3.79}$$

The instability is maximal for low radial wavenumber k_x. It increases with g and the density gradient. Note also that the real frequency is equal to zero: $\Re(\overline{\omega}) = 0$. As mentioned in Section 2.2, the interchange instability phase velocity is neither of the ion nor electron diamagnetic frequency sign.

Then, let us consider the purely drift instability case, with finite C and τ but with $g = 0$, assuming the same simplifications. The dispersion relation then reads as follows:

$$\overline{\omega}^2 + \overline{\omega}\left[iC(1+\tau+k_\perp^{-2}) + \tau\omega_{\star e}\right] - i\frac{\omega_{\star e}C}{k_\perp^2} = 0. \tag{3.80}$$

In the cold ion limit, $\tau = 0$, one is left with the Hasegawa-Wakatani system [167], for which two limits can be distinguished. The case $C \to 0$ corresponds to the hydrodynamic, highly collisional, regime while $C \to +\infty$, corresponds to the adiabatic regime. Keeping only the leading order terms, the solution in the hydrodynamic case reads

$$\overline{\omega}_\pm \approx \pm\frac{1+i}{\sqrt{2}}\left(\frac{C\omega_{\star e}}{k_\perp^2}\right)^{1/2}. \tag{3.81}$$

Thus one recovers the resistive drift instability, mostly unstable at large radial scales ($k_x \approx 0$), with the instability growth rate increasing with both the density gradient and the adiabaticity parameter. It exhibits no threshold in the absence of dissipation coefficients, and the instability develops whatever the sign of the density gradient. In the asymptotic limit $C \longrightarrow +\infty$, the system reduces to the Hasegawa-Mima equation and one is left with stable drift waves,

$$\overline{\omega}_+ = \frac{\omega_{\star e}}{1+k_\perp^2}, \tag{3.82}$$

where $\overline{\omega}_+$ corresponds to the drift waves frequency as given in [49]. The system is stable and oscillates at the drift frequency. CDW instability then appears to be stable at both small and large C.

Also, the two cases of separated instabilities ($C = 0$ and $g = 0$) can be distinguished from their linear cross phase. On the one hand interchange displays a much larger sine of the cross phase, typically close to $\Delta\varphi_k \approx \pi/2$. This is verified taking $C = 0$ and neglecting the compressibility terms in both Eq.3.77 and Eq.3.75. One is left with,

$$F(k,\overline{\omega}) = \frac{\overline{\omega}}{\omega_{\star e}}$$
$$\text{with, } \overline{\omega} = i\left(\frac{gk_y\omega_{\star e}}{k_\perp^2}\right)^{1/2}$$

The phase relation is purely imaginary and the corresponding cross phase reads $\sin\Delta\varphi_k = -1$.

On the other hand, the drift waves instability exhibits a lower cross-phase which decreases as C increases. At $C \longrightarrow +\infty$, the adiabatic regime forces $N_k \sim \phi_k$. It leads to a vanishing phase shift $\sin\Delta\varphi = 0$ implying a vanishing quasi-linear transport. Taking the limit at large C one can replace $\overline{\omega}$ with the drift waves solution in Eq.3.75. This leads to $\Im F(k,\overline{\omega}) = 0$ and thus $\sin\Delta\varphi_k = 0$. At low C using Eq.3.81, the phase relation at leading order reads,

$$F(k,\overline{\omega}) \approx -(1+i)\left(\frac{C}{2k_\perp^2\,\omega_{\star e}}\right)^{1/2} \tag{3.83}$$

which implies $\sin\Delta\varphi_k = -1/\sqrt{2}$.

General case: coupling CDW and interchange instabilities

Both CDW and interchange instabilities are expected to coexist in the edge of tokamak plasmas [50]. Understanding their coupling is therefore essential. Drift waves are linearly stable at both small and large C. We show here that the interchange instability does not take over in the high C regime: it is also stabilized as the adiabaticity parameter is increased. Note that the linear analysis can be solved for the $2d$ system by scanning both k_x and k_y and for the specific Tokam1D case by fixing $k_y = 0.3$.
In the following, the dispersion relation is solved for different cases with fixed equilibrium parameters. Whenever used, the density gradient is fixed to $-N'_{eq} = \rho_s/L_N = 1/100$, L_N being the gradient length. The diffusion parameters are set to $D_1 = \nu_1 = 10^{-2}$. The size of the radial domain is $L_x = 400$ (this constrains $\min(k_x)$).

The growth rate is plotted as a function of k_x and k_y for $C = 10^{-3}$ and $g = 2\times10^{-3}$ in Figure 3.8a. The white contour corresponds to the linear threshold $\gamma(k_x,k_y) = 0$ with these parameters. The white crosses note the position of the maxima for positive and negative poloidal wavenumbers. In Figure 3.8b, the effect of C and g on the growth rate is explored. Here, the wavenumbers are fixed: $(k_x,k_y) = (0.06,0.3)$. Three cases are shown: a CDW only case with $g = 0$, an interchange only with $C = 0$ and a case 'both' with $g = C$.
In Figure 3.8a, the growth rate is maximum for the largest radial scale, $k_x = 2\pi/L_x$, and finite poloidal scale $k_y \sim 0.35$. Note that in practice the solution $k_x = 0$, although given by the linear analysis, would corresponds to a constant fluctuation along x direction which is imposed to zero by the Dirichlet boundary condition on both boundaries. The growth rate displays a symmetric pattern for positive and negative poloidal and radial wavenumbers. Also, it decays like $-k_\perp^2$ due to small scale dissipation governed by the D and ν coefficients. In Figure 3.8b, the growth rate of the $(k_x = 2\pi/400, k_y = 0.3)$ mode is plotted as a function of g and C parameters. The case interchange only leads to a larger growth rate, with γ increasing rapidly with g. It is abruptly stabilized at $g = 10^{-2}$ due to compressibility terms. CDW are found to be stable, as expected, in both small and large C limits. For the chosen equilibrium parameters, the CDW only case ($g = 0$) exhibits a smaller growth rate as compared to interchange. When both instabilities are taken into account, the growth rate stays relatively small. CDW then proves to have a stabilizing effect on the interchange instability when $C = g$ with the growth rate being barely above the pure drift wave case.

A more thorough analysis is provided by studying the full parameter space (C,g) while scanning the values of k_x and k_y. The radial and poloidal wavenumbers of interest here are those that

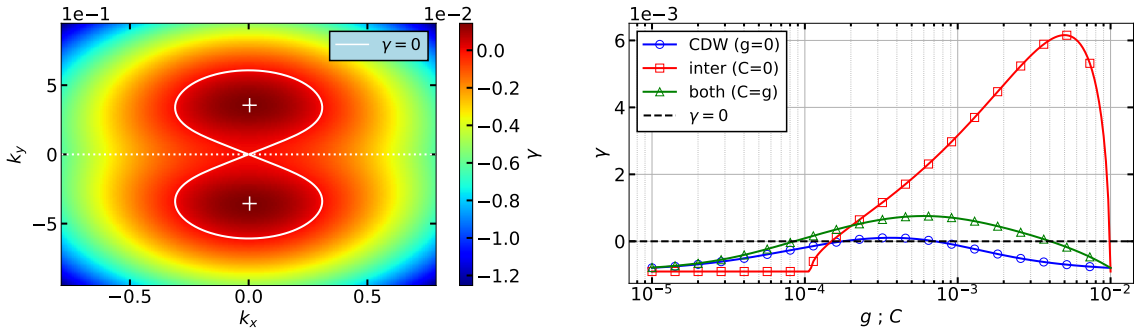

(a) (b)

Figure 3.8 – (a) Growth rate without equilibrium flows as a function of k_x and k_y for $g = 2\times10^{-3}$, $C = 10^{-3}$. White crosses correspond to maxima in positive and negative k_y. White contour denotes the threshold $\gamma(k_x,k_y) = 0$. (b) Growth rate for the case drift waves (CDW) $g = 0$, interchange (inter) $C = 0$ and coupled CDW-inter $C = g$, as a function of C and g for $k_x = 2\pi/400$ and $k_y = 0.3$. Both figures are computed considering: $1/L_N = 1/100$, $D_1 = \nu_1 = 10^{-2}$ and $V_{eq} = V'_{eq} = N''_{eq} = 0$

maximize the growth rate. The result is shown in Figure 3.9 as a function of C and g. The black contour corresponds to the threshold $\gamma(g,C) = 0$. This figure displays the growth rate γ, the frequency ω, the absolute value of the sine of the cross phase $|\sin\Delta\varphi|$ and k_y corresponding to the maximum growth rate. The radial wavenumber that maximizes γ is always equal to $k_x = 2\pi/L_x$.

The growth rate governed by the two coupled instabilities, in Figure 3.9a, is maximal at large g and small C: the interchange instability alone leads to a larger growth rate. The drift C parameter acts as a stabilization to the interchange instability. At large g, the growth rate is always negative whatever the value of C. This is due to the compressibility terms as stated in the previous section.
The frequency, is positive (electron direction) for large values of C until $g = 4\times10^{-3}$. As stated in Section 2.2, the collisional drift wave instability arises due to a phase shift between the density and electric potential fluctuations that is governed by the parallel dynamics of the electrons. As such, we expect the CDW instability phase velocity to be in the electron direction. Conversely, the interchange instability arises due to the charge separation of electrons and ions in the vertical motion. There is no well defined sign of the linear frequency. This is demonstrated analytically for the case without compressibility in Equation 3.79. Here, the parts at small C and large g are understood to be dominated by the interchange, with ω that can be positive or negative. In agreement with the analytical developments, the sign reversal disappears when compressibility terms are neglected.
In Figure 3.9c, the sine of the cross-phase is maximal for interchange dominated cases, at large g for a fixed C, consistently with the analytical developments performed in Section 3.4.3. Indeed, the case interchange only is expected to yield $\sin\Delta\varphi = -1$ when the compressibility terms are neglected. In the case of Figure 3.9c, the compressibility terms do not seem to change this behavior. The cross-phase decreases with C at fixed g. That is also expected from the asymptotic analysis performed earlier. The growth rate is negative at high C whatever the value of g. In

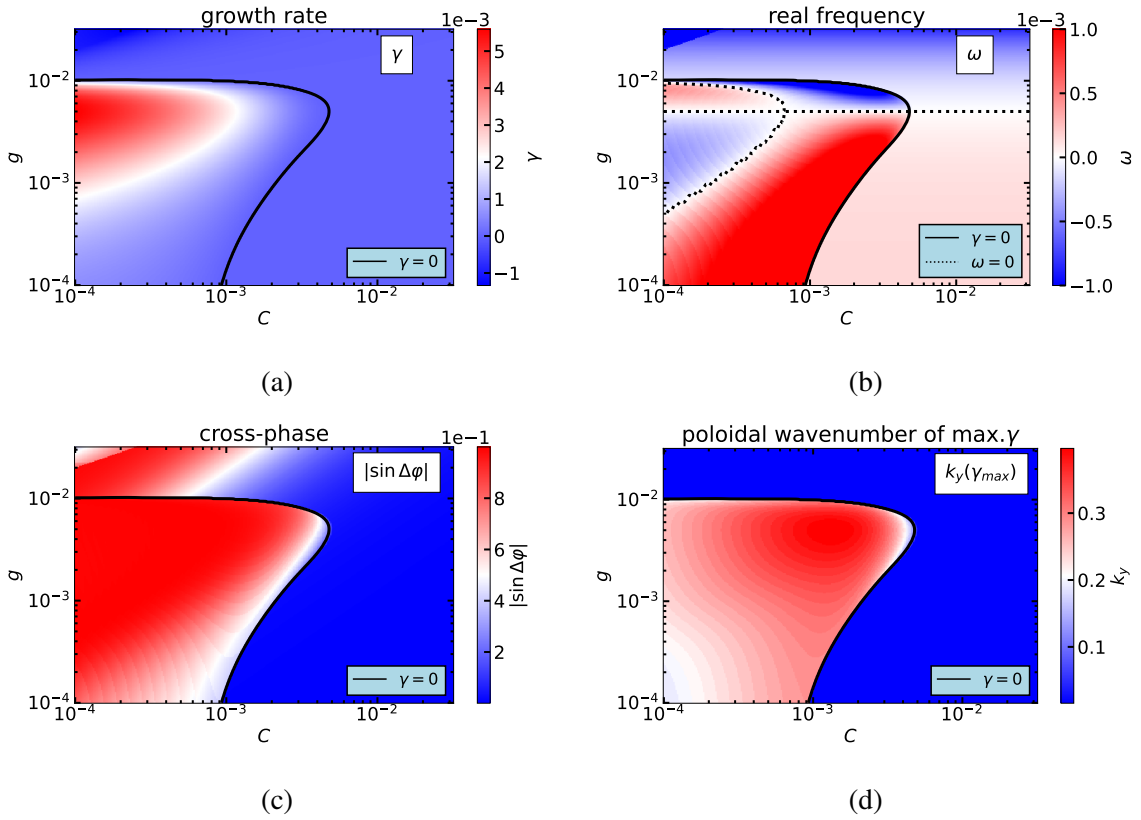

Figure 3.9 – Linear analysis of the system without equilibrium flows as a function of C and g for a fixed density gradient. (a) Growth rate γ. (b) Frequency ω (c) Sine of the cross-phase between density and electric potential fluctuations. (c) Poloidal wavenumber k_y corresponding to the maximum growth rate. The radial and poloidal wavenumbers (k_x, k_y) are chosen such that the growth rate is maximal. Other parameters: $1/L_N = 1/100$, $D_1 = \nu_1 = 10^{-2}$ and $V_{eq} = V'_{eq} = N''_{eq} = 0$

other word, drift waves dominate at large C while interchange takes over at low C. Finally, the most unstable poloidal wavenumber varies from 0.15 to 0.4 in the studied parameter domain. The variation remains marginal considering g and C are changed over two decades each.

Remember that Tokam1D considers a constant and unique poloidal wavenumber k_y ($k_y = 0.3$ in the simulations). In turn, this can lead to spurious effects such as the stabilisation of interchange instability at very large gradients (the instability shifts towards higher values of k_y as the gradient increases). For physics-relevant parameters the stabilization does not occur as the density profile stays close to the instability threshold. Moreover, the density starts from a flat profile and slowly builds up with the source. Therefore, there is little chance that the profile suddenly stiffens to reach stabilisation. Also, we note that taking a single k_y leads to a stabilisation of the interchange instability at very low values of C and g, $C < 10^{-7}$ and $g < 10^{-5}$, which is out of the scanned parameter space. Other than these specific cases, we expect the role of k_y to be marginal on the linear results, and no strong qualitative changes have been observed. A possible upgrade of the reduced Tokam1D would consist in considering a non constant poloidal wave vector k_y, that would depend on the equilibrium gradients. Such a

refinement has not been retained in the present study.

Finally, the critical equilibrium density gradient threshold is analysed as a function of C and g. The result is displayed in Figure 3.10.

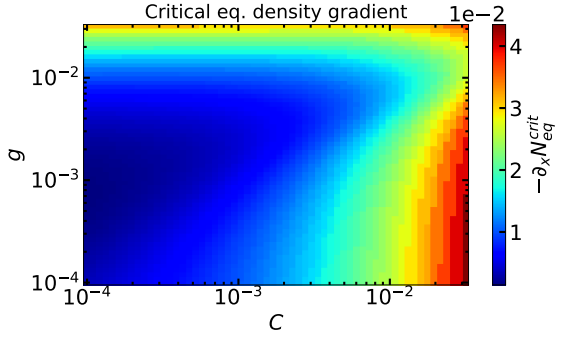

Figure 3.10 – Linear instability threshold as a function of C and g. The radial and poloidal wavenumbers (k_x, k_y) are chosen such that the growth rate is maximal. Other parameters: $1/L_N = 1/100$, $D_1 = \nu_1 = 10^{-2}$ and $V_{eq} = V'_{eq} = N''_{eq} = 0$.

The instability threshold follows the same trend as the growth rate: it increases at large C due to the stabilisation of the instabilities and at large g due to compressibility terms.

Compressibility terms stabilize the interchange instability

Taking the same case as in Figure 3.9 and turning off the compressibility terms (terms proportional to g in Equation 3.12), one obtains the growth rate presented inFigure 3.11a. In that case the interchange instability is not stabilized and the growth rate continues to increase with g. Additionally, one can look for the minimum gradient needed to destabilize the system, in Figure 3.11b. Similarly, due to compressibility terms, the critical gradient $(\rho_s/L_N)^{crit}$ increases at large magnetic curvature. Note that there is a threshold for both cases at low g due to the dissipation terms D_1 and ν_1.
Consistently with the derivation performed earlier, the compressibility terms lead to a threshold for the interchange instability at large g. Adding dissipation, finite temperature τ and non-zero C does not change this conclusion.

Compressibility terms, in particular the one originating from the divergence of the $E \times B$ drift reveal important and, as such, should be kept in reduced models. This is even more important when one wants to explore large magnetic curvature as the stabilization becomes important. However, note that this is for an interchange instability linked to the density gradient. The same work should be done considering a temperature driven instability.

3.4.4 SOL Tokam1D-ES: no CDW instability

In this section, we show that although the SOL model shares similarities with the core model, it exhibits some key differences. First of all, the CDW instability disappears due to the assumptions of the sheath-limited regime. As a result, the C_{sol} parameter only results in the stabilization of the interchange instability. Let us first derive the dispersion relation for the SOL model. Then we will compare the core to the SOL.

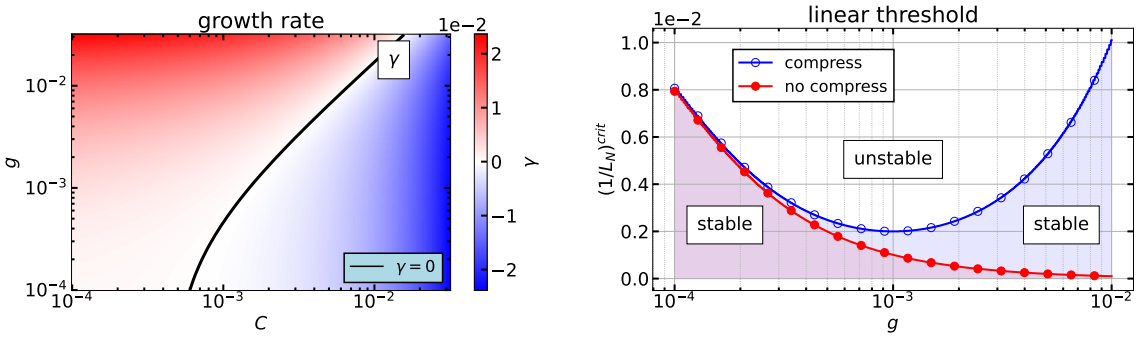

(a) (b)

Figure 3.11 – (a) Growth rate computed using parameters of Figure 3.9 without the compressibility terms. (b) First density gradient $(1/L_N)^{crit}$ to destabilize the system as a function of g for $C = 10^{-4}$. The red and blue shaded regions corresponds the stable parts of the *no compress* and *compress* curves respectively. Other parameters: $D_1 = \nu_1 = 10^{-2}$, $V_{eq} = V'_{eq} = N''_{eq} = 0$.

From, Equation 3.66-3.67, the determinant reads,

$$D(k,\overline{\omega}) = \begin{vmatrix} \overline{\omega} + \mathscr{A} & \mathscr{B} \\ \overline{\omega} k_\perp^2 \tau + \mathscr{C} & \overline{\omega} k_\perp^2 + \mathscr{D} \end{vmatrix} \tag{3.84}$$

With the following notations:

$$\mathscr{A} = -g k_y + i\left(k_\perp^2 D_1\right) \tag{3.85}$$
$$\mathscr{B} = -\omega_{\star e} + g k_y - i C_{sol} \tag{3.86}$$
$$\mathscr{C} = (1+\tau) g k_y + i\left(k_y k_x \tau V'_{eq} + \nu_1 \tau k_\perp^4\right) \tag{3.87}$$
$$\mathscr{D} = -k_y V''_{eq} + i\left(C_{sol} - k_y k_x \tau N''_{eq} + \nu_1 k_\perp^4\right) \tag{3.88}$$

The determinant is similar to Equation 3.70 - 3.73, except that the C parameter is absent from $\mathscr{A}$ and $\mathscr{C}$. The linear growth rate and frequency are solutions of $D(k,\overline{\omega}) = 0$.

The case interchange only ($C = 0$) is left unchanged as compared to the core plasma. However, the CDW instability disappears. Taking the CDW case $g = 0$ and removing dissipation $D_1 = \nu_1 = 0$ together with velocity and higher order effects $V'_{eq} = V''_{eq} = N''_{eq} = 0$, one is left with,

$$\overline{\omega}^2 + \overline{\omega}\left(i C_{sol}(\tau + k_\perp^{-2}) + \tau \omega_{\star e}\right) = 0 \tag{3.89}$$

The solution is either $\overline{\omega} = 0$ or:

$$\overline{\omega} = -\tau \omega_{\star e} - i C_{sol}(\tau + k_\perp^{-2}) \tag{3.90}$$

As a result, under the chosen assumptions, the SOL plasma is driven only by the interchange instability.

The role of C_{sol} on the interchange instability can be studied by taking the same parameters as in Figure 3.9a. The growth rate and frequency for the SOL plasma are shown in Figure 3.12.

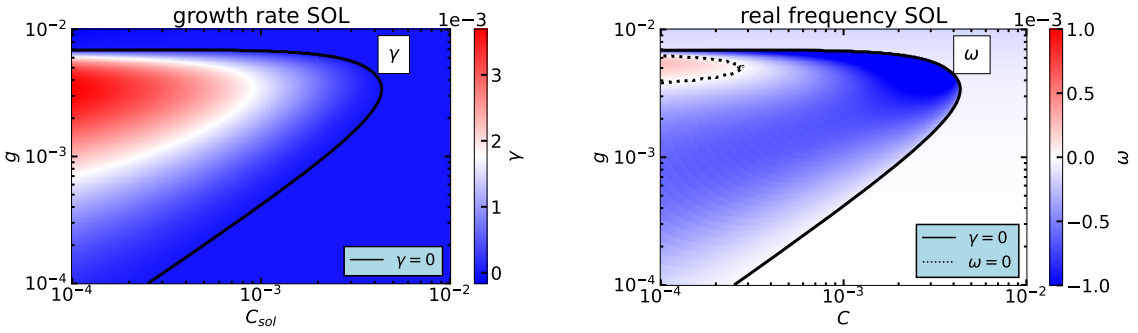

(a) (b)

Figure 3.12 – (a) Growth rate γ. (b) Frequency ω. Both as a function of C and g for a fixed density gradient $1/L_N = 1/100$ in the SOL plasma. (k_x, k_y) are chosen such that the growth rate is maximal. Other parameters: $D_1 = \nu_1 = 10^{-2}$ and $V_{eq} = V'_{eq} = N''_{eq} = 0$

For a SOL plasma, the instability at very low g is lost and C_{sol} is still stabilizing at large g. The instability displays a negative frequency, as expected since CDW is stabilized and only interchange remains.

The stabilisation of the CDW instability in the SOL region is the result of sheath-limited assumption made in Section 3.3. This assumption imposes the coefficients for the parallel current (eqs 3.66 and 3.67). More details can be found in refs.[153, 168]. In these two contributions, a similar model is considered with: $\partial_t n = ...\sigma_{n,n} n + \sigma_{n,\phi}\phi$ and $\partial_\phi = ...\sigma_{\phi,n} n + \sigma_{\phi,\phi}\phi$. It is shown that in the sheath-limited case,$\sigma_{\phi,n} = 0$ and the CDW instability is ruled out. With a conduction-limited assumption, one could assume varying currents in the pre-sheath and solve the Ohm's equation instead of relying on the sheath condition.

3.5 Tokam1D-electromagnetic

It has been shown previously that electromagnetic effects were important to describe regimes with conditions closer to H-mode [62]. Indeed, it can be shown that the key parameter is not the solely $\beta = 2\mu_0 p/B^2$, but:

$$\beta_{eff} = \beta \left(\frac{qR}{L_p}\right)^2 \tag{3.91}$$

With q the safety factor, R the major radius and L_p the pressure gradient length [62]. It results that in high gradient zones, such as the pedestal, L_p reduces and β_{eff} becomes large.

In this section is derived an electromagnetic (EM) version of Tokam1D, dubbed Tokam1D-EM. The principal difference with the core electrostatic model is that the parallel current is not solved using a collisional closure but computed from the parallel momentum conservation equation of the electrons: the generalized Ohm's law. It results in similar equations for the density

and vorticity but an equation is added to solve the parallel vector potential. First, we derive the electromagnetic model Tokam1D-EM. Then, we perform its linear analysis. It is shown that β is stabilizing in CDW dominated plasmas and destabilizing for interchange dominated plasma. At large β, the growth rate dramatically increases leading to an ideal electromagnetic interchange instability akin to ideal ballooning modes.

As a preamble to the derivation of the model itself, we derive some useful expressions for the following. The magnetic field $\mathbf{B}_t$ is the sum of the equilibrium $\mathbf{B}_{eq} = B\mathbf{b}$ and the fluctuations $\widetilde{\mathbf{B}} = -\boldsymbol{\nabla} \times \psi\mathbf{b}$, with ψ the opposite of the parallel vector potential $\psi = -A_\parallel$. In the regime of small fluctuations considered herafter: $B_t \approx B$. Note that with this form $A_\perp = 0$ and the magnetic compression is neglected.
Three effects will be added in the EM version: the electron inertia, the magnetic flutter and the magnetic induction. Magnetic flutter adds a perturbation to the parallel gradient that slows the electron parallel dynamics (see schematic Figure 2.8). In the regime of small fluctuations amplitude, the parallel gradient reads as follows:

$$\begin{aligned}\nabla_\parallel \equiv \frac{\mathbf{B}_t}{B_t}\cdot\boldsymbol{\nabla} &= \frac{\mathbf{B}_{eq}}{B_t}\cdot\boldsymbol{\nabla} - \frac{\boldsymbol{\nabla}\times(\psi\mathbf{b})}{B_t}\cdot\boldsymbol{\nabla} \\ &= \mathbf{b}\cdot\boldsymbol{\nabla} + \frac{1}{B}\{\psi,\cdot\} - \frac{\psi}{B^2}\{B,\cdot\} - \frac{\mu_0}{B^2}\mathbf{j}\cdot\boldsymbol{\nabla} \\ &\approx \mathbf{b}\cdot\boldsymbol{\nabla} + \frac{1}{B}\{\psi,\cdot\} \end{aligned} \tag{3.92}$$

Magnetic induction modifies the parallel electric field. From the induction law, the electric field now derives from both the electric potential and the vector potential,

$$\mathbf{E}_\parallel = -\nabla_\parallel\phi + \partial_t\psi \tag{3.93}$$

Finally, Ampère's law provides the relation between the parallel current $j_\parallel$ and ψ. It reads:

$$\begin{aligned}\boldsymbol{\nabla}\times\widetilde{\mathbf{B}} &= -\boldsymbol{\nabla}\times[\boldsymbol{\nabla}\times(\psi\mathbf{b})] \\ &= -\boldsymbol{\nabla}[\boldsymbol{\nabla}\cdot(\psi\mathbf{b})] + \nabla^2(\psi\mathbf{b}) \\ &= -\boldsymbol{\nabla}[\psi\boldsymbol{\nabla}\cdot\mathbf{b} + \mathbf{b}\cdot\boldsymbol{\nabla}\psi] + \nabla^2(\psi\mathbf{b}) \\ &\approx \nabla_\perp^2\psi\mathbf{b} - \nabla_\perp\nabla_{\parallel 0}\psi \end{aligned} \tag{3.94}$$

Where we have neglected terms originating from $\mathbf{B}$ inhomogeneity. Further neglecting the second term on the right hand side leads to,

$$\mu_0 j_\parallel \mathbf{b} = \nabla_\perp^2\psi\mathbf{b} \tag{3.95}$$

And the gradient of the parallel current reads,

$$\nabla_\parallel j_\parallel = \left(\nabla_{\parallel 0} + \frac{1}{B}\{\psi,\cdot\}\right)\frac{\nabla_\perp^2\psi}{\mu_0} \tag{3.96}$$

3.5.1 Model equations

One considers a magnetized plasma of constant ion T_i and electron T_e temperatures. The density and vorticity equations are similar to the electrostatic version Equation 3.5 and 3.7 with the parallel current derived from Ampere's law. Their dimensional forms are recalled:

$$\partial_t n + \frac{1}{B}\{\phi, n\} - \frac{2nT_e}{eRB}\partial_y\left(\frac{e\phi}{T_e} - \ln\frac{n}{n_0}\right) - \frac{1}{e}\left(\nabla_{\|0} + \frac{1}{B}\{\psi,\cdot\}\right)\frac{\nabla_\perp^2\psi}{\mu_0} = S_N$$

$$\frac{nm_iT_e}{eB^2}\partial_t\Omega = \frac{-nm_i}{B^3}\frac{T_e^2}{e^2}\nabla_{\perp,i}\left\{\frac{e\Phi}{T_e}, \nabla_{\perp,i}\left(\frac{e\Phi}{T_e} + \tau\ln\frac{n}{n_0}\right)\right\} - \frac{2T_e}{RB}(1+\tau)\partial_y n + \left(\nabla_{\|0} + \frac{1}{B}\{\psi,\cdot\}\right)\frac{\nabla_\perp^2\psi}{\mu_0}$$

The generalized Ohm's law derives from the parallel electron momentum equation without source:

$$nm_e\left[\partial_t + (\mathbf{v}_E + \mathbf{v}_e^\star)\cdot\boldsymbol{\nabla}\right]v_{\|e} + T_e\nabla_\| n = -en(\nabla_\|\phi + \partial_t\psi) + \frac{m_e\nu_{ei}}{e}j_\| \tag{3.97}$$

Similarly to the electrostatic version, we neglect the parallel advection assuming that the parallel gradient length remains small as compared to transverse ones. Replacing $v_{\|e}$ by the parallel current $v_{\|e} = -j_{\|e}/en \approx -j_\|/en$ and using the expression of the parallel gradient (Equation 3.92) leads to:

$$nm_e\left(\partial_t + \frac{T_e}{eB}\left\{\frac{e\phi}{T_e} - \ln n, \cdot\right\}\right)\frac{j_\|}{en} = -nT_e\nabla_\|\left(\frac{e\phi}{T_e} - \ln n\right) + en\partial_t\psi - \frac{m_e\nu_{ei}}{e}j_\| \tag{3.98}$$

Finally, using Ampère's law (Equation 3.96) and the parallel gradient definition, one is left with the following relation:

$$\frac{e}{T_e}\partial_t\left(\psi - \frac{m_e}{e^2n\mu_0}\nabla_\perp^2\psi\right) + \frac{1}{B}\left\{\frac{e\phi}{T_e} - \ln n, \psi - \frac{m_e}{e^2n\mu_0}\nabla_\perp^2\psi\right\} = \nabla_{\|0}\left(\frac{e\phi}{T_e} - \ln n\right) + \frac{m_e\nu_{ei}}{neT_e\mu_0}\nabla_\perp^2\psi \tag{3.99}$$

The system of equations is normalized using Table 3.2 and $\hat{\psi} = ec_s/(\beta_0 T_e)\psi$. The following constants are introduced:

$$\beta_0 = \frac{\mu_0 n_0 T_e}{B^2} \;\;;\;\; \mu = \frac{m_e}{m_i} \;\;;\;\; \eta_0 = \frac{\nu_{ei,0}}{\omega_{ce}}$$

These constants correspond to the plasma to magnetic pressure ratio β, the mass ratio and the normalized electron-ion collision frequency taken at the reference density n_0. The density is made explicit in the electron-ion collision frequency, similarly to the parallel conductivity in the electrostatic version,(Section 3.2.3): $\eta_0 = \eta n_0/n$. Dropping the hats and considering each

quantity as normalized, the dimensionless $3d$ system of equations reads,

$$\partial_t n + \{\phi, n\} = gn\partial_y(\phi - \ln n) + \left(\nabla_{\|0} + \beta_0\{\psi, \cdot\}\right)\nabla_\perp^2\psi + S_n \tag{3.100}$$

$$\partial_t \Omega + \nabla_{\perp i}\{\phi, \nabla_{\perp i}(\phi + \tau\ln n)\} = -(1+\tau)g\partial_y \ln n + \frac{1}{n}\left(\nabla_{\|0} + \beta_0\{\psi, \cdot\}\right)\nabla_\perp^2\psi \tag{3.101}$$

$$(\partial_t + \{\phi - \ln n, \cdot\})\left(\beta_0\psi - \frac{\mu}{n}\nabla_\perp^2\psi\right) = \nabla_{\|0}(\phi - \ln n) + \eta_0\nabla_\perp^2\psi \tag{3.102}$$

This set of equations solves the density n, the generalized vorticity $\Omega = \nabla_\perp^2(\phi + \tau\ln n/n_0)$ and the inverse of the vector potential ψ. The model is equivalent to the one derived by B.D. Scott when taking the isothermal limit [62] albeit with different normalizations. The electrostatic limit is recovered by neglecting electron inertia (proportional to μ) and β_0 terms. The case $\mu = \beta_0 = 0$ leads to the Tokam1D-ES core model (eqs. 3.12 − 3.13).

3.5.2 Reduction to $1d$

The system of equations is further reduced using the method described in Section 3.2.5. This time, the density is separated between equilibrium and fluctuations, not its logarithm. Additionally, the parallel vector potential is split as follows,

$$\begin{pmatrix} n \\ \phi \\ \psi \end{pmatrix} = \begin{pmatrix} n_{eq} \\ \phi_{eq} \\ \psi_{eq} \end{pmatrix}(x,t) + \begin{pmatrix} n_k \\ \phi_k \\ \psi_k \end{pmatrix}(x,t)\exp[i(k_y y + k_\| z)] + \text{ cc} \tag{3.103}$$

The derivation is the same as for the core Tokam1D-ES model. Details are only provided where deemed necessary. Radial derivatives of the equilibrium quantities are written as: $\partial_x n_{eq} = n'_{eq}$. In order to develop the $1/n$ and density logarithms originating from the Boussinesq assumption, $\widetilde{n}/n_{eq}$ is assumed small in the remainder of this section. Consistently, the following considerations hold:

$$\frac{1}{n} \approx \frac{1}{n_{eq}} \tag{3.104}$$

$$\partial_y \ln n \approx \frac{\partial_y \widetilde{n}}{n_{eq}} \tag{3.105}$$

Note that we do not perform the Taylor expansion in the small parameter $\widetilde{n}/n_{eq}$. It would otherwise breaks the conservative form of the equilibrium charge conservation. The assumption is acceptable in the core but can be challenged when approaching the separatrix. A possible solution to this would be to alleviate the Boussinesq assumption, it is further discussed in the following sections.

Density

The equilibrium density equation reads,

$$\partial_t n_{eq} + \langle\{\widetilde{\phi}, \widetilde{n}\}\rangle = g\langle\widetilde{n}\partial_y\widetilde{\phi}\rangle + \beta_0\langle\{\psi, \nabla_\perp^2\psi\}\rangle = S_n$$

Which reduces to,

$$\partial_t n_{eq} = -(\partial_x + g)\Gamma_{ES} - \beta_0 \partial_x^2 \Pi_{EM} + S_n \tag{3.106}$$

Where $\Gamma_{ES} = -2k_y \Im(n_k \phi_k^*)$ is the electrostatic turbulent flux derived before (Equation 3.18), and $\Pi_{EM} = \langle \partial_x \widetilde{\psi} \partial_y \widetilde{\psi} \rangle = 2k_y \Im(\psi_k^* \partial_x \psi_k)$ is an electromagnetic tensor. The fluctuation density equation is obtained by subtracting the equilibrium from the density equation. By linearizing the equation on $\widetilde{n}$ and projecting onto the single mode $(k_y, k_\parallel)$, one gets the equation in the framework of Tokam1D:

$$\partial_t n_k = -ik_y(V_{eq} + g)n_k + ik_y(n'_{eq} + g n_{eq})\phi_k + ik_\parallel \nabla_\perp^2 \psi_k + ik_y \beta_0 (\psi'_{eq} \nabla_\perp^2 \psi_k - \psi'''_{eq} \psi_k) \tag{3.107}$$

Vorticity

The equilibrium vorticity equation involves $\Omega_{eq} \approx \partial_x^2(\phi_{eq} + \tau \ln n_{eq}) = \partial_x(V_{eq} + \tau n'_{eq}/n_{eq})$, the equilibrium generalized vorticity. It reads,

$$\partial_t \Omega_{eq} + \partial_x \langle \{\phi, \partial_x(\phi + \tau \ln n)\} \rangle = \left\langle \frac{1}{n} \nabla_{\parallel 0} \nabla_\perp^2 \psi \right\rangle + \beta_0 \left\langle \frac{1}{n} \{\psi, \nabla_\perp^2 \psi\} \right\rangle$$

The second term on the left hand side is developed using Equation B.6 and Equation B.5. It reads,

$$\partial_x \langle \{\phi, \partial_x(\phi + \tau \ln n)\} \rangle = -2k_y \partial_x^2 \left[\Im \left(\phi_k^* \left(\partial_x \phi_k + \tau \frac{\partial_x n_k}{n_{eq}} \right) \right) \right] \tag{3.108}$$

The first term on the right hand side vanishes due to the assumption, $1/n \approx 1/n_{eq}$. Finally, the second term on the right hand side reads,

$$\left\langle \frac{1}{n} \{\psi, \nabla_\perp^2 \psi\} \right\rangle \approx \frac{\langle \{\psi, \nabla_\perp^2 \psi\} \rangle}{n_{eq}} = -\frac{1}{n_{eq}} \partial_x^2 \Pi_{EM}$$

and the equilibrium vorticity can be written as,

$$\partial_t \Omega_{eq} = 2k_y \partial_x^2 \left[\Im \left(\phi_k^* \left(\partial_x \phi_k + \tau \frac{\partial_x n_k}{n_{eq}} \right) \right) \right] - \frac{\beta_0}{n_{eq}} \partial_x^2 \Pi_{EM}$$

If the density was developed using a Taylor expansion in the form: $1/n \approx (1/n_{eq})(1 + \widetilde{n}/n_{eq})$, the second term on the right hand side would have resulted in $1/n_{eq}^2$ terms outside of the derivatives. In turn, conservation would have broken down. Even though, the equation on Ω_{eq} is still not satisfactory. Indeed, the term $(\beta_0/n_{eq})\partial_x^2 \Pi_{EM}$ also breaks conservation. Two options are possible: replace n_{eq} by a reference n_0 or consider $\beta_0 \partial_x(\partial_x \Pi_{EM}/n_{eq})$. The second option is preferred for the following. The conservative form of the equilibrium vorticity equation then reads,

$$\partial_t \Omega_{eq} = -\partial_x^2 \Pi_{ES} - \beta_0 \partial_x \left(\frac{\partial_x \Pi_{EM}}{n_{eq}} \right) \tag{3.109}$$

Where Π_{ES} is the electrostatic Reynolds stress defined as:

$$\Pi_{ES} = -2k_y \Im \left[\phi_k^* \left(\partial_x \phi_k + \tau \frac{n_k}{n_{eq}} \right) \right] \tag{3.110}$$

Remembering that $\Omega_{eq} = \partial_x (V_{eq} + \tau \partial_x \ln n_{eq})$, we get the equation on the equilibrium velocity by first integrating once in x,

$$\partial_t (V_{eq} + \tau \partial_x \ln n_{eq}) = -\partial_x \Pi_{ES} - \frac{\beta_0}{n_{eq}} \partial_x \Pi_{EM} \tag{3.111}$$

One then has to remove the density contribution to the generalized vorticity (Equation 3.106). It reads,

$$\begin{aligned} \partial_t \frac{n'_{eq}}{n_{eq}} = \frac{\partial_{xt}^2 n_{eq}}{n_{eq}} - \frac{n'_{eq} \partial_t n_{eq}}{n_{eq}^2} = \frac{\partial_x S_n}{n_{eq}} - \frac{1}{n_{eq}} \left(\partial_x^2 \Gamma_{ES} + g \partial_x \Gamma_{ES} + \beta_0 \partial_x^3 \Pi_{EM} \right) \\ + \frac{n'_{eq}}{n_{eq}^2} \left(\partial_x \Gamma_{ES} + g \Gamma_{ES} + \beta_0 \partial_x^2 \Pi_{EM} - S_n \right) \end{aligned}$$

So that one finally obtains an equation on the equilibrium velocity:

$$\begin{aligned} \partial_t V_{eq} = &- \partial_x \Pi_{ES} - \frac{\beta_0}{n_{eq}} \left[\partial_x \Pi_{EM} + \frac{n'_{eq}}{n_{eq}} \tau \partial_x^2 \Pi_{EM} - \tau \partial_x^3 \Pi_{EM} \right] \\ &+ \frac{\tau}{n_{eq}} \left[(\partial_x + g) \left(\partial_x \Gamma_{ES} - \frac{n'_{eq}}{n_{eq}} \Gamma_{ES} \right) \right] \end{aligned} \tag{3.112}$$

We neglect the terms linked to the particle source, considering that the source is only fueling in particles and not in momentum. The vorticity fluctuation equation is written on $\widetilde{\Omega} = \nabla_\perp^2 (\widetilde{\phi} + \tau \widetilde{\ln n})$. Its equation reads,

$$\begin{aligned} \partial_t \widetilde{\Omega} = &- \nabla_{\perp i} \{ \phi_{eq}, \nabla_{\perp i} (\widetilde{\phi} + \tau \widetilde{\ln n}) \} - \partial_x \{ \widetilde{\phi}, V_{eq} + \tau \partial_x \ln n_{eq} \} \\ &- (1+\tau) g \frac{\partial_y \widetilde{n}}{n_{eq}} + \frac{1}{n_{eq}} \nabla_{\parallel 0} \nabla_\perp^2 \widetilde{\psi} + \frac{\beta_0}{n_{eq}} \left[\{ \psi_{eq}, \nabla_\perp^2 \widetilde{\psi} \} + \{ \widetilde{\psi}, \psi''_{eq} \} \right] \end{aligned}$$

The fluctuations on the mode k then reads,

$$\begin{aligned} \partial_t \Omega_k = &- ik_y \left[V_{eq} \nabla_\perp^2 \left(\phi_k + \tau \frac{n_k}{n_{eq}} \right) + V'_{eq} \partial_x \left(\phi_k + \tau \frac{n_k}{n_{eq}} \right) \right] \\ &+ ik_y \left[\partial_x \phi_k \left(V'_{eq} + \tau \partial_x \left(\frac{n'_{eq}}{n_{eq}} \right) \right) + \phi_k \left(V''_{eq} + \tau \partial_x^2 \left(\frac{n'_{eq}}{n_{eq}} \right) \right) \right] \\ &- i(1+\tau) g k_y \frac{n_k}{n_{eq}} + i \frac{k_\parallel}{n_{eq}} \nabla_\perp^2 \psi_k + i \frac{k_y}{n_{eq}} \beta_0 \left(\psi'_{eq} \nabla_\perp^2 \psi_k - \psi'''_{eq} \psi_k \right) \end{aligned} \tag{3.113}$$

Ohm's law

Following the same assumptions as for the density and vorticity, the equation on the equilibrium vector potential is obtained by taking the flux-surface average of Equation 3.102 and by using Equation B.5. It reads,

$$\begin{aligned}\partial_t\left[\beta_0\psi_{eq}-\frac{\mu}{n_{eq}}\partial_x^2\psi_{eq}\right] &= -\langle\{\widetilde{\phi}-\widetilde{\ln n},\beta_0\widetilde{\psi}-\frac{\mu}{n_{eq}}\nabla_\perp^2\widetilde{\psi}\}\rangle+\eta_0\psi_{eq}'' \\ &= -2k_y\partial_x\Im\left[\left(\phi_k-\frac{n_k}{n_{eq}}\right)\left(\beta_0\psi_k^*-\frac{\mu}{n_{eq}}\nabla_\perp^2\psi_k^*\right)\right]+\eta_0\psi_{eq}'' \qquad (3.114)\end{aligned}$$

The linearized equation on $\widetilde{\psi}$ reads,

$$\begin{aligned}\partial_t\left[\beta_0\widetilde{\psi}-\frac{\mu}{n_{eq}}\nabla_\perp^2\widetilde{\psi}\right] =& -\left\{\phi_{eq}-\ln n_{eq},\beta_0\widetilde{\psi}-\frac{\mu}{n_{eq}}\nabla_\perp^2\widetilde{\psi}\right\}-\left\{\widetilde{\phi}-\widetilde{\ln n},\beta_0\psi_{eq}-\frac{\mu}{n_{eq}}\nabla_\perp^2\psi_{eq}\right\} \\ &+\nabla_{\|0}(\widetilde{\phi}-\widetilde{\ln n})+\eta_0\nabla_\perp^2\widetilde{\psi}\end{aligned}$$

Projecting the equation onto k_y and $k_\|$ leads to,

$$\begin{aligned}\partial_t\left[\beta_0\psi_k-\frac{\mu}{n_{eq}}\nabla_\perp^2\psi_k\right] =& -ik_y\left(V_{eq}-\frac{n_{eq}'}{n_{eq}}\right)\left(\beta_0\psi_k-\frac{\mu}{n_{eq}}\nabla_\perp^2\psi_k\right) \\ &+ik_y\left(\phi_k-\frac{n_k}{n_{eq}}\right)\left(\beta_0\psi_{eq}'-\mu\partial_x\left(\frac{\psi_{eq}''}{n_{eq}}\right)\right) \\ &+ik_\|\left(\phi_k-\frac{n_k}{n_{eq}}\right)+\eta_0\nabla_\perp^2\psi_k \qquad (3.115)\end{aligned}$$

Semi-spectral formulation of Tokam1D-EM

The semi-spectral system of equations involves 6 fields: 3 real fields for the equilibrium components, and 3 complex fields for the fluctuating parts. A diffusive term is added to each equation to prevent small scale instabilities. The equations for the equilibrium density n_{eq}, velocity $V_{eq}\equiv\partial_x\phi_{eq}$ and vector potential ψ_{eq} read:

$$\partial_t n_{eq} = -(\partial_x+g)\Gamma_{ES}-\beta_0\partial_x^2\Pi_{EM}+S_n+D_0n_{eq}'' \qquad (3.116)$$

$$\begin{aligned}\partial_t V_{eq} =& -\partial_x\Pi_{ES}-\frac{\beta_0}{n_{eq}}\left(\partial_x\Pi_{EM}+\frac{n_{eq}'}{n_{eq}}\tau\partial_x^2\Pi_{EM}-\tau\partial_x^3\Pi_{EM}\right) \qquad (3.117)\\ &+\frac{\tau}{n_{eq}}\left[(\partial_x+g)(\partial_x\Gamma_{ES}-\frac{n_{eq}'}{n_{eq}}\Gamma_{ES})\right]+\nu_0V_{eq}''\end{aligned}$$

$$\partial_t\left[\beta_0\psi_{eq}-\frac{\mu}{n_{eq}}\partial_x^2\psi_{eq}\right] = -2k_y\partial_x\Im\left[\left(\phi_k-\frac{n_k}{n_{eq}}\right)\left(\beta_0\psi_k^*-\frac{\mu}{n_{eq}}\nabla_\perp^2\psi_k^*\right)\right]+\eta_0\psi_{eq}'' \qquad (3.118)$$

The equations for the fluctuations of density n_k, vorticity $\Omega_k = \nabla_\perp^2(\phi_k + \tau n_k/n_{eq})$ and vector potential ψ_k are defined for the mode k as follows:

$$\begin{aligned}
\partial_t n_k = & -ik_y(V_{eq}+g)n_k + ik_y(n'_{eq}+gn_{eq})\phi_k + ik_\parallel \nabla_\perp^2 \psi_k \\
& + ik_y\beta_0(\psi'_{eq}\nabla_\perp^2\psi_k - \psi'''_{eq}\psi_k) + D_1\nabla_\perp^2 n_k
\end{aligned} \tag{3.119}$$

$$\begin{aligned}
\partial_t \Omega_k = & -ik_y\left[V_{eq}\nabla_\perp^2\left(\phi_k + \tau\frac{n_k}{n_{eq}}\right) + V'_{eq}\partial_x\left(\phi_k + \tau\frac{n_k}{n_{eq}}\right)\right] \\
& + ik_y\left[\partial_x\phi_k\left(V'_{eq} + \tau\partial_x\left(\frac{n'_{eq}}{n_{eq}}\right)\right) + \phi_k\left(V''_{eq} + \tau\partial_x^2\left(\frac{n'_{eq}}{n_{eq}}\right)\right)\right] \\
& - i(1+\tau)gk_y\frac{n_k}{n_{eq}} + i\frac{k_\parallel}{n_{eq}}\nabla_\perp^2\psi_k + i\frac{k_y}{n_{eq}}\beta_0\left(\psi'_{eq}\nabla_\perp^2\psi_k - \psi'''_{eq}\psi_k\right) + \nu_1\nabla_\perp^2\Omega_k
\end{aligned} \tag{3.120}$$

$$\begin{aligned}
\partial_t\left[\beta_0\psi_k - \frac{\mu}{n_{eq}}\nabla_\perp^2\psi_k\right] = & -ik_y\left(V_{eq} - \frac{n'_{eq}}{n_{eq}}\right)\left(\beta_0\psi_k - \frac{\mu}{n_{eq}}\nabla_\perp^2\psi_k\right) \\
& + ik_y\left(\phi_k - \frac{n_k}{n_{eq}}\right)\left(\beta_0\psi'_{eq} - \mu\partial_x\left(\frac{\psi''_{eq}}{n_{eq}}\right)\right) \\
& + ik_\parallel\left(\phi_k - \frac{n_k}{n_{eq}}\right) + \eta_0\nabla_\perp^2\psi_k
\end{aligned} \tag{3.121}$$

Where we have defined the electrostatic flux of particles Γ_{ES} in Equation 3.18, the electromagnetic tensor $\Pi_{EM} = \langle\partial_x\widetilde{\psi}\partial_y\widetilde{\psi}\rangle = 2k_y\Im(\psi_k^*\partial_x\psi_k)$ and the electrostatic Reynolds stress Π_{ES} in Equation 3.110.

This set of equations has been derived under the strong Boussinesq assumption, where the full density n is commuted with the divergence (details on this assumption can be found in Section 3.2.2). In turn, the assumptions leads to $1/n$ terms that limit the Taylor expansion in the small parameter $\widetilde{n}/n_{eq}$ so as to not break the conservative form of the system. Some more work is needed to explore either the implications of the weak Boussinesq assumption, or the relaxation of the assumption.

3.5.3 Linear analysis

As a first step towards the analysis of Tokam1D-EM, we perform the linear analysis under the following simplifying assumptions:

1. No compressibility terms.
2. No flows and high order derivatives: $V_{eq} = V_{eq}^{(n)} = \psi_{eq}^{(n)} = 0$.
3. Cold ion approximation: $\tau = 0$.
4. No electron inertia: $\mu = 0$.
5. Simplified density profile: $n_{eq} = 1$, $n'_{eq} = cte$.
6. Collisionality is set to $\eta_0 = 0.1$.

Under those assumptions, the determinant of the system reads,

$$D(k,\omega) = \begin{vmatrix} \omega + iDk_\perp^2 & -\omega_{\star e} & -k_\parallel k_\perp^2 \\ k_y g & \omega k_\perp^2 + i\nu k_\perp^4 & k_\parallel k_\perp^2 \\ -k_\parallel & k_\parallel & \omega\beta_0 - \omega_{\star e}\beta_0 + i\eta_0 k_\perp^2 \end{vmatrix} \tag{3.122}$$

The non trivial solutions are given by solving $D(k,\omega) = 0$ numerically. The growth rate is first obtained as a function of (k_x, k_y) for a constant density gradient $n_{eq} = -0.5$. The turbulence parameters are set to $k_{\|} = 1$, $\beta_0 = 50$ and $g = 0.1$. The resulting growth rate is shown in Figure 3.13

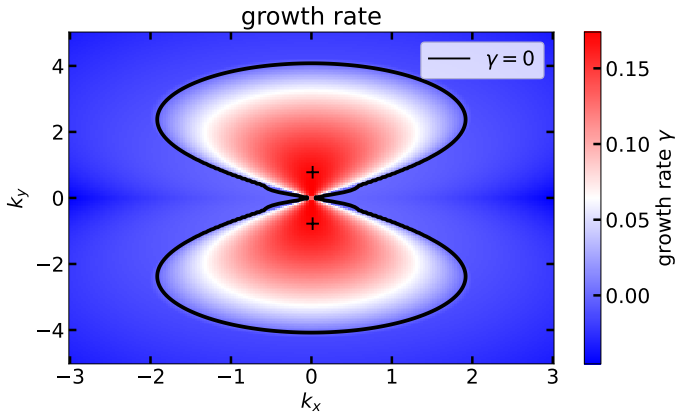

Figure 3.13 – Growth rate as a function of k_x and k_y. Maxima are located for the lowest value of k_x accessible and $k_y \approx \pm 0.8$. Dissipation and viscosity $D = \nu = 10^{-2}$.

Large growth rate, $\gamma > 10^{-1}$, in comparison to the electrostatic cases ($\gamma \approx 10^{-3}$ in Figure 3.9) are obtained when β_0 is large. The maximum of the instability is located at the smallest k_x available for the system and $k_y = \pm 0.8$.

The parameter β_0 is shown to have a different role depending on the dominant instability. In Figure 3.14 is shown the growth rate as a function of β_0 for three different configurations: large $g = 0.1$, small $g = 0.01$, and small g with a reversed gradient.

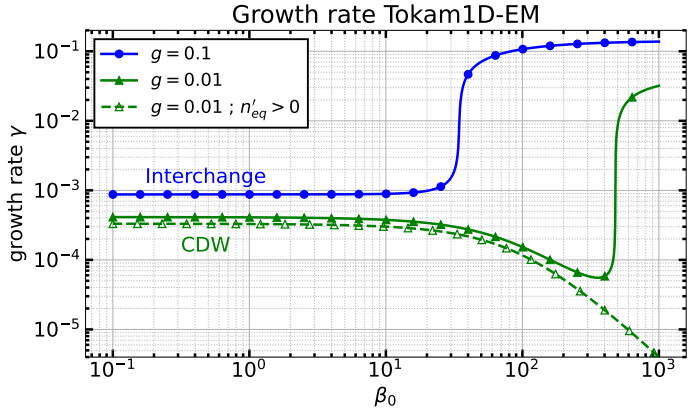

Figure 3.14 – Growth rate as a function of β for large $g = 0.1$ (blue circles), small $g = 0.01$ (green triangles). The dotted line curve indicate a case with a reversed gradient $n'_{eq} > 0$. Other parameters: $(k_x, k_y, k_{\|}) = (0.02, 0.8, 1)$, $n'_{eq} = \pm 0.2$, $D = \nu = 0$.

When the density gradient is negative (i.e. of the same sign as the magnetic amplitude gradient), the growth rate greatly increases at large β_0. This instability is similar to the ideal ballooning

instability described in ref.[60]. The instability is shown absent when the density gradient is reversed which further emphasizes that the instability is of interchange-type.
When β_0 is small, it is shown to stabilize collisional drift wave (CDW) instability and to destabilize interchange.

All in all, an electromagnetic model has been developed in the framework of Tokam1D. The preliminary linear analysis unveiled a mode at large β_0 akin to the ideal ballooning instability. The role of β on RBM and CDW is coherent with results reported in [60]. More work have to be performed to identify the role of the other parameters: electron inertia μ, collisions η_0 should be investigated first. Then, nonlinear electromagnetic simulations have to be performed. A possible next step would then consist in alleviating the Boussinesq assumption. This assumption can break the conservative form of the current continuity equation. As such, it imposes $\widetilde{n}/n_{eq} \ll 1$ and greatly limit the option for a Taylor expansion.

3.6 Strengths & limitations of the model: ways forward

In this section, we revisit the strengths of the Tokam1D, as well as some of the underlying assumptions on which it is based. We remind the model objectives:

- Study the generation and structure of ZFs in competing turbulence.
- Investigate interplay between ZFs and avalanches.
- Assess the influence of ZFs radial structure on the turbulent transport.
- Identify experimental signatures of ZFs and avalanches.

First, to allow the turbulence to self-organize and interact with the equilibrium profiles, we made the system flux-driven. This means that the density profile is a balance between the source of particles and the turbulent flux of particles. No scale separation assumption is involved. As such, the density profile can develop small scale corrugations and form staircase-like pattern.
Second, to perform large parameter scans and get an idea of the instability landscape, the model has to run fast. Given its flux-driven formulation, the simulations are run until the equilibrium profiles reach a statistical steady-state. In order to reach that goal, we made the system $1d$ by selecting a single poloidal and parallel mode for the fluctuating components.
Third, three extensions to the model have already been detailed: adding the force balance flow, the SOL region and electromagnetic effects.

In the following, we discuss briefly three possible ways forward. The first is trivial. Adding more equations, such as the ion and electron temperature equations could lead to a more complex turbulence. The second discusses the possibility to include the geodesic acoustic modes without having to develop a $2d$ model. Finally, the lack of magnetic shear and mode localization is addressed.

3.6.1 Type of turbulence included & isothermal assumption

Tokam1D-ES, contains two equations: density and vorticity. Only instabilities linked to those dynamical variables are included. The first is the CDW instability, linked to the finite parallel phase shift between density and electric potential fluctuations. The second is interchange. It is linked to the magnetic inhomogeneity through an effective gravity parameter g.

As already discussed, the interchange instability represents a 'broad' class of instabilities. It encompasses many different modes at different scales, such as ITG, RBM, ideal ballooning modes etc. An obvious and immediate extension to the model is to alleviate the isothermal assumption. Doing this would enable ion and / or electron temperature dynamics, possibly leading to ITG and ETG turbulence. Also, it would uncouple the density and temperature dynamics, leading to different turbulent fluxes for heat and particles. A work has been started going into this direction by developing a 5-fields model. The model consists in Tokam1D-ES (core version) with added equations for ion and electron temperatures and ion parallel velocity. It could be extended to include electromagnetic effects such as described in Section 3.5.

However, we emphasize that interchange such as included in the present model still contains enough interesting properties. First, it is stabilized by the positive magnetic curvature. Second, it does not require a finite $k_{\|}$ to exist (*flute* modes). Additionally, we showed in Section 3.5, that the ideal electromagnetic interchange limit was also recovered in the framework of the model. For all these reasons, we consider that it contains enough physics to be considered as the abstract class of interchange instabilities, sharing properties with both RBM and ITG.

A more significant addition would consist in the physics of the trapped electron modes (TEM). However, it appears difficult to add the TEM physics, essentially kinetic, in a reduced fluid model. Some attempts have been made in developing fluid TEM models, refs.[169, 170, 171, 114] provide possible ways forward in this direction.

3.6.2 Reduction to 1d

One of the central assumptions is the reduction from $3d$ to $1d$ by selecting a single poloidal and parallel wave vector. By doing so, nonlinear mode coupling is not accounted for. The consequence is that energy and enstrophy cascades are missing from the analysis. Effectively this removes a saturation mechanism for the turbulence, thus considering that saturation of fluctuations is primarily from profile relaxation and zonal flow self-regulation, respectively governed by particle flux and Reynolds stresses.

A refinement of the model has been proposed by adding a nonlinear saturation mechanism to the fluctuations, mimicking the missing nonlinear interactions. The resulting term is of the form $\partial_t N_k = ... - D_{NL}|N_k|^2 N_k$ [154]. A number of simulations have been performed with such a term present. The resulting dynamics was qualitatively analogous to simulations with stronger diffusion but a more extensive study would be required to assess the impact of such terms in the various regimes of turbulence. The Reynolds stress is still crucial to have a spectral transfer in k_x and enable complex dynamics.

A second important shortcoming of $1d$ models is the absence of geodesic acoustic modes (GAMs). These pressure sidebands modes result from the toroidal compression of ZFs [172]. GAMs also extract energy from ZFs. They act as a sink and limit their development [173, 174]. They should be included in the model if one wants to study interaction between turbulence and ZFs. An alternative to a $2d$ model would consist in adding equations for the GAM modes $(m,n) = (\pm 1, 0)$ with m the poloidal and n the toroidal mode numbers. This extension is similar to the extension from quasi-linear to generalized quasi-linear described in Section 2.4.2 and in ref.[119]. With this addition, the energy could be exchanged between the zonal mode, the GAM mode and the turbulence represented by the mode $k_y = cte$.

Finally, discarding $2d$ effects removes the geometry contribution. Deliberately removing these lead to the absence of shaping effect, such as negative triangularity [175], on the turbulence. However, no easy way to include shaping effects has been found without evolving towards a $2d$ model. For now, this physics is discarded.

3.6.3 Lack of magnetic shear and mode localization

The model assumes a simple magnetic geometry further reduced into 1 dimension. Also, there is no q-profile or magnetic shear included. The latter is particularly important for turbulence as it plays a similar role to the perpendicular velocity shear induced by the radial electric field [22] and can lead to transport barriers [176]. In essence, the magnetic shear leads to an "equilibrium" shear fixed by the magnetic topology. Having this shear effectively reduces the linear drive and contributes to the decorrelation of turbulent eddies. To include it, for example following ref.[177], one would need to include a $2d$ geometry. However, by considering a static equilibrium magnetic field, the magnetic shear is not a dynamical variable and interacts less with the underlying turbulence. For this reason and since the goal, for now, is to stay in $1d$, such improvement is not retained.

More importantly, turbulent modes (m,n) tend to localize on rational q-surfaces such that $q = -m/n$ [7, 84]. For Tokam1D, this is the case of interchange instability but not of CDW that requires a finite $k_\parallel$ to exist. The principal effect for modes that are radially localized is that they rapidly lose energy when they are moved away from their rational surface. The presence of sheared poloidal and parallel flows shift the modes away from their resonant surface thus leading to their decrease [84]. For now, no easy way has been found to add a sort of radial localization while keeping a $1d$ model.

3.7 Conclusion

In conclusion, this chapter has provided a set of tools to analyse turbulence-flows interaction. The reduced model Tokam1D has been derived for three different configurations: a core electrostatic plasma, a transitional core to scrape-off layer electrostatic plasma and a core electromagnetic plasma. In each case, reduction to $1d$ is done by selecting a single poloidal and parallel wavenumber. So far, the model is isothermal and contains two intrinsic instabilities: collisional drift-wave (CDW) controlled by the adiabatic parameter $C = \sigma_0 k_\parallel^2$ and interchange (akin to RBM) driven by $g = 2\rho_s/R$. The linear analysis of the Tokam1D model and its variants has been performed. The competition between CDW and RBM appears clearly in the core plasma: CDW dominates at low magnetic inhomogeneity or large adiabatic parameter (small collisionality). Whatever the value of g, the interchange instability is stabilized when C becomes very large. In the edge of tokamaks, various temperatures and densities can be achieved, leading to a broad range of accessible C and g with the former being often larger than the latter. That stands in exception to spherical tokamaks such as MAST-U that have a larger magnetic inhomogeneity and thus a greater g. In the SOL plasma, CDW is shown to be stable whatever the plasma parameters. It results in a SOL driven by interchange instability and stabilized by a larger conductivity. Finally, adding electromagnetism results in the modification of the already existing instabilities: CDW is stabilized by β, interchange is destabilized. Furthermore, it adds an electromagnetic

instability at large β leading to a very large growth rate. This latter instability is akin to ideal ballooning modes.

The derived model fulfills the objective of running fast on particle confinement timescales while resolving turbulence-equilibrium interactions self-consistently. This has been done thanks to a flux-driven formulation. The numerical speed has been met at the cost of losing mode-mode interactions: this limitation will be discussed while analysing nonlinear results in the next chapter. The model contains the minimal physics to include the role of the diamagnetic component of the Reynolds stress. With all these effects, the generation of ZFs in competing turbulence becomes possible.

Possible ways forward have been discussed. The first and most important consists in merging the three derived models into one. The resulting electromagnetic model would then encompass both the core and the SOL. Second, a possible way to include GAM physics has been discussed. This could enable the transfer of energy between the three players: zonal flows, GAMs and turbulence. Finally, a model has already been written with 5 fields: density, vorticity, ion temperature, electron temperature and ion parallel velocity. It is however not the main focus for the moment as we consider having enough physics with the isothermal assumption.

The developments performed here set the stage for the next chapter where we will perform nonlinear simulations with different parameters C and g. The questions of ZFs generation depending on turbulent regime and their impact on transport will be a central part of the analysis. In particular, regimes leading to the emergence of staircases will be pointed out.

Chapter 4

Flow generation & structure in competing drift-wave - interchange turbulence

Contents

In this chapter, we propose to come back on the turbulence parameter space by focusing on the turbulence self-organization: which parameters lead to zonal flows and to their radial structure? Which parameters lead to avalanche-like transport? Additionally, we approach the question of ZFs - avalanches interaction, staircase generation and of their impact on confinement.

For this analysis, we scan the turbulence parameter space using the reduced model derived in chapter 3. Note that we use the model Tokam1D-ES core without force balance velocity: Equation 3.32 − 3.35. This is done first because some simulations were performed before the model extensions were developed and implemented and also to simplify the problem at hand. Since the goal is mainly the generation in ZFs at the edge of the confined plasma, we expect that contribution from the force balance or the scrape-off layer is not yet crucial.
The model includes two instabilities present at the edge of tokamaks: collisional drift waves (CDW) driven by the non-adiabatic response of electron density fluctuations [48], and interchange caused by the inhomogeneity of the magnetic field [78]. They are respectively controlled by 2 non-dimensional parameters: $C = \sigma_0 k_\parallel^2$ with $\sigma_0 = \omega_{ce}/\nu_{ei}$ the conductivity, and $g = 2\rho_s/R$ the inhomogeneity of the magnetic field. The typical range of their experimental values is computed in Table 3.3 for WEST, TCV and MAST-U devices.

Results presented in this chapter constitute the backbone of two papers, the first one being in the review process, the other one almost completed and to be submitted in the coming months. The first describes the model and the importance of the flux-driven regime [145], the second focuses on the flows dynamics in the full (C, g) parameter space [178].

4.1 Simulations performed & distance to threshold

A total of 120 flux-driven simulations are performed on a box size $L_x = 400$ using a grid of $N_x = 1024$ radial points. The cases are run using the time step $\omega_{cs}dt = 0.1$ with constant dissipation $D_{0,1} = \nu_{0,1} = 10^{-2}$ and friction $\mu = 10^{-4}$ coefficients. The choice of dt is discussed in Section B.1. The poloidal wavenumber and ion to electron temperature ratio are chosen constant at $k_y = 0.3$ and $\tau = 1$. Neumann boundary conditions with vanishing gradients are used for the density at $x = 0$ and for the velocity at both ends. Dirichlet is used for the density imposed to $N_{eq} = 0.1$ at $x = L_x$ and the fluctuations set to zero at both boundaries. Note that, since we have decided not to take into account the density dependence of the parallel resistivity for the sake of simplicity (cf. Section 3.2.3), the absolute value of N_{eq} does not play a role in the equations. Therefore, the value imposed at the edge only translates vertically the whole density profile without impacting the dynamics.

The simulations are conducted until the particle confinement time τ_p reaches statistical steady-state. It is computed from the density profile and the source,

$$\tau_p = \frac{\int N_{eq} dx}{\int S_N dx} \tag{4.1}$$

It can be understood as the total number of particles divided by the inflowing particle flux. The source is Gaussian, with the maximum located at the innermost boundary, $S_N(x = 0)$. An example of the resulting steady-state density profile along with the source is shown Figure 4.1a. The density profile is taken after the simulation has reached steady state ($t > 15 \times 10^6$ iterations here). The method to compute quantities at the steady-state will be used throughout the whole chapter, it is detailed here for convenience. One first computes the root-mean-square (rms) radial profiles:

$$(\partial_x N_{eq})^{rms}(x) = \sqrt{\langle (\partial_x N_{eq})^2(x,t) \rangle_t} \tag{4.2}$$

With $\langle ... \rangle_t$ a time average performed on $\omega_{cs}t = 3 \times 10^4$. To get a single value per simulation, the radial average of $(\partial_x N_{eq})^{rms}$ is then performed on $20 < x < 380$ to exclude boundary effects. An example of the resulting rms density gradient is shown in Figure 4.1b.

Small scale corrugations are visible on the density gradient due to the action of shear flows. So as to have a single value per simulation we consider the profile as roughly linear and we take its mean radial value. A few things should however be noticed. First, the density profile is defined as the logarithm of the density $N = \ln n/n_0$. It results in the 'real' density profile to behave exponentially. Second, the density profile goes up to very large unrealistic values for a fusion reactor. This is the result of having a fixed density at $x = L_x$, a fixed large source and a large simulation box. In practice, large gradients such as this one may exist but on small radial portion of the machine. These simulations should be looked at as if we stretched the radial axis to better observe the high gradient zone. A solution to this problem is to use Neumann boundary condition on the right hand side for density. In this case, a large source would result in a large value of density at the separatrix. This situation is achieved in simulations including the scrape-off layer.

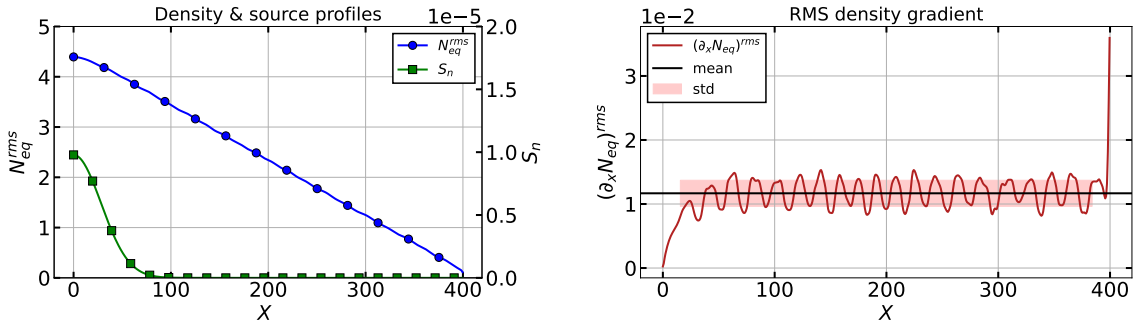

(a) (b)

Figure 4.1 – (a) Steady-state ($t > t_p$) rms density profile averaged over 3×10^4 ω_{cs}^{-1} (blue circles). The source (green squares) is set to $S_N(0) \approx 10^{-5}$. (b) Corresponding rms density gradient. Simulation parameters: $(C, g) = (10^{-3}, 5 \times 10^{-3})$.

The equilibrium density profile is a result of the balance between the imposed source and the transport: diffusive and turbulent. While the former is imposed through numerical dissipation parameters $(D_{0,1}\ ;\ \nu_{0,1})$, the latter depends on turbulence characteristics. Depending on the source amplitude and plasma parameters (C, g), the steady-state density profile sits at a certain distance from its linear threshold. This distance to marginality has an influence on the nonlinear dynamics and impacts in particular staircases which are expected to exist close to the threshold [106]. So as to control the distance to marginality, two sets of simulations are performed using different sources. The first set is performed at constant source amplitude, $S_N(0) = 10^{-4}$ such that every simulation is above its linear threshold. As a result, some simulations at the edge of the scanned parameters space exhibit very large gradients, much above their linear threshold. The second set, as reported in [145], ensures that each simulation is above, but close to its linear threshold. To do so, we define the *diffusive gradient* $|\partial_x N_{eq}^{diff}| = \int S_N / D_0$. It is the necessary gradient for the diffusive flux of particles to balance the driving flux imposed by the source. This gradient corresponds to the equilibrium state of the system without turbulence. The source is then chosen such that the diffusive gradient is above the linear instability threshold defined by the *critical gradient*. Depending on the instabilities parameters, the critical gradient is modified. We can then choose the corresponding source such that the system is 'forced' similarly for different values of C and g. An example of this kind of simulations is presented in Figure 4.2 for the scan CDW only ($g = 0$). The method using a constant source for all simulations is called *constant source* while the second is called *adapted source*.
In Figure 4.2, the critical gradient corresponds to the linear threshold. It is obtained from the linear analysis using the values of (C, g) and considering no flow shear. The objective is then to adjust the source so that the resulting diffusive equilibrium gradient (the one obtained in the absence of turbulent transport) is "slightly" above this critical gradient. In practice, we choose $|\partial_x N_{eq}^{diff}| = 6|\partial_x N_{eq}^{crit}|$. The source is chosen so that the equilibrium state of the equilibrium density equation (Equation 3.32) with $\Gamma_{turb} = 0$ is equal to the diffusive profile: $\partial_x N_{eq}^{diff} = \int S_N / D_0$. Provided that the shape of the source is not modified, the relation between the source amplitude and the diffusive gradient is linear. Therefore, we choose a source amplitude 6 times the one needed to reach the critical gradient.

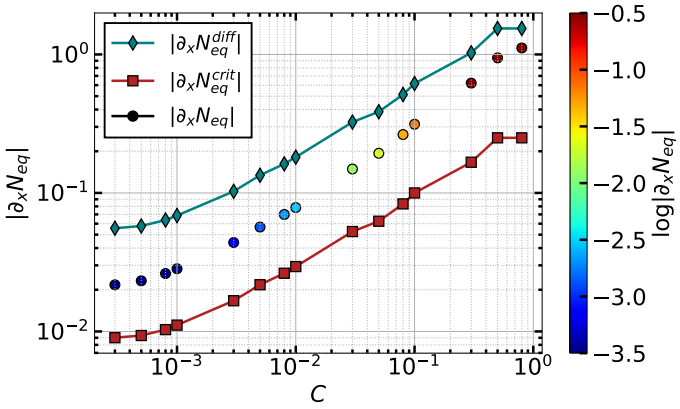

Figure 4.2 – Absolute critical density gradient indicating the instability threshold, corresponding diffusive gradient ($|\partial_x N_{eq}^{diff}| = 6\,|\partial_x N_{eq}^{crit}|$) and steady-state gradient as a function of the adiabatic parameter. Scan of C at $g = 0$, adapted source.

Choosing a diffusive gradient equal to 6 times the critical gradient can seem large. However, one must remember that the system will develop turbulence as soon as the critical gradient is reached. Then, turbulent transport will develop and constrain the system to stay close to the linear threshold. The present choice have been made so that each simulation in the scanned parameter space develops a significant turbulent flux of particles Γ_{turb}, at least larger than the diffusive flux Γ_{diff}. Both fluxes are compared in Figure 4.23. Other trials have been performed with a smaller forcing resulting in a transport dominated by diffusion. In principle, the marginality is defined as the proximity to the critical flux. Meaning one should scan the source until the change of the equilibrium density gradient stops (or slows down) due to the action of the turbulent flux. In practice, performing this work for 120 simulations would take too much time. Therefore, the choice is made to compare the steady-state gradient to the critical gradient instead of using the fluxes.
The resulting density gradient at the steady-state is shown with the colour indicating the value of the gradient. One can notice that the steady-state profile obtained in the simulations gets closer to the diffusive one as C is increased. It is a direct consequence of the system linear properties: as C increases, both the linear growth rate and sine of the cross-phase decrease. It results in a system that is less *stiff*: meaning that an increased gradient leads to only a small change in transport.

Giving the system the freedom to adapt freely its gradient to the injected source is one of the strengths of a flux-driven model. The model now evolves in a $3d$ parameter plane delimited by $(C, g, \partial_x N_{eq})$. Bearing this in mind, we scan the adiabaticity parameter from $C = 2 \times 10^{-4}$ to 8×10^{-2} for three different values of g: 10^{-4}, 10^{-3} and 5×10^{-3}. The curvature parameter is scanned from $g = 10^{-4}$ to 3×10^{-2} for $C = 10^{-3}$. The scanned parameter space in terms of C and g for a constant source is presented in Figure 4.3. The colour indicates the radially averaged gradient at the steady-state computed for $15 < x < 385$ to exclude boundary regions.
The figure features a total of 52 simulations, performed at constant source. Including simulations performed with an adapted source (and test case at $g = 0$), the number of analysed steady-state simulations is 120. Simulations with an adapted source are not shown here as the

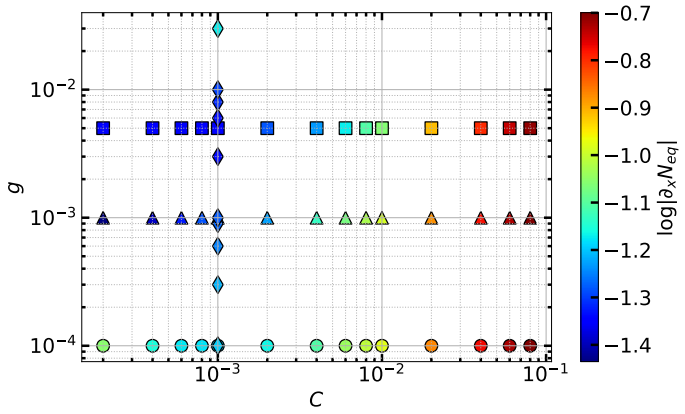

Figure 4.3 – Scanned parameter space: each point corresponds to a simulation that reached steady-state. (circle) scan of C at small $g = 10^{-4}$. (triangle) scan of C at medium $g = 10^{-3}$. (square) scan of C at large $g = 5.10^{-3}$. (diamond) scan of g at medium $C = 10^{-3}$. The colour indicates the absolute value of the mean gradient at steady state.

trend is similar although with different steady-state density gradients. Large gradients at high C result from the stabilization of the instabilities when getting closer to the adiabatic regime. As a matter of fact, simulations at large $C > 6 \times 10^{-2}$ correspond to low turbulence regimes where the turbulent flux is comparable to the diffusive flux. For the case at small g, the gradient decreases at $C \approx 10^{-3}$ then increases again. This is typical of CDW instability, stabilized at both small and large C (already discussed in the linear analysis: Figure 3.8b). Scans at medium and large g display no stabilization at small C due to the interchange instability taking over.

It should be emphasized that the variation of C only is not enough to conclude on the transition from an hydrodynamic to an adiabatic regime. Instead, some authors consider the transition to the adiabatic regime when $C/\partial_x N_{eq}$ is large [179]. For flux-driven simulations, the density gradient evolves together with the adiabaticity parameter. In particular, the density gradient increases with C resulting in a more gradual evolution of $C/\partial_x N_{eq}$. However, computing $C/\partial_x N_{eq}$ is not straightforward in a flux-driven system. Indeed, it is not obvious whether one should take into account only the large scale gradients or also include small scale structures in the adiabaticity estimation. Therefore, our choice of primary parameters are C and g, the density gradient being indicated wherever deemed necessary.
The different scans performed are summed up in Table 4.1.

4.2 Transition from CDW to interchange dominated plasma

As a first step to study the landscape of instabilities we characterize the turbulence in terms of phase velocity, amplitude, and cross-phase. The characterization of drift wave - interchange turbulence has been studied for a long time in particular by B.D. Scott [121, 172, 180] for a gradient driven core plasma and more recently by P. Ghendrih [153] for a flux-driven scrape-off layer plasma. The fluctuation characteristics, in turn, influence the turbulence self-organization that will be studied in Section 4.3 and 4.4.

Source type	Scanned parameter	Fixed parameter	Number of simulations
Constant	C	$g = 10^{-4}$	14
	C	$g = 10^{-3}$	14
	C	$g = 5 \times 10^{-3}$	14
	g	$C = 10^{-3}$	10
Adapted	C	$g = 0$	16
	C	$g = 10^{-4}$	14
	C	$g = 10^{-3}$	14
	C	$g = 5 \times 10^{-3}$	14
	g	$C = 10^{-3}$	10

Table 4.1 – Summary of conducted scans using Tokam1D-ES core without force balance effects, $D_{0,1} = \nu_{0,1} = 10^{-2}$, $\mu = 10^{-4}$. *Constant* source: $S_N(0) = 10^{-4}$. *Adapted* source imposed such that $|\partial_x N_{eq}^{diff}| = 6\,|\partial_x N_{eq}^{crit}|$. C is scanned from 2×10^{-4} to 8×10^{-2}, except for $g = 0$ where it is scanned from $C = 3 \times 10^{-3}$ to 8×10^{-1}. g is scanned from 10^{-4} to 3×10^{-2}.

4.2.1 Turbulence structure in Tokam1D

First, let us look at the space-time structure of the turbulence in Tokam1D. Since the model is reduced to $1d$, the turbulence is not fully described in the $2d$ (x,y) plane. Instead, the choice has been made to keep a single poloidal wave vector $k_y = 0.3$. Figure 4.4a displays an example of the density fluctuations for the Fourier component N_k as a function of time and space. In Figure 4.4b, the corresponding fluctuating density field, $\widetilde{N}(x,y,t) = N_k(x,t)\exp(ik_y y) + cc$ (cf eq.3.15 at $z = 0$), is shown in the (x,y) plane for a given time. On top of the density fluctuations, is shown the equilibrium velocity coarse-grained on a few time and radial points.

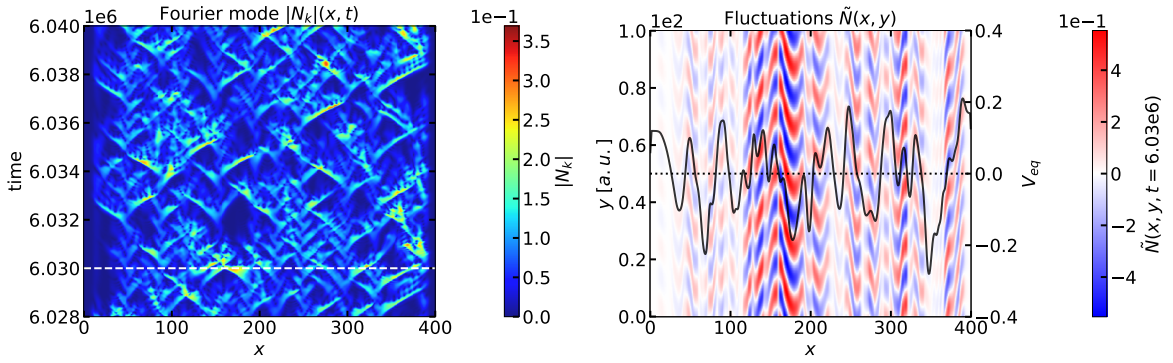

(a) (b)

Figure 4.4 – Density fluctuation for case $C = 10^{-2}$. (a) Amplitude of the Fourier component N_k as a function of time and space, the white line notes the snapshot for which is plotted the fluctuation field. (b) Two-dimensional fluctuating density field for $t = 6.03 \times 10^6$. The black line shows the equilibrium velocity around the same time snapshot.

In Figure 4.4a, density fluctuations are propagating both inward and outward at similar speed. The associated turbulent particle flux is always positive, resulting in an outward transport. In

Figure 4.4b the turbulent structures are displayed in their $2d$ form. As a single k_y is chosen, they are periodic in the y-direction. The tilt of the turbulent structures in the (x,y) plane appears to be governed by the equilibrium velocity direction, indicating that the flows elongate turbulent structures in the poloidal direction. Even though the code is reduced to $1d$ and is periodic in the y-direction, one observes a complex dynamics due to the interaction with equilibrium flows. Transfer to higher k_x leads to various sizes of structures depending on the underlying flow shear and transport. Noticeably, the phase of the fluctuations can exhibit quasi discontinuities along the radial direction, as visible e.g. at $x \sim 160$.

4.2.2 Method to assess the dominant instability

Estimating the dominant instability in specific plasma condition will reveal helpful for the interpretation. The main purpose is to understand the underlying physical character of the turbulence: drive, saturation mechanisms etc. As a word of caution, it should be noted that the analysis of turbulent systems based on linear properties assumes that those properties still matter in the nonlinear regime. This analysis should only be seen as a guide for the nonlinear and not as a concrete result.[1]

To identify whether the system is dominated by CDW instability, one can verify the turbulence phase velocity. We expect CDW to be electron driven, i.e. its frequency of the sign of the electron drift frequency: $\omega_{\star e} - k_y \partial_x N_{eq}$. Conversely, we do not have prediction for the interchange instability frequency. As it appeared in Figure 3.9, it can leads to both ion and electron type frequencies. Note that in the absence of the temperature dynamics, hence of modes such as ITG, there is no reason *a priori* for the interchange to be driven by the ions more than the electrons.
As an additional information to estimate whether the instability is of 'interchange' or 'drift wave' type, one can compute the cross-correlation between density and electric potential fluctuations [121, 181]. Based on the linear analysis performed Section 3.4.1, one expects interchange type of instabilities to have a much larger cross-phase: $\sin\Delta\varphi \approx 1$ as compared to drift waves.
Ultimately to differenciate between instabilities that are driven by the same species and that are of the same 'class' (drift waves, interchange), one needs to perform scans of plasma parameters: density, temperatures and compare the behaviour with theoretical predictions. In that case, one can rely on simulations such as local gyrokinetics to estimate linear parameters from local plasma parameters: pressure gradient, plasma shape etc. [180, 182, 50].

Bearing this in mind, one can compute the linear analysis of the Tokam1D system using the density gradient at steady-state and considering no flows: $V_{eq} = \partial_x V_{eq} = \partial_x^2 V_{eq} = 0$. The density profile is taken as linear $\partial_x N_{eq} = cst$ and computed from Equation 4.2. For simplicity, one neglects the possible effects of the equilibrium profile corrugations, hence considering vanishing higher order derivatives of N_{eq}. Doing this makes sense since the most unstable mode is large scale ($k_x \approx 0$) so that it is expected to be mostly sensitive to the large scale gradient. The

[1] Consider for example the case of a system including two instabilities: the first with a low gradient threshold (grad1) and a low stiffness, the second with a large threshold (grad2 $\gg$ grad1) and a very large stiffness. The stiffness here relates to the importance of the turbulent flux as one gets above the threshold. For a large source, the system's profile can reach the second threshold (grad2). Based on the linear we might deduce that the first instability is dominant: far away from its threshold, hence very large growth rate. But it is actually the second, stiff, instability that governs the final gradient.

linear frequency computed this way is displayed Figure 4.5 for the 4 scans performed using a constant source. Note that the three scans in blue (circles), red (triangle) and green (square) are performed as a function of C for fixed values of g, while the purple (diamond) is performed as a function of g for a fixed C.

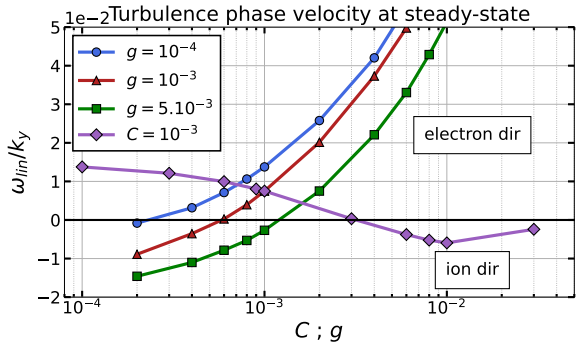

Figure 4.5 – Frequency from linear analysis using equilibrium parameters at the steady state as a function of C and g. The source is imposed for all simulations at $S_N = 10^{-4}$. Other parameters: $V_{eq} = \partial_x V_{eq} = \partial_x^2 V_{eq} = 0$, $D_{0,1} = \nu_{0,1} = 10^{-2}$.

Scans of C at constant g, leads to a negative frequency at low C even more so when g is large. For the g-scan, the frequency is negative at large g. In both cases, we understand the system to be interchange dominated whenever $\omega_{lin} \lesssim 0$, which was expected at small C and large g.

4.2.3 CDW dominated by density fluctuations & low cross-phase

In this section, the regimes are characterized in terms of fluctuation amplitude and cross-phase. Those two quantities govern the turbulent transport, $\Gamma_{turb} = -2k_y|N_k||\phi_k|\sin\Delta\varphi$. They are also crucial for the ZFs generation because of their critical role on the two components of the Reynolds stress. In particular, the density to electric potential fluctuation amplitude ratio impacts the relative amplitude of the two tensors.

The rms-values of the fluctuations of density and electric potential are shown in Figure 4.6a, the sine of the cross phase is displayed in Figure 4.6b for two cases: the g-scan at fixed $C = 10^{-3}$ and a C-scan at fixed $g = 5 \times 10^{-3}$. Both are shown as a function of C/g, the last section highlighted that an interchange driven regime is reached at both very small C or very large g. The linear estimates of the ratio of the fluctuation amplitudes and cross-phases are shown in dotted line.
Three regimes can be identified. The first, at low C/g, bears the characteristics of interchange. It has the large $\sin\Delta\varphi$ predicted in Section 3.4.1. This regime is dominated by electric-potential fluctuations and both cases at fixed C or fixed g display a similar behaviour at low C/g. The second and third regimes, at large C/g, depend on whether C is large or g is small. Large C for finite g, displayed in green (squares), is characterized by $N_k^{rms} \approx \phi_k^{rms}$ and a very low cross-phase. It corresponds to a regime getting close to the adiabatic state. The other, in purple (diamond), leads to a large N_k^{rms}/ϕ_k^{rms} and an almost constant cross-phase. It is close to the CDW case detailed Section 3.4.3, with a sine of the cross-phase close to $1/\sqrt{2}$. In the end, these results show that the ratio C/g is not a good parameter to discriminate turbulent regimes in Tokam1D:

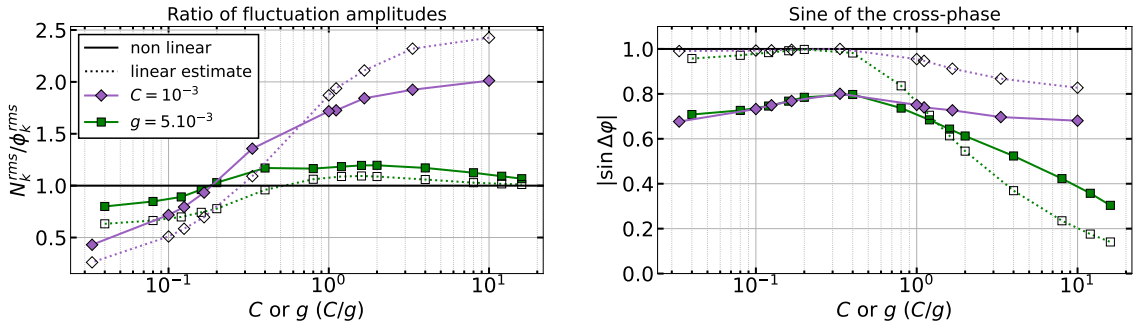

(a) (b)

Figure 4.6 – Nonlinear fluctuation amplitude and cross-phase as a function of C/g for cases g-scan at fixed $C = 10^{-3}$ and a C-scan at fixed $g = 5 \times 10^{-3}$. Both for a constant source $S_N(0) = 10^{-4}$. The linear estimates computed from the steady-state density gradient are shown in dotted lines.

one needs to scan the full $2d$ (C,g) plane. This stands in contrast to ref. [122] where the parameter α_t, proportional to the ratio of C and g is found instrumental in discriminating L- and H-mode regimes in Asdex-Upgrade plasma discharges. One of the key differences comes from the isothermal assumption in Tokam1D; in particular, this results in the fact that large C values are characterized by stable CDW and interchange.

In all cases, the linear estimate follows the same trend as nonlinear calculations. However there is a constant offset of the cross-phase and of the fluctuation amplitude ratio at low C/g. At large C/g the offset changes sign for the amplitude ratio in the g-scan and for the cross-phase in the C-scan. This can be a result of the absence of sheared flows in the linear analysis. Indeed, a finite V'_{eq} impacts both linear and nonlinear properties. Taking it into account could close the gap. However, since V'_{eq} is hardly accessible to experimental measurements, we have decided not to take it into account in the linear analysis. Additionally, a radially-constant rms-density gradient is considered for the linear analysis, discarding corrugations.

As a conclusion, let us sum up the turbulence parameters as a function of C and g.

- Large C: low cross-phase and $N_k \approx \phi_k$ ($\approx$ adiabatic).
- Large g: large cross-phase and $\phi_k > N_k$ ($\approx$ interchange).
- Low g: $N_k > \phi_k$ ($\approx$ CDW).

4.2.4 Auto-correlation time and correlation length reduced in interchange driven plasmas

In this section, the auto-correlation time of the turbulence τ_{turb} is computed together with the radial correlation length L_{turb}. They will be used to differentiate turbulent regimes, but also to serve as a reference for the different scans. Indeed, the size and time duration of the simulations are constant even though the underlying dynamics is not. For the average and coarse-graining to be consistent, they have to be adapted for each simulation. In the rest of the chapter, the coarse-graining will then be done on a number of τ_{turb} and L_{turb} to ensure similar statistics between

simulations.

Considering two discrete complex signals x and y, their correlation reads,

$$C_{xy}[k] = \sum_{i}^{N} y[i]x^*[i+k] \tag{4.3}$$

With N the number of points in the signal and k the delay (in time or space) given in a number of points. Then, the coherence is obtained by normalizing the correlation by the auto-correlation of each signal at zero-delay,

$$\mathscr{C}_{xy}[k] = \frac{C_{xy}[k]}{(C_{xx}[0]C_{yy}[0])^{1/2}} \tag{4.4}$$

From the Wiener-Khinchin theorem [183, 184], $\mathscr{C}_{xy}[k]$ can also be obtained in Fourier space. Using cross-spectral density S_{xy} and power spectral densities S_{xx}, S_{yy}, the spectral coherence reads, $\mathscr{S}_{xy}(f) = S_{xy}/(S_{xx}S_{yy})^{1/2}$. Note that the spectral coherence is given as a function of frequencies instead of time delays.

The auto-correlation function at position x_0 is computed on the steady-state density fluctuations by splitting the time arrays in 39 independent samples of 750 ω_{cs}^{-1} each that are then averaged out to produce a single estimate. The time length of the samples needs to be sufficiently large so that a full correlation function can be computed. The radial correlation is performed by taking a reference time signal of the density fluctuations at x_0, $|N_k(x_0,t)|$ and correlating with the neighbouring time signals at positions $x_0 \pm \Delta x$. Examples of averaged time auto-correlation and radial correlation functions are shown in Figure 4.7.

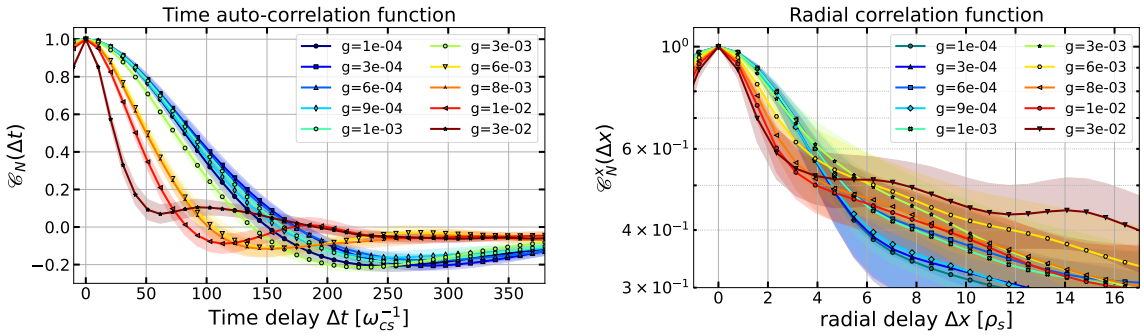

(a) (b)

Figure 4.7 – (a) Time auto-correlation functions. (b) Radial correlation functions. Both for g-scan simulations at constant source computed at position $x_0 = 197$.

The auto-correlation functions are symmetric around $\Delta t = 0$, where they reach their maximum equal to 1. Two groups of simulations can be identified. The first one, $g < 3.10^{-3}$, exhibits a Gaussian shape. The second group, at large g, displays a much more narrow auto-correlation function further reducing as g increases. The same behaviour is observed on the radial correlation function. It gets more narrow for the second group of simulations. Interestingly, a tail

appears for simulations at large g. These tails are understood as the signature of avalanches and will be thoroughly analysed in Section 4.5.

From the correlation functions, we compute the turbulence auto-correlation time τ_{turb} and radial correlation length L_{turb}. τ_{turb} is obtained when the correlation has dropped below $1/e$. The operation is repeated at several radial locations x_0 to get a global average for the simulation. Estimating, L_{turb} is slightly more sublte. In regimes where the correlation function exhibits different short and long scale behaviours, only the short scale part is filled by a Gaussian, hence ignoring the tail. Then, L_{turb} corresponds to the radial lag where this Gaussian fit is equal to $1/e$. Both the τ_{turb} and L_{turb} are displayed in Figure 4.8.

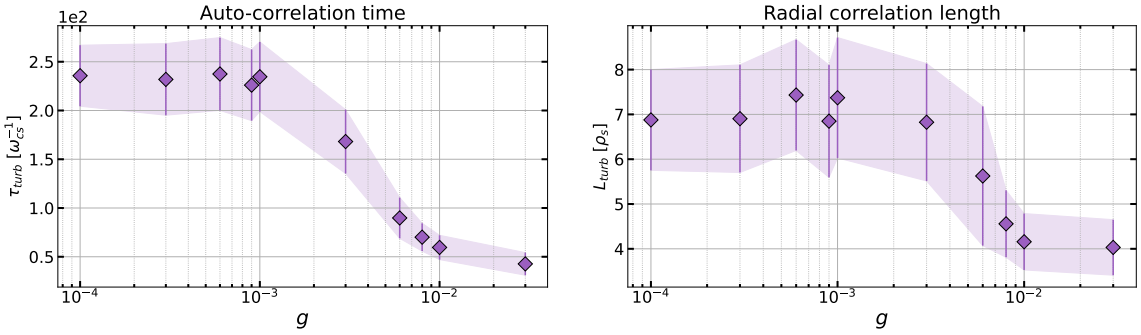

(a) (b)

Figure 4.8 – (a) Auto-correlation time τ_{turb} defined as the delay for which correlation has dropped to $1/e$. (b) Radial correlation length L_{turb}. Both are radial average estimate for g-scan simulations at constant source. Radial standard deviation is indicated as a shaded area.

Once again, the transition from CDW to interchange dominated turbulence is made clear. At low g, the auto-correlation time is roughly equal to $\omega_{cs}\tau_{turb} \approx 230$. Similarly, L_{turb} is constant at roughly 7 ρ_s. At larger values of g the auto-correlation time quickly drops to $\omega_{cs}\tau_{turb} \approx 50$ indicating a shorter lifetime for the turbulent structures. The auto-correlation length drops to $L_{turb} \approx 4\rho_s$.

The auto-correlation time of the turbulence provides a measure of the time required for the turbulence eddies to become statistically uncorrelated. A faster dynamics leads to a smaller τ_{turb}. Here, the first group corresponds to CDW dominated turbulence while the second is likely mainly driven by interchange instability. The latter is characterized by larger linear growth rates which lead to a fast dynamics and a low τ_{turb}. Also, the velocity shear is expected to elongate and decorrelate turbulent structures if it persists on timescales larger than a few τ_{turb}. The reduction of L_{turb} can well be linked to the presence of flow shear, as will be investigated in the following sections.

4.3 Zonal flows generation in competing turbulence

In this section, the generation of ZFs in the competing drift waves - interchange turbulence is studied. First, we use the energy channel analysis derived Section 3.2.7. Some regimes, in particular at large g and large C are characterized by a large flow to turbulence energy ratio. The

flux-driven characteristics of the system proves crucial for the energy partition. Then, we delve deeper into the generation of ZFs by looking at the Reynolds stress itself and its decomposition into electric and diamagnetic components. The role of the diamagnetic component is essential as it reinforces the electric component in CDW turbulence and opposes to it in interchange-driven regimes. Advancing one step further, the components of the Reynolds stress are decomposed into quantities that involve the fluctuation amplitude, cross-phase and turbulent flux of particles. In the last section, the impact of the distance to marginality is discussed.

4.3.1 Flow dominated regimes at large C and g

ZFs act as a repository for the energy of the system. The more energy is stored by the ZFs, the less is available for turbulence, hence the lower the transport. Numata et al. have shown in a gradient-driven Hasegawa-Wakatani type of model that there was a collapse of relative energy stored into the flows at low C [124]. Remember that $C \propto 1/\nu_{ei}$, therefore a large collisionality is expected to lead to a strong decrease of ZFs activity. First, we show that in flux-driven regimes, the density gradient also adapts to the presence of flows and turbulence. Therefore, the transition from turbulence dominated to flow dominated regimes is much less abrupt. This is in agreement with the work done by Numata, provided one accounts for the fact that the density gradient evolves together with the flows. A flux-driven regime then appears crucial to the study of turbulence-flows interaction. Second, the role of the curvature parameter g is made explicit: even at low C the system can exhibit important flow to turbulence energy ratios provided that g is sufficiently large.

Case CDW only: the importance of the density gradient

Using the energy channels defined, Equation 3.42 - 3.45, we evaluate whether the free energy is captured by turbulence or is stored in the flows. Flows and turbulence energy E_{Veq} and E_{turb} are coarse-grained on a few turbulence auto-correlation times. Then the rms values are computed following Equation 4.2. To account for the possible spatial structure of the flow, we perform the radial average on the ratio: $\langle E_{Veq}^{rms}/(E_{Veq}^{rms}+E_{turb}^{rms})\rangle_x$. The flow and turbulence energy channels are shown in Figure 4.9b as a function of C for the case $g=0$. Their energy is normalized to the total energy of the system $E_{tot} = E_{Neq} + E_{Veq} + E_{turb} + E_{Neq-Veq}$. The flow to turbulence energy partition ratio is displayed in Figure 4.9a. The colour of the points corresponds to the steady-state density gradient, already shown in Figure 4.2.
The flow to turbulence energy partition ratio increases with the adiabaticity parameter, Figure 4.9a. At low C the system is dominated by turbulence with about 0.001% of the energy stored in the flows. In the adiabatic regime, at large C, flows account for 80 % of the flow and turbulence energy. Consistently, the density gradient increases with C. It is illuminating to look at each channel separately. In Figure 4.9b, most of the energy variation is carried by turbulence: it decreases by nearly two decades as C increases. Also, one can notice that the case $C = 2\times10^{-4}$ is missing on both figures. This case displays a total collapse of the flows energy. However, it should be considered with care because the k_y corresponding to the maximum growth rate is different from the one used by the simulation. It stands at the limit of the model validity and we choose not to consider it in the following.

On the basis of these observations, we focus on the expected impact of the equilibrium density on ZF and turbulence dynamics. Although taken constant in the present simulations, the

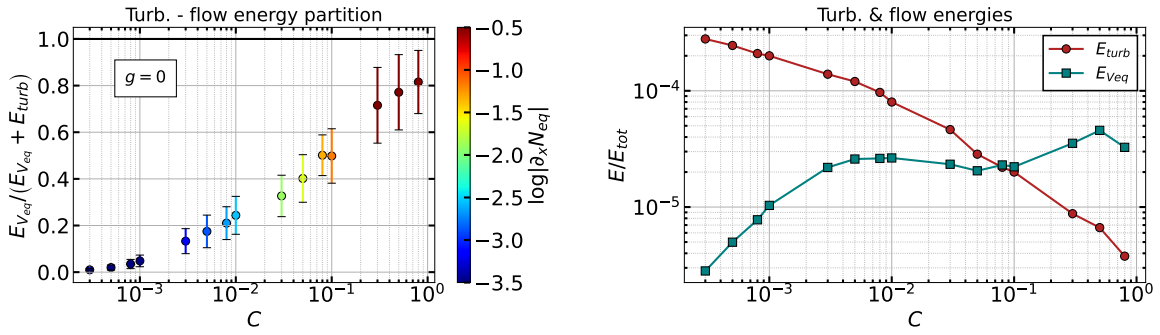

(a) (b)

Figure 4.9 – Energy channels as a function of C for $g = 0$, case with adapted sources. (a) Flow to turbulence energy partition ratio as a function of C with the colour indicating the absolute value of the density gradient in log scale. Error bars represent the standard deviation of the rms profiles. (b) Flow and turbulence energies normalized to $E_{tot} = E_{Neq} + E_{Veq} + E_{turb} + E_{Neq-Veq}$.

adiabaticity parameter $C = (k_{\|}\rho_s)^2\omega_{cs}/\nu_{ei}$ should actually scale like $1/N_{eq}$. High density plasmas are then characterized by small C values (assuming constant $k_{\|}\rho_s$). In this case, on the basis of Figure 4.9a, one expects a low zonal flow to turbulence energy ratio. This suggests that the turbulent transport should increase when density increases or respectively when C decreases. The trend is qualitatively similar to the results reported in ref.[124] but not quantitatively. More precisely, the ZF magnitude decreases rather monotonously at large density (collisionality) and does not exhibit the collapse reported in [124]. The reason for the difference comes from the self-consistent evolution of N_{eq} in flux-driven simulations. In the absence of mode-mode coupling, the system has two ways to saturate turbulence: by profile relaxation (transport) and ZFs generation. At vanishing g, the energy stored in ZFs in low C cases is minimal and the profile relaxation is favoured. The richness of the saturation channels permitted by flux-driven simulations thus leads to a less abrupt transition of the system. It should be noted that Figure 4.9a is consistent with the ZF collapse reported in [124] provided one also moves from one density gradient to another when decreasing C (green and red curves in fig.5 of [124]). A steep increase of ZFs energy has also been found in gyrofluid modified Hasegawa-Wakatani simulations when including warm ions [185]. In this latter contribution, mode-mode interactions are retained leading to a self-consistent turbulent cascade, but the background density gradient is imposed, limiting the liberty of the system to explore the $(C, \partial_x N_{eq})$ parameter space.
The energy partition is modified when the interchange instability is added to the system, as detailed in the next section.

Energy partition as a function of the dominant instability

Exploring now the full parameter space in terms of C and g one can redo the previous computation with simulations performed at fixed and adapted sources. The results are summarized in Figure 4.10 for the cases $g = 10^{-4}$, $g = 10^{-3}$ and $g = 5 \times 10^{-3}$ as a function of C. Cases with an adapted source ('fixed' distance to marginality) are displayed with dotted lines.
The behaviour at large C is qualitatively similar to Figure 4.9 whatever the value of g. However, the trend at low C is different. The low g case is analogous to the previous result: although

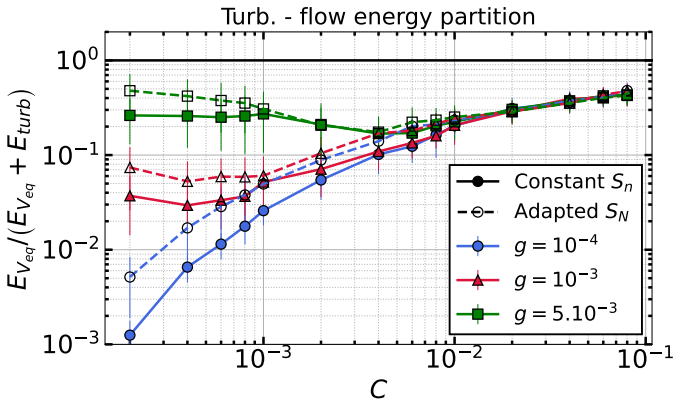

Figure 4.10 – Energy partition between turbulence and flows as a function of C for three scans at different values of g. Cases at constant source $S_N(0) = 10^{-4}$ are indicated with full lines, those with an adapted source are shown with dotted lines.

not collapsing, the ZF energy is very low as compared to that of turbulence. When g increases, more energy is stored in the flows up to the point of rivaling simulations at large C with about 30 % of the free energy captured. Although both large g and large C simulations share a large flow to turbulence energy ratio, the system properties are very different. At high g, flows are stable in time and present a clear radial structure, see Section 4.4. The cross-phase between density and electric potential fluctuations is large leading to an important transport. At large C, flows tend to be less stable in time. Also, the turbulence intensity is relatively low in the latter regime, leading to a low amount of turbulent transport (comparable to the diffusive flux).
At low C, simulations with an adapted source always display a larger flow to turbulence energy ratio. ZFs appear to efficiently store energy near marginality. We demonstrate this point further in Section 4.3.3.
Once again it should be noted that the friction exerted on the flows $-\mu V_{eq}$ is set constant in those simulations. However, increasing density also increases the friction coefficient. The large amount of energy captured by the flows at large g small C, may be less pronounced if the friction to the flows increases with density (low C). Reference [161] provides a heuristic expression for this neoclassical coefficient. Simulations taking into account the dependence of C and μ with density would be desirable. This density dependency has also been proven key to the modelling of L-H like bifurcations in flux-driven simulations of resistive ballooning turbulence [146, 162].

In conclusion, a few experiments have reported the strong reduction of ZFs - or proxies for ZFs - when approaching the density limit in L-mode tokamak plasmas [186, 187, 188]. In this context, the ZF collapse at large density in gradient-driven simulations of Hasegawa-Wakatani turbulence [124] has recently been put forward as a possible explanation to these observations [125, 189]. Our simulations suggest however that, in the flux-driven regime relevant to tokamak plasmas, this reduction of ZF could be much more gradual or even absent if g is large enough (high magnetic field inhomogeneity experiments). Although not discarding the physics as a possible explanation to the issue of density limit in L-mode, these new results advocate for a renewed exploration of the link between ZF reduction and density limit in a self-consistent flux-driven regime.

4.3.2 Electric and diamagnetic Reynolds stress: synergy or competition

The generation of ZFs and the associated velocity shear ultimately depends on the total Reynolds stress Π_{tot} being the sum of two contributions: electric Π_E and diamagnetic $\Pi_\star$. While the former has been considered crucial for years [91, 89], the latter is much less studied [92, 95, 190]. Π_{tot} being the sum of two contributions, it ultimately depends on their relative amplitude and whether they are in phase. In this section, we study both contributions to the Reynolds stress, with the objective to understand the two regimes leading to a large flow to turbulence energy ratio, namely at high C and high g.
To clarify the following discussion, remember that in the Tokam1D framework, the electric contribution reads $\Pi_E = -2k_y\Im(\phi_k^*\partial_x\phi_k)$ and the diamagnetic is written as $\Pi_\star = -2k_y\Im(N_k^*\partial_x\phi_k)$ (see Section 3.2.5).

First, let us take a look at the general behaviour of Π_{tot} through the correlation and relative amplitude of its two contributions. In Figure 4.11, the rms-value of the total Reynolds stress is shown as a function of C for three different values of g in cases with a constant source (left) and with a adapted sources (right).

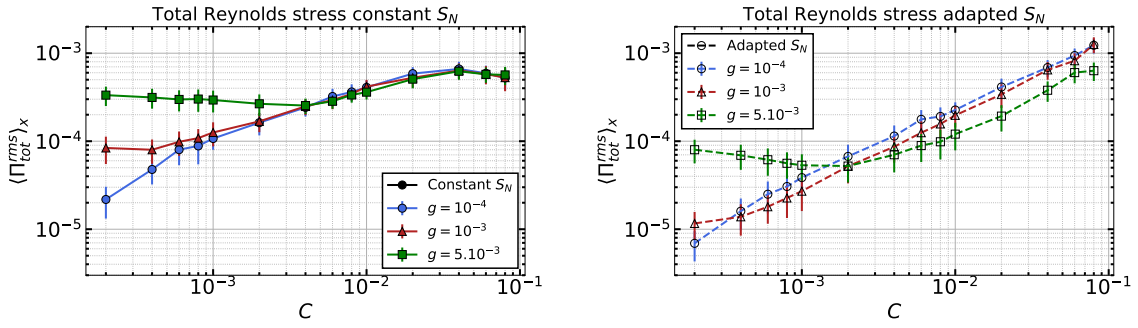

(a) (b)

Figure 4.11 – Radial average of the rms profile of Π_{tot} as a function of C for three values of g. (left) Simulations with constant source $S_N(0) = 10^{-4}$. (right) Simulations with adapted sources.

The total Reynolds stress increases with C in most of the parameter domain. At low C, the case at large g stands out with a large Reynolds stress that stays roughly constant until the CDW instability takes over at $C \approx 4 \times 10^{-3}$. The simulations sitting closer to their linear threshold and displayed on the right of Figure 4.11, depart from the results on the left. First, the total Reynolds stress is smaller for the same equilibrium parameter. That is understood linearly: as the gradient keeps increasing so does the growth rate, leading to a stronger turbulence and a larger resulting Reynolds stress. At large C, simulations at large g display a slightly lower total Π_{tot}. Although the difference is small, that could indicate that g is detrimental to the generation of flows at large C. However this effect is not recovered on the energy partition between flows and turbulence Figure 4.10. Also note that the total Reynolds stress reduces for the three largest values of C in the constant source cases. The reduction is linked to a decreased turbulence intensity in those regimes ($\Gamma_{turb} \sim \Gamma_{diff}$).
Overall the behaviour of the Reynolds stress is in agreement with the energy partition presented

Figure 4.10. Interestingly, the cases at fixed source present a larger total Reynolds stress, but a smaller flow to turbulence energy ratio as compared to adapted source ones. This indicates that turbulence intensity keeps increasing with the gradient, thus leading to larger Π_{tot} but that flows are not able to capture all the added energy. More details on the flow generation as a function of the distance to marginality is given Section 4.3.3. The maximum of energy captured by the flows most likely also depends on the imposed friction and viscosity. In particular the dissipation due to friction increases together with the flow amplitude hence limiting their development.

To get more insight on the behaviour of Π_{tot}, the correlation between the electric and diamagnetic contributions to the total Reynolds stress is shown in Figure 4.12 together with their relative amplitude. The correlation is computed on flattened arrays (transforming a multi-dimensional array into $1D$) after a coarse-grain of 4 τ_{turb} and one L_{turb}, respectively the turbulence auto-correlation time and correlation length. To take into account the possible radial structure of the Reynolds stress, the radial average of the rms-values is computed after having performed the amplitude ratio.

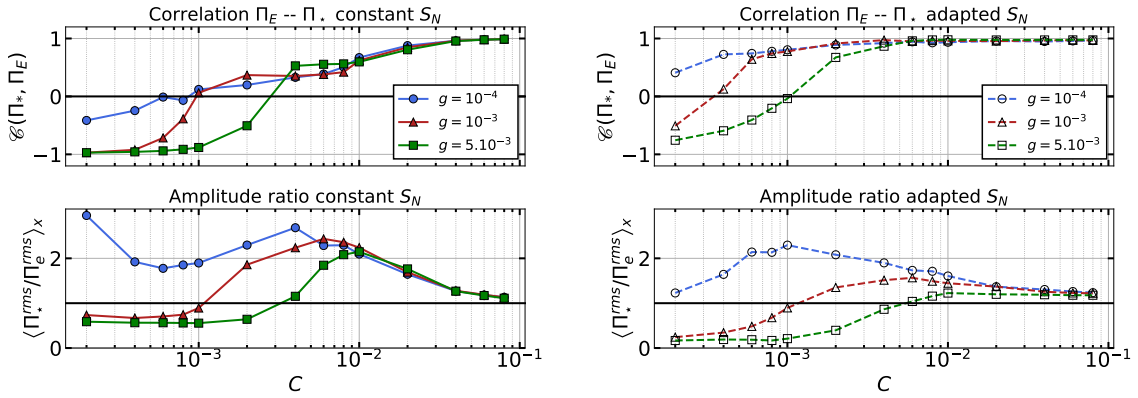

(a) (b)

Figure 4.12 – (top) Correlation between electric and diamagnetic contributions to the Reynolds stress. (bottom) Amplitude ratio $\langle \Pi_\star^{rms} / \Pi_E^{rms} \rangle_x$. (left) Simulations with constant source $S_N(0) = 10^{-4}$. (right) Simulations with adapted sources.

Three different behaviours are visible in Figure 4.12. The first at large C, displays the two contributions correlated and in phase, independently of g. The second, at small C, shows the contributions in phase opposition all the more so when g is large. Finally, the third at medium $C \gtrsim g$, indicates that the diamagnetic contribution is dominant for CDW-driven simulations.
The amplitude ratio reaches its maximum at a value that depends on both C and the distance to marginality. It decreases towards 1 at large C. At low C, for cases at medium and large g, the electric contribution is dominant, even more so when the simulation is close to the linear threshold (Figure 4.12b). The resulting behaviour of Π_{tot} as a function of C can be summarized as follows:

- Small C: $\Pi_E > \Pi_\star$, contributions in phase-opposition.
- Medium C: $\Pi_\star > \Pi_E$, contributions weakly correlated.
- Large C: $\Pi_E \sim \Pi_\star$, contributions in phase.

The cases at small C and large g display a large total Reynolds stress even though the contributions are in phase-opposition because Π_E is largely dominant.

The behaviour of Π_{tot} is consistent with the turbulence regimes elucidated in Section 4.2.3. On the one hand, getting closer to the adiabatic regime at very large C leads to $N_k \sim \phi_k$, leading to in-phase and roughly equal Reynolds stress contributions. On the other hand, at low C interchange turbulence is characterized by electric potential fluctuations being greater than density fluctuations. This directly impacts the resulting tensors with $|\Pi_E| > |\Pi_\star|$.
The anti-correlation between the electric and diamagnetic components of the Reynolds stress at low C depends on the turbulence frequency. Consider the simpler case of the density equation 3.12 at low C with no compressibility, source or diffusion:

$$\partial_t N + \{\phi, N\} = 0$$

The density equation reduces to the advection of the density by the electric drift, meaning that the density now behaves as a passive scalar. Then, the Fourier transform on the fluctuations reads,

$$\hat{N}_{k\omega} = \frac{\omega_{\star e}}{\omega}\hat{\phi}_{k\omega} \tag{4.5}$$

In the absence of compressibility terms, whenever C is negligible, the density and electric potential are always correlated and either in phase or in phase-opposition depending on the sign of the frequency. In Section 4.2.2, we have seen that high C cases were characterized by a positive $\omega_{\star e}/\omega$ while interchange cases were characterized by a low or negative $\omega_{\star e}/\omega$. The above calculation, implies – at least in this simplified situation – that a negative frequency leads to the N_k and ϕ_k being in phase-opposition which then leads to the phase-opposition of Π_E and $\Pi_\star$. From the present result, we deduce that including compressibility does not significantly change this behaviour. Note that in ref. [95] using the gyrokinetic code Gysela for ITG turbulence, the diamagnetic contribution is found roughly two times larger than the electric contribution with adiabatic electrons. Also, both contributions are found in phase. The dependency on the type of turbulence (ITG, TEM, interchange, CDW etc.) of both the respective weight of the two components of the Reynolds stress – Π_E and $\Pi_\star$ – and of their relative phase is still a matter of debate and active research.

One can gain some insight regarding the correlation between Π_E and $\Pi_\star$ analytically. Bearing in mind that fluctuations can be decomposed into amplitude and phase, $\phi_k = |\phi_k| e^{i\varphi_k^\phi}$, the electric component of the Reynolds stress can be recast as:

$$\Pi_E = -2k_y |\phi_k|^2 \partial_x \varphi_k^\phi \tag{4.6}$$

The diamagnetic component can be decomposed in the same way. Considering the conjugate of density fluctuations as $N_k^* = |N_k| e^{-i\varphi_k^N}$, the tensor reads,

$$\Pi_\star = -2k_y \tau |N_k||\phi_k| \left[\partial_x \varphi_k^\phi \cos\Delta\varphi_k + \frac{\partial_x|\phi_k|}{|\phi_k|}\sin\Delta\varphi_k\right] \tag{4.7}$$

With $\Delta\varphi_k = \varphi_k^\phi - \varphi_k^N$ the cross-phase between density and electric potential fluctuations (cf. Equation 3.76). The first term on the right hand side is proportional to the electrostatic component Π_E of the Reynolds stress while the second relates to the amplitude of the electric potential fluctuations and the turbulent flux of particles. The diamagnetic tensor then reads as follows,

$$\Pi_\star = \tau \frac{|N_k|}{|\phi_k|} \cos\Delta\varphi_k \Pi_E + \tau \partial_x(\log|\phi_k|)\Gamma_{turb} \tag{4.8}$$

The degree of correlation between the two components of the total Reynolds stress ultimately depends on the relative weight of the second term with respect to the first. If it is negligible, then the two tensors are well correlated. In this situation, $\cos\Delta\varphi_k$ then determines the sign of the phase coupling, i.e. whether $\Pi_\star$ and Π_E are in or out of phase.
The real and imaginary parts of $\tau N_k/\phi_k$ which correspond respectively to $\cos\Delta\varphi_k|\phi_k|/|N_k|$ and $\sin\Delta\varphi_k|\phi_k|/|N_k|$, are shown in Figure 4.13 for the constant source case. The linear estimate of these quantities obtained by considering no flows or density profile curvature is shown in dotted lines.

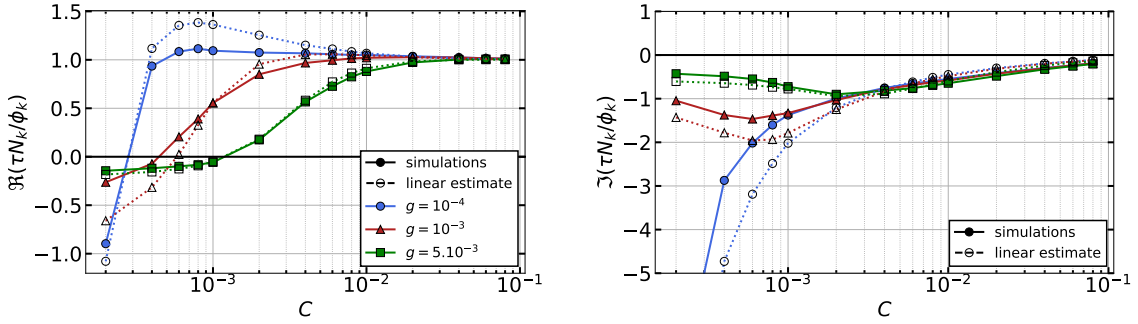

(a) (b)

Figure 4.13 – Real (a) and imaginary (b) part of ratio $\tau N_k/\phi_k$ for three scans as a function of C. Simulations performed with a fixed source $S_N(0) = 10^{-4}$.

Once more, the linear analysis estimate is close to the nonlinear fluctuation ratio even though the analysis is performed without including flow or shear. Consistently with Equation 4.7, the real part of the fluctuation ratio is negative at low C, indicating the two tensors in phase opposition. It becomes positive when C increases and roughly equals unity for large C values in agreement with $\Pi_E \sim \Pi_\star$. Similarly, Figure 4.13b displays a low value of $\Im(\tau N_k/\phi_k)$ at both low and large C leading to a good correlation between the two contributions. The case $(C,g) = (2\times 10^{-4}, 10^{-4})$ stands out for its very low level at $\Im(\tau N_k\phi_k) \approx -8$. This case is peculiar: as previously mentioned it yields very small levels of turbulence and the poloidal wavenumber leading to the maximum wavenumber is shifted ($k_y(\gamma_{max}) \approx 0.15$ instead of $k_y = 0.3$). It is possible that this case is beyond the limit of the model validity.

From the linear analysis in the general $2d$ case, we identified a small region at large g where it is possible to have a positive frequency (electron direction) even though the turbulence is interchange-driven. In practice, this case did not occur in our simulations. This region of the parameter space would lead to the correlation of the two contributions to the Reynolds stress

even in the interchange regime. This phenomena can also occur in ITG-driven turbulence, where a small growth rate can exist such that the phase velocity is in the electron direction [53].
One can also remark that the results bear some similarities with recent work of P. Ivanov [190]. In the developed 'ITG' model, $C = 0$ and the compressibility terms are neglected such that the temperature behaves as a passive scalar. In turn, Π_E and $\Pi_\star$ can either be in phase or in phase-opposition (cf. Equation 4.5). In [190], $\Re(T_k/\phi_k) < 0$ is observed for all unstable modes, consistently with Tokam1D at low C. The sudden transition from phase opposition to in-phase observed in [190], is understandable in this framework.

In this section some characteristics of the total Reynolds stress Π_{tot} have been unraveled. It has been shown that it ultimately depends on the turbulence regime through the correlation and relative amplitude of its two contributions: electric and diamagnetic. Let us summarize the lessons learned on the synergy and competition between the electric and diamagnetic components of the Reynolds stress.

1. $\Pi_{tot} = \Pi_E + \Pi_\star$, is important at both large g and C. The first case yields more intense turbulence.

2. Π_E and $\Pi_\star$ anti-correlate at low C and correlate at large C. Π_E and $\Pi_\star$ are in phase opposition at low C (interchange dominated) whereas they are in phase at large C. This behaviour is directly linked to the density and electric potential fluctuations that start to align in phase as C increases.

3. $\Pi_\star$ dominates for a large part of the parameter space: especially when the interchange drive is low.

4.3.3 Distance to linear and nonlinear threshold

Here, the objective is to compare two simulations that share the same flows to turbulence energy partition but have different control parameters and hence different linear properties. The first, standing at large $C = 2 \times 10^{-2}$ and small $g = 10^{-4}$, is dominated by drift waves. The second, at large $g = 5 \times 10^{-3}$ small $C = 4 \times 10^{-4}$, is driven by interchange instability. Their relative energy partition are shown in Figure 4.10: both have around 35 % of their free energy stored in the flows. They differ in their radial structure: the latter is highly structured with very stable flows. The former is an intermediate case with meandering staircases where merging and splitting events occur.

To vary the distance to threshold, the source is slowly lowered ensuring that the simulation reaches a steady state at each step. When reducing the source, the simulation comes closer to its nonlinear threshold, until turbulence is lost. So as to monitor the amount of 'turbulence', the ratio between the turbulent and diffusive fluxes is computed together with the flow-turbulence energy partition. The result is shown in Figure 4.14, as a function of the distance to the linear threshold Δ_{lin} defined as:

$$\Delta_{lin} = \left| \frac{\partial_x N_{eq} - \partial_x N_{eq}^{crit}}{\partial_x N_{eq}^{crit}} \right| \tag{4.9}$$

The horizontal errorbars account for the corrugation of the equilibrium density gradient, the vertical errorbars indicate the standard deviation for each dataset.

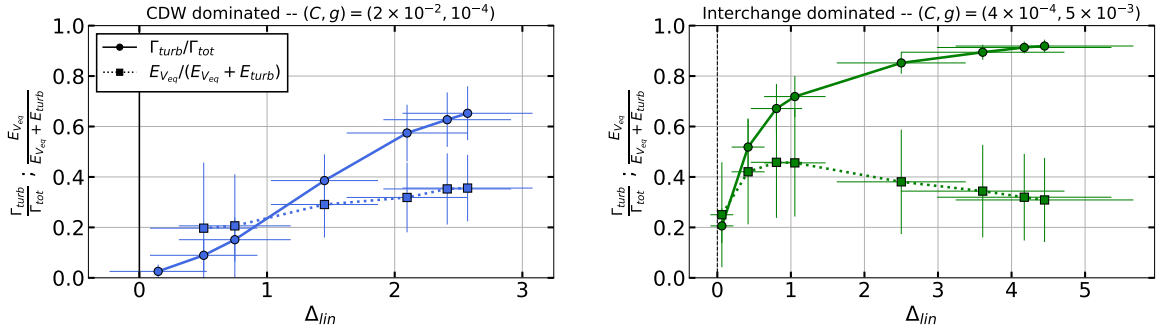

(a) (b)

Figure 4.14 – Relative turbulent flux $\Gamma_{turb}/\Gamma_{tot}$, energy partition $E_{V_{eq}}/(E_{V_{eq}} + E_{turb})$ and distance to linear threshold as a function of the source S_n. (a) For a case without staircases, $g = 10^{-4}$, $C = 2.10^{-2}$. (b) For a case strongly structured, $g = 5.10^{-3}$, $C = 4.10^{-4}$.

As the simulations get closer to the linear threshold, the turbulence intensity decreases and so does $\Gamma_{turb}/\Gamma_{diff}$: turbulence accounts for a lower part of the total transport. There is a difference in stiffness for drift wave and interchange turbulence, the latter leading to a much larger turbulent flux of particles just above its threshold. In both figures, the nonlinear threshold is very close to the linear critical gradient. No significant upshift is found [191, 190]. However, the simulations being flux-driven it is very difficult to define properly the gradient and the threshold [192]. Since the profile can be corrugated, larger gradients can occur locally and produce turbulence even though the averaged profile is below the linear threshold.

Interestingly, the case at large g in Figure 4.14b presents an increased flow to turbulence energy ratio as the threshold is approached. That is in agreement with Figure 4.10: in interchange turbulence the flows are better at keeping the energy close to the threshold.

To sum up, in this section the flow generation has been studied as a function of parameters C and g leading to drift wave and interchange turbulence. Conversely to previous results, zonal flows are not found to collapse at very large density (small C). Instead, the flux-driven system allows the density gradient to adapt to the source leading to a more gradual transition from flow dominated (large C) to turbulence dominated regimes (small C). Additionally, another flow dominated regime has been found for large values of the curvature parameter g. The two regimes have been further analysed in terms of Reynolds stress. The role of the diamagnetic contribution has been shown crucial and even dominant in the drift wave regime. Also, the correlation between the electric and diamagnetic contribution appears more clearly, in part thanks to the linear analysis. Large C regimes lead to a correlation of the two tensors and thus to very large values of Π_{tot}. In the interchange dominated regime (small C large g), the two contributions are in phase opposition but the electric contribution is highly dominant. As a consequence, the total Reynolds stress stays at a high level. Finally, the distance to linear threshold has been shown to matter. In particular in interchange dominated turbulence: when getting closer to the threshold, the flow to turbulence energy ratio increases. The interchange also appears to be more stiff: a

slight departure from the critical gradient leads to large amount of turbulent flux.

Now that regimes leading to important zonal flows have been elucidated, some questions remain. In particular, the conditions leading to their radial structure is still an open question. In the following section, we study the radial structure and staircase formation in the parameter space of C and g.

4.4 Radial structure & staircase formation

Zonal flows are generated nonlinearly by the two components of the Reynolds stress [91]. These sheared flows then regulate turbulence and the underlying transport. The determining factor is not only the amplitude of the flows, but whether or not they are organized into well defined sheared layers [106, 127]. A strong shear is expected to tilt and elongate turbulent structures, leading to their decorrelation, provided that the shear persists longer than the lifetime of the turbulent eddies [19].

In Figure 4.15 are presented four different velocity patterns as a function of time and radial coordinate for different values of C and g. Each case is taken when profiles have reached steady state. The two top cases are computed for simulations with a fixed source. The bottom cases (c) and (d) have a 'fixed' distance to marginality and therefore an adapted source. Remember that the radial electric field presented here oscillates around zero. This is a result of neglecting radial force balance equilibrium that would otherwise add a contribution due to the ion pressure gradient. Adding this for a negative density gradient would lead to a globally negative $\langle E_r \rangle$ such as observed in experiments.
In all simulations, ZFs are active and prove crucial to mitigate turbulence. When the flows are artificially switched off by removing the Reynolds stress drive ($\Pi_{RS} = 0$ in Equation 3.33), a large, system-size radial mode develops. In those cases, the system enters a quasi-periodic regime where a large density gradient builds up and relaxes through a strong transport event. An example of this dynamics is presented in Section C.1. When flows are present, they can be radially structured and stable, as in Figure 4.15b and Figure 4.15d, or intermittent as in Figure 4.15c. For the other cases, such as Figure 4.15a, the system exhibits an intermediate level of structuring characterized by meandering, splitting and merging events. An example of splitting appears in case (a) at $x = 175$ with a fork-like pattern. Merging also occurs on case (a) at $x = 50$.
The dynamics depends on both the adiabatic and the curvature parameters. At low C and g, the system develops smooth structures that evolve slowly. At large C or g, the dynamics of turbulence and flows get faster. In Figure 4.15c, diagonal stripes are visible. They are associated to avalanche-like ballistic transport events of particles (cf. Section 4.5.1). It was reported that staircases can act as micro-barriers for these avalanches, efficiently limiting their radial extension [127]. In general, the flows can either stop the avalanches or, if the avalanches are strong enough, they can cross the shear layer, perturbing it in the process. In the observed cases, when the flows are radially structured, they always manage to recover their radial structure after an avalanche. In some cases, avalanches may even reinforce the staircase structures, see Section 4.5.2.
Importantly, it is found that the radial size of the zonal flow is an emergent property independent of the box size L_x. For simulations performed at very low $L_x \approx 10$, a single zonal flow can fill

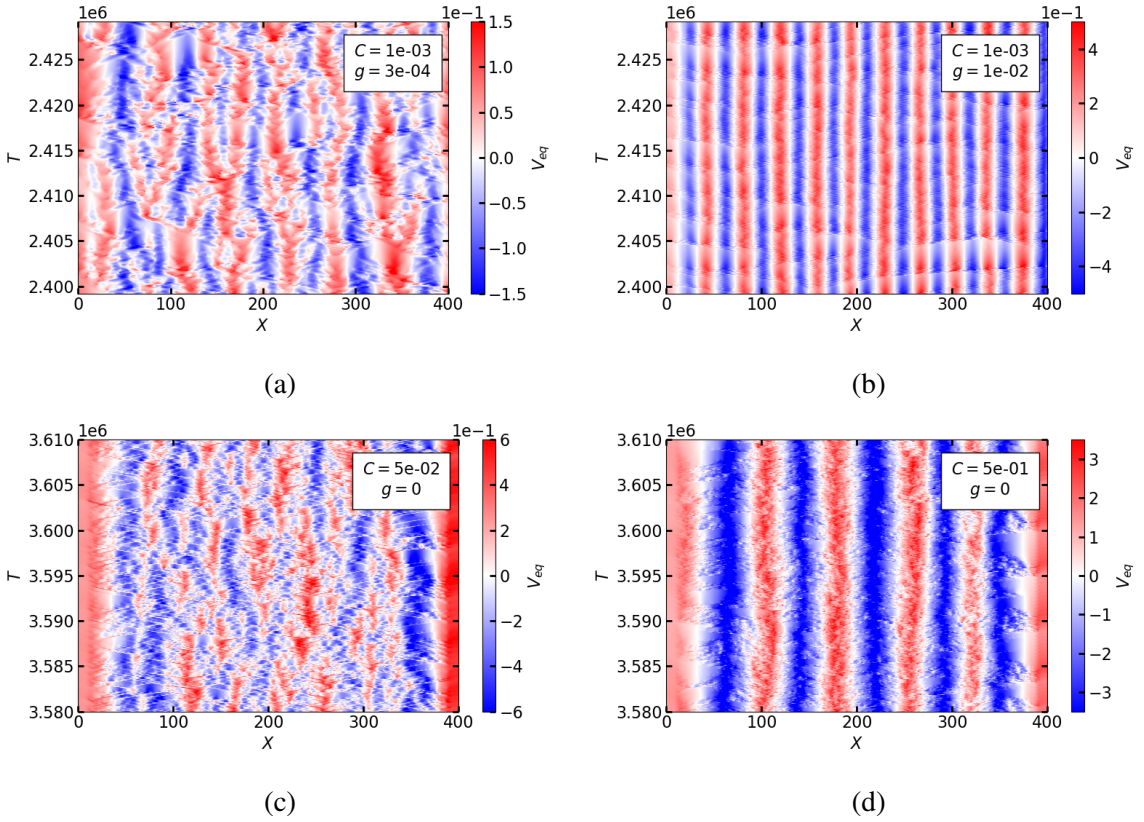

Figure 4.15 – Examples of equilibrium (zonal) velocity $V_{eq} = -\langle E_r \rangle$ at steady state. (a) $(C,g) = (10^{-3}, 3\times10^{-4})$. (b) $(C,g) = (10^{-3}, 10^{-2})$. (c) $(C,g) = (5\times10^{-2}, 0)$. (d) $(C,g) = (5\times10^{-1}, 0)$. Cases (a) and (b) are computed with a fixed source $S_N(0) = 10^{-4}$. (c) and (d) are computed with an adapted source, respectively $S_N(0) = 1.1\times10^{-4}$ and $S_N(0) = 4.35\times10^{-4}$.

up all the simulation domain.

Why some cases yield structured flows and some others do not is still an open question. Some trends however emerge. Very large values of C lead to a structured flow pattern, in particular when the density profile is close to marginality: that is the case of Figure 4.15d displaying wide structures. Large values of g also lead to a structured flow pattern with narrower structures. The stabilization and localization of flow patterns at large g is a salient feature in Tokam1D simulations. The next section is dedicated to it.
Additionally, the role of two quantities should be noticed. First, the distance to marginality: close to the linear threshold, some degree of radial structuring is observed in most of the parameter space. This is developed in the next section. That should be nuanced given that the most structured flows are obtained for cases such as Figure 4.15b, far from threshold. The distance to marginality has already been deemed important for staircase formation [106, 107]. Second, the turbulence and flow damping: a greater stability in time of the flow pattern is obtained when the dissipation coefficients on fluctuations (D_1, ν_1) are large. An example of a simulation with different values for (D_0, ν_0) and (D_1, ν_1) is detailed in Section C.2. Finally, the interaction with the avalanches is often sometimes put forward as a possible mechanism for staircase generation

[127]. It will be shown in Section 4.5.2, that passing avalanches can actually reactivate the standing ZFs structures by transferring them energy.

4.4.1 Zonal flows structure into staircases in interchange dominated plasmas

In order to study the spatial structure of the velocity, one can use their energy spectral density, $S_V(k_x)$, computed from the radial Fourier transform of the equilibrium velocity. As presented in Figure 4.16, it provides a good proxy to identify the flows radial structure and size. The radial Fourier transform $\hat{V}_{eq}(k_x,t)$ is computed for $N = 100$ independent time samples that are then averaged: $S_V(k_x) = \sum|\hat{V}_{eq}|^2/N$. The spectra are shown in Figure 4.16 for different values of g.

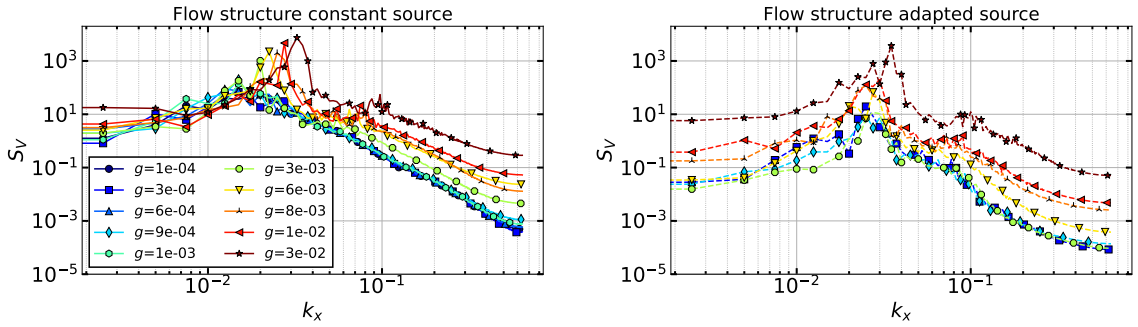

(a) (b)

Figure 4.16 – Energy spectral density of the equilibrium velocity as a function of k_x for different values of interchange parameter g. Each spectrum is the average of 100 independent spectra. (a) Simulations using constant source $S_N(0) = 10^{-4}$. (b) Simulations using adapted sources.

Two groups of simulations can be distinguished in Figure 4.16 similarly to already shown in Figure 4.5. The group at low g, dominated by CDW instability and the group at large g dominated by interchange instability.
The first one, from $g = 10^{-4}$ to 10^{-3} exhibits a broad extremum around $k_x \approx 0.015$. There is little contrast among the different curves: their amplitude and decay are qualitatively similar. The second group, for $g > 10^{-3}$, exhibits a larger spectral density than the first one. In this group, the spectrum amplitude now varies with g and gets larger at both low and large k_x. For fixed source, Figure 4.16a, a peak appears and the maximum slightly shifts from $k_x \approx 0.02$ to $k_x \approx 0.032$ as g increases. The simulations at adapted source always display a peak, although slightly less prominent.
The first group corresponds to unstructured flows. The peak is relatively low and broad, meaning that the size of the velocity structures is roughly of the order of 60 ρ_s. The second group yields a higher spectral density, indicating that the amplitude of the flows is larger as g increases. Moreover, the appearance of a peak in the spectrum indicates a clear structuring of the velocity pattern for $g > 10^{-3}$. Structures have a size between 50 and 30 ρ_s and are slightly thinner at large g. However the change in width is small, with only about 70 % change on k_x when g is increased by a factor 30. Simulations closer to marginality (adapted source), always display

some degree of radial structuring. In most cases the flows are very stable at the exception of very small g where some merging and splitting events occur.

Simulations presenting a radial structure in ZFs lead to staircases in the form of steps in the density profile. This is illustrated in Figure 4.17 for case $(C,g) = (10^{-3}, 10^{-2})$. The equilibrium density and velocity are plotted as a function of X for $t = 1.985 \times 10^6$. The effective diffusivity $D_{eff} = -\Gamma_{turb}/\partial_x N_{eq}$ is shown Figure 4.17b. To remove small scale effects, both profiles are coarse grained on $\omega_{cs}t = 3 \times 10^4$.

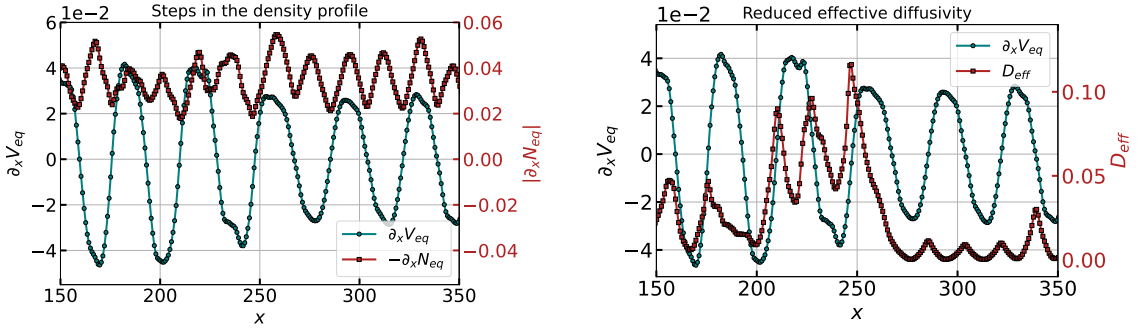

(a) (b)

Figure 4.17 – Equilibrium velocity shear $\partial_x V_{eq}$ and equilibrium density gradient $|\partial_x N_{eq}$. (b) Equilibrium velocity shear and effective diffusivity $D_{eff} = -\Gamma_{turb}/\partial_x N_{eq}$. Both are averaged on $\omega_{cs}\Delta t = 3 \times 10^4$ around time $\omega_{cs}t = 1.985 \times 10^6$ and taken from the case $(C,g) = (10^{-3}, 10^{-2})$ with constant source.

The velocity shear oscillates around zero in an almost symmetric pattern. The density gradient, in red (squares), is always negative, as a result of the particle source located at $x = 0$. When the velocity pattern is stable in time, the density profile is modulated by the shear so that large (in absolute value) density gradients are located at velocity shear extrema, independently of the sign of the shear. This corresponds to 'steps' in the density profile commonly described in staircase regimes [106, 107]. Also, the local effective diffusivity D_{eff} exhibits local minima where the flow shear is maximum, although in a less systematic way. Seemingly, micro-barriers of transport are generated in location of large shear.
From these results only, we expect that the micro-barriers observed in the presence of staircases lead to a better overall confinement. However, it will appear in Section 4.5 that properly renormalizing simulations to unveil the effect of flows on the global confinement is a difficult task and one should refrain from making hasty conclusions.

It is interesting to note that in reduced models, such as Tokam1D or Hasegawa-Wakatani, the generated zonal flows have a sinusoidal pattern see for example refs.[124, 193, 194, 185]. Therefore, the distance between the staircase steps is similar to the size of the velocity structures. In more complex models, including flux-driven $5D$ gyrokinetic codes such as Gysela, the distance between staircase steps is larger than the steps themselves and closer to the avalanche size ≈ 40 ρ_s [106]. A possible explanation is the lack of q-profile and mode localization effects such as discussed in Section 3.6. Including this, one could expect the turbulence, when dominated by instabilities favouring $k_{||} \approx 0$, to localize on rational surfaces and then to generate zonal flow

structures accordingly. This has been hinted at experimentally on the TJ-II stellarator [136]. Finally, one can mention the interesting model – based on the wave kinetic equation accounting for the dynamics of drift waves coupled to an equation governing the zonal flow dynamics – proposed by Garbet et al.[195] where different shapes of staircase patterns can be obtained. There, it is found that staircases result *"from the interaction between propagating wave packets (understood as avalanches) and waves that are trapped in zonal flow velocity wells"*. The detailed characteristics of the staircases (amplitude, shape and periodicity) are determined by those of the background fluctuations, notably their spectra and growth rates. In particular, structured zonal flows appear to exhibit non-sinusoidal radial profiles, peaked at their maxima (located at the O-points of the islands that trap the drift waves in their phase space), when the growth rate of the drift waves is maximum at vanishing radial wavenumber.

To sum up, zonal flows are found to be radially structured in near-marginal, interchange driven plasmas. For all studied cases, a stable and radially localized flow shear always leads to staircase steps in the density profile. The sign of the zonal shear does not matter in this and the density steps follow the flow sinusoidal pattern. Usually, although not systematically, this is associated with the formation of a micro-barrier of transport in the form of a reduced effective diffusivity.

4.4.2 Staircase nucleation: critical role of the cross-phase

Staircases are robust structures. We have found that they always manage to recover after a perturbation. Here, we look at the nucleation of a staircase when restarting a steady-state simulation after having smoothed out the corrugation in N_{eq} and V_{eq} and damped out the fluctuations N_k, Ω_k. The system then has no memory of the past structures. The nucleation of the flow pattern is shown in Figure 4.18 for simulation $(C,g) = (5\times10^{-4},0)$. The steady-state turbulence case continues until $t = 3\times10^4$ where the structures are removed. The black rectangle indicates the time window of the nucleation process which is studied in the following.

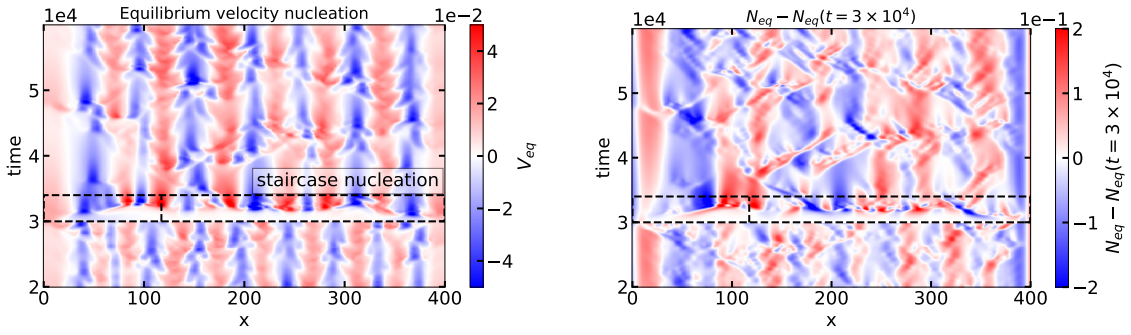

(a) (b)

Figure 4.18 – (a) Equilibrium velocity after being smoothed out at $t = 3\times10^4$. The nucleation part is indicated with dotted lines. (b) Evolution of the equilibrium density as compared to its value at the restart: $N_{eq} - N_{eq}(t = 3\times10^4)$.

Upon restart, at $t = 3\times10^4$ in Figure 4.18, the equilibrium density gradient is above the linear

threshold. Therefore, instability and flows appear directly on the whole domain after a short growth time. Qualitatively, a similar staircase structure is recovered. However, there is about 7 structures in Figure 4.18, as compared to the initial 9 structures.

Focusing on the nucleation of a particular staircase step located at $x = 123$, indicated with a vertical dashed line on Figure 4.18, the time evolution of the flows and Reynolds stress at this location are shown in Figure 4.19 as a function of time.

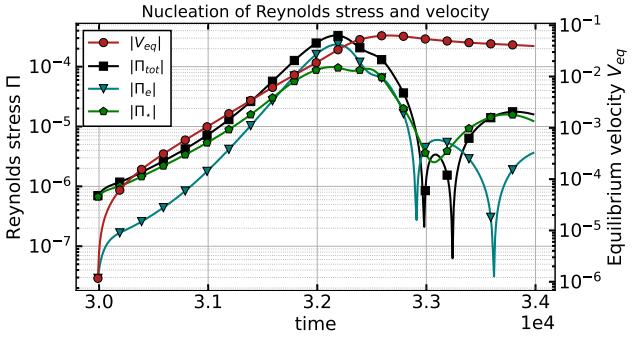

Figure 4.19 – Energy of the equilibrium flow, total Reynolds stress and its components as a function of time for $x = 123$.

An exponential growth of both electric and diamagnetic components of the Reynolds stress is observed. The flow results from a secondary instability [89] and is governed by the Reynolds stress components. For this simulation, both components of the Reynolds stress are important for the generation of the flows, with the diamagnetic one being slightly larger at initial times.

The dynamics of the phase is essential in the generation of both components. Bearing in mind that fluctuations can be decomposed into amplitude and phase, $\phi_k = |\phi_k| e^{i\varphi_k^\phi}$, the electric component of the Reynolds stress can be recast as:

$$\Pi_E = \langle \widetilde{v}_{Ex} \widetilde{v}_{Ey} \rangle = -2k_y |\phi_k|^2 \partial_x \varphi_k^\phi \tag{4.10}$$

The divergence of the Reynolds stress, $\partial_x \Pi_E$ is understood as a Reynolds force. Using the above decomposition one looks at the logarithmic derivative of Π_E,

$$\frac{\partial_x \Pi_E}{\Pi_E} = -2k_y \frac{2\partial_x |\phi_k|}{|\phi_k|} + \frac{\partial_x^2 \varphi_k^\phi}{\partial_x \varphi_k^\phi} \tag{4.11}$$

Π_E is displayed in Figure 4.20a together with its decomposition. The Reynolds force is detailed in Figure 4.20b.
In Figure 4.20a, it appears that both the amplitude and the phase are important for the growth of Π_E. When computing the Reynolds force, Figure 4.20b, the phase itself dominates the dynamics. The key role of the phase was already pointed out in [196] and in [95]. It shows that it is essential for a reduced model to self-consistently compute the amplitude and phase as they both play a role in the generation of flows.

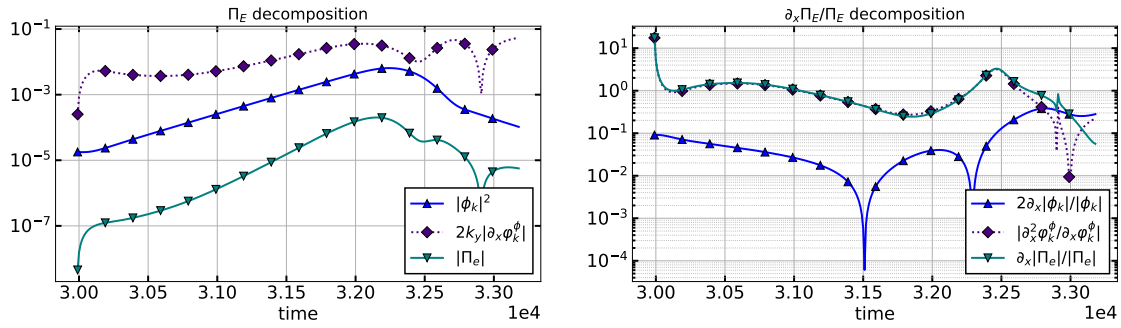

(a) (b)

Figure 4.20 – Electric Reynolds stress decomposition as a function of time for $x = 123$. (a) Reynolds stress. (b) Logarithmic derivative of the Reynolds stress, relating to the Reynolds force. The phase jumps have been removed by "unwrapping" the phase in the post-processing.

4.4.3 Importance of the flux-driven regime for staircase dynamics

The energy transfer between equilibrium density and flows associated with profile relaxation appears to be a crucial mechanism for the staircase formation and sustainment. In this section, to assess the importance of these mechanisms, we artificially prevent any profile relaxation by fixing the density gradient. We perform a restart of a steady-state flux-driven (FD) simulation in a gradient-driven (GD) framework. It should be emphasized that it is a 'hard' GD framework, meaning that the equilibrium profile is completely frozen in time and not just its two end values. The second option would allow for corrugations while maintaining a constant 'mean' profile.

We choose the case $(C, g) = (5 \times 10^{-4}, 0)$ and continue the simulation while fixing the gradient. The equilibrium density profile at restart is smoothed so that corrugations are mainly absent. In Figure 4.21, the equilibrium velocity V_{eq} is shown as a function of space and time. The smoothed density profile and its radial derivative are displayed on the right side of Figure 4.21. The first half of the simulation is the steady state FD simulation. At $t = 3 \times 10^4$, N_{eq} is smoothed using a Savitzky-Golay filter of order 3 on a 301 points window size. The second half of the simulation corresponds to the GD regime using the smoothed density profile.
Figure 4.21 shows that the flows exhibit roughly the same amplitude in both FD and GD settings. However, their radial structure is very different. The chosen case is radially structured in the steady-state FD case, while the GD regime is characterized by the absence of layering. The flow layers are still present just after the restart but this configuration cannot be sustained in the GD regime. These observations suggest that the system – at least in the regimes explored – must be able to store energy in the density (pressure) profile in addition to the flows in order to develop well-localized flow layers. In other words, the staircase structure requires two critical ingredients: localized shear flow layers in association with large density (pressure) gradients, which appear to reinforce each other. The loss of one of these ingredients seems to prevent the appearance of the whole structure. In the GD regime, the density gradient is frozen in time so that this mechanism is absent. This symbiotic relationship between flow layers and pressure corrugations appears to be instrumental in the staircase dynamics.

The electrostatic potential fluctuations, plotted in Figure 4.22a, exhibit a slightly larger mag-

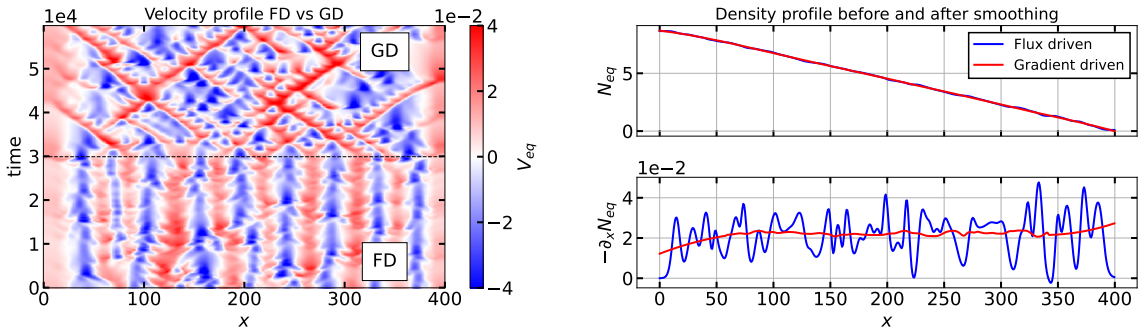

(a) (b)

Figure 4.21 – (a) Equilibrium velocity from gradient driven restart of steady-state simulation at $C = 5 \times 10^{-4}$: switch from FD to GD is made at $t = 3 \times 10^4$. (b) Density gradient and its radial derivative before and after the gradient driven restart. The density profile before the restart is taken at $t = 2.9 \times 10^4$.

nitude in the GD regime as compared to the FD regime. Also, their dynamics looks similar to the one of the equilibrium flow in the GD regime, from $t = 3.10^4$ onwards. In particular, the radial distance of avalanche propagation is much larger in the GD regime, sometimes reaching almost the system size.

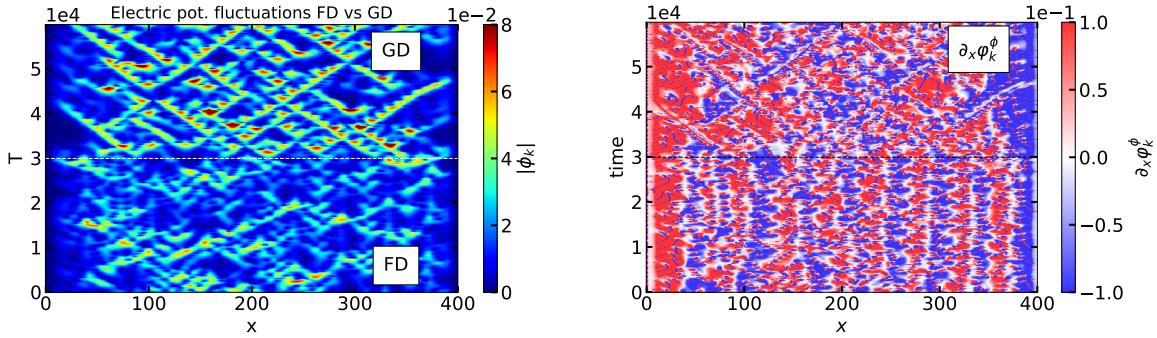

(a) (b)

Figure 4.22 – (a) Electric potential fluctuations for the gradient driven restart of the steady-state simulation $C = 8\ 10^{-4}$. (b) Radial derivative of electric potential fluctuations phase.

The presence of avalanches itself may appear surprising. Indeed, avalanches are often understood, by analogy with sandpiles, as resulting from a domino-like effect [72]: a localized strong flux tends to flatten the profile locally and steepens it on both sides due to conservation laws. The strong gradients on both sides then lead to strong local fluxes, further leading to local flattening. The process can repeat over long distances, resulting in the formation of voids and bumps that propagate radially up and down hill, respectively. Local profile relaxation then appears to be key to the whole dynamics. In GD simulations where the density gradient is frozen in time, this mechanism is absent and cannot therefore explain the existence of avalanches on V_{eq}. Interestingly, it appears that the magnitude of the electric potential fluctuations $|\phi_k|$ and its phase gradient $\partial_x \varphi_k^\phi$ exhibit an avalanche dynamics, as can be seen in Figure 4.22b. They both

govern the electric component of the Reynolds stress, Eq. 4.10. It is so far unclear whether one or the other – or both – is the main drive for the dynamics of V_{eq}, the other quantity being slaved to it via the back-reaction of the flow shear. Note that both terms, the phase gradient and the fluctuation magnitude, are contributors to the turbulent energy. Therefore, discriminating one scenario with respect to the other is not obvious solely from an energetics standpoint. This remains an open issue for future works.

One could argue that flow structure formation also occurs in some GD models. That is true for 'soft' GD where the pressure profile can corrugate. However, as it already appeared in the previous sections, the full FD description is crucial for the system's energy partition. Indeed, the system adapts its density gradient when the values of C and g are scanned.

4.5 Impact of turbulence & flows on transport and confinement

Ultimately, the generation of zonal flows is crucial for a fusion machine because they mitigate the turbulent transport [103]. Two mechanisms are at play: being a sink of energy for the turbulence [21] and inducing a shearing [19, 91]. In particular, the existence of radially localized time stable shear layers of flows is expected to lead to a better confinement [106]. However, the transport itself is also complex and self-organizes into various structures. For Tokam1D in the confined region, we know from the linear analysis that the growth rate is maximum for the lowest values of k_x accessible by the system. As a result, turbulence tends to develop into radially-extended vortices, often called *streamers*, that mix large portions of the plasma [18]. The flow shear is instrumental in breaking those extended structures into smaller cells.
Transport also exhibits complex structures in the form of avalanches: almost ballistic transport events of heat and particles. A transport barrier resulting from a large shear could possibly stop the transport event [197] but the role of micro-barriers in the form of staircases is still debated. In this section, the transport is analysed in the drift wave and interchange regimes. It is shown that the confinement largely depends on the control parameters C and g. Then, the role of avalanches is analysed. They prove to be of importance both as a mean to carry particles and as a quantity that interacts with the dynamical zonal structures. Finally, the influence of staircases on transport is assessed.

First, let us analyse the confinement in a statistical sense by looking at the confinement time of particles (Equation 4.1) and the ratio of turbulent to diffusive fluxes of particles. Both quantities yield a similar information since a better confinement is obtained when the diffusive flux of particles accounts for a larger part of the transport. Actually, the theoretical 'maximum' of confinement achievable is the one with no turbulence, hence $\Gamma_{turb} \approx 0$ and $\partial_x N_{eq} \approx \partial_x N_{eq}^{diff}$. Both τ_p and $\langle \Gamma_{turb}/\Gamma_{diff} \rangle_x$ provide complementary information, as well as simulations performed with constant or adapted sources.
The confinement time τ_p is related to the steady-state density profile and the source. If the latter is constant, τ_p is mostly governed by the distance to the linear threshold [72]. If the source is adapted, then the simulation is renormalized and the ability of the system to depart from marginality, i.e. whether it is stiff or not, plays a key role. The turbulent to diffusive flux ratio and confinement time are displayed in Figure 4.23.

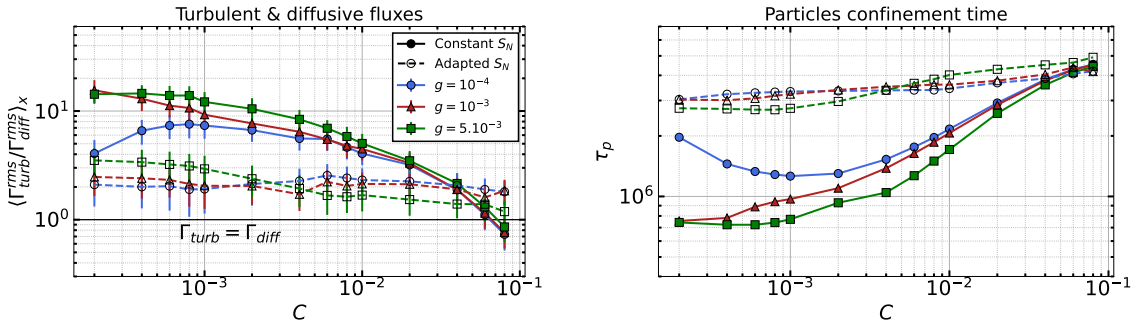

(a) (b)

Figure 4.23 – Confinement properties of the system as a function of C for three values of g. (a) Radial average of the rms turbulent to diffusive flux ratio. (b) Confinement time of the particles τ_p. Simulations with a constant source are shown using full lines, those with an adapted source are displayed with dotted lines.

Three elements are key for the confinement: the linear threshold, the stiffness and the forcing. The forcing is not exactly equal to the source itself, it also depends on the critical gradient. Indeed, the source sets the diffusive gradient (profile in the absence of turbulence). Then, the forcing can be considered as the difference between the critical and the diffusive gradient. If the diffusive is below the critical, no instability arises and the forcing vanishes.[2] Therefore, simulations at constant source have a forcing that varies with the control parameters whereas simulations with an adapted source have a constant forcing. The difference in the confinement time for simulations at constant and adapted source is understood by a difference in forcing, mainly for the cases at low C that have a lower critical equilibrium density gradient. Also, as the distance to threshold is increased, the growth rate increases leading to larger turbulence and transport. It follows that simulations that are more 'forced' or further from threshold exhibit a lower confinement and larger normalized turbulent flux.

In Figure 4.23b, the confinement time increases with C for two main reasons: the critical gradient increases with C (cf. Figure 3.10) and the stiffness reduces with C. The threshold is also larger at small C, small g, leading to an increased confinement.
The same behaviour is recovered on the turbulent flux. It depends on the amplitude and cross-phase of the density and electric potential fluctuations. A large growth rate tends to produce higher fluctuation amplitudes which increases the turbulent flux. At large C, the growth rate (Figure 3.8b) and cross-phase becomes small (Figure 3.9c), such that the turbulent transport is largely reduced $\Gamma_{turb} \sim \Gamma_{diff}$.

In the following sections, we will unveil some of the physical mechanisms behind the behaviour of Figure 4.23 and attempt to look past the linear to delve deeper into the nonlinear behaviour. In the next section, the transition from mixing-like to avalanche-like transport will be explicited. Then, one will show how these avalanches interact with zonal flows. Finally, we

[2]Consider two simulations with different critical density gradients, the first threshold being much lower than the second. If the source used for both simulations is the same, then the first simulation will tend to be more forced. Consequently, if both systems have a similar stiffness, the first may exhibit a larger confinement.

normalize the confinement time to understand whether staircases lead to a better confinement.

4.5.1 Transition to avalanche-like transport at large g

The turbulent transport displays different dynamics when instability parameters are varied. In particular it is shown to transit towards avalanche-like transport when increasing g at fixed C.

Choosing the cases (a) and (b) of Figure 4.15, we plot the turbulent flux of particles as a function of X and T Figure 4.24 with a low $g = 3 \times 10^{-4}$ on the left and a large $g = 10^{-2}$ on the right.

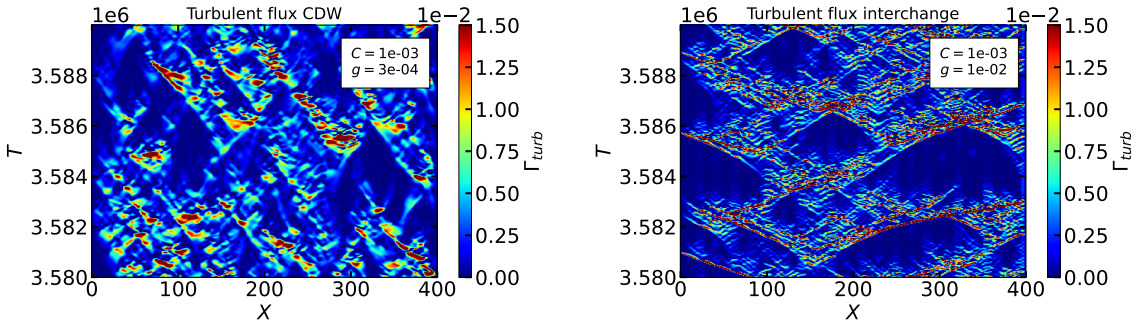

(a) (b)

Figure 4.24 – Examples of turbulent flux of particles $\Gamma_{turb} = -2k_y\Im(N_k\phi_k^*)$ at steady state. (a) $(C,g) = (10^{-3}, 3\times10^{-4})$. (b) $(C,g) = (10^{-3}, 10^{-2})$. Both are computed with a fixed source at $S_N(0) = 10^{-4}$.

At larger g, the turbulent flux of particles displays diagonal stripes across large portions of the simulation domain. Those correspond to ballistic transport events of particles resembling avalanches. Note that as stated in the introduction of the section, the information of the avalanche travels both in and outwards while the flux is always positive, i.e. the transport of particles is always outwards of the domain. Actually, it is possible to check on the density profile whether there is a propagation of voids and bumps by plotting $N_{eq}(x,t) - \langle N_{eq}\rangle_t(x)$, this is done in Figure 4.25 for the case $(C,g) = (10^{-3}, 10^{-2})$.
The diagonal stripes still appear clearly. This time, events travelling to the right hand side are positive perturbations (bumps) while events travelling to the left are negative (voids). The basic mechanism of avalanche propagation presented in Figure 2.11 is recovered.

The avalanche-like pattern presented above occurs in the simulation presenting a highly structured flow (Figure 4.15 (a and b)). In the observed simulations, when the zonal flows are structured, there is always an avalanche-like dominated transport. The avalanches are also visible directly on the flow pattern, as they perturb it when propagating across. more details regarding the interaction with flows are given in the next section.
Note also that the two cases presented Figure 4.24 are at both ends of the g-scan. The intermediate values of g lead to intermediate behaviours with avalanches that propagate on smaller parts of the domain. Avalanches can also be studied statistically by computing the skewness and

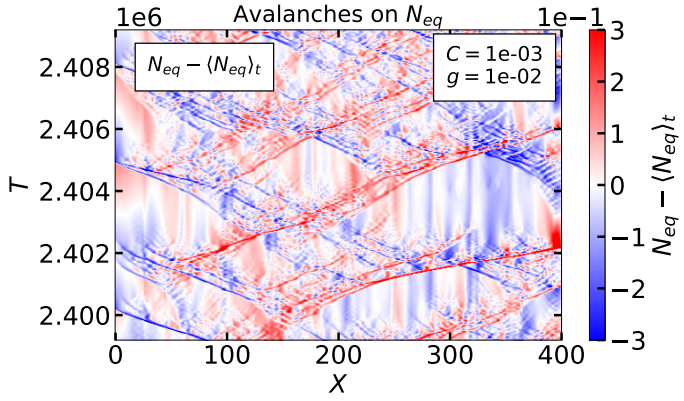

Figure 4.25 – Propagating avalanches on the density profile, case $(C,g) = (10^{-3}, 10^{-2})$ with constant source $S_N(0) = 10^{-4}$.

kurtosis: respectively third and fourth moments of their probability distribution function (pdf):

$$S(X) = E\left[\left(\frac{X-\mu}{\sigma}\right)^3\right] \;\; ; \;\; K(X) = E\left[\left(\frac{X-\mu}{\sigma}\right)^4\right] . \tag{4.12}$$

These functions measure respectively the pdf asymmetry and width (weight of the tails). For a Gaussian statistics, $S = 0$ and $K = 3$. In the present case, avalanches are radially extended and 'rare' events. Therefore, we expect them to lead to important values for skewness and kurtosis. Both pdf quantities are plotted against each other in Figure 4.26 for the g-scans. Simulations with a constant source are indicated in red (left), the ones with adapted sources are in blue (right).

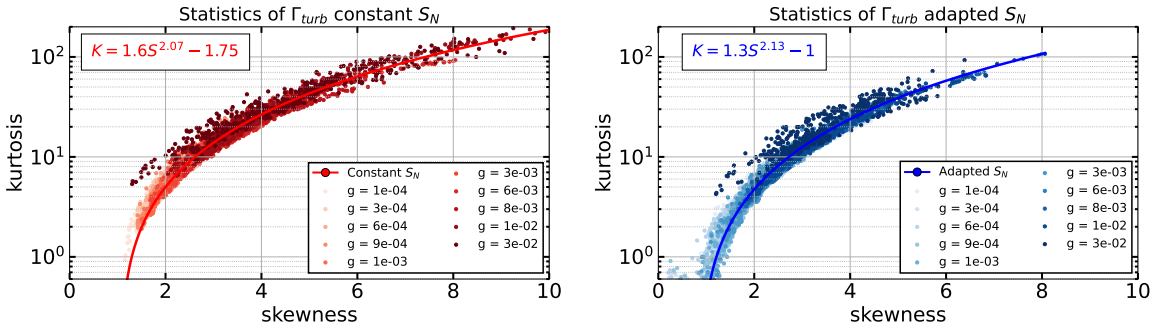

(a) (b)

Figure 4.26 – Probability distribution function of the turbulent flux for simulations at constant (a) and adapted (b) sources as a function of g. All the simulations are computed for $C = 10^{-3}$. Statistics are computed at each radial position.

The kurtosis increases with the skewness in an almost polynomial way. Interestingly, the relation between kurtosis and skewness is similar to the one reported in experiments [198]. Also, both the skewness and the kurtosis are shown to increase with larger values of g, displaying

a more skewed and deviated pdf. Note that this behaviour is not universal, see for example ref.[154]. Overall, the avalanches account for a larger part of the statistics as g is increased and as the system is far from the linear threshold.

4.5.2 Reactivation of zonal flows by passing avalanches

As stated in the previous sections, staircases are observed at large g together with avalanches. When large enough, the avalanches rip through the standing zonal flow structures perturbing them in the process. To get more insight on the interaction between flows and avalanches, we use Figure 4.15 and plot on top of it the 90 % quantile of the turbulent flux presented in Figure 4.24. In other words, we add the largest events of the turbulent flux of particles. The result is shown in Figure 4.27.

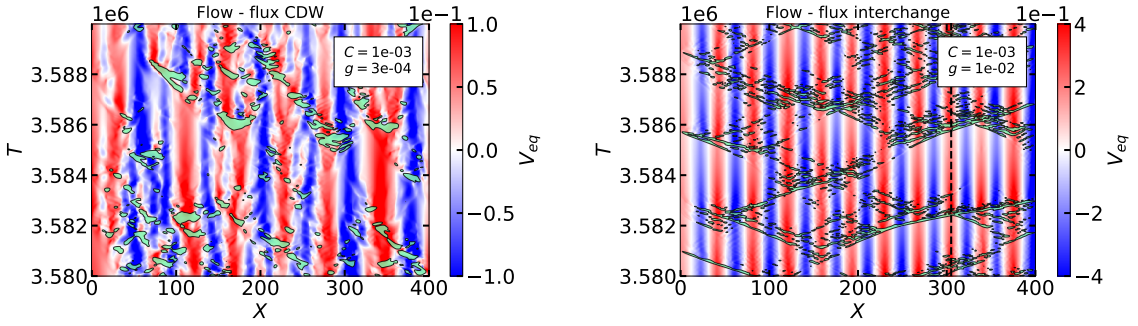

(a) (b)

Figure 4.27 – Example of flows as a function of X and T with super-imposed 90 % quantile of the particle flux. (a) $(C,g) = (10^{-3}, 3\times10^{-4})$. (b) $(C,g) = (10^{-3}, 10^{-2})$. Both with constant source $S_N(0) = 10^{-4}$.

On the left hand side, their size is comparable or smaller to the structures themselves. They are sometimes associated with the modification of the topology of the staircases, including splitting ($X \sim 340$, $T \sim 3.586\times10^6$) and merging ($X \sim 70$, $T \sim 3.585\times10^6$). On the right hand side the events are powerful enough to travel through zonal structures.

More importantly, ZFs interact with passing avalanches. Taking the right hand side case, we plot both the turbulent flux and the equilibrium velocity at position $X = 305$ as a function of time. The result is shown in Figure 4.28.
The established flow decays exponentially due to the imposed collisional friction. Whenever an avalanche passes through the layer, it reactivates the structure by giving it energy. On this example, the flow is maintained solely due to the passing avalanches event. This generation mechanism has been considered in ref.[199] for a Hasegawa-Wakatani model and in ref.[127] for a different model. In the latter contribution, the key element is to consider a delay between the instantaneous and the mean heat flux thus leading to "jams" of heat flux waves.

4.5.3 Do staircases improve confinement?

In this section we normalize both the turbulent flux and the confinement time of particles in order to find whether the radial structure of ZFs, namely staircases, play a role in improving the

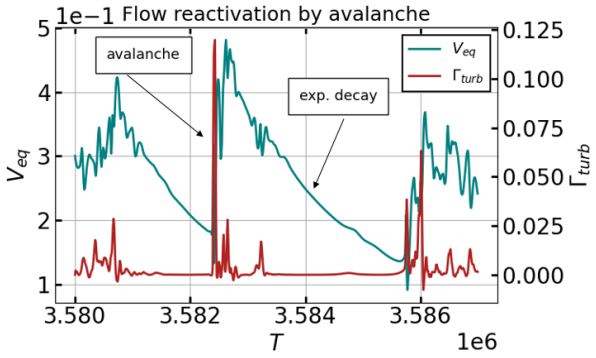

Figure 4.28 – Reactivation of an existing zonal flow structure by passing avalanche. Spatial slice of case $(C,g) = (10^{-3}, 3\times10^{-4})$ with constant source taken at $X = 305$.

global confinement. Since the confinement properties of the system largely rely on its linear properties, cf. Figure 4.23, the issue ultimately involves finding the proper normalizations so as to extract information on the role of nonlinear structures of the flows on confinement.

Normalizing the particle confinement time

The particle confinement time is normalized using a linear estimate so as to remove the role of the linear growth rate and cross-phase. In the framework of the mixing length theory, simulations with a large growth rate lead to a large turbulent transport. The linear cross-phase is also used in the estimate to account for the efficiency of the turbulent transport. The linear estimate then reads,

$$\tau_{ML} = \frac{k_y^2 L_x^2}{-\gamma_k \sin\Delta\varphi_k} \tag{4.13}$$

With L_x the radial size of the simulation, γ_k the growth rate and $\Delta\varphi_k$ the cross-phase between density and electric potential fluctuations. The minus sign comes from the fact that a negative $\sin\Delta\varphi_{lin}$ leads to an outwards turbulent flux Γ_{turb}.
Remember that the linear quantities γ_k and $\sin\Delta\varphi_k$ are computed without taking into account profiles corrugations. Corrugations might be important for simulations that include staircases. If corrugations were considered, it would lead to a larger estimation of γ_k – large gradient zones leading to large growth rate – and would reduce the mixing-length estimate.

In the situation where the growth rate or the cross-phase vanishes, the mixing length estimate for the confinement time diverges as no transport is expected. Instead, we choose $\tau_L = \min(\tau_{ML}, \tau_{diff})$ with $\tau_{diff} = \int N_{eq}^{diff} dx / \int S_N dx$ the maximum confinement achievable in a Tokam1D simulation. The particle confinement time normalized by the linear estimate is shown in Figure 4.29 as a function of C and g. The normalization is performed on cases with an adapted source so that the forcing is the same across the parameter space.
The trend is different from the non-normalized τ_p (Figure 4.23b). Simulations leading to the largest τ_p/τ_L are those at large values of g. The normalized confinement time also increases with C at low and medium g but then reaches a plateau. The normalized confinement time is consistent with the flows energy and radial structure analysed in the rest of the chapter. Flow

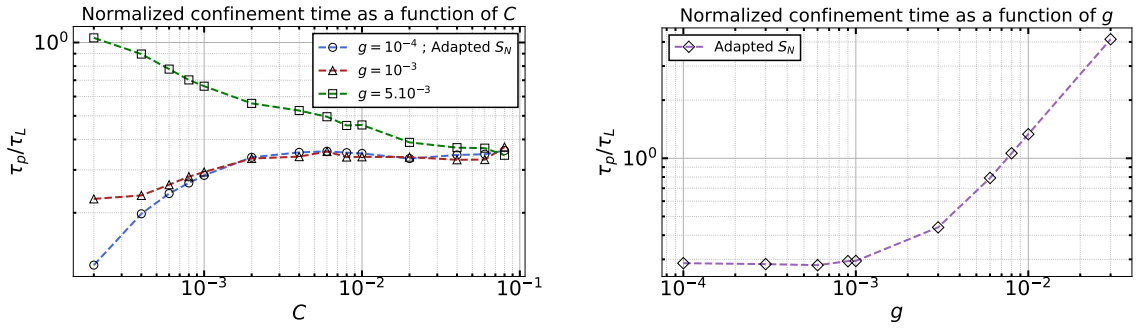

(a) (b)

Figure 4.29 – Normalized particle confinement time τ_p/τ_L. (a) As a function of C. (b) As a function of g for $C = 10^{-3}$. Both for simulations with an adapted source $S_N(0) = 10^{-4}$.

dominated regimes are found at both large C and large g, with the latter favouring radially structured flows. This normalization supports the conclusion that flows, and in particular radially structured flows, lead to a better overall confinement. It should be kept in mind that the values explored for the g parameter are large and hardly reached in experiments (Table 3.3). Therefore, we do not expect quantitative agreement with experiments. However, qualitative trends should be recovered.

We also made an attempt at normalizing the quasi-linear flux of particles in Section C.3. The method consists in estimating the flux of particles with the electric potential fluctuations and the linear relation between density and electric potential fluctuations, Equation 3.75. The electric potential fluctuations are Fourier transformed in both time and space. A turbulence broadening is considered in the form of a Lorentzian when integrating the electric potential fluctuations on the frequencies. However, the method proves unsatisfactory because it largely depends on the choice made for the frequency broadening parameter.

To summarize this section, the confinement time of the particles in Tokam1D depends on three main parameters: the linear threshold, the stiffness and the forcing. Performing simulations at an adapted source allows us to compare the parameter space while forcing the simulation similarly. The confinement is shown to decrease for low values of C and large values of g. This is understandable in a linear framework: low C leads to a larger sinus of the cross-phase, hence a more efficient transport. Large values of g usually imply large growth rates. Additionally, the transport is shown to be dominated by avalanche-like events when g is increased. Although those ballistic transport events are considered detrimental for the confinement, they also reactivate zonal flows by giving them energy while crossing the radial domain. Finally, by normalizing the confinement time, we manage to remove the role of the growth rate and the sine of the cross-phase. By doing so, staircases are observed to improve the confinement.

4.6 Possible experimental signatures of turbulence self-organization

This last section aims at identifying signatures of the turbulent self-organization that would be accessible to experimental identification and characterization. The measurements will be done principally using a two-channel Doppler backscattering (DBS). Its physical and working principle are detailed in the next chapter. The DBS measures the density fluctuations at a specific wavenumber $k_\perp$. When several DBS are used together, one can measure the correlation – radial or long-range – between the fluctuations.

The objective of this section is to use the model to guide the experiments but also to test some diagnostics that could then be applied to the DBS data. The final aim is to characterize experimentally the turbulence self-organization. First, we briefly review regimes where the self-organization is most likely to occur according to the many simulations performed. Then, a section is devoted to the observation of avalanches using a correlation analysis. Finally, we focus on the observation of radially structured zonal flows.

As a foreword, given the many assumptions of the Tokam1D model, we acknowledge that it cannot be used for quantitative comparisons. Yet, we argue that the general trends that are observed in the parameter scans keep some relevance, especially regarding turbulent self-organization issues.

4.6.1 Turbulent regimes where self-organization occurs

It has been highlighted in the previous sections that ZF-dominated regimes occur mostly at large C and g. The first regime leads to meandering flows, unless reaching the adiabatic regime $C \longrightarrow +\infty$ where flows are structured. A meandering flow is likely difficult to measure. Indeed, DBS typically estimates the perpendicular velocity of the plasma with a 5 *ms* time resolution. For a TCV plasma, this corresponds to roughly $\omega_{cs}t = 6 \times 10^4$ using a magnetic field at the separatrix of the order of 1.4 T. Then, one needs about 20 measures at different probing frequencies to infer an edge perpendicular velocity profile. That means the flow radial structure have to stay stable on $\omega_{cs}t \sim 10^6$. To give an idea, the examples of flows presented in Figure 4.15 are shown for $\omega_{cs}t = 3 \times 10^4$. Therefore, meandering cases, such as (a) and (c) might be difficult to characterize on such long time scales. It is therefore crucial to be in a regime where flows are stable on time scales larger than the time resolution of the diagnostic.

For this reason, cases at large g should be preferred since they produce large amplitude radially structured and time stable flows. However, having a large g/C typically corresponds to high-density scenarios which brings two issues - on top of the already operational constraint of the tokamak at large densities. The first one is that the collisional friction will be large, hence reducing the flow amplitude. The second one is that the localization of DBS measurements largely depends on the density profile and on the frequencies achievable by the DBS systems. At large densities, measuring far inside the plasma is difficult. Another option would be to measure in high magnetic curvature tokamaks such as low-aspect ratio machines (MAST-U) that could perform at large $g > C$ with accessible density. In measurements done on TCV, regimes that favour interchange characteristics should be considered. This means looking at ITG/RBM

types of turbulence yielding large stiffness and important growth rates. As it will appear later on, TCV is often dominated by TEM instability which might not be the ideal ground for the observation of staircases [107].

The simulation results suggest that the measurements should be performed when the plasma is close to its linear threshold. Plasmas are expected to be near-marginal [71, 72, 200]. The distance to marginality can be slightly modified by injecting power. However, the transport being usually stiff, this is difficult. Previous experimental observations also highlight that staircases are observed in near-marginal ion-driven turbulence [107].

Finally, the measurement location is of importance for several reasons. Measuring too close to the separatrix is difficult because the plasma has a large collisionality and may be governed by neoclassical and force balance effects. Far in the core (after the pedestal) is also difficult because the turbulence intensity is lower resulting in a decreased ZF drive. Finally, the DBS requires sufficiently high turbulence levels to obtain a decent signal to noise ratio. The best option is then to measure just after the radial electric field well (see Figure 1.17), typically from $\rho = 0.7$ to 0.9.

At last, it should be noted that we did not take into account the geodesic acoustic modes (GAM) in the analysis. Since ZFs and GAMs are expected to exchange energy, there is a possibility that a large GAM activity hinders the generation and subsequent measurement of the ZFs. Actually, this point will be thoroughly investigated in Section 5.2, we show that by removing the GAM component, we can better observe the low frequency zonal flows.

4.6.2 Two correlation lengths as an indication of avalanche-like transport

In this section, avalanches are studied using a correlation analysis with the objective to apply the same method to experimental data. In the experiments, data are more scarce than in simulations and the direct observation of ballistic traveling events is unlikely. A contribution by P.A. Politzer [85] stands out with the measurement of avalanches using the electron cyclotron emission diagnostic. Using DBS with two channels, the avalanche measurement will be indirect. Using the code helps to identify whether the measurements can be identified as avalanches.

We look for signatures of avalanches on the correlation function of density fluctuations amplitude. An example of this measurement is shown in Figure 4.30, for the two test cases of the chapter at low and large g (see flows Figure 4.15 (a)-(b) and turbulent flux Figure 4.24). The colour represents the coherence, the black crosses note the time delays at which the coherence is maximal. Two contour lines, delimit $\mathscr{C} = 0.75$ (red) and $\mathscr{C} = 1/e$ (white).
The radial structure of turbulence changes with the dominant instability. For a low interchange drive, turbulent structures exhibit broad and circular shapes. Their typical size of a few ρ_s is labelled l_c. In interchange-dominated plasmas, two characteristic lengths appear. The smaller, which is similar to the first regime, shows up without any time delay. The larger is tilted diagonally, indicating a travelling event. The size and tilt of L_a are comparable to the observed avalanches in the turbulent flux (Figure 4.24). Also, one can observe a second, small length in the opposite direction. As the radial correlation is a statistical measurement, it captures events travelling outward and inward therefore displaying both directions on the resulting function. Note that the preferred direction (in or out) depends on the measurement location and particularly on the underlying velocity shear. In Figure 4.30, the measurement is performed roughly at

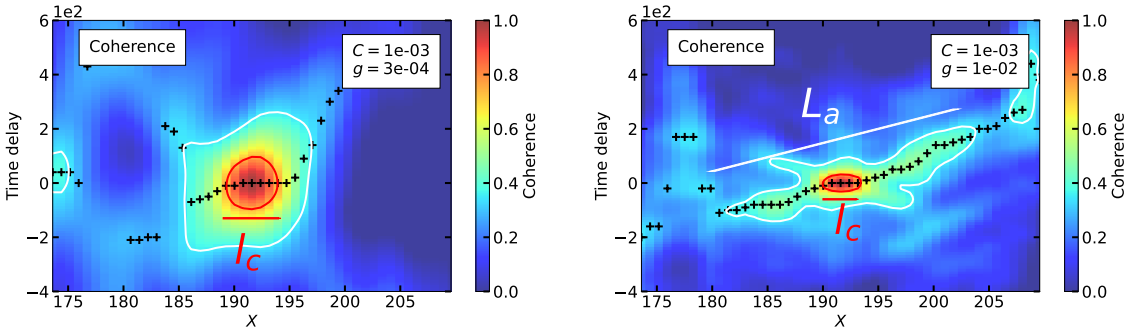

(a) (b)

Figure 4.30 – Radial correlation function of density fluctuations amplitude for cases: (a) $g = 3 \times 10^{-4}$ and (b) $g = 10^{-2}$. Both at $C = 10^{-3}$ using constant source $S_N(0) = 10^{-4}$.

a ZF maximum. When done at a ZF minimum, the travelling events tend to form a 'V' shape because a similar number of inward and outward events occur.

The interchange dominated case thus displays 2 slopes for the correlation function. This is best seen when plotting the maximum of coherence at each position, see Figure 4.31.

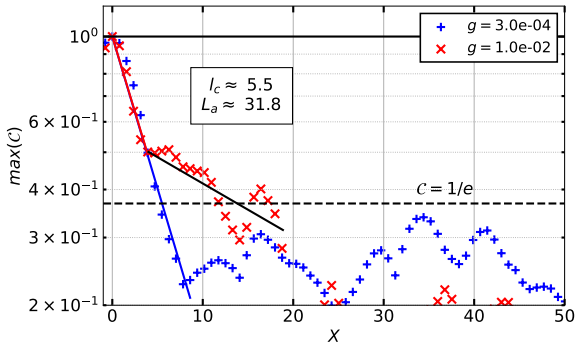

Figure 4.31 – Radial correlation function: maximum of coherence. (a) $g = 3 \times 10^{-4}$ and (b) $g = 10^{-2}$. Both at $C = 10^{-3}$ using constant source $S_N(0) = 10^{-4}$.

The double slope of correlation appears clearly in the case at large g only. The fits are performed on the logarithm of the radial correlation, therefore assuming an e-folding decay e^{-x/l_c}. The two small correlation lengths are of roughly the same amplitude at $l_c \approx 5.5\ \rho_s$. The second slope for the case $g = 10^{-2}$ is roughly equal to $L_a \approx 32\ \rho_s$, which is consistent with Figure 4.30. In the next chapter, we show that these two slopes of correlation are accessible with the Doppler measurements. Based on the present results, we assume that the length of the avalanche (in a statistical sense) is comparable to the inverse of the exponential decay. Doing so, the study of the turbulence structure in various regimes of turbulence is made possible.

4.6.3 Possible experimental signatures of ZFs and staircases

ZFs are notoriously difficult to measure. They are low amplitude and depending on the turbulent regime, the flows may be meandering or with no well defined radial structure. In these cases,

there is little chance for a diagnostic to have a sufficient radial and time resolution for a direct observation of their velocity. Ideally, several key aspects needs to be verified on the fluctuations themselves, they are summarized in Section 2.5.1.

Here, we use the correlation analysis made available by the DBS to observe staircases footprints. The shear induced by staircases is expected to decorrelate turbulent structures, see for example ref.[107]. Additionally, turbulent structures are observed to localize in velocity wells. These two effects are expected to modify the local estimation of the radial turbulence correlation length (l_c), the avalanche correlation length (L_a) and the turbulence auto-correlation time (τ_{turb}). The modulation of the radial correlation length by flows does not appear clearly in Tokam1D simulations. The two other effects are observable, and plotted Figure 4.32.

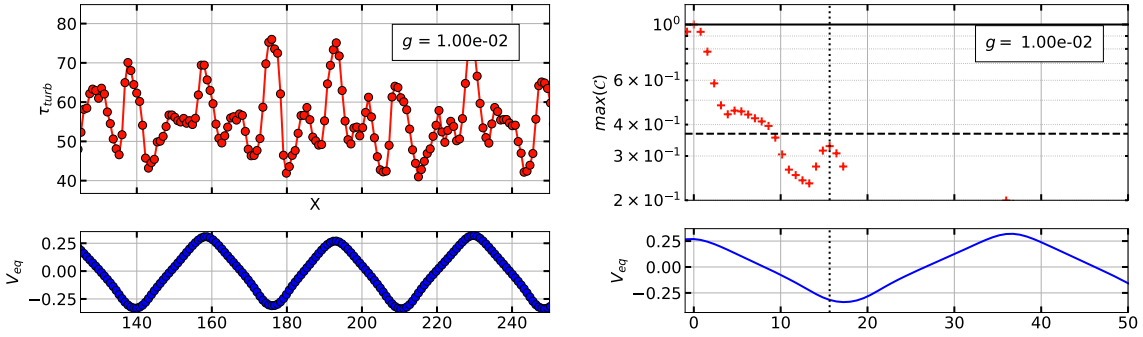

(a) (b)

Figure 4.32 – Possible signatures of radially structured ZFs. (a) On the turbulence auto-correlation time τ_{turb}. (b) On the turbulence radial correlation length. Both are shown for case $(C,g) = (10^{-3}, 10^{-2})$ at fixed source.

On the left hand side, the turbulence auto-correlation time is shown to depend on the underlying velocity. In particular, since density fluctuations are localized on both velocity minima and maxima, the turbulence correlation time appear larger at these locations. It has been observed that density fluctuations can localize on both minima and maxima of V_{eq} or only in minima depending on the chosen turbulence parameters. The electric potential fluctuations are always located on both minima and maxima. On the right hand side, the radial correlation of the density fluctuation is shown together with the flows. It is the same case as the one studied in the previous section. The radial correlation in the avalanche section is shown to be modulated by the underlying flow. In particular, it increases again when approaching the ZF minima. Both effects have been observed on several simulations where structured flows are present and have been shown lacking in simulations displaying unstructured flows.

Those two estimations do not provide a strong argument for a radially structured flows by themselves. However, they can support the conclusion if a low amplitude corrugation is observed on the perpendicular velocity measurement performed by the DBS.

4.7 Conclusion

In this chapter zonal flows generation and structure have been studied using the reduced model Tokam1D in its electrostatic version. The model is driven by two instabilities: collisional drift

waves (CDW) controlled through the adiabatic parameter C, and interchange driven by the magnetic inhomogeneity g.
A total of 120 simulations have been performed at varying C and g to cover the experimentally relevant parameter space. The distance to marginality is key in the nonlinear properties of the system. Therefore, two types of simulations have been performed. The first set, closer to the experimental set up, uses a constant source. That means, the system is sometimes driven far beyond its linear threshold. As a result, the forcing itself is not so constant since it depends on the distance between the diffusive profile (maximum profile achievable with a given source) and the instability threshold. So as to force each simulation similarly, all cases have also been run using an adapted source for each case. This time, the source is chosen depending on the linear instability threshold, such that the diffusive gradient is 6 times the critical gradient. The second set of simulations is mostly adapted for a 'theoretical' view of the simulations behaviour. However, it is insightful since it takes into account the role of marginality which then impacts the nonlinear results.

Depending on the values for C and g, turbulence has been shown to exhibit different properties. In the collisional drift wave (CDW) regime, at medium C and low g, the plasma is dominated by density fluctuations and a yields a low density-electric potential fluctuations cross-phase. The interchange dominated regime, at large g, is driven by electric potential fluctuations. While the first instability leads to low growth rate and cross-phase, the second is stiff and displays large turbulent fluxes even close to marginality. At very large C, one reaches the adiabatic regime. In this particular regime, both instabilities are stabilized, the system displays a low cross-phase together with density and electric potential fluctuations roughly equal. These three regimes directly impact the generation of ZFs since their characteristics govern the two components of the Reynolds stress.
In regimes with dominant interchange turbulence, where density and electric potential fluctuations exhibit the same order of magnitude (cf. Figure 4.6), the electric component of the Reynolds stress – driven by electric potential fluctuations – is dominant. The diamagnetic component dominates in CDW turbulence regime where density fluctuations are larger. The correlation between the two components of the Reynolds stress also depends on the turbulent regimes. While they are in phase opposition in interchange driven turbulence, they align in phase in CDW turbulence.

Two regions of the parameter space exhibit a large flow to turbulence energy ratio. The simulations at large g, low C – driven by interchange – and the simulations at very large values of C, whatever g. In both cases, the flow accounts for more than 30% of the turbulence-flow energy partition. The system displays an even larger flow to turbulence energy ratio when closer to marginality.
The two regimes are however different in terms of the ZFs radial structure. Interchange cases lead to strongly structured flows whereas large C simulations display intermediate structures where meandering, splitting and merging events occur. It is not clear why the former leads to such radially structured flows. However, these simulations also correspond to cases where a large amount of avalanche-like transport is found. These ballistic transport events of particles can propagate over a large part of the simulation domain greatly increasing the average turbulent transport. Structured zonal flows are also found in the limit $C \longrightarrow +\infty$. In those cases, the flows

are broader than their interchange counterparts. In the performed simulations, structured ZFs always lead to staircases – corrugations in the density gradient – often resulting in micro-barriers of transport.

The transport is then studied as a function of C and g and some attempts at unveiling the interplay with ZFs are made. The linear properties of the systems are key: at fixed forcing source, large instability thresholds lead to a good confinement. That is not the case for simulations performed with an adapted source, since the distance to the threshold is kept close to constant by the adapted forcing. On those adapted cases, the stiffness is better observed. Regimes characterized by low growth rate or cross-phase exhibit low levels of transport. They can therefore depart from their instability threshold. That is typically the case at large C when both instabilities vanish. Finally, comes the role of the flows and of their radial structure. To quantify their effect, the confinement time is normalized to a mixing-length estimate taking into account the growth rate and the cross-phase. When the confinement is normalized to remove the role of the growth rate, cross-phase and forcing, simulations displaying large flow to turbulence energy ratios are found to perform better. Staircases dominated simulations display an even better confinement.

Finally, possible experimental signatures of turbulence self-organization are explored. These features will reveal particularly when analysing experimental data in the next chapter. Focusing on data available from a two-channel Doppler backscattering (DBS), the results are analysed in terms of correlation. When avalanches are present, the radial correlation function displays two distinct slopes. The first one appears to be linked to the size of the underlying turbulent eddies while the second carries information on avalanche propagation lengths. The effect of velocity shear is visible on the radial correlation function and on the auto-correlation time. It may not give additional information with respect to the velocity directly accessible from the DBS, but it can be helpful when the evidence for staircases is weak.

The time spent (i) on the derivation of the model, (ii) on its numerical implementation and verification, and ultimately (iii) on the characterization of its linear properties has not allowed us to (iv) explore exhaustively the parameter space in the nonlinear regime. Key additional physics should be included to go beyond the results presented in this chapter. In particular, considering the equilibrium radial electric field arising from the radial force balance on the one hand, and the one governed by the parallel physics of plasma-wall interaction in the SOL on the other hand, should likely be the two next priorities. We have also discussed on possible ways to account for the physics of GAMs, which can reveal important at the edge by competing with the zonal flows. However, it should be emphasized that this physics enrichment of the model comes at the price of an increase of the number of parameters to scan – such as the e.g. the collisionality or the density and electron temperature e-folding lengths in the SOL. Extending the model to alleviate the isothermal closure and to include electromagnetic effects – likely important when bifurcating towards improved confinement regimes – would then be the natural way forward. We have shown how to proceed in this direction.

Chapter 5

Experimental characterization of the turbulence structure using Doppler backscattering

Contents

This chapter aims at measuring zonal flows and avalanches. As already stated in Section 2.5, measuring those aspects of plasma self-organization is particularly difficult. For zonal flows, one needs to verify the mode structure $m = n = 0$, m being the poloidal and n the toroidal mode number and one would need to resolve the radial structure. For avalanches, one needs to identify ballistic like transport events which requires a diagnostic with important time and spatial resolutions.
In the previous chapter, using Tokam1D, we identified the turbulence regimes most likely to generate zonal flows, avalanches and staircases. Those are found mainly in near-marginal interchange driven turbulence. Furthermore, we have seen that the avalanches were characterized by a second slope in the radial correlation function of the density fluctuations.

In the present chapter, we use a Doppler backscattering (DBS) in two different configurations. First, using two channels separated both poloidally and toroidally, we aim at measuring zonal flows by using long range correlation (LRC). The LRC is performed on the perpendicular velocity extracted using a time-frequency analysis called MUSIC adapted for the DBS data by the LPP team [42, 134]. To better observe the low frequency zonal flows, we isolate and remove the high frequency noise and the GAM component using empirical mode decomposition (EMD). This method decomposes the signal into a set of intrinsic mode functions of narrow band fluctuating frequencies. Its main advantage is its capacity to identify non-stationary – in both amplitude and frequency – signals. Second, we aim at measuring avalanches by their signature in the radial correlation function using two co-located DBS channels. This method has been already presented on Tokam1D simulations and previously used in ASDEX-Upgrade [86] by the LPP team. Several heating schemes have been used in an attempt to modify the profiles and underlying turbulent regimes. The DBS also gives access to the perpendicular velocity profile. Measuring both avalanches and the velocity enables, in principle, the measurement of staircases.

5.1 Measuring with Doppler backscattering (DBS)

As a first step towards the description of the Doppler backscattering, we briefly introduce reflectometry diagnostics that are used to characterize density profiles and fluctuations in magnetic confinement devices. Using an electro-magnetic wave sent into the plasma, reflectometry and its variants provide local measurements at locations inaccessible for material probes. A review on microwave reflectometry for magnetically confined plasmas is available ref.[201].

In standard reflectometry, a probing micro-wave is sent at normal incidence to the plasma surface. It propagates into the plasma until it reaches the cut-off layer where the beam is reflected towards the receiving antenna. The cut-off layer position depends on the probing frequency, the local plasma density and in general also on the local B-field magnitude. Therefore, by ramping the probing frequency, the plasma density profile can be reconstructed. Details on the cut-off frequencies for the case of a non-turbulent plasma are provided in Section D.1. In the case of short-pulse reflectometry (SPR), singular pulses are sent to the plasma at various probing (carrier) frequencies. The time-of-flight is detected for each pulse, leading to the reconstruction of the profile. Standard reflectometry performs a continuous frequency sweep. The density profile is then computed from the received frequency spectrum.
In both cases, measurements are affected by turbulent density perturbations. Therefore, some approaches to turbulence measurement have been developed using fast sweeping reflectometry (FSR) [107] and SPR [202].

5.1.1 Doppler backscattering principle: collective scattering

Doppler backscattering (DBS) - also called Doppler reflectometry - consists in sending the probing wave at an angle θ with respect to the cut-off surface. It is not the reflected but the backscattered wave that is measured. This has the advantage to select the probing wavenumber and to allow for an estimation of the perpendicular velocity from the Doppler shift. DBS have been introduced in the early 2000 on W7AS [203], ASDEX [204] and Tore supra [205]. The diagnostic enables the measurement of multiple turbulence related properties, making it particularly popular in fusion plasmas despite its complexity. Those measurements include:

1. The perpendicular velocity of the plasma (radial electric field).
2. The density fluctuations at a selected wavenumber: $n(k,t)$.
3. The k-spectrum of the density fluctuations: by varying the wavenumber in a broad range $k \in [3-20]\ cm^{-1}$ ($\approx k\rho_i \in [0.3-3]$ at the edge of TCV plasmas).
4. The spatial structure of the turbulence (requires several DBS).

The diagnostic relies on the collective scattering of a wave by turbulent structures. With a lower inertia, electrons are mostly responsible for the scattered field. If those electrons are organized into structures, the sum of the scattered field by each electrons lead to a significant form factor at the typical wavenumber of the structures.

To delve deeper into the details, we consider the general case of a wave scattering on fluctuations. Let us consider an incident monochromatic plane wave, $E_i(\mathbf{r},t) = E_{i,0}\exp(i(\mathbf{k}_i \cdot \mathbf{r} - \omega t))$ of incident wave vector $\mathbf{k}_i$ and frequency ω. Electrons act as local emitters of spherical waves at the same frequency ω. The receiving antenna receives the superposition of the emitted waves. In the far-field approximation at a distance, distance $R \gg r_j$, where r_j is the position of the j

scatterer, and considering that the wavenumber modulus is conserved, the collective scattered electric field is the sum over all scatterers j [206]:

$$\mathbf{E}_s = r_0 \frac{e^{ik_i R}}{R} e^{-i\omega t} (\mathbf{n} \times \mathbf{n} \times \mathbf{E}_{i0}) \sum_j e^{i\mathbf{k}_f \cdot \mathbf{r}_j} \tag{5.1}$$

Where $r_0 = \mu_0 e^2/(4\pi m_e) \approx 2.8 \times 10^{-15}$ m is the classical electron radius and $\mathbf{n}$ the scattering direction. The phase term involves the analysis wave vector $\mathbf{k}_f$ linked to the incident wave vector $\mathbf{k}_i$ and the scattered wave vector $\mathbf{k}_s$ by the Bragg's rule: $\mathbf{k}_f = \mathbf{k}_s - \mathbf{k}_i$. In the continuous medium approximation, we assume that the collective behaviour of the electrons is represented by the electron density $n(\mathbf{r},t)$. The sum is replaced by an integral over the scattering volume $\mathscr{V}$ as follows:

$$\mathbf{E}_s = r_0 \frac{e^{ik_i R}}{R} e^{-i\omega t} (\mathbf{n} \times \mathbf{n} \times \mathbf{E}_{i0}) \int_{\mathscr{V}} n(\mathbf{r},t) e^{i\mathbf{k}_f \cdot \mathbf{r}_j} \, \mathrm{d}^3\mathbf{r} \tag{5.2}$$

The scattering volume is defined by the superposition of the probing and the 'receiving' beams (the area visible to the receiving antenna). This measurement then gives access to the Fourier transform of the density fluctuations $n(\mathbf{r},t)$ at a specific wavenumber k_f. Consequently, by varying k_f, a k-spectrum of the density fluctuations can be inferred.

The particular case of Doppler back-scattering is sketched in Figure 5.1. On the left is presented the orientation of the diagnostics main quantities in the poloidal plane. On the right, a zoom on the cut-off layer is performed. The slab geometry is considered at short scale for simplicity. A wave is sent into the plasma at an angle θ from the cut-off layer. It scatters on the turbulent structures, indicated as blue and red pebbles in the figure. Then the backscattered wave is received by the DBS antenna.

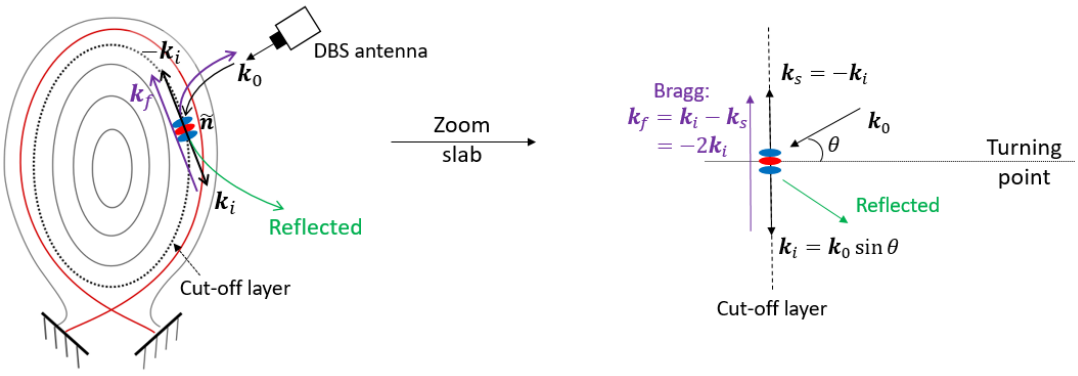

Figure 5.1 – Beam orientation in comparison to magnetic field lines. $\mathbf{k}_0$ is the vacuum wave vector, $\mathbf{k}_i$ is the local incident probing wave vector. $\mathbf{k}_f$ is the selected wave vector through the Bragg's rule.

In that case, the selected wavenumber that matches the Bragg's rule is given by: $\mathbf{k}_f = -2\mathbf{k}_i$. The probing wave vector is determined by the angle θ of the incident beam to the normal of the cut-off surface. In the particular case of a linear density profile in O-mode the incident wave vector reduces to $k_i = k_0 \sin\theta$ in the y direction, since k_r vanishes at the cutoff. Since there is

no analytical formula for the general case, the local $\mathbf{k}_i$ is computed using a beamtracing code that takes into account the geometry of the beam and of the plasma [207]. By adding a small toroidal angle ($\approx 5^\circ$) to take into account the helicity of the field lines, we can match as best as possible the Bragg's condition so that the analysis wave vector is roughly perpendicular to the magnetic field, thus adapted to the fluctuations known to be aligned along the magnetic field ($k_\parallel \ll k_\perp$).

All in all, the analysis wave vector $k_f \approx k_\perp$ is selected by adjusting the antenna of the launcher. The power of the received signal relates to the amplitude of the density fluctuations of wavenumber $k_\perp$. By varying the angle of the launcher, thus scanning the selected scattering wavenumber, a k-spectrum of the turbulence can be measured [42, 43]. If the density fluctuations are advected, the perpendicular velocity can be computed from the Doppler shift of the received spectra, see Section 5.1.3.

5.1.2 Measurement localization and resolution

In the previous paragraph we have assumed that the location of the measurement is close to the cutoff. However, in a back-scattering experiment, the signal can originate from the substantial part of the beam trajectory, the scattered beam being superposed to the probing beam. Nevertheless, both the beam propagation and the turbulence properties imply that the measured signal mostly comes from the cut-off region.

First, it can be shown by solving the Maxwell equations of the wave propagation in a homogeneous medium that the field is amplified closed to the cutoff [201]. Second, since the fluctuation k-spectrum peaks at low wavenumbers ($k_r \longrightarrow 0$ and $k_\perp \rho_i \lesssim 0.3$), these will be selected mainly close to the cutoff and weight heavier in the signal. Conversely, far from the cutoff, where k_f is essentially radial and remains large close to k_0, the corresponding selected fluctuations have a low level and contribute much less to the signal.
Forward diffusion can still occur along the beam propagation path. Mostly the large structures contribute, such that the amplitude can be important. However, since the radial velocity is very small in front of the perpendicular velocity, the back-scattered field from the edge of the plasma (where $k_\perp < k_r$) is centered on the spectrum zero-frequency component whereas the contribution from the cut-off region (where $k_r \ll k_\perp$) is Doppler shifted. Forward diffusion can widen the received spectrum, such that the interpretation of small Doppler shifts is made more difficult.

The scattered field amplitude depends in the end on the fluctuation amplitude (proportional in the linear regime). The measurement range is then limited to regions that yield enough turbulence. In the core, or in H-mode, the relative density fluctuation level tends to be very low $\delta n/n < 1\%$ which makes the signal to noise ratio (SNR) low. Conversely, for $\rho > 0.8$, the relative fluctuation amplitude can be of a few % up to about 30 % close to the separatrix. Henceforth, we mostly measure in the region $\rho \in [0.8 - 1]$.

The spatial resolution depends on the beam localization close to the cutoff. It depends on the beam waist which can be of the order of a few *mm* to the *cm* depending on the refractive index gradient. In X-mode polarization, the refractive index profile is more steep, such that the spatial resolution tends to be larger as compared to O-mode polarization. The radial sensitivity is larger than the resolution as the probing frequency can be varied very precisely. The sensitivity is typically close or below the Larmor radius ($\lesssim \rho_s$).

The signals delivered by the LPP DBS systems are digitized at a high sampling rate (5 to 25 MHz, depending on the plasma conditions) which allows to resolve the fluctuation dynamics (typical auto-correlation time from $\lesssim 1$ to $10\mu_s$). This high sampling rate is also necessary to avoid spectrum aliasing when the Doppler shift associated with high fluctuation velocities reaches several MHz (H mode).

As stated above, to have a sufficient SNR, one needs to gather enough statistics on the advected turbulent structures. In principle, only a few number of probed advected structures is sufficient to infer a Doppler shift. In practice, due to the RF noise and the various structures that are probed at slightly different locations the received spectrum represent a distribution of velocities (see next section). In practice, to have enough statistics, the measurement of the density fluctuations and velocity is made on longer time scales. To be confident in the measure of the velocity the computation is typically done on 5 *ms* signals. Other methods such as sliding FFT or MUSIC algorithm can estimate the Doppler shift on 16 to 128 points, greatly increasing the instantaneous velocity measurements (see Section 5.2). Using the standard method, a velocity profile can be obtained in ≈ 100 *ms*, less when several DBS are coupled together.

5.1.3 Perpendicular velocity measurements

If the measured fluctuation propagates with a velocity $v_\perp$, the frequency of the scattered signal is Doppler shifted by $\Delta\omega = v_\perp k_\perp$. By computing $k_\perp$ with the beam-tracing code, the velocity is inferred. Provided that B is roughly constant on the scattering volume, one can also infer the radial electric field:

$$v_\perp = \frac{\Delta\omega}{k_\perp} \approx E_r/B \; . \tag{5.3}$$

The measured perpendicular velocity is the sum of two components: the fluctuations phase velocity that could potentially depend on $k_\perp$ (but in general also on other parameters: heating, turbulence regime, ...) and the plasma background velocity given by $E \times B$ drift:

$$v_\perp = v_\varphi + v_E \; . \tag{5.4}$$

At the edge of the plasma, it is usually considered that $v_\varphi \ll v_E$ such that the Doppler shift gives a measure of the perpendicular $E \times B$ drift [208, 203, 204].

Estimating the perpendicular velocity then requires to infer the Doppler shift in the received signal spectrum. In practice, the complex signal is reconstructed from the received signal and demodulated using a process called heterodyne detection. Details on the hardware and heterodyne detection are provided in Section D.2.

The power spectral density (PSD) computed from the complex signal with a direct Fourier analysis gives a high frequency resolution $\delta f \sim 1/T$ but also presents an important variance which can be detrimental in the interpretation of the spectra. Instead, we prefer to use an averaged spectral estimator such as Welch [209]. The method consists in splitting the signal into m segments of n_{FFT} points, overlapping by 50 %. Each segment is multiplied by an apodization window such as a Hanning window. The PSD is computed for each segment that are then averaged to produce a single estimate. The variance of the estimate decreases in a $1/\sqrt{m}$ fashion.

Welch's method is then a balance between losing frequency resolution and reducing the variance. For a 5 ms signal of 50000 points, we typically take $n_{FFT} = 1024$ points which leads to $\delta f \sim 10kHz$. The estimator is then an average over $m \sim 48$ segments.

The resulting PSD is the sum of the Doppler shift component and diverse other contributions such as forwards diffusion (linked to large scale structures), beam reflection over machine elements or backwards diffusion (small scale structures) (cf. Section 5.1.2). Those often result in a noise that makes the interpretation of the Doppler shift more difficult. Generally, we only exploit data where the Doppler peak is well above the rest of the contributions.

Several methods exist to evaluate the Doppler frequency by analysing the PSD. The first is to identify the position of the maximum in the spectrum either directly or by considering the weighted average – also called center of gravity (cog) – of the Doppler spectrum. Those two methods work fine when the Doppler shift is large and the SNR is important but the interpretation can become tricky when the velocity is closer to zero or the SNR is low. Another option is to fit the spectrum. The spectrum can be associated with the distribution function of the turbulent structures velocities. It can be shown that depending on the structures dynamics, the spectrum will exhibit more of a Gaussian or a Lorentzian shape [42]. One can compare the characteristic size of the measure – that depends on the wavenumber $1/k_\perp$ – to the characteristic size of the structures motion $u\tau_L$, where u is the characteristic velocity and τ_L the Lagrangian correlation time of the velocity. Two limits can be identified:

- If $ku\tau_L \gg 1$: the structure moves nearly ballistically across the measurement region. In that case it can be shown that the spectrum is closer to a Gaussian.
- If $ku\tau_L \lesssim 1$: the structure moves slowly across the measurement region. Then, the characteristic displacement is closer to a random-walk across the detector area. In this situation, the spectrum is closer to a Lorentzian.

Depending on the dynamics, the best option can be the Gaussian fit, the Lorentzian fit or, most likely, something intermediate between the two. In practice, we use a Taylor fit which takes into account this underlying dynamics [210] and exhibits the two limits detailed above. As such it often matches best the signal in the various situations. Finally, it is also necessary to give an initial guess for the fits. Routinely, the first guess is estimated by fitting the odd part of the spectrum with a Gaussian fit. This assumes that there is indeed a Doppler shift, so that the relevant information is in the asymmetric part of the spectrum [211]. In Figure 5.2, a typical spectrum obtained through Welch and its corresponding fits are displayed.
In practice, the Doppler shift is given by the median of the fits performed. Note that on the given example, the fits do not match very well the tail of the distribution. This asymmetric noise at large frequency is caused by spurious components. Routinely, we remove these tails by hand before performing the fits.

The sign of the perpendicular velocity is given by the convention displayed in Figure 5.3. Note that due to the negative magnetic field, $v_\perp$ is of the same sign as E_r.

By scanning the probing frequencies, one can measure at different radial location inside the plasma. Then, performing the above analysis on obtains the Doppler shift for each programmed frequency. By using the beam-tracing code, frequency steps are matched with their localization inside the plasma and their local $k_\perp$. Combining those information, one produces a profile of

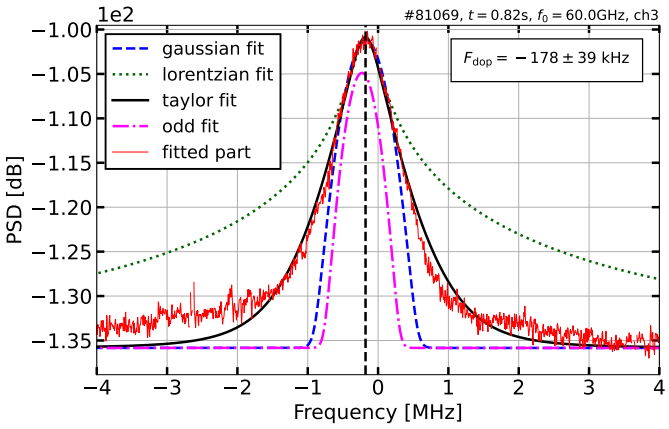

Figure 5.2 – Power spectral density estimated using Welch's method with the different fits used for the estimation of F_{dop}. Shot #TCV81069, sweep 5, $F_{ref} = 60\ GHz$.

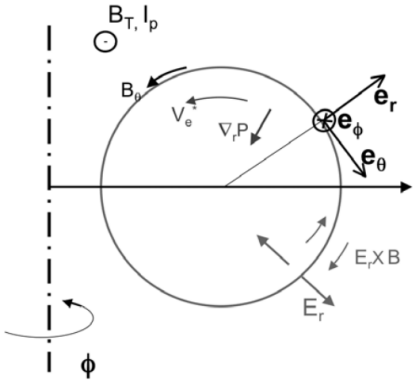

Figure 5.3 – Convention for radial, poloidal and toroidal orientation. Here, $\mathbf{B}_T, \mathbf{I}_p < 0$. The radial electric field is considered positive outside the separatrix and negative inside the plasma. Figure taken from [212].

perpendicular velocity, such as presented in Figure 5.4 for shot #80328.

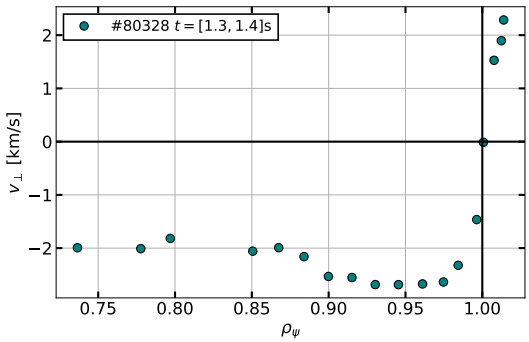

Figure 5.4 – Example of a $v_\perp$ profile estimated using DBS channel 1 on shot #TCV80328 at time 1.3 - 1.4 s.

Remark that the perpendicular velocity tends to be negative in the confined region close to the separatrix and becomes positive in the scrape-off layer. This behaviour has already been introduced fro Tokam1D (eg. Figure 3.5). The core perpendicular velocity is shown to depends on the force balance equation:

$$v_\perp = \frac{\langle E_r \rangle}{B} = +\frac{\nabla p_i}{ne} + v_\phi B_\theta - v_\theta B_\phi \ . \tag{5.5}$$

The action of the pressure gradient generally leads to a negative perpendicular velocity. An example highlights the role of the force balance equation in Figure 5.28 where different heating schemes are used in TCV for the same magnetic configuration configuration. The E_r well shape in the transition region is not easy to predict. It might depend on several factors, possibly related to turbulence and neoclassical effects. See for example the experimental study on the role of the magnetic configuration and q-factor ref.[26] and a gyrokinetic study aimed at reproducing similar trends [27].

5.2 Long range correlation measurements in Tore Supra

A ZF is an electric potential mode that verifies $m = n = 0$, m being the toroidal wavenumber and n the poloidal wavenumber. Measuring the degree of correlation of signals from two similar but distant diagnostics, located at different poloidal and toroidal ports for instance, is one way to verify the zonal activity on the electric potential. Alternatively, this method can be applied to the velocity fluctuations (linked to the potential through the electric drift).

In Tore Supra, a second V band DBS system was installed viewing vertically, separated toroidally and poloidally from the former equatorial DBS system. This system has been used to characterize GAMs [133]. Unfortunately, the diagnostic operated only during one campaign before the breakdown of the general power supply which has ended Tore Supra operation before WEST took over some years later. It was not possible to reinstall the vertical diagnostic in the WEST configuration.

The idea in this section is to take advantage of the shots performed at the time to perform LRC with the aim of observing low frequency zonal flows. We only have a few numbers of discharges where the diagnostic is set to probe simultaneously fluctuations using the same probing frequency (same radial location) at similar or close wavenumbers, with a sufficient acquisition length in stable plasma conditions. We show that the correlation at long distance is dominated by the GAM feature. However, after removing them along with the high frequency noise using empirical mode decomposition, a low frequency zonal flow signal is recovered.

5.2.1 DBS systems installed on Tore Supra

A first DBS system (DIFDOP) was installed on Tore Supra using O mode V band [205], soon completed by an X mode W band to probe across the separatrix. The second system (DREVE), viewing vertically from the top in O mode V band, was designed beginning of 2010 to study the structure of the flows, their poloidal asymmetries as well as the GAMs [134, 133]. It was operated during two short campaigns before being stopped by the major breakdown of Tore Supra power supplies (2012). Therefore, the available data in a configuration suitable to study

the long range correlation (synchronous, long enough time sequences, similar probed locations and wavenumbers) are scarce. We focus here on two shots obtained during dedicated experiments ($\nu_\star$ scan and GAMs studies): #45510 and #47500. The location of the two systems in comparison to TS is indicated in Figure 5.5, together with an example of beamtracing.

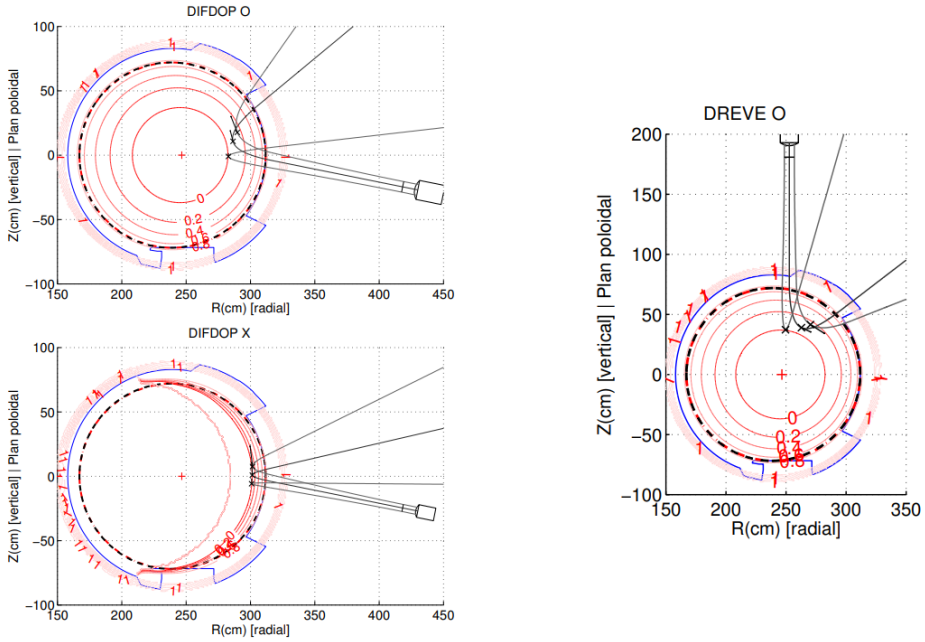

Figure 5.5 – Location of DIFDOP (left) and DREVE (right) in comparison to Tore Supra. The channels are separated by 120° toroidally and more than 90° poloidally. Examples of beamtracing are indicated for each channel. Red circles correspond to iso-index surfaces, the blue line corresponds to machine elements (limiter, antennas...).

Discharge #45510 was performed with a scan of the wavenumber k on the equatorial (DIFDOP) but not on the vertical (DREVE) leading to a mismatch in k making it difficult to seek for long range correlations (see Figure 5.8). The main analysis will then be focused on #47500. The discharge scenario is presented in Figure 5.6. On the upper panel the integrated density is displayed in blue together with the ICRH heating constant at 2 MW. The bottom panel features the DBS parameters: motor angle (red), rms values of each DBS channel. The DBS data are acquired for both DIFDOP and DREVE at four triggers indicated by vertical lines. For each of those triggers, five different frequencies are used ($F = (49, 51.8, 54.5, 57.2, 60)$), each representing 12 ms of data. The first two sequences were still in a non stationary phase of the radio frequency coupling but the last two, especially the $4th$ one are in steady state, allowing for the study of the correlation.
In the following sections the use of MUSIC algorithm and empirical mode decomposition (EMD) are detailed for #47500 trigger 4 frequency 4 corresponding to $\rho = 0.85$.

5.2.2 Long range correlation on the instantaneous velocity

The DBS delivers a complex signal featuring $n(k,t)$, whose phase carries information on the Doppler frequency $\propto k.v$. One then needs to compute the instantaneous velocity before performing the LRC. However, standard techniques like Welch, such as described in Section 5.1.3,

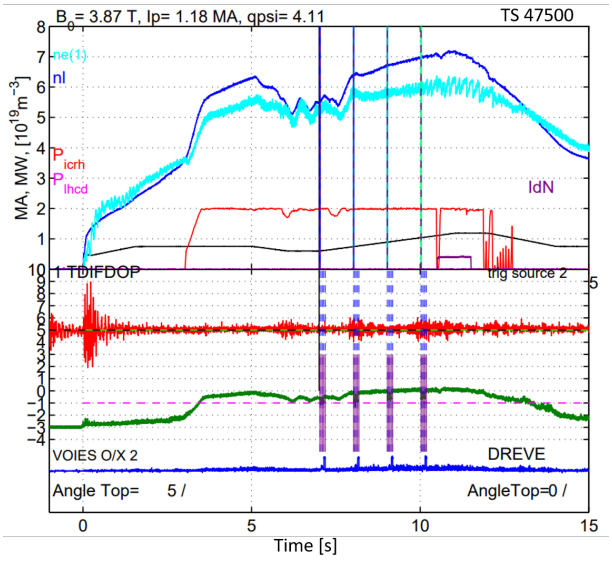

Figure 5.6 – Details of shot #47500. (Upper panel) Integrated density (blue) and heating scheme (red). (Lower panel) DBS configuration: angle of DIFDOP is indicated in black and red lines and the RMS values of DIFDOP and DREVE signals are shown in green and blue.

computed on long time series, gives only an average estimate of the velocity. Alternatively, one can use sliding Fourier transform or time frequency methods such as the multiple signal classification analysis (MUSIC) algorithm. Here, the latter will be used. It has been introduced already by the LPP group in ref.[42, 134]. The details of the algorithm, its implementation for GAMs study and its comparison with Welch and sliding Fourier transform can be found in ref.[134].

The MUSIC algorithm is a parametric method for the pseudo-spectral analysis of signals with a reduced spectral content. The algorithm is based on the idea that the signal can be represented by a finite number n_f of frequency components plus an incoherent noise part:

$$x(t) = x^{(s)}(t) + n(t) = \sum_{k=1}^{n_f} B_k e^{-i2\pi f_k t} + n(t) \tag{5.6}$$

Where $x^{(s)}(t)$ is the relevant part of the signal, B_k the amplitude of the frequency components and $n(t)$ the time dependent noise. This algorithm is suited when one frequency is particularly present in the signal. This is the case for DBS data where spectra are dominated by the Doppler frequency. The algorithm can go to windows as small as $n_w = 16$ pts. As a result, MUSIC algorithm manages to identify the instantaneous fluctuations of frequency around the Doppler peak, with a better time resolution than sliding FFT. Since the goal is the identification of low frequency ZFs, the window size choice is a tradeoff between better characterizing low frequency instantaneous velocity while still resolving the GAMs. Tests using $n_w = (64, 32, 16)$ have been performed resulting in poorer results, with a GAM feature less traceable. Therefore, the choice have been made to use $n_w = 128$ for the rest of this analysis. Here, we use the MUSIC algorithm with windows of size $n_w = 128$ pts overlapping over $n_{overlap} = 64$ pts, leading to a time resolution of $dt = 6.4\ \mu s$ for the Doppler frequency time sequence (1806 points long).

As a first step, the spectral coherence analysis is performed on the instant velocity extracted

from DIFDOP and DREVE and displayed in Figure 5.7. On the left is indicated the power spectral density of each channel along with their cross-spectral density computed using Welch's method. On the right is shown the spectral coherence C:

$$\mathscr{C}^2 = \frac{|csd|^2}{psd_{difdop} \times psd_{dreve}} \tag{5.7}$$

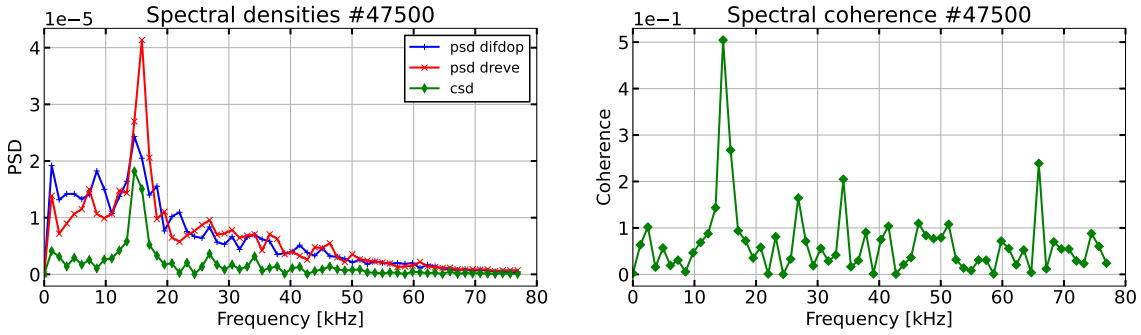

(a) (b)

Figure 5.7 – Spectral analysis of DIFDOP and DREVE using Welch's method. (left) Power spectral density and cross-spectral density. (right) Spectral coherence. Performed on #47500, trigger 4, frequency 4.

In both DIFDOP and DREVE, a peak at roughly 15 kHz dominates the spectrum. Moreover, a significative cross-spectral density also appears at this frequency. This results in a large long range spectral coherence for this mode indicating poloidal and toroidal coupling. This peak is close to GAM frequencies observed on similar discharges in Tore Supra [133, 4]. On this signal, no coherence at very low frequency emerges from the noise. In order to better identify this region, empirical mode decomposition (EMD) is used. With the EMD analysis, the GAM component is identified and isolated. It is then removed from the signal along with high frequency noise.

The above analysis has also been performed on shot #45510. The GAM feature is recovered on DREVE but not on DIFDOP: see the spectral densities and coherence in Figure 5.8.
In this shot, the level of LRC is vanishing ($\max \mathscr{C} \approx 4 \times 10^{-2}$). The low level of the GAM in the DIFDOP signal and of the coherence possibly comes from the wavenumber scan performed on DREVE which leads to different location and / or structures probed for both diagnostics. Therefore, only #47500 is analysed in this section.

5.2.3 Isolating the GAM component with empirical mode decomposition

Empirical mode decomposition is a method to split a signal into a sum of components called *intrinsic mode functions* (IMF). It has been developed by N.E. Huang in the early 2000 [213] and already tested on DBS data [4]. The particularity of EMD is that the decomposition depends on the properties of the signal itself and not on a well-defined mathematical object. EMD presents many advantages in comparison to other decomposition methods such as Fourier and Wavelets.

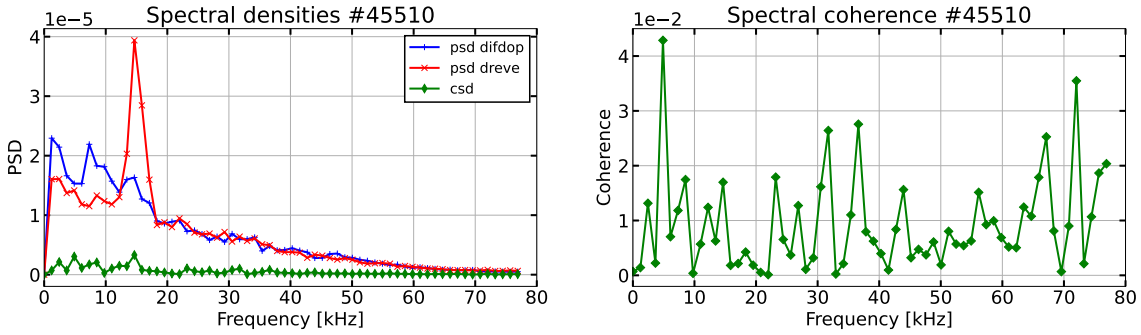

(a) (b)

Figure 5.8 – (a) PSD and CSD of DIFDOP and DREVE. (b) Spectral coherence. Analysis done on instantaneous velocity of TS45510, trigger 4, frequency 1.

The method can work on non-stationary signals and identify modes that appear sporadically or with a varying frequency [133]. Also, by coupling the results of the EMD with an Hilbert transform, one can produce a *Hilbert-Huang transform* (HHT) and get instantaneous frequency data. In the following, the EMD and HHT are detailed and applied to the identification of the GAM and other less dominant components in DIFDOP data.

The EMD is performed iteratively through a process called *sifting*. The decomposition uses the following steps:

1. Identification of extrema: e_{min} and e_{max} on signal $y(t)$.
2. Upper and lower envelopes are computed through cubic spline interpolation of the maxima and minima. It results in a continuous envelope defined by $e_{min}(t)$ and $e_{max}(t)$.
3. The mean of the envelope $m(t) = (e_{min}(t) + e_{max}(t))/2$ is removed from the signal: $I[y](t) = y(t) - m(t)$.

These three steps are repeated a certain number of times until the algorithm converges to a function $I[x](t)$ that fulfills the IMF conditions:

1. In the whole data set, the number of extrema and the number of zero crossings must be either equal or differ at most by one.
2. At any point, the mean value of the envelope defined by the local maxima and the envelope defined by the local minima is zero.

The first is a narrow-band selection criteria. It ensures that the IMF has a frequency content concentrated around a particular frequency. The second is here to ensure that the local (in time) frequency selected by the IMF does not have unwanted fluctuations induced by asymmetric wave forms. Other authors have proposed alternatives for the second condition. For example, ref.[214] proposes to consider an IMF when maxima are all positive, minima all negative and for which the envelope (positive and negative) is symmetric in comparison to zero.
From the first sift, one is left with the first IMF, $I_1[x](t)$ that represents the high frequency part of the signal and $R_1(t) = y(t) - I_1(t)$ the low frequency residual. The sifting is then applied on the residual until the second IMF $I_2[R_1](t)$ and second residual $R_2(t) = R_1(t) - I_2(t)$ are obtained. This is done several time, each time identifying an IMF with a smaller frequency

until a stopping criteria is met. Depending on the cases, or algorithm, different stopping criteria can be used: standard-deviation, energy, amplitude. In all cases, one needs to ensure that the last residual is negligible either in terms of frequency or amplitude as compared to the other IMFs.

The sifting process relies on local information in the signal. Therefore, even if the first IMF manages to extract the fastest component from the signal, the definition of 'fastest' can depend on the different segments inside the signal. This is especially true for a transient fast signal that disappears in some segments of the signal. If one wants to extract its component, the standard sift process cannot be used because the fast and slower components will be mixed. This problem is identified in EMD as *mode mixing* [214].
One possible solution is provided by performing *masked sifting* [215]. It consists in adding a masking signal of known frequency to the analysed signal. Any component which are lower in frequency than this mask are ignored by the sift in favour of the known masking signal. After the sifting process is completed, the known mask is removed and the desired IMF is obtained. However, it is important to have mask frequencies that correspond to the components that need to be isolated. A rule of thumb based on ref.[216], is to consider that a mask with a frequency F can be expected to remove frequencies below $0.7 \times F$. Choosing the masks then becomes the primary concern, as it is crucial to avoid projecting preconceived expectations onto the data itself which may lead to biased interpretations.

In the case of GAM analysis the selection of the mask frequency is informed by the underlying physics. Based on Figure 5.7, the GAM is shown well localized around 15 kHz. An example of EMD using masked sifting with mask frequencies $F_{mask} = (30, 17, 10, 3)\ kHz$ is shown in Figure 5.9 for DIFDOP instantaneous velocity signal, #47500, trigger 4, frequency 4. The stopping criteria is determined by a maximum of 4 IMFs. IMF-5 represents the residuals such that the sum of all 5 IMFs is equal to the input signal.
As it will appear in the following, IMF-1 contains high frequency noise, IMF-2 contains the GAM component, IMF-3 is an intermediate mode in between GAM and low frequencies but present no long range correlation. Finally, IMF-4 and -5 contains low frequency information. To identify each mode, instead of relying on Fourier, we make use of the Hilbert-Huang transform (HHT) directly linked to the IMF. HHT provides a description of how the energy within a signal is distributed across frequency. The distribution is based on the instantaneous frequency and amplitude of the IMFs.

Using the IMFs and Hilbert transform, one reconstruct the signal as a complex sum of the IMF *analytic representations*: $X(t) = \sum_k^N [I_k(t) + i\mathscr{H} I_k(t)]$, with I_k the IMF-k. $\mathscr{H}[I_k]$ is the Hilbert transform of IMF-k given by the Cauchy principal value of the convolution with the function $h(t) = 1/(\pi t)$:

$$\mathscr{H}[s](t) = (h \star s)(t) = p.v. \left\{ \int_{-\infty}^{+\infty} s(\tau) h(t-\tau) d\tau \right\}$$

Where $\star$ is the convolution operation and $p.v$ the Cauchy principal value (it removes singular values from the integral). In summary, the Hilbert transform gives the instantaneous phase of a given signal at the same time resolution. However, in case of signals with multiple components (many frequencies) the Hilbert transform leads to distorted phases. Since IMFs contain a singu-

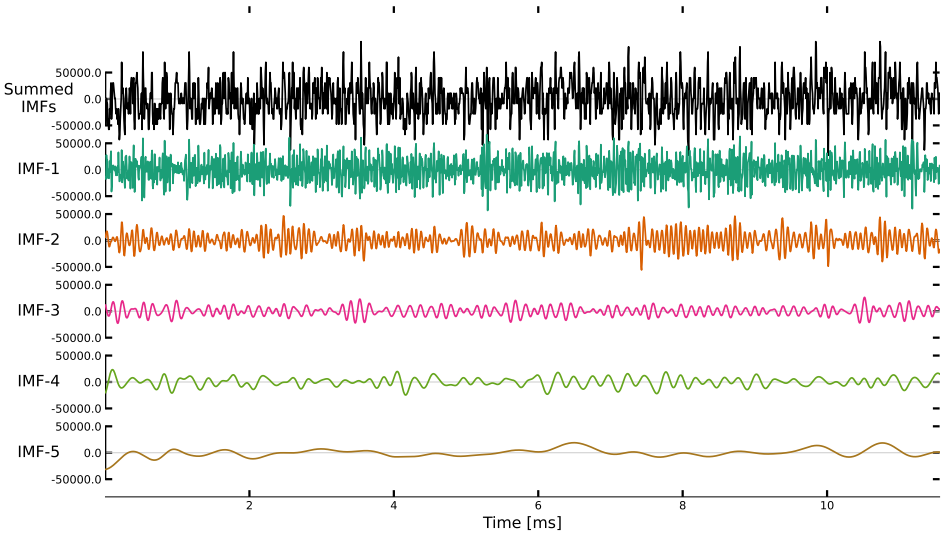

Figure 5.9 – Empirical mode decomposition of DIFDOP instantaneous velocity for shot TS47500, trigger 4, frequency 4. IMF-1 represent the largest frequency component identified by the EMD. The isolated components are of smaller frequency until IMF-5 that represents the residuals and is not an IMF-component *per se*.

lar frequency component (narrow band condition), they are well suited for the Hilbert transform. The use of EMD coupled to a Hilbert transform has been renamed *Hilbert-Huang transform*.

Applying the HHT to each IMF of the above decomposition gives the instantaneous frequency that can be presented in a $2d$ (time - frequency) plot, such as in Figure 5.10 for the GAM component.

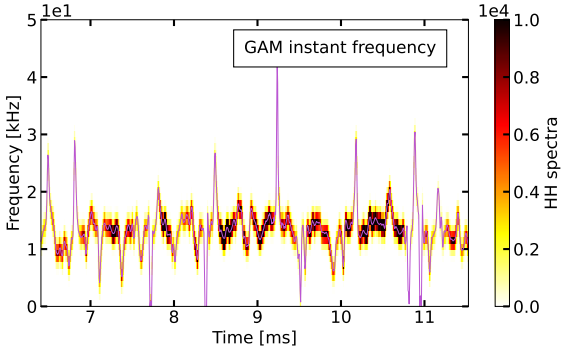

Figure 5.10 – Instantaneous frequency of IMF-2 weighted by its amplitude.

This method thus provides the instantaneous GAM frequency and its amplitude evolution. It has already been applied for the characterization of GAMs [134, 133]. See that the isolated GAM feature frequency varies in a broad range $5-20\ kHz$ despite using a mask at $F = 17\ kHz$. However, the amplitude of the signal is maximum around $13-15\ kHz$.

Summing the HHT over time for each IMF leads to a spectra weighted by the relative amplitude of each signal. The result is displayed in Figure 5.11.

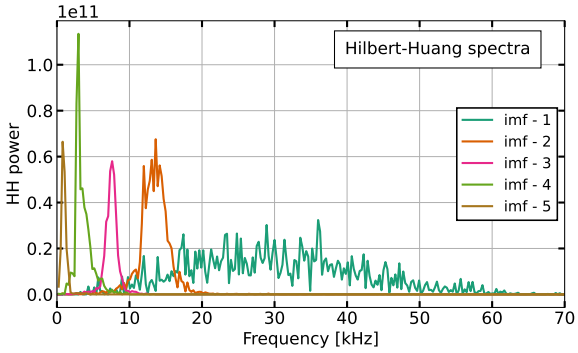

Figure 5.11 – 1D Hilbert-Huang spectra of decomposed IMFs. Instantaneous velocity of DIFDOP shot TS47500, trigger 4, frequency 4.

As expected, the distribution of the frequency content of each IMF is centered on the mask. The first IMF, contains all the high frequency information. Since the signal is the instantaneous velocity we discard this IMF afterwards considering that it contains mostly noise. The second IMF peaks at the GAM frequency, we will show later on that it is well-correlated at long distance. Thus we consider that this contains most of the information regarding the GAM identified in Figure 5.7. The third IMF is a sub-GAM mode. It is important for the analysis because it helps to separate more clearly the GAM from the low frequencies. It probably contains couplings of the intermittent GAM signal and the high frequency part of higher order IMFs. It is discarded in the following, but should be the focus on more development in the future. Finally, IMF-4 and 5 are linked to LFZFs, they are summed. A trial has been performed with a separate analysis on IMF-4 and IMF-5 and no qualitative change in the results has been observed.

5.2.4 Separate analysis on GAM and low frequency zonal flow

Now that the GAM component has been isolated we perform again the long range correlation. This time, we use the GAM (IMF-2) and the LFZF (IMF-4+5) signals. First, the PSD and CSD are shown for each IMF in Figure 5.12. In blue is indicated DIFDOP values, in red DREVE and in green their cross-spectral density.
Comparing these two figures to the whole signal spectral analysis in Figure 5.7, we notice that IMF-2 peaks at around 15 kHz as expected from the GAM feature. Also, the low frequency IMFs leads to a significant CSD signal as compared to the amplitude of each PSD.

Normalizing each CSD by their respective PSD yields the coherence presented in Figure 5.13.

IMF-2 appears correlated further supporting that the GAM has been well isolated. More interestingly, IMF-4+5 now emerges from the noise. In this case, removing higher frequency components and GAMs enables a better visualization of low frequencies. The coherence spectra is now similar to other contributions showing both LFZF and GAM such as ref.[140] for DIII-D and ref.[137] for HL-2A.

To conclude on this section, let us sum up the principal results:

1. Two similar but distant V-band DBS channels were used on a Tore Supra ICRH heated plasma.

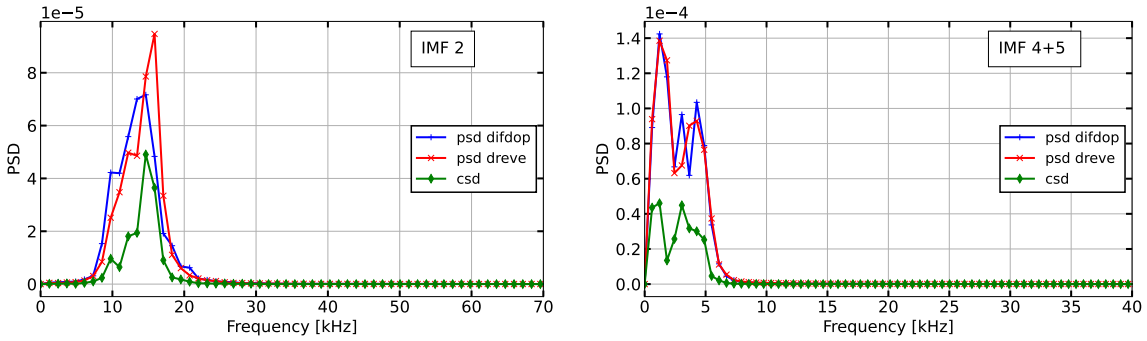

(a) (b)

Figure 5.12 – Power spectral densities and cross spectral density for IMF-2 (left) and IMF-4 (right). Analysis done on instantaneous velocity of #47500, trigger 4, frequency 4.

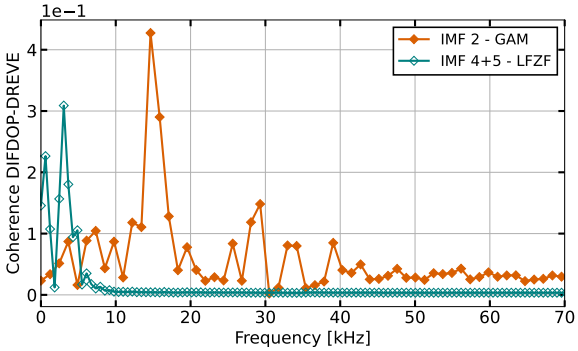

Figure 5.13 – Spectral coherence for IMF-2 (empty diamonds) and IMF-4 (diamonds). Analysis done on instantaneous velocity of TS47500, trigger 4, frequency 4.

2. Instantaneous fluctuation velocity is obtained through the MUSIC algorithm.
3. Long range correlation is performed on the velocity signal and shown to be dominated by a component at the GAM frequency.
4. The GAM component is isolated using empirical mode decomposition and its instantaneous frequency is obtained through Hilbert-Huang transform.
5. Low frequency zonal flows are isolated with the same method and appear with a significant correlation when the GAM feature is removed.

However, considering the amount of post-processing used, this method requires more statistics to be validated in different conditions. Unfortunately this configuration (top / equatorial DBS) couldn't be reinstalled in WEST so that these studies can be continued. It pushes towards jumping on any opportunity to install a second DBS system at any distant toroidal location (if not poloidal and toroidal) on any machine.

5.3 Avalanche-like transport characterization in TCV

In this section, the turbulence radial structure is studied in TCV plasmas using two radially coupled DBS channels in a configuration often called *correlation Doppler backscattering (CDBS)*.

Both the short scales (turbulent structure) and large scales (avalanches) are identified. While the short scale 'structure size' has been studied using various diagnostics [217, 218, 219], including CDBS [220], the second is more difficult to assess. One can note the work of P.A. Politzer [85] who observed avalanches propagation using the ECE diagnostic and the recent contribution of the LPP group [86] using CDBS.

The aim here is to modify the heating schemes so that the profiles and turbulent regimes are varied. By doing this, one can study the turbulence regimes most likely to generate avalanches and possible radial structures in the perpendicular flow.

5.3.1 The "Tokamak à Configuration Variable" (TCV)

The experiments are performed in TCV. The Ohmic heating is completed by an extended electron cyclotron resonance heating (ECH) system and two NBI beams providing up to 4.5 *MW* of additional heating power. The NBI system is composed of a co-current and counter-current beams (NBI-1 and 2). They are represented in Figure 5.14a. They are completed by a DNBI beam used for the charge exchange recombination spectroscopy (CXRS) diagnostic. The ECH system comprises several gyrotrons and launchers, indicated in Figure 5.14b by their line of sight, that can deposit power from equatorial and upper ports. Additionally, the lateral launchers poloidal and toroidal angles can be modified leading to a precise control of the power deposition.

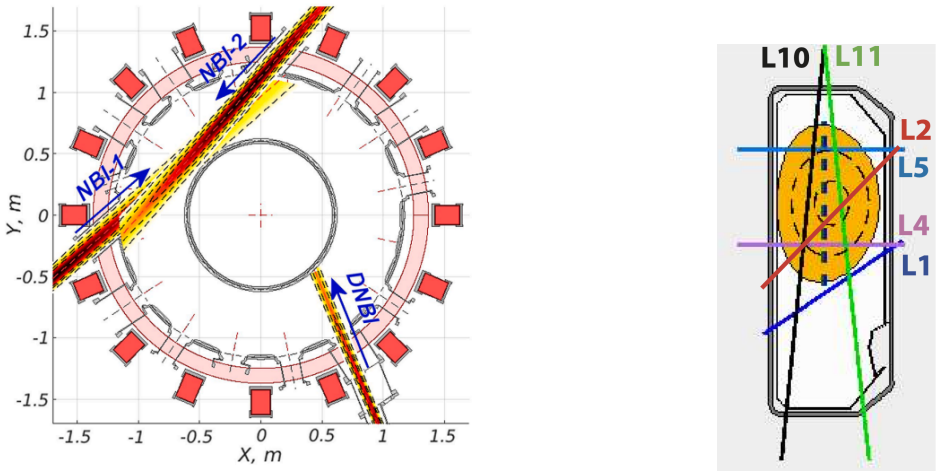

(a) (b)

Figure 5.14 – Auxiliary heating systems at TCV. (a) NBI system, figure adapted from [221]. (b) ECH launcher system, from SPC wiki.

The two NBI beams being opposite in direction, it enables the control of toroidal rotation. During the experiments conducted for this study NBI-2 was not fully operational. Therefore, there is only a little number of shots with both NBIs.

To characterize the turbulent regimes we need to measure the profiles of density and electron / ion temperatures. Additionally, we are interested by the toroidal velocity as it plays a role on the radial electric field. Knowing the velocity, one can better interpret the behaviour of the perpendicular velocity in the region dominated by the force balance equilibrium. For

these measurements, we rely on the Thomson scattering and charge exchange recombination spectroscopy (CXRS) systems.
The Thomson scattering system is the main diagnostic used for the measurement of electron density and temperature. The principle is to send a laser beam through the plasma that accelerate the electrons which will re-emit radiation. The electron temperature is then determined from the broadening of the scattered radiation spectra. The density is proportional to the total scattered power. In the present setup, 117 spectrometers are installed, covering various radial locations [222]. The Thomson scattering system is used in the following for the analysis of electron temperature and density profiles with the latter used for the beamtracing code of the DBS system.
The diagnostic is completed by a CXRS system used for the measure of toroidal velocity and temperature of carbon impurities. The principle is to send a neutral atom in the plasma that will collide with an ion. It results in the transfer of one of the neutral atom's electron to an excited state of the target ion. The charge exchanged excited state then decays to its ground state through a cascade of transitions that emit multiple characteristic lines. The integral of the obtained line is proportional to the density, the width to the temperature and the shift to the velocity in the line of sight (LoS) direction. In TCV, the measurements are optimized for carbon ions which is the principal impurity (≈ 1 %) due to carbon walls. Considering that ions and main plasma impurities are in thermal equilibrium, the measure of impurity properties gives a good proxy for the behaviour of main ions. In the present setup, the CXRS system makes use of the diagnostic neutral beam (DNBI) and comprises three optical observation systems: low and high field side (toroidal view) and a vertical view [223]. Specific information for the CXRS at TCV are indicated in ref.[224].

Access to TCV data is achieved in Python using a homemade code to navigate the MDSplus trees. Alternatively, jScope (java-based) can be used to access quickly TCV signals during the experiments. An example of a shot summary is shown in Figure 5.15 for #81069.

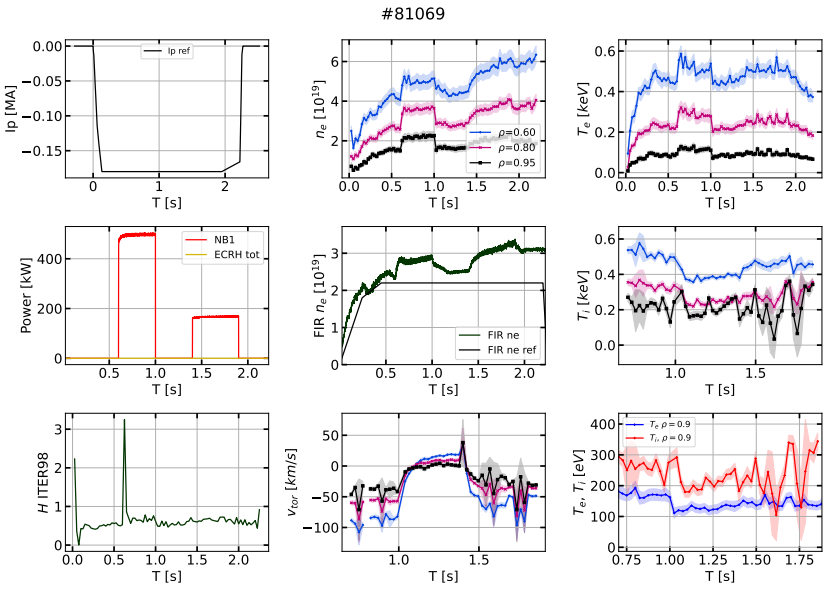

Figure 5.15 – Shot summary plot used for quick post-shot analysis. Example for #81069.

The summary contains basic time series information such as the plasma current I_p and heating scheme (left column). The electron density n_e and temperature T_e are estimated from Thomson measurements. The FIR n_e is taken from the far infrared interferometer and represents the line-integrated density for a central chord taken in the vertical direction together with the reference value for the gas injection. Finally, the data for T_i and v_{tor} are evaluated from CXRS measurements.

For turbulence measurements, we will rely on CDBS introduced in Section 5.1 to perform radial correlations. A brief comparison is also performed with short-pulse reflectometry (SPR) and thermal ion beam (THB), detailed in Section 5.3.6.

5.3.2 Designed experiments

As stated previously, the objective is to use the same equilibrium configuration with different heating schemes so that the profiles and consequently the underlying dominant instability are modified. Even if the instability stays the same, modifying the profiles enables the control the ion / electron temperature and the distance to threshold. The analysis is done for L-mode Deuterium plasmas. To be sure not to transit in H-mode even at larger NBI power, the chosen configuration is an unfavourable upper single null (USN) with a slight positive triangularity. The magnetic equilibrium is shown in Figure 5.16 for the shot #81084 along with the DBS launcher system. Examples of beamtracing are displayed in blue and pink. The last mirror is tiltable to adapt for different configurations and measurements at different $k_\perp$. Details on the launcher can be found in ref.[225]. The main shaping parameters are indicated on the right hand side.

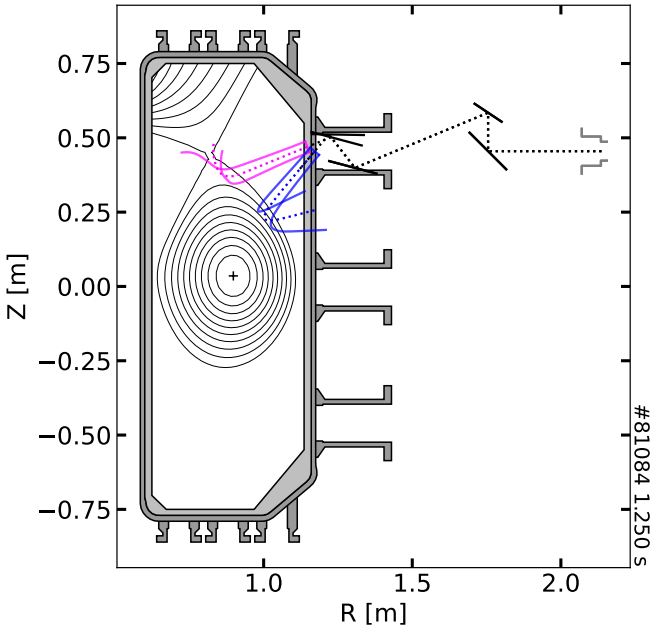

Figure 5.16 – Magnetic equilibrium of #81084 along with launcher system for DBS and SPR. Courtesy of S.Rienäcker.

Magnetic equilibrium
$I_p = -177\ kA$
$B_0 = -1.44\ T$
$q_{95} = 4$
$\beta_t = 0.355\ \%$
$\beta_N = 0.674$
$vol = 1.269$
$area = 0.231$
$R_{ax} = 0.898$
$Z_{ax} = 0.034$
$a = 0.233$
$\kappa = 1.535$
$\delta = 0.123$
$\delta_{top} = 0.233$
$\delta_{bot} = 0.014$

Table 5.1 – Magnetic parameters, using matlab routine 'liuqeplot'.

This shape has proven very stable in terms of MHD activity and plasma breakdown and has

been preferred to the equivalent unfavourable lower single null. Note that in this configuration, NBI-1 is co-current while NBI-2 is counter-current. Additionally, the DBS system probes the plasma from the top. It is comfortable to have an upper single null so that the diagnostic can probe as close as possible to the low field side to take advantage of the ballooned form of the turbulence. As such, the angle at which the DBS is used is also constrained from the plasma geometry. In the following we use an angle of $-50°$, which corresponds to the blue lines in Figure 5.16.

To maximize the use of the shots, since one correlation measurement takes only around $100ms$, two heating steps are used, such as shown in Figure 5.15. Note that the density is difficult to control in NBI heated plasmas at TCV, especially for the chosen configuration (see FIR $n_e > ref$ in Figure 5.15). Therefore, the recipe has been to separate the two heating steps with a central ohmic phase so that the density stays roughly constant throughout the discharge. The density control is particularly important for DBS since it imposes the location of the measurement through the cut-off frequency. The difficult density control also makes the coupling between NBI and ECH tricky. Indeed, ECH heating largely depends on the plasma density, and if it is too large the ECH power can be reflected anywhere in the vaccuum chamber and in the launcher. In the performed experiments, it proved very difficult to use both at the same time and ultimately the choice have been made to use them separately. The summary of the performed discharges is indicated in Table 5.2. Each row correspond to a heating plateau (usually two per shot). Since the SPR shares the antenna with the DBS, some discharges are repeated a second time to have correlation measurements with both diagnostics.

Shot	**Time window** $[s]$	**ECH** [kW]	**NBI-1** (ref) $[kW]$	**NBI-2** $[kW]$	**SPR**
82607	$[1.2-1.8]$	0	140 (170)	0	no
81069	$[1.4-1.8]$	0	167 (200)	0	81100
82607	$[0.6-1.2]$	0	250 (300)	0	no
81084	$[0.6-1]$	0	250 (300)	0	no
81065	$[0.6-1]$	0	260 (315)	0	no
81084	$[1.4-1.8]$	0	300 (355)	0	no
82615	$[1.2-1.8]$	0	300 (390)	0	82619
81065	$[1.4-1.8]$	0	355 (420)	0	no
82615	$[0.6-1.2]$	0	406 (480)	0	82619
81069	$[0.6-1]$	0	500 (590)	0	81100
82609	$[0.6-1.2]$	0	304 (360)	240	no
82609	$[1.2-1.8]$	0	358 (420)	280	no
81087	$[0.6-1]$	590	0	0	no
82611	$[0.6-1.2]$	590	0	0	no
82611	$[1.2-1.8]$	810	0	0	no
82612	$[0.6-1.2]$	890	0	0	no
82612	$[1.2-1.8]$	1180	0	0	no
81087	$[1-1.4]$	590	173 (210)	0	no

Table 5.2 – Deuterium unfavourable USN shots for correlation measurements. Each row corresponds to a heating step plateau. ECH, NBI-1 and NBI-2 represent the total injected power. The reference value is also indicated for NBI-1 (about 15% mismatch).

The resulting profiles are analysed using linear gyrokinetics to infer what type of instability is dominant. Six heating plateaus have been chosen at $P_{NBH} = 167, 260, 355, 500\ kW$ and at $P_{ECH} = 590, 1180\ kW$. The profiles of electron temperature T_e, ion temperature T_i, electron density n_e and toroidal velocity v_{tor} are displayed in Figure 5.17.

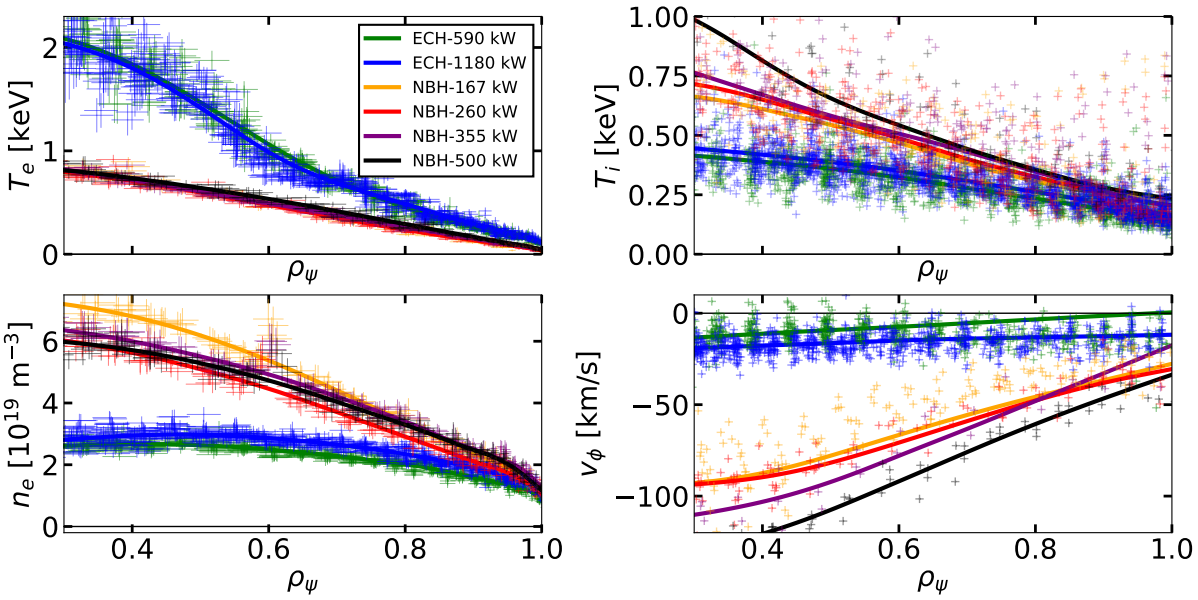

Figure 5.17 – Kinetic profiles used for the linear analysis. The NBH heated plasma profiles are taken at: $t = [1.65-1.75]; [0.85-0.95]; [1.45-1.55]; [0.65-0.75]$ for NBH= $167, 260, 355, 500\ kW$ respectively. ECH heated plasma profiles are taken at $t = [0.8-1.1]; [1.3-1.7]$ for ECH=$590, 1180\ kW$.

As expected, ECH and NBH scenarios lead to different profiles. The former leads to a large electron temperature and a comparatively low ion temperature. The electron density is lower in ECH plasmas so as to better couple the cyclotron wave. The NBH scenario leads to $\tau = T_i/T_e \approx 1$ and an important toroidal velocity. Note that the velocity in the core is negative because we used NBI-1 which is co-current ($I_p < 0$). While the different heating power leads to a slight modification of the ion temperature, no strong modification is observed for the electron temperature. Furthermore, the profiles are modified in the core, but edge ($\rho \approx 0.8-1$) gradients are similar in the selected shots. The main difference at the edge comes from the density profile, difficult to control as stated, and the toroidal velocity which increases with the NBH power.

Based on the above profiles, linear estimation of the growth rate and frequency are obtained with GENE by taking values of the gradient at $\rho = 0.95$. They are displayed in Figure 5.18. The simulations have been performed by A.Balestri.
In every tested cases, the dominant instability is in the electron direction. It is assumed that trapped electron modes (TEM) are the main instability as it is often the case for TCV plasmas [226, 227]. Some shots have been performed at different NBI powers and various densities to attempt modifying the dominant instability, without success. Indeed, part of the objective was to transit into regimes dominated by ITG/RBM like instabilities and / or collisional drift waves for a better comparison with simulations described chapter 4.

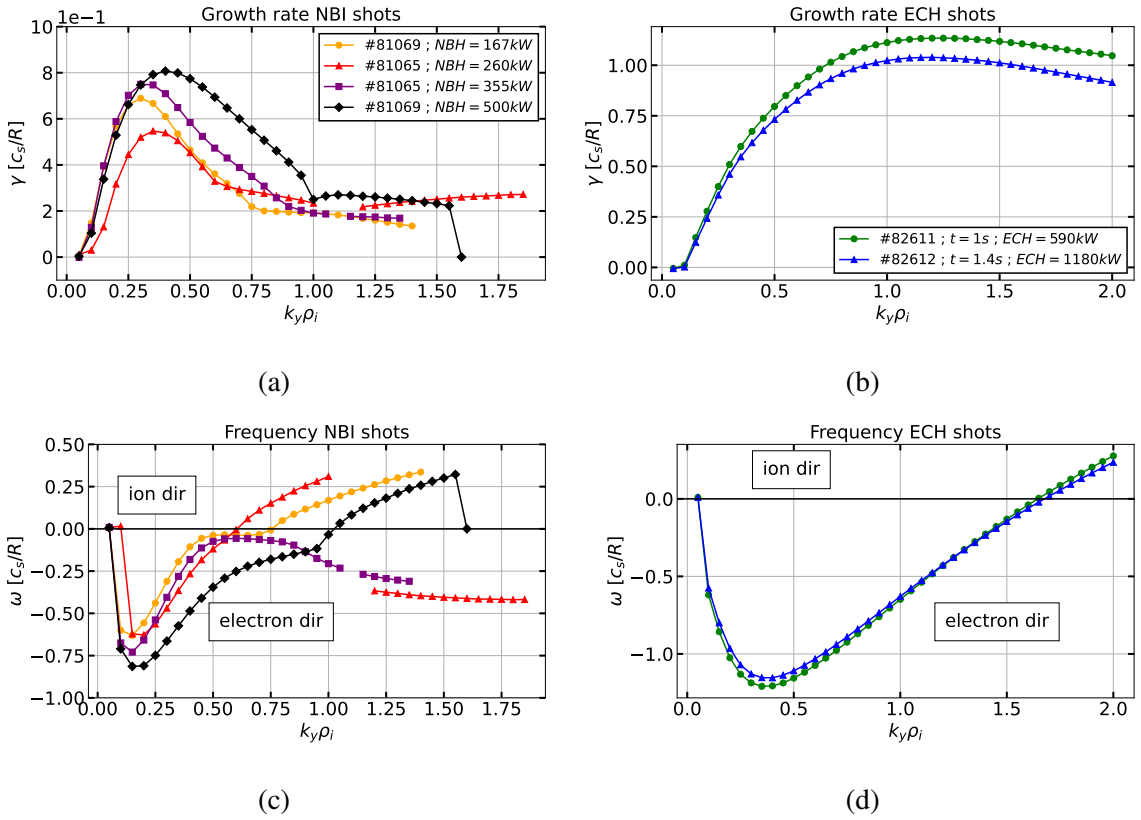

Figure 5.18 – Growth rate (a) and frequency (b) for four heating plateaus. Performed with linear gyrokinetic (GENE) by A. Balestri.

To compare the turbulence correlation length to characteristic scales we compute the Larmor radius $\rho_s = \sqrt{m_i T_e}/(eB)$ for each measurement using the local electron temperature and toroidal magnetic field. Note that here we compute it with the electron temperature because Thomson data are often more reliable than CXRS data. The Larmor radius is evaluated at the position of the reference DBS measurement for each heating plateau. The results are shown in Figure 5.19 as a function of ρ. The colour indicates the NBH and ECH heating power.

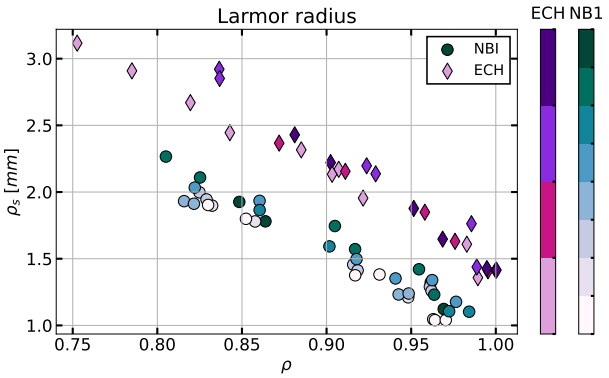

Figure 5.19 – Larmor radius $\rho_s = \sqrt{m_i T_e}/(eB)$ as a function of ρ and heating for discharges in Table 5.2. ECH ranges from 590 to 1180 kW and NBI from 140 to 500 kW.

Consistently with the above profiles, ρ_s only vary slightly of about $10-20\%$ as a function of the heating power. In ECH cases, it is mainly the electrons that are heated, so ρ_s also tends to be larger. The small variation of ρ_s is a direct consequence of the profiles being very stiff in the experiments. The local value of ρ_s will be used to normalize the correlation and avalanche lengths.

The DBS is configured as described in Figure 5.20: sweeps are repeated with the same frequency pattern. Each plateau indicated Table 5.2 corresponds to two sweeps. For shots $<$ #82607, a sweep represents two reference frequencies (200 *ms*). From #82607 onwards, the choice have been made to use three reference frequencies (300*ms*) to cover a larger part of the plasma radius.

5.3.3 Radial correlation measurement using a CDBS

In this section, we detail the method used to evaluate the radial correlation length (short scale and avalanches). CDBS was first been introduced by coupling two DBS such that microwave beams are launched from the same antenna with a small frequency difference resulting in each DBS probing a slightly different radial location [25]. It enabled the measure of the instantaneous velocity shear [25] ($\delta E_r/\delta r$). Additionally, this method led to the measure of the turbulence radial correlation length [220] and turbulent structures tilt angle [228, 229]. At last, more DBS can be coupled together, increasing spatial resolution and improving correlation measurements, for example with the *comb-frequency* DBS [230, 225].

In order to probe the turbulence radial structure, one DBS channel is used with a reference fixed frequency while the other channel scans the frequencies around the reference. A typical frequency scheme used at TCV for radial correlation is shown in Figure 5.20 for the example shot #81069.

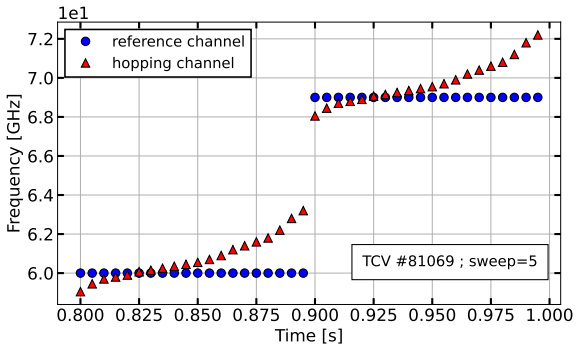

Figure 5.20 – Frequency pattern *sweep* used for correlation. Reference channel is indicated in blue (circles), hopping channel is in red (triangles). Shot #TCV81069, sweep 5.

Two reference locations are probed, at 60 and 69 GHz. Each point represents 5 *ms* of acquisition. Using the density profile and equilibrium magnetic field we compute the measurement locations using the beamtracing code. The result is displayed in Figure 5.21 for reference frequency 60 GHz. The poloidal section of the diverted upper single null plasma is shown on the left and a zoom on the turning points is indicated in the inset. The blue line (circle) corresponds to reference, the reds (triangles) to the hopping channel.

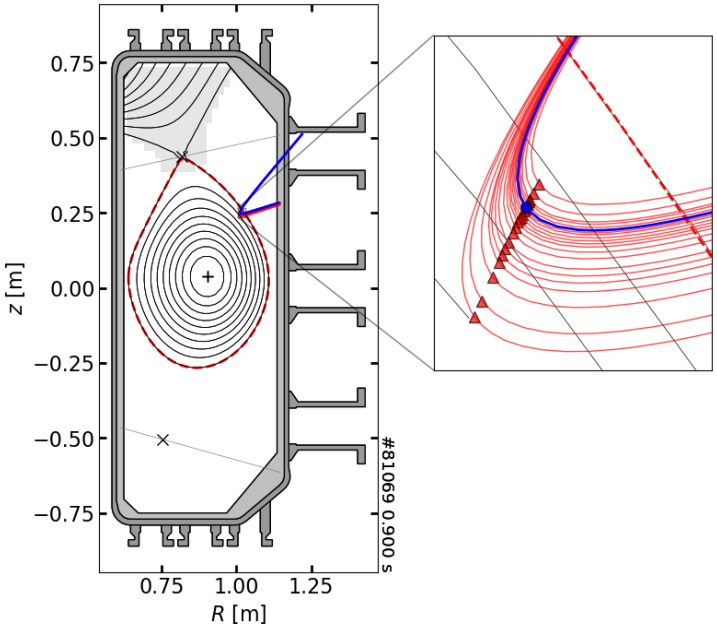

Figure 5.21 – Beamtracing for #TCV81069, sweep 5, angle $\theta = -50°$, $F_{ref} = 60\ GHz$.

Here the diagnostic is located on the upper part of the machine. Since the measurement depends on the turbulent activity, it is better to probe as close as possible to the outer mid plane to take advantage of the ballooned form of the turbulence.

We review briefly the method to perform the radial correlation using the example: #81069 ; sweep 5. The reference signal is taken at $F_{ref} = 60\ GHz$, the hopping signal is taken at 60.15 GHz. Two methods can be used to compute the correlation function: in direct or in Fourier space. The first consists in computing directly the amount of correlation at a time delay Δ_t by delaying one of the data time sequence by Δ_t. This gives a correlation function that depends on the time delay $\mathscr{C}(\Delta t)$, sometimes called *Pearson* correlation. The second, preferred in this work, consists in using Fourier space since the Wiener-Khintchine theorem states that the cross-power spectral density is the Fourier transform of the cross-correlation function. Using the same method as for evaluating the Doppler shift from the power spectral density of the signal, each signal is split in m segments of $n_{FFT} = 1024$ points with an overlap of 512 points. The PSD and CSD are displayed in Figure 5.22a. The spectral coherence is obtained by normalizing the CPSD by the PSD:

$$\mathscr{C}^2 = \frac{|csd|^2}{psd_{ref} \times psd_{hop}} \tag{5.8}$$

It provides a value of coherence between zero and one as a function of frequency, shown in Figure 5.22b.
Each spectrum is shifted with respect to zero due to the Doppler shift. Note that the zero frequency component is not plotted as it is at numerical noise level ($\approx 10^{-30}$). In this example both signals are obtained with close probing frequencies, hence the two beams probe close to each other and the Doppler shift is roughly similar. In case of larger distance, PSD maxima can be at different frequencies leading to a lower CSD signal. In those cases, the amplitude

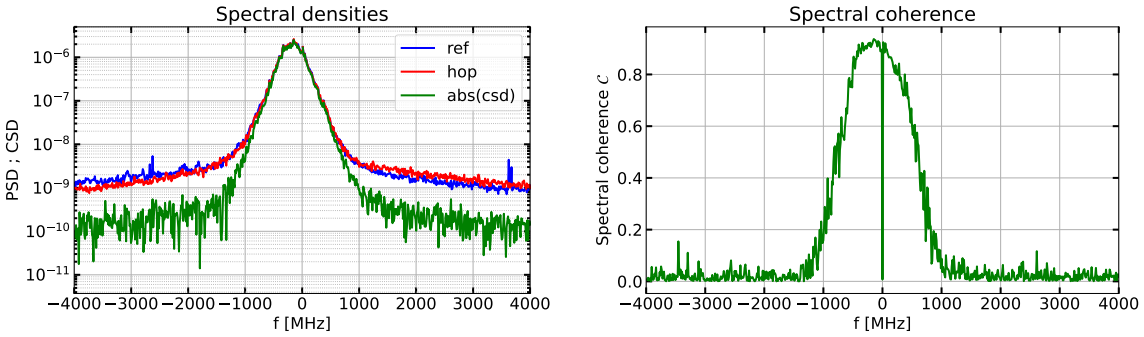

(a) (b)

Figure 5.22 – (a) Power spectral density and cross-spectral density (psd, csd) of reference and hopping signals. (b) Spectral coherence evaluated from csd and psd. Taken from #TCV81069 ; sweep 5 ; $(F_{ref}, F_{hop}) = (60, 60.15)$ GHz.

of the complex signals z_{ref} and z_{hop} can be used so as to center each spectrum around zero. Both signals being spatially close to each other, the maximum of spectral coherence is large ($\max \mathscr{C} \approx 0.9$). The time correlation function is then obtained by performing the inverse Fourier transform of the CPSD. The correlation function as a function of time is shown in Figure 5.23.

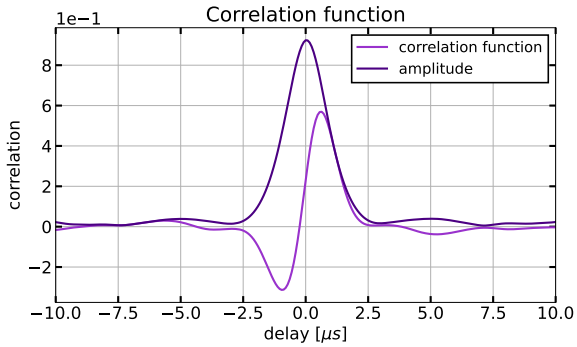

Figure 5.23 – Correlation function as a function of time delay, evaluated from the cross-spectral density. #TCV81069 ; sweep 5 ; $(F_{ref}, F_{hop}) = (60, 60.15)$ GHz.

Both the correlation function and its amplitude are indicated. The radial correlation function is then obtained by performing the correlation analysis and computing the maximum of correlation / coherence for each hopping frequency. Note that for signal with a large signal to noise ratio (SNR), both the Pearson and the Fourier methods lead to the same correlation as a function of time.

It should be emphasized that the correlation function which depends on time delay and the spectral coherence that depends on the frequencies bear different information. While the former measures the degree of similarity between two signals, the second considers the distribution of this correlation between the different frequencies. For the estimation of the maximum of correlation this is of upmost importance. Indeed, for noisy signals, the maximum of the correlation function collapses much faster than the spectral coherence. Conversely, for signals with good

signal to noise ratio, the correlation function gives a better estimation since it tends to have a lower variance.

When the signal to noise ratio is lower, a possible solution is to use the coherence spectrum instead of the correlation. However, due to the spectrum variance, the estimation of the maximum can be tricky. To solve this, we perform a fit of the coherence function. Depending on the nature of the signal we use a Gaussian or a Lorentzian fit so that the maximum of the spectral coherence is better fitted. The details on the methods used to perform the fits together with synthetic signals are provided in Section D.3.

The radial correlation function is estimated by performing the above analysis for each of the hopping frequencies (Figure 5.20). Since, the DBS does not probe from the midplane, the distance between the reference and the hopping locations is not estimated as a function of ρ but as a function of R and Z:

$$\Delta = \sqrt{(R_{ref} - R_{hop})^2 + (Z_{ref} - Z_{hop})^2} \tag{5.9}$$

With X and Z the probed location of the reference and hopping channels given by the beamtracing code.

Two radial correlation functions are displayed in Figure 5.24, one with a large signal to noise ratio (SNR): 81069 sweep 5 at $\rho = 0.96$, and a second with low SNR: 82607 sweep 5 at $\rho = 0.83$. For both cases, the different methods to estimate the maximum of correlation are shown: 'corr' corresponds to the maximum of the correlation function,'raw spec' to the maximum of the coherence function and 'fit spec' to the fit of the coherence function.

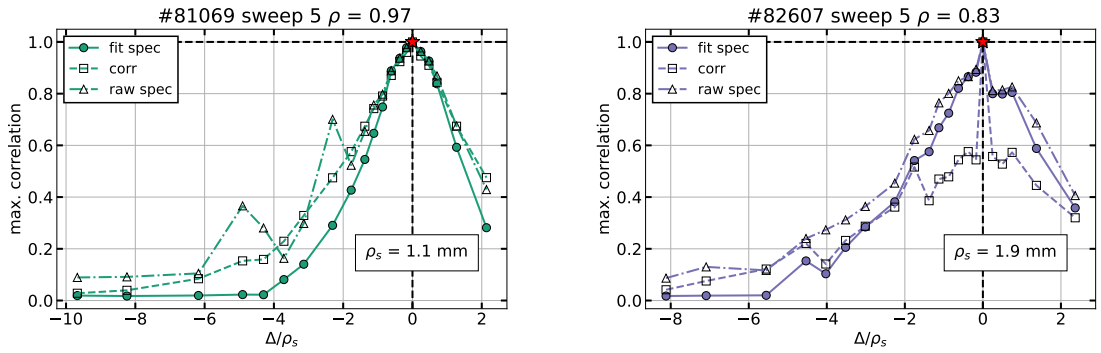

(a) (b)

Figure 5.24 – Radial correlation function evaluated from the maximum of correlation as a function of the distance between the two DBS channels Δ. The distance is estimated as a function of ρ_s the sound Larmor radius computed at the reference location. The red star notes the theoretical maximum of correlation at $\Delta = 0$.

On the left hand side, the signal is good. At small Δ each method provides a similar estimation of the maximum of correlation. At larger Δ the maximum of correlation estimated from the fit is below the rest of the estimates but exhibits less oscillations than its 'raw' estimate counterpart. On the right hand side, the DBS probes closer to the core at $\rho_{ref} = 0.83$ and the signal to noise ratio is lower. In that case, the maximum of the correlation function saturates at 0.6 due to the

noise. All in all, it is necessary to keep the same estimate when comparing between different shots. So as to have a good signal even in the core, the choice is made to use the 'fit' method in the following.

There is some debate over the best type of reflectometer signal to determine radial correlation length. In the above example, we used the full complex signal: $z(t) = x + iy(t) = Ae^{i\varphi}$ with $x = A\cos\varphi$ and $y = A\sin\varphi$ the results of the heterodyne detection. Therefore, one can perform the correlation measurements on the full signal z, its real and imaginary parts x, y, the amplitude A or on the phase $e^{i\varphi}$. In refs.[231, 220], the choice is made to use the full complex signal z to study the radial correlation length of the turbulence. However, as stated previously, when performing correlation at large radial distance, the Doppler shift of the two signals can be very different (depending on the local velocity shear). Conversely, if one takes the amplitude signal, the PSD maximum is located at the zero frequency component (the Doppler shift is removed). It results in a larger CSD signal and a better estimation of the density perturbation extension.

In Figure 5.25, radial correlation functions evaluated with z, A and $e^{i\varphi}$ are displayed. It shows that despite the short length correlation being similar in the full and amplitude signals, the second correlation slope only appears in the amplitude signal.

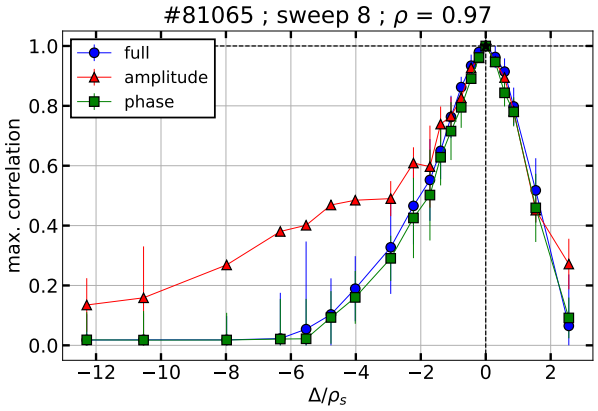

Figure 5.25 – Radial correlation function obtained from the max. of the fit performed on the spectral coherence. The computation is applied to the full complex signal (blue circles), the amplitude signal (red triangles) and the phase (green squares).

Ultimately, we aim at observing avalanches. Therefore, the amplitude is used in the following.

At last, the minimum level of correlation considered significant is estimated using the mixed files technique, detailed in Section D.4: random pairs of DBS reference and hopping signals are correlated. Using the fit of the coherence function, random pairs of signals are shown correlated at roughly $\mathscr{C} = 0.02$. In the following, no correlation below 0.05 will be considered significant. The mixed file technique has also been performed at specific frequencies and locations in the plasma to check whether probing further in the core leads to a larger correlation noise. No significative difference has been found. Thus, signals that are noisy lead to a lower overall correlation but do not modify the minimum of correlation considered significant.

5.3.4 Identification of avalanches using CDBS

In Figure 5.26, 4 typical examples of radial correlation functions are shown. Figure 5.26a and 5.26b are NBI-heated plasmas whereas Figure 5.26c and 5.26d are ECH-driven. The computation is made on the amplitude signal, using the maximum of the fit estimation. The errorbar is evaluated from the difference between the fit and the maximum of the raw spectral coherence. 3 different fits are performed on the logarithm of the signal. At short scale, for positive and negative Δ, the red and blue fits indicate the first slope of correlation. When the maximum of the radial correlation is not too low, this fit is imposed to 1 at $\Delta = 0$. The second slope, in green, corresponds to the avalanche signature. The structure size l_c and avalanche length L_a are evaluated from the inverse of the slopes. This amounts to consider that the correlation decreases like: $\max \mathscr{C} \propto \exp(-\Delta/l_{c,a})$, at short and large scale.

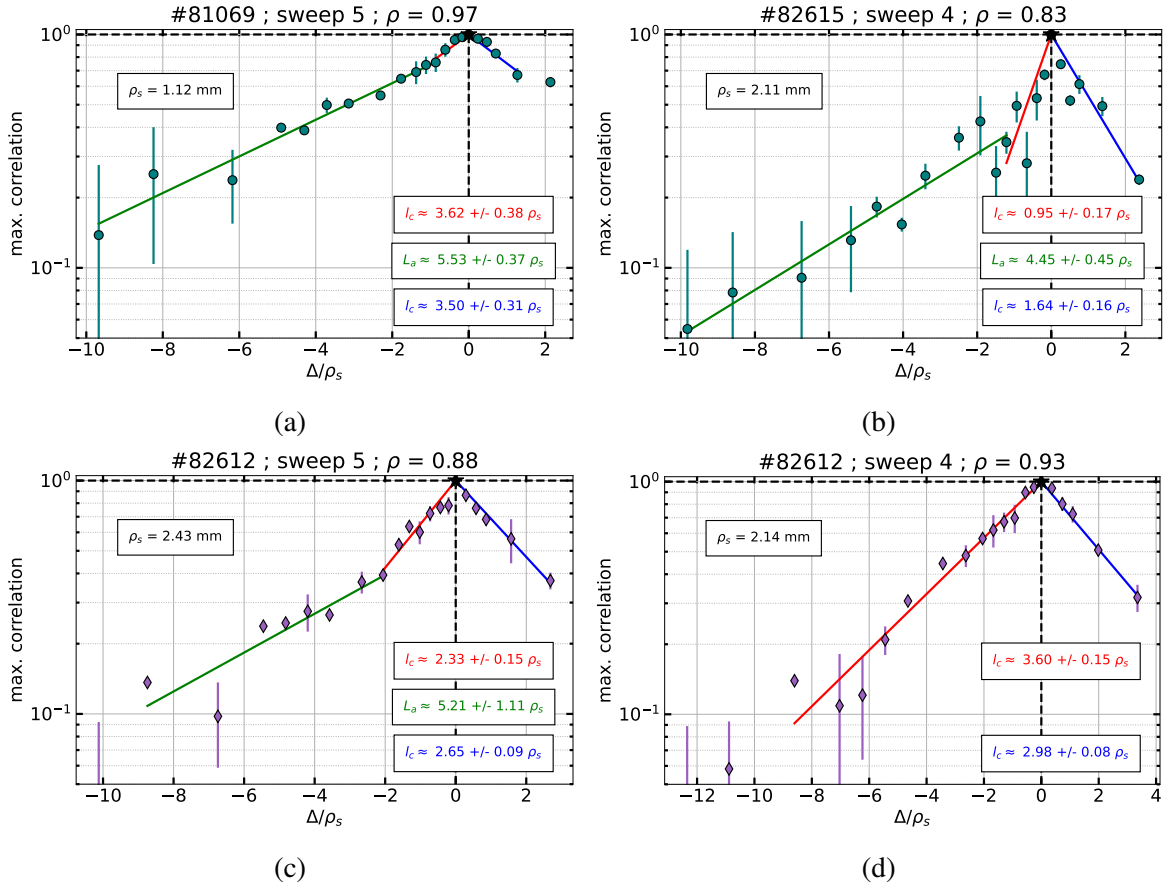

Figure 5.26 – Examples of semi-log radial correlation function evaluated from the amplitude signal through the maximum of the fit of the spectral coherence. Fits of the radial correlation function are performed at short scale (blue, red) and large scale (green). The correlation length is inferred from the inverse of the slope. The two upper cases correspond to NBH plasmas, bottom cases to ECH plasmas.

In some cases, such as (a) and (c), the radial correlation function clearly displays two slopes at small and large scale. It can even be difficult to assess the small scale correlation length as the avalanche can take up most of the signal. In other cases, such as (d), there is simply no evidence for a second slope of correlation. Finally, the most difficult cases to consider are the ones further

inside the plasma such as (b). Here, the signal is less good, data is noisy, and the maximum of correlation saturates at $\mathscr{C} = 0.75$. Additionally, the fits are more difficult to perform and no clear slope is present. In the presented case, an avalanche-like length is still observable but the short correlation length is difficult to infer. Moreover, the correlation function is not symmetric and the two estimates for l_c are different.

5.3.5 Smaller turbulent structures & avalanches near the separatrix

The size of turbulent structures and avalanches are analysed for every ECH and NBI-1 heated shots from Table 5.2. They are shown as a function of ρ_{ref} in Figure 5.27. Each point correspond to a DBS measurement (2 or 3 DBS measurements per heating plateau). The triangles indicate the small scale turbulence correlation length l_c, the empty circles display the spatial extension of the avalanches. Note that not every triangle is associated with a circle because avalanches have not been found in every correlation measurement.

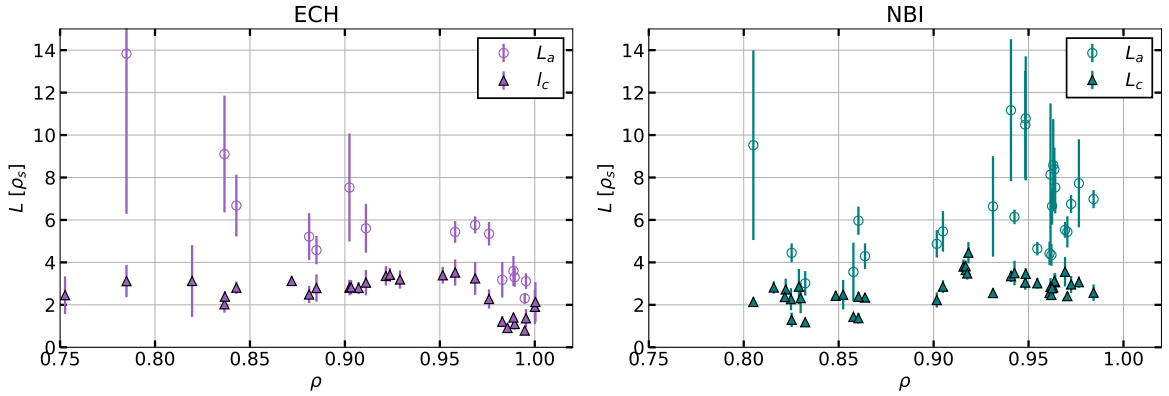

(a) (b)

Figure 5.27 – Radial correlation length of the turbulent structures l_c and avalanches L_a for every ECH and NBH plasmas as a function of ρ. The errorbar of l_c is given by the difference between the two estimates of l_c (both side of $\mathscr{C} = 1$) plus their standard deviation. The errorbar of L_a is given by the quality of the fit performed on the radial correlation function.

The turbulent structures are found to have a variable size between 2 and 4 ρ_s in most of the measured range. Close to the edge, l_c strongly decreases for the ECH plasmas to reach values of the order of unity. This area corresponds to the E_r well and will be described with more details in the following. Unfortunately, the measurements were not located in the E_r well for NBI cases and there is no comparison of the radial electric field and radial correlation length between ECH and NBI in this region.
Avalanches are found in both ECH and NBI plasmas. Their measured extension is mostly below 10 ρ_s. In NBI plasmas they are found mostly at the edge at $\rho > 0.92$, but it is also where the best DBS data is found so it is possible that the diagnostic misses some avalanches further in the core. They are of various size, with no dependence on ρ. In ECH plasma, the avalanches are also found to decrease strongly at the edge.
Interestingly, avalanches are found smaller than in simulations and earlier experiments. First, in the last chapter using Tokam1D, avalanches were found with a size of roughly 30 ρ_s. In

gyro-kinetic simulations, they are measured of the order of ($L_a^{sim} \sim 20-40\ \rho_i$) [104]. In AUG they have been found at $L_a^{AUG} \sim 20-30\ \rho_i$ with a turbulence correlation length of $l_c \approx 6-8\rho_i$ [86]. Note that those contributions use the ion Larmor radius and not the Larmor radius evaluated with T_e. In the case of TCV, electron temperature measurements are more reliable so the latter is preferred. Actually, both AUG and TCV data display avalanches of a few turbulence correlation length ($L_a \sim 2-5l_c$). The turbulence correlation and avalanche lengths normalized to the ion Larmor radius can be found in Section D.5. Why AUG and TCV have different turbulence correlation lengths could be due to different magnetic / velocity shear or to different turbulence regimes in those experiments. Additionally, TCV has a larger $\rho_\star = \rho_i/a$ since it has a comparatively low magnetic field with the same edge temperature as AUG. At this stage, the cause for the difference in l_c remains unresolved.

It is reasonable to ask the question of the role of the perpendicular velocity shear on the radial correlation measurements. Indeed, from the BDT model [19] we expect the velocity shear to reduce the radial correlation length of the turbulence. In the experiments performed, the core ($\rho < 0.9$) perpendicular velocity is largely dependent on the chosen heating power as shown in Figure 5.28.

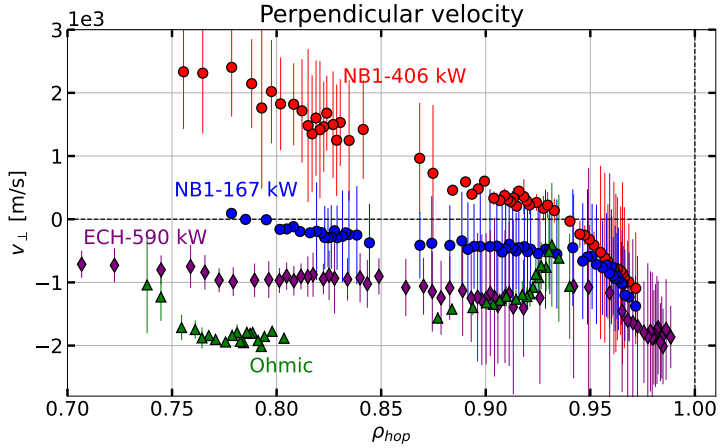

Figure 5.28 – Perpendicular velocity profile from the hopping channel as a function of heating. From top to bottom the cases are taken from: #82615 sweep 4, #82607 sweep 5, #82611 sweep 3 and #81065 sweep 6.

The perpendicular velocity profile is found to be articulated in two parts probably the sign of different physics. Close to the separatrix, in the E_r well zone, a similar profile is found whatever the chosen heating. This is not always the case obviously, especially in favourable configuration or with NBI at high power. Here, the experiments are performed in unfavourable configuration and far from L-H transition threshold. If one would approach the threshold, the $v_\perp$ well would deepen with the increased power. Interestingly a "bump" is observed between the E_r well region and the core region where the perpendicular velocity is larger (more positive) between the well and the core. In Figure 5.28 it can be seen on the Ohmic profile. It also occurs in some ECH and NBI discharges without a clear trend in heating scheme or power. Further inside the core, $v_\perp$ behaviour is in agreement with the radial force balance. The role of the toroidal rotation is particularly noticeable. Considering that B_θ, B_ϕ are negative and the convention displayed in

Figure 5.3, we recall the radial force balance:

$$v_\perp = \frac{\langle E_r \rangle}{B} = +\frac{\nabla p_i}{ne} + v_\phi B_\theta - v_\theta B_\phi \ . \tag{5.10}$$

In the present scenario, NBI-1 is co-current and $\mathbf{I}_p < 0$. That means a large NBI-1 power leads to a negative v_ϕ. In turn, provided that ∇p_i and v_θ do not vary too much, this results in a positive $v_\perp$ in the core. Note also, that increasing NBI-1, tends to increase the ion temperature which impacts $v_\perp$ through ∇p_i in the opposite way. The profiles of density n_e, electron temperature T_e, ion temperature T_i and toroidal velocity v_ϕ are displayed in Figure 5.29 for the same cases as in Figure 5.28. The electron density and temperature are taken from Thomson measurement. The toroidal velocity and ion temperature are inferred from CXRS data. The CXRS data is more noisy, in particular for the toroidal velocity. Therefore, in some cases, the errorbars are not assessed, but note that our primary focus here is the qualitative trends of the profiles.

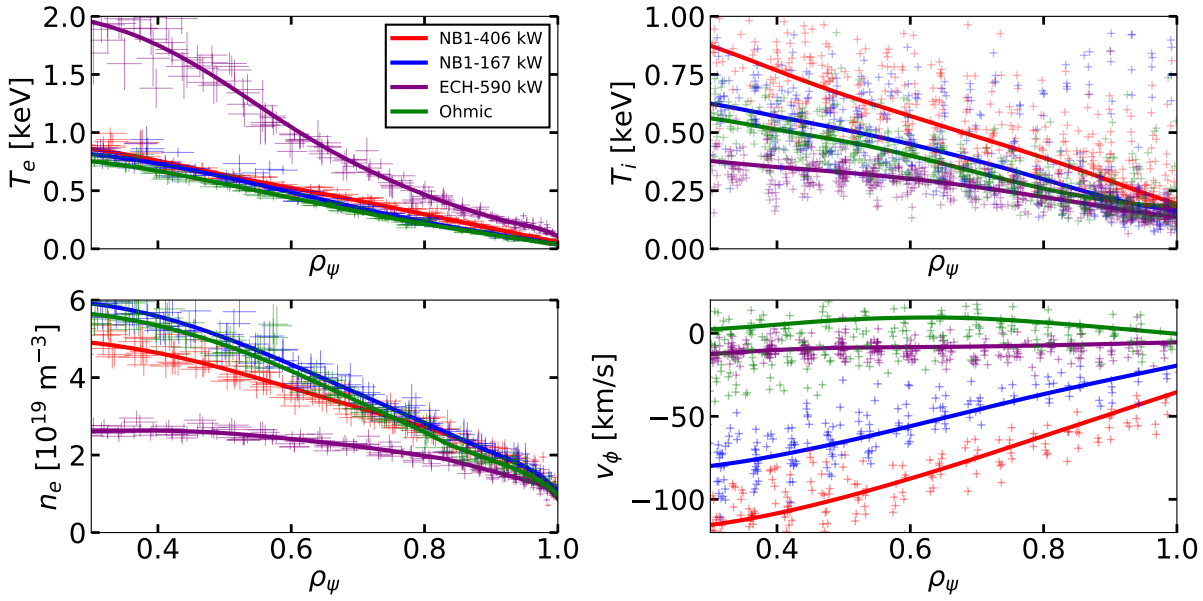

Figure 5.29 – Profiles of electron temperature T_e, ion temperature T_i, density n_e and toroidal velocity v_ϕ averaged over 100ms as a function of ρ and heating. The data is taken from Thomson (top row) and CXRS (bottom row) for discharges: #82615 sweep 4 (red), #82607 sweep 5 (blue), #82611 sweep 3 (purple) and #81065 sweep 6 (green).

Despite increasing the perpendicular velocity shear in the core, no effect of NBI-1 power is observable on the avalanches or correlation lengths, see Figure 5.30 (left). However, a slight effect of the heating might be observable on the 'importance' of the avalanche signal as compared to the rest of the statistic. To compute the importance of the avalanche, we measure the value of the correlation at which the second slope, thought linked to avalanche signal, begins on the correlation function. This gives a proxy bounded by 0 where no avalanche occurs and 1 which describes a signal with only avalanches. The increase of the avalanche 'importance' can be linked to either an increased frequency or increased amplitude of the avalanche-like events. The lengths l_c and L_a and the correlation at the beginning of the avalanche slopes are displayed in Figure 5.30. The colour indicates NBI-1 power.

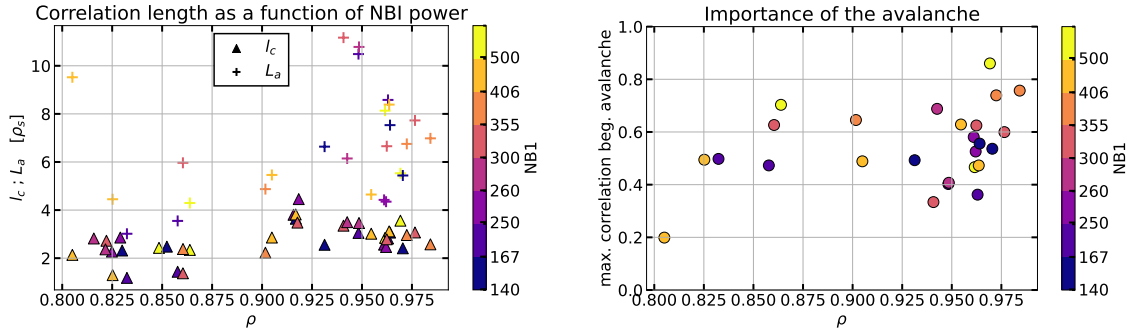

(a) (b)

Figure 5.30 – (a) Radial correlation length l_c and avalanche length L_a. (b) Beginning of the avalanche slope on the radial correlation function. The colour is set by the NBI-1 power.

The size of the turbulent structures l_c slightly increases at the edge of the plasma but no discernible impact of the heating power is observable. Similarly, the avalanches are shown scattered at different sizes without a clear dependence on the heating power. It is possible that the induced shear rate in the core is not large enough as compared to the growth rate of the underlying structures to decorrelate them. The proxy for the importance of the avalanche does not set a clear trend either. However, for $\rho < 0.92$, increasing the power at a given radial location leads to a more important avalanche. This observation also stands for the edge-most values measured in those simulations. We lack the necessary statistics to draw conclusions on the role of the NBI-1 power but this should be looked at in future experiments.

For ECH experiments, some measurements are inside the E_r well close to the separatrix. At these locations, the radial correlation length and the avalanche length are shown to decrease. The perpendicular velocity and radial correlation length of the turbulence l_c are shown in Figure 5.31 for the ECH cases.
The correlation length of the turbulence reduces from $l_c \sim 3\ \rho_s$ before the well to $l_c \sim 1.5\ \rho_s$ in the well. Interestingly, the avalanches lengths are also reduced in the E_r well but less than the radial correlation length. As a result, the normalized avalanche length L_a/l_c still increases.

5.3.6 Comparison of correlation lengths with SPR and THB

The characterization of the turbulence structure is compared with two other diagnostics: the short pulse reflectometry (SPR) already mentioned in the previous sections, and the thermal helium beam (THB). The first can measure density fluctuations by sending pulses into the plasma. As such, it measures locally and can be expected to measure larger structures as compared to the DBS. The second provides an estimate of the electron density and temperature while also enabling fluctuation measurements. The physical principle of THB consists in measuring the ratio between the intensity of different neutral helium lines puffed into the plasma edge. Further details on this diagnostic along with its specific application to TCV can be found in ref.[232].
SPR shares the launcher system with the DBS, it provides measurement from the same upper lateral port although at a different angle regarding the plasma surface. The THB consists in 8 lines of sight located at the outer mid-plane close to the separatrix. Their localization is shown in Figure 5.32 for the upper-single null shape used for this study.

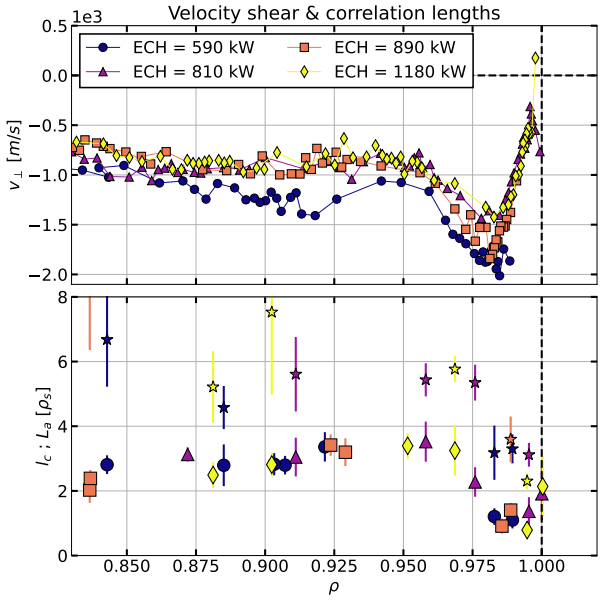

Figure 5.31 – (top) Perpendicular velocity profile for four ECH powers. (bottom) Associated turbulence correlation length l_c (various marker) and avalanches ($\star$)

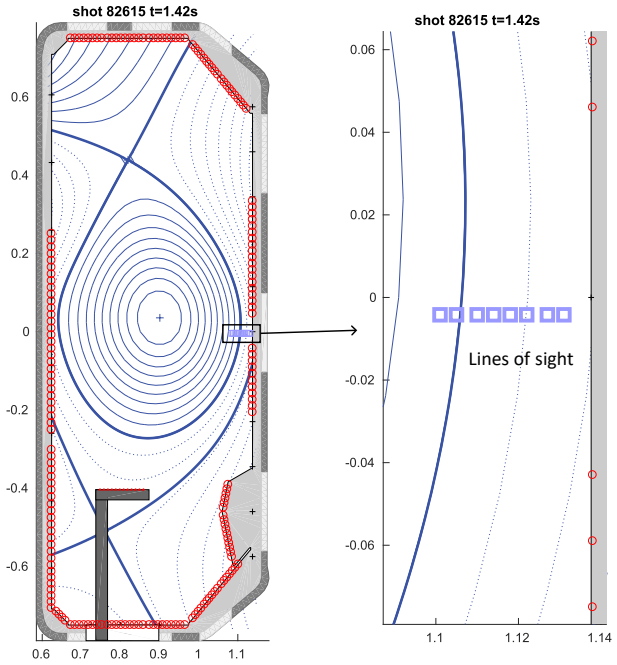

Figure 5.32 – Location of THB measurements courtesy for the magnetic equilibrium of shot #81084. Courtesy of M. Ugoletti.

For this scenario, the THB takes measurements in the scrape-off layer, from $\rho = 0.99$ to $\rho = 1.05$.

We compare the three diagnostics for the case $NBH = 300kW$ corresponding to shot #82615 for DBS and THB and #82619 for SPR. The radial correlation function computed with the SPR is plotted along with the DBS radial correlation function in Figure 5.33 against the absolute

distance normalized to the local Larmor radius Δ/ρ_s. For this heating plateau, one can infer one radial correlation function for the SPR and two for the DBS (sweep 5 and sweep 6). The DBS reference is located at $\rho = 0.92$ for sweep 5 and $\rho = 0.94$ for sweep 6. The SPR measurement is around $\rho \approx 0.93$. Here, $\rho_s \approx 1.4mm$.

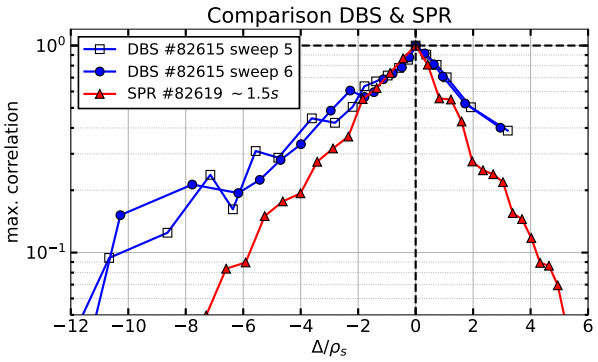

Figure 5.33 – Comparison of the radial correlation length obtained from SPR and DBS on two repeated shots as a function of the absolute distance normalized to the local sound Larmor radius. SPR analysis performed by U.Kumar and O.Krutkin.

On one side of the maximum of correlation, at short scale, both SPR and DBS are in very good agreement. They estimate a similar short scale turbulence correlation length $l_c \approx 3\rho_s$. At larger distance, the DBS amplitude signal stays better correlated than the SPR. However, note that no second slope is noticeable on the DBS signal. The result is preliminary and should be further investigated along with other discharges. However, it is encouraging and shows that a joint study between DBS and SPR can be carried out.

The THB is a complementary diagnostic relative to the other two. Indeed, in this configuration it measures in the scrape-off layer. 8 radial correlation functions are obtained by correlating one line of sight with the others. They are shown in Figure 5.34 (left) for discharge #82615 at $t = 1.42s$. Each color indicate the correlation of one LoS with the others. The width of each radial correlation function is evaluated, the result is shown on the right.
In the scrape-off layer ($\rho = 1 - 1.04$), the local hybrid Larmor radius is comprised between $\rho_s = 0.6 - 0.9mm$ depending on taking the measurement from the THB or the Thomson scattering system. The radial correlation length is of the order of the centimer, which corresponds to $l_c \approx 10 - 20\ \rho_s$. In the confined region, the radial correlation length is much smaller, of the order of $3\rho_s \approx 4 - 5mm$. It is expected that the filamentary structures in the SOL are bigger than those in the confined region. Actually, past experiments on ASDEX [233] and TCV [234], have characterized the blobs – filamentary structures in the SOL – of the order of the *cm*.

In this section, avalanche-like events have been observed on the radial correlation measurements done with CDBS. Those occured for USN unfavourable TCV plasmas driven by ECH and NBI. In every tested cases the plasma is dominated by an instability of electron type, likely TEM. The avalanches are observed at various heating power without clear scaling on the heating power. The avalanches are of the order of 5 to 14 ρ_s which is smaller than previously measured on AUG and predicted by gyrokinetic simulations. The chosen heating scheme is shown to modify the perpendicular velocity profile, especially through the role of the toroidal velocity.

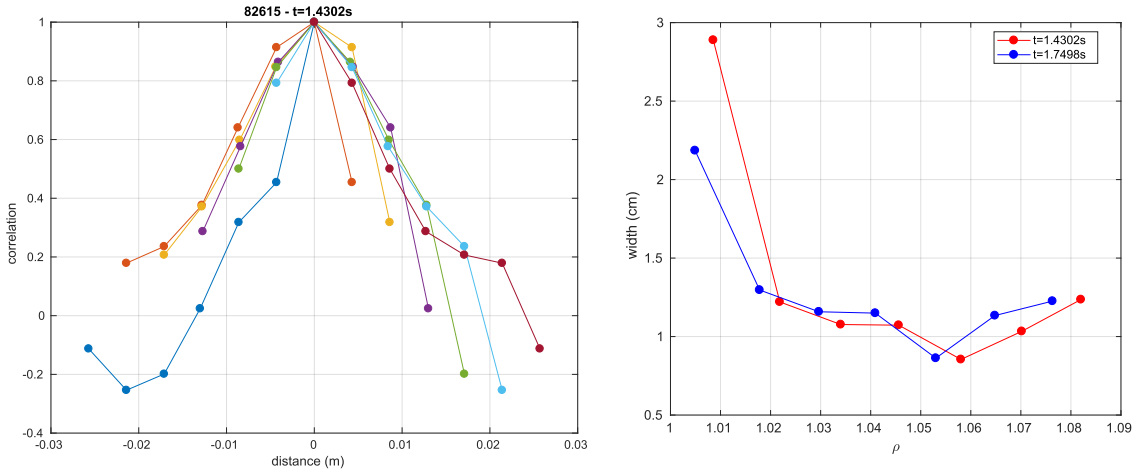

(a) (b)

Figure 5.34 – (a) Radial correlation function of each THB line of sight with the others at time $t = 1.42s$. (b) Width of the correlation functions as a function of ρ for two snapshots at $t = 1.42s$ and $t = 1.74s$. Analysis performed by M.Ugoletti.

In the core plasma, radial force balance effects are shown important to set the perpendicular velocity profile. Finally, only large shears such as found in the E_r well are found to reduce the size of the turbulent structure and avalanches.

5.4 Conclusion

In conclusion, the Doppler backscattering (DBS) has been used coupling two channels to analyse turbulence self-organization into flows and avalanches. DBS enables the measurement of the plasma perpendicular velocity from $\rho = 0.7$ to $\rho \gtrsim 1$, together with the measurement of the density fluctuations at a specific $k_\perp$. Correlating signals from two channels allows for additional insight on fluctuations and flow spatial structure

First, we utilize data collected from Tore Supra during the period when two DBS were installed. The two channels are separated poloidally and toroidally enabling long range correlation measurements. In order to observe low frequency zonal flows (LFZF), the density fluctuations signal is first processed using the MUSIC algorithm. This gives an estimate of the instantaneous Doppler frequency, thus of the perpendicular velocity fluctuations. By correlating at long distance the two velocity fluctuations signals, the velocity mode $(m,n) = (0,0)$, m being the poloidal and n the toroidal wavenumbers, is observed to oscillate at the GAM frequency. To better observe the low frequencies, the high frequencies and GAM feature are isolated and removed from the signal using empirical mode decomposition (EMD). The EMD proves efficient to identify and extract a signal of varying frequency and amplitude. The correlation of the "cleaned" signal is shown to be better correlated at small frequencies, possibly as a sign of a LFZF activity. Although being only performed on one discharge, this method is promising for the study of LFZF. Ideally, this method should be applied to longer time sequences on a stable plasma to better observe the low frequencies. Then, one would need to repeat this operation at various densities and with different heating schemes to compare the properties of the LFZF

with theories and simulations.

Then, using two co-located DBS channels in TCV, radial correlation length measurements are performed. A large number of discharges are analysed in L-mode, unfavourable, USN configuration, where the plasma is shown dominated by trapped electron modes. In addition to the usual decay of the radial correlation function at small scale, a second slope (larger scale) is observed in most of the discharges, principally at the edge of the confined plasma. By analogy with Tokam1D, the second slope of correlation is understood as a signature of avalanches. The avalanche-like events are observed at various heating power – both ECH and NBH – with lengths ranging from 5 to 14 ρ_s. In the core, no relation between the size of the turbulent structures and the velocity shear is observed, though the perpendicular velocity profile (and its shear) could be changed by momentum injection through the heating beams. In regions of large velocity shear, such as the E_r well, the radial correlation length is shown to decrease along with the avalanche length.
The same analysis at larger power – approaching the L-H transition – should be performed to see if the increased velocity shear further impacts the avalanches and turbulent structure sizes. For future analysis, discharges in Deuterium and Hydrogen with matched profiles of electron and ion temperatures, density and toroidal velocity have already been performed. The scaling of the avalanches with the characteristic Larmor radius size can be studied. Additionally, the radial correlation between velocity fluctuations obtained with the MUSIC algorithm should be performed to measure the scaling of the velocity structures. Hydrogen plasmas tend to be more stiff – about 30% more heating required in NBI to get the same profiles – so we can expect stronger avalanche activity. This increased avalanche activity could manifest as a break in the slope of the radial correlation function. It is expected that the break in the slope will occur at higher correlation values in hydrogen. Avalanche extents could also be larger in Hydrogen as compared to Deuterium.

Finally, it should be noted that no corrugated perpendicular flows have been observed in the performed experiments. It is possible that the turbulent regime does not favour the appearance of radially structured flows or that the time needed for a velocity profile ($\sim 100-200$ *ms*) is too long for their relative stability. In the previous chapter simulations, structured flows were found mostly in interchange driven plasmas close to the threshold whereas in the experiments, the plasma is driven by trapped electron modes. Developing a scenario dominated by an interchange-like instability such as RBM or ITG at TCV should be the focus of a future work.

Conclusion

This thesis work focuses on the study of turbulence and its self-organization in fusion plasmas. Understanding turbulence is key for present and future fusion experiments. It governs the transport of heat and particles from the hot core to the edge of the tokamak. As such, it controls the energy confinement time which is a size-determining factor for future machines. The physics of turbulence itself is also a fundamental subject, for which there is still much to discover. Turbulence in magnetized plasmas is predicted and sometimes observed to lead to complex dynamics such as avalanching processes and mesoscale structures called zonal flows. While the first leads to an important transport of heat and particles, the second is beneficial for the confinement as it produces no transport while constituting a well for the turbulence energy. The combination of avalanches and radially localized stable zonal flows - called an $E \times B$ staircase - can possibly lead to micro-barriers beneficial for the overall confinement.

The thesis first objective is to study turbulence regimes leading to the appearance of such mesoscale structures. Can we better identify regimes favouring the generation of zonal flows, avalanches and staircases? Additionally, the work aims at giving insight on the self-organization itself: what kind of interplay characterizes avalanching processes and zonal flows? Finally, while these aspects of self-organization are crucial in turbulence simulations, their experimental characterization is challenging. Can we better predict turbulence self-organization and its impact on measurable signals, possibly in various turbulence regimes?

The results of this work can be summarized on two levels. At a general level, we developed a reduced fluid model aimed at the turbulence and flows interaction study. We used the model extensively to characterize both the linear and the nonlinear behaviours in the turbulence parameter space. Various ways forward have been explored by introducing further elements of physics to account for more complex effects regarding turbulence and flows. The model is not made to reproduce quantitatively experimental result but (i) to identify some underlying physical mechanisms of turbulence self-organization and (ii) to explore the behaviour in a vast parameter space. As such, the model is also a guide for experiments: it provides possible signatures of turbulence self-organization that could be observed in experiments and suggest regimes in which these structures are most likely to emerge. Based on this, experiments are performed with a Doppler backscattering (DBS) to measure density fluctuations at a specific wavenumber. On a more detailed level, each chapter has addressed a specific problem. The key findings along with future perspectives are detailed in the following.

In chapter 3 we develop a reduced model aimed at the turbulence and flow interaction for which several key elements have to be included. First and foremost, the equilibrium profiles have to be evolved self-consistently. Turbulence self-organization is tightly linked to equilibrium profiles. Indeed, profiles can develop small scale corrugations, crucial for the onset of

avalanches and staircases. This physics is included by making the model flux-driven: the equilibrium profiles can evolve consistently as a balance between a source and a turbulent transport generated by the fluctuations themselves. Second, the model needs to involve several relevant instabilities. This is done by including two instabilities expected important at the edge: collisional drift waves (CDW), linked to the parallel phase shift between density and electric potential fluctuations, and interchange, driven by the inhomogeneity of the magnetic field. Third, the edge region - both sides of the last closed flux surface - has already been identified as key. In this region occurs the transition from close to open flux surfaces and the development of the edge transport barrier leading to improved confinement regimes. It is characterized by an important collisionality making the fluid approach possible. Fourth, the model needs to run fast, on confinement timescales. This is necessary to perform turbulence parameter scans where profiles have the time to adapt to turbulence and reach statistical steady-state. To this aim, the model is reduced to one dimension by keeping a single poloidal and parallel wavenumber for the fluctuations. As such, the primary saturation mechanisms for turbulence are due to the density profile relaxation - in the spirit of quasilinear theory - and the storage of turbulent energy into equilibrium flows. These two mechanisms play important roles in weakly forced systems that remain close to marginality. The model is derived first for an electrostatic, L-mode, isothermal plasma. Some extensions are discussed by including scrape-off layer physics and electromagnetic effects.

The linear study of the derived model is conducted in the different configurations: electrostatic confined region, electrostatic scrape-off layer and electromagnetic. Both interchange and CDW are observed with the former leading to a larger growth rate and sine of the cross-phase than the second. The adiabatic parameter is shown stabilizing for the interchange. The compressibility terms, originating from the divergence of the velocity, are also shown stabilizing when the magnetic curvature g becomes large. Under the assumptions of the model, the SOL is stable to CDW and driven only by interchange. Finally, the electromagnetic linear analysis is conducted. The parameter β stabilizes the CDW instability and destabilizes the interchange instability. In the large β limit, the ideal MHD instability is recovered.

Using the so-called Tokam1D in the electrostatic core version, the turbulence parameter space in scanned in chapter 4.
First, zonal flows are found to emerge principally at large parallel conductivity, in CDW dominated plasmas. A reduction of the ZF activity is found when lowering the conductivity but no collapse of the ZF energy is observed. This stands in contrast to previous contributions and is found to result from the nature of the forcing, flux-driven instead of gradient-driven. The system has more freedom to adapt, leading to a smoother transition from turbulence to flow dominated regimes.
Second, a flow dominated regime is also found in interchange driven plasmas, at high magnetic inhomogeneity. This second regime leads to stable in time, radially localized ZF layers. Overall, radially structured flows are mainly found in interchange turbulence, close to marginality. In the performed simulations, radially localized flows always lead to staircase-like corrugations of the density profile.
Third, both the electric and the diamagnetic contributions to the Reynolds stress appear crucial for the generation of ZFs although their effect can be synergistic or competitive depending on

the turbulent regime. In interchange driven plasmas, both components are in phase opposition but the electric contribution is much larger than the diamagnetic. In CDW driven plasmas, the diamagnetic contribution is dominant. Finally, at large C, both components are in phase and of the same magnitude. The Reynolds stress behaviour is consistent with the quasi-linear dynamics of the underlying instabilities. The density, electric potential fluctuations and their cross-phase are found in qualitative agreement with the linear predictions.
Fourth, avalanches are also found in interchange driven plasmas. They can propagate on small or large fraction of the simulation domain depending on the interchange parameter. When large, they are not found to be bounded by shear flows. Conversely, they are shown to reactivate the flow structures, giving energy to the shear layers while travelling through them.
Finally, the simulations confinement time is assessed. While being principally governed by linear properties such as the instability threshold and stiffness, simulations exhibiting larger flow to turbulence energy ratio yield a larger particle confinement time. When normalizing the confinement time with a mixing-length estimate, it is found that simulations displaying staircase-like structures perform better.

At last, these characteristics of the spatial structure of turbulence and ZFs have been seeked in experiments. Two configurations of a multi-channel Doppler backscattering (DBS) system have been used. The DBS enables the measurements of the density fluctuations at a selected wavenumber and their advection velocity in the edge region of tokamaks.
On Tore Supra, the zonal structure was studied through correlations between two distant channels poloidally and toroidally separated, while measuring the same radial location. A detailed analysis of existing data showed that the long range correlation signal is dominated by a geodesic acoustic mode (GAM) component. To better identify low frequency zonal flows, the high frequency noise is removed along with the GAM using empirical mode decomposition. This method enables the identification of time-varying frequency components inside a signal. When the signal is cleaned from its high frequencies, a long-range correlation signal is obtained at low frequency, reminiscent of zonal flows.
On TCV the radial structure was investigated from correlation of two co-located channels in L-mode trapped electron mode dominated turbulence. Two slopes are identified on the radial correlation function of the density fluctuations. By analogy with the reduced model simulations, the first slope is identified with small scale turbulence correlation length and the second slope with avalanches. Both lengths are robustly found at various heating powers using electron cyclotron resonance heating (ECH) and neutral beam heating (NBH).
Although no staircases have been identified in those experiments, the methods tested pave the way towards other experiments, in different turbulent regimes and closer to H-mode.

The present work opens perspectives. First, on the derived model itself. A few model additions have already been implemented and need to be tested thoroughly in nonlinear simulations:

1. Include an equilibrium force balance velocity. This velocity depends on the density profile and plays a role in setting an edge transport barrier through a positive retroaction loop: increased gradient leading to a larger velocity shear.
2. Add the transition from the confined core plasma to the outer scrape-off layer (SOL). First, the radial electric field is shown to changes sign in the SOL thus impacting the equilibrium flow and shear. Second, the interaction with the wall and neutrals is key in

the whole dynamics. Including the SOL opens possibility for studying plasma-wall and plasma-neutral interactions.

3. Evolve towards an electromagnetic nonlinear turbulence model. Those effects are key in cases of large gradient zones such as the pedestal during the L-H transition. Having an electromagnetic model enables the study of turbulence-flow interaction when getting closer to H-mode conditions.

Additionally, two pieces of physics can be included at lower cost while providing significant value. First, taking into account the density dependence of the adiabaticity parameter. The parameter controls the amount of energy stored into the flows, and more insight on the development of flows close to the edge could be gained if their development would depend on the underlying density value. Second, the GAM physics. They represent an interesting third party possibly able to exchange energy with both the zero-frequency flows and the turbulence.

On the experimental point of view, we have shown the interest of having distant DBS channels for identifying ZFs. The analysis method used to clean the long range correlation signal from high frequency noise and GAM is promising. Unfortunately, only limited data were available in this configuration. Although tokamaks often lack the space to accomodate these systems, these findings push towards further experiments in such configurations with long range coupled Doppler backscattering systems. Based on the model, they should be performed in interchange-driven plasmas at intermediate density. To characterize whether the observed low frequency signal is reminiscent of zonal flows, its dependence on density can be assessed. From the simulations, we expect a higher density to lead to a decrease turbulence drive (lower adiabatic parameter) and stronger collisional damping. Additionally, avalanche measurements are robust and should be performed in other turbulence regimes. Experiments have already been performed using matched profiles between Hydrogen and Deuterium plasmas, their analysis will provide more knowledge on the scaling of turbulence structures with the normalized Larmor radius $\rho_\star$.

Interestingly, turbulence self-organization is a generic enough problem to be shared with other plasma and neutral fluid systems. This spans from large-scale atmosphere circulation and ocean staircases to solar tachocline stability and planetary formation. Much can be gained by integrating insight from these different fields and engaging in cross-field collaboration.

Bibliography

[1] John D Lawson. Some criteria for a power producing thermonuclear reactor. *Proceedings of the physical society. Section B*, 70(1):6, 1957. 23

[2] Samuel E Wurzel and Scott C Hsu. Progress toward fusion energy breakeven and gain as measured against the lawson criterion. *Physics of Plasmas*, 29(6), 2022. 25

[3] AB Zylstra, OA Hurricane, DA Callahan, AL Kritcher, JE Ralph, HF Robey, JS Ross, CV Young, KL Baker, DT Casey, et al. Burning plasma achieved in inertial fusion. *Nature*, 601(7894):542–548, 2022. 24

[4] Alexandre Storelli. *Étude du transport turbulent dans les plasmas du tokamak Tore Supra : observation des écoulements perpendiculaires stationnaires et du mode acoustique géodésique*. PhD thesis, Ecole Polytechnique, 2015. 27, 179

[5] F.L. Hinton and C.W. Horton. Amplitude Limitation of a Collisional Drift Wave Instability. *Phys. Fluids*, 14:116, 1971. 29, 59

[6] A.I. Smolyakov. Gyroviscous forces in a collisionless plasma with temperature gradients. *Can. J. Phys.*, 76:321–331, 1998. 29

[7] John Wesson and David J Campbell. *Tokamaks*, volume 149. Oxford university press, 2011. 31, 36, 124

[8] Per Helander and Dieter J Sigmar. *Collisional transport in magnetized plasmas*, volume 4. Cambridge university press, 2005. 31, 35, 37, 91

[9] Nicolas Rivals. *Understanding density regimes and divertor detachment in ITER relevant conditions*. PhD thesis, Aix-Marseille university, 2023. 32

[10] Yann Munschy. *Kinetic physics of edge-core interaction in fusion plasmas*. PhD thesis, Aix-Marseille university, 2024. 32

[11] Virginia Quadri. *Turbulence - neutrals interaction and its impact on density regimes in the edge plasma of tokamaks*. PhD thesis, Aix-Marseille university, 2024. 32

[12] Peter C Stangeby et al. *The plasma boundary of magnetic fusion devices*, volume 224. Institute of Physics Pub. Philadelphia, Pennsylvania, 2000. 32, 97

[13] Fulvio Militello. *Boundary Plasma Physics*. Springer, 2022. 32

[14] Yann Munschy, Emily Bourne, Guilhem Dif-Pradalier, Peter Donnel, Philippe Ghendrih, Virginie Grandgirard, and Yanick Sarazin. Kinetic plasma-wall interaction using immersed boundary conditions. *Nuclear Fusion*, 64(5):056027, 2024. 32

[15] Harold P Furth, John Killeen, and Marshall N Rosenbluth. Finite-resistivity instabilities of a sheet pinch. *The physics of Fluids*, 6(4):459–484, 1963. 37, 80

[16] Emily A Belli and J Candy. Neoclassical transport in toroidal plasmas with nonaxisymmetric flux surfaces. *Plasma Physics and Controlled Fusion*, 57(5):054012, 2015. 37

[17] Guilhem Dif-Pradalier, Philippe Ghendrih, Yanick Sarazin, Elisabetta Caschera, Frédéric Clairet, Yann Camenen, Peter Donnel, Xavier Garbet, Virginie Grandgirard, Yann Munschy, et al. Transport barrier onset and edge turbulence shortfall in fusion plasmas. *Communications Physics*, 5(1):229, 2022. 38

[18] L. Prandtl. 7. bericht über untersuchungen zur ausgebildeten turbulenz. *ZAMM - Journal of Applied Mathematics and Mechanics / Zeitschrift für Angewandte Mathematik und Mechanik*, 5(2):136–139, 1925. 39, 155

[19] Hamed Biglari, PH Diamond, and PW Terry. Influence of sheared poloidal rotation on edge turbulence. *Physics of Fluids B: Plasma Physics*, 2(1):1–4, 1990. 40, 41, 147, 155, 198

[20] N Fedorczak, Ph Ghendrih, Pascale Hennequin, GR Tynan, PH Diamond, and P Manz. Dynamics of tilted eddies in a transversal flow at the edge of tokamak plasmas and the consequences for l–h transition. *Plasma Physics and Controlled Fusion*, 55(12):124024, 2013. 40, 41

[21] P Beyer, S Benkadda, Xavier Garbet, and PH Diamond. Nondiffusive transport in tokamaks: Three-dimensional structure of bursts and the role of zonal flows. *Physical review letters*, 85(23):4892, 2000. 41, 56, 82, 155

[22] KH Burrell. Effects of e× b velocity shear and magnetic shear on turbulence and transport in magnetic confinement devices. *Physics of Plasmas*, 4(5):1499–1518, 1997. 41, 124

[23] Bruce D Scott, PW Terry, and PH Diamond. Saturation of kelvin–helmholtz fluctuations in a sheared magnetic field. *The Physics of fluids*, 31(6):1481–1491, 1988. 41

[24] Fritz Wagner, G Becker, K Behringer, D Campbell, A Eberhagen, W Engelhardt, G Fussmann, O Gehre, J Gernhardt, G v Gierke, et al. Regime of improved confinement and high beta in neutral-beam-heated divertor discharges of the asdex tokamak. *Physical Review Letters*, 49(19):1408, 1982. 41

[25] J Schirmer, GD Conway, H Zohm, W Suttrop, ASDEX Upgrade Team, et al. The radial electric field and its associated shear in the asdex upgrade tokamak. *Nuclear fusion*, 46(9):S780, 2006. 41, 191

[26] Laure Vermare, P Hennequin, C Honoré, M Peret, Guilhem Dif-Pradalier, X Garbet, J Gunn, Clarisse Bourdelle, Frédéric Clairet, J Morales, et al. Formation of the radial electric field profile in the west tokamak. *Nuclear Fusion*, 62(2):026002, 2021. 42, 90, 96, 176

[27] Robin Varennes, Laure Vermare, Xavier Garbet, P Hennequin, G Dif-Pradalier, Yanick Sarazin, Virginie Grandgirard, Olivier Panico, Peter Donnel, and K Obrejan. Safety factor influence on the edge e× b velocity establishment in tokamak plasmas. *Plasma Physics and Controlled Fusion*, 66(2):025003, 2023. 42, 176

[28] J-M Moret, S Franke, H Weisen, M Anton, R Behn, BP Duval, F Hofmann, B Joye, Y Martin, Ch Nieswand, et al. Influence of plasma shape on transport in the tcv tokamak. *Physical review letters*, 79(11):2057, 1997. 42

[29] A Colagrossi, S Marrone, P Colagrossi, and D Le Touzé. Da vinci's observation of turbulence: A french-italian study aiming at numerically reproducing the physics behind one of his drawings, 500 years later. *Physics of Fluids*, 33(11), 2021. 44

[30] Andrey Nikolaevich Kolmogorov. The local structure of turbulence in incompressible viscous fluid for very large reynolds numbers. *In Dokl. Akad. Nauk SSSR*, 30:301, 1941. 45

[31] Oka Sunao Tsuruhashi Tomonori, Goto Susumu and Yoneda Tsuyoshi. Self-similar hierarchy of coherent tubular vortices in turbulence. *Phil. Trans. R. Soc*, 2022. 46

[32] Ragnar Fjørtoft. On the changes in the spectral distribution of kinetic energy for twodimensional, nondivergent flow. *Tellus*, 5(3):225–230, 1953. 46

[33] Marcel Lesieur. *Turbulence in fluids: stochastic and numerical modelling*, volume 488. Nijhoff Boston, MA, 1987. 46

[34] Robert H Kraichnan and David Montgomery. Two-dimensional turbulence. *Reports on Progress in Physics*, 43(5):547, 1980. 47

[35] C-G Rossby. On the distribution of angular velocity in gaseous envelopes under the influence of large-scale horizontal mixing processes. *Bulletin of the American Meteorological Society*, 28(2):53–68, 1947. 47, 57

[36] Fabian Waleffe. The nature of triad interactions in homogeneous turbulence. *Physics of Fluids A: Fluid Dynamics*, 4(2):350–363, 1992. 47

[37] Fabian Waleffe. Inertial transfers in the helical decomposition. *Physics of Fluids A: Fluid Dynamics*, 5(3):677–685, 1993. 47

[38] E Mazzucato. Low-frequency microinstabilities in the plt tokamak. *The Physics of Fluids*, 21(6):1063–1069, 1978. 48

[39] A Truc, A Quéméneur, P Hennequin, D Grésillon, F Gervais, C Laviron, J Olivain, SK Saha, and P Devynck. Altair: An infrared laser scattering diagnostic on the tore supra tokamak. *Review of scientific instruments*, 63(7):3716–3724, 1992. 48

[40] C Honoré, R Sabot, P Hennequin, F Gervais, A Quéméneur, A Truc, G Antar, P Devynck, C Fenzi, X Garbet, et al. Small scale density fluctuations in tore supra: Rupture in the scaling law. In *Proceedings of the 25th EPS Conference on Controlled Fusion and Plasma Physics, Prague*, page 647, 1998. 48

[41] P Hennequin, R Sabot, C Honoré, GT Hoang, X Garbet, A Truc, C Fenzi, and A Quéméneur. Scaling laws of density fluctuations at high-k on tore supra. *Plasma Physics and Controlled Fusion*, 46(12B):B121, 2004. 48

[42] P Hennequin, C Honoré, A Truc, A Quéméneur, C Fenzi-Bonizec, C Bourdelle, X Garbet, GT Hoang, Tore Supra team, et al. Fluctuation spectra and velocity profile from doppler backscattering on tore supra. *Nuclear fusion*, 46(9):S771, 2006. 48, 169, 172, 174, 178

[43] Laure Vermare, Pascale Hennequin, Özgür D Gürcan, C Bourdelle, F Clairet, X Garbet, R Sabot, Tore Supra Team, et al. Impact of collisionality on fluctuation characteristics of micro-turbulence. *Physics of Plasmas*, 18(1), 2011. 48, 172

[44] Laure Vermare, Özgür D Gürcan, Pascale Hennequin, Cyrille Honoré, X Garbet, JC Giacalone, R Sabot, F Clairet, Tore Supra Team, et al. Wavenumber spectrum of micro-turbulence in tokamak plasmas. *Comptes Rendus. Physique*, 12(2):115–122, 2011. 48

[45] Özgür D Gürcan, X Garbet, Pascale Hennequin, PH Diamond, A Casati, and GL Falchetto. Wavenumber spectrum of drift-wave turbulence. *Physical review letters*, 102(25):255002, 2009. 49

[46] Paulett C Liewer. Measurements of microturbulence in tokamaks and comparisons with theories of turbulence and anomalous transport. *Nuclear Fusion*, 25(5):543, 1985. 49, 52

[47] B. B. Kadomtsev and O. P. Pogutse. *Turbulence in Toroidal Systems*, pages 249–400. Springer US, Boston, MA, 1995. 52

[48] Akira Hasegawa and Masahiro Wakatani. Plasma edge turbulence. *Physical Review Letters*, 50(9):682, 1983. 52, 88, 127

[49] Akira Hasegawa and Kunioki Mima. Pseudo-three-dimensional turbulence in magnetized nonuniform plasma. *The Physics of Fluids*, 21(1):87–92, 1978. 52, 107

[50] N Bonanomi, C Angioni, PC Crandall, A Di Siena, CF Maggi, PA Schneider, JET Contributors, ASDEX Upgrade Team, EUROFusion MST1 Team, et al. Effect of the isotope mass on the turbulent transport at the edge of l-mode plasmas in asdex upgrade and jet-ilw. *Nuclear Fusion*, 59(12):126025, 2019. 52, 80, 108, 133

[51] Wendell Horton Jr, D-I Choi, and WM Tang. Toroidal drift modes driven by ion pressure gradients. *Physics of Fluids*, 24(6):1077–1085, 1981. 52

[52] GS Lee and PH Diamond. Theory of ion-temperature-gradient-driven turbulence in tokamaks. *The Physics of fluids*, 29(10):3291–3313, 1986. 52

[53] Ft Romanelli. Ion temperature-gradient-driven modes and anomalous ion transport in tokamaks. *Physics of Fluids B: Plasma Physics*, 1(5):1018–1025, 1989. 52, 145

[54] Anders Jarmén, Per Andersson, and Jan Weiland. Fully toroidal ion temperature gradient driven drift modes. *Nuclear fusion*, 27(6):941, 1987. 52

[55] RD Sydora, JN Leboeuf, ZG An, PH Diamond, GS Lee, and TS Hahm. Dynamics and fluctuation spectra of electrostatic resistive interchange turbulence. *Physics of Fluids*, 29(9):2871, 1986. 52

[56] PN Guzdar, JF Drake, D McCarthy, AB Hassam, and CS Liu. Three-dimensional fluid simulations of the nonlinear drift-resistive ballooning modes in tokamak edge plasmas. *Physics of Fluids B: Plasma Physics*, 5(10):3712–3727, 1993. 52

[57] P Beyer, Xavier Garbet, and Philippe Ghendrih. Tokamak turbulence with stochastic field lines. *Physics of Plasmas*, 5(12):4271–4279, 1998. 52

[58] BB Kadomtsev and OP Pogutse. Trapped particles in toroidal magnetic systems. *Nuclear Fusion*, 11(1):67, 1971. 53

[59] BN Rogers and JF Drake. Enhancement of turbulence in tokamaks by magnetic fluctuations. *Physical Review Letters*, 79(2):229, 1997. 53

[60] BN Rogers, JF Drake, and A Zeiler. Phase space of tokamak edge turbulence, the l- h transition, and the formation of the edge pedestal. *Physical Review Letters*, 81(20):4396, 1998. 53, 68, 69, 79, 96, 122

[61] Bruce D Scott. Computation of electromagnetic turbulence and anomalous transport mechanisms in tokamak plasmas. *Plasma physics and controlled fusion*, 45(12A):A385, 2003. 53

[62] Bruce Scott. Three-dimensional computation of drift alfvén turbulence. *Plasma Physics and Controlled Fusion*, 39(10):1635, 1997. 53, 82, 94, 113, 116, 236

[63] Wonjae Lee, Justin R Angus, Maxim V Umansky, and Sergei I Krasheninnikov. Electromagnetic effects on plasma blob-filament transport. *Journal of Nuclear Materials*, 463:765–768, 2015. 53

[64] Anthony W Leonard. Edge-localized-modes in tokamaks. *Physics of Plasmas*, 21(9), 2014. 54

[65] RD Hazeltine, D Dobrott, and TS Wang. Kinetic theory of tearing instability. *The Physics of Fluids*, 18(12):1778–1786, 1975. 54

[66] JF Drake and YC Lee. Kinetic theory of tearing instabilities. *The Physics of Fluids*, 20(8):1341–1353, 1977. 54

[67] WM Tang, JW Connor, and RJ Hastie. Kinetic-ballooning-mode theory in general geometry. *Nuclear Fusion*, 20(11):1439, 1980. 54

[68] WW Heidbrink and GJ Sadler. The behaviour of fast ions in tokamak experiments. *Nuclear Fusion*, 34(4):535, 1994. 54

[69] A Fasoli, CBHL Gormenzano, HL Berk, B Breizman, S Briguglio, DS Darrow, N Gorelenkov, WW Heidbrink, Andre Jaun, SV Konovalov, et al. Physics of energetic ions. *Nuclear Fusion*, 47(6):S264, 2007. 54

[70] Samuele Mazzi, Jeronimo Garcia, David Zarzoso, Ye O Kazakov, Jozef Ongena, Mykola Dreval, Massimo Nocente, Ž Štancar, Gabor Szepesi, Jens Eriksson, et al. Enhanced performance in fusion plasmas through turbulence suppression by megaelectronvolt ions. *Nature Physics*, 18(7):776–782, 2022. 54

[71] Wallace M Manheimer and Thomas M Antonsen. A theory of electron energy confinement in tokamaks. *The Physics of Fluids*, 22(5):957–970, 1979. 55, 163

[72] Patrick H Diamond and TS Hahm. On the dynamics of turbulent transport near marginal stability. *Physics of Plasmas*, 2(10):3640–3649, 1995. 55, 57, 88, 154, 155, 163

[73] KW Gentle, WL Rowan, RV Bravenec, G Cima, TP Crowley, H Gasquet, GA Hallock, J Heard, A Ouroua, PE Phillips, et al. Strong nonlocal effects in a tokamak perturbative transport experiment. *Physical review letters*, 74(18):3620, 1995. 55

[74] Pablo Rodriguez-Fernandez, AE White, NT Howard, BA Grierson, GM Staebler, JE Rice, X Yuan, NM Cao, AJ Creely, MJ Greenwald, et al. Explaining cold-pulse dynamics in tokamak plasmas using local turbulent transport models. *Physical review letters*, 120(7):075001, 2018. 55

[75] Clemente Angioni, Emiliano Fable, Francois Ryter, Pablo Rodriguez-Fernandez, Thomas Pütterich, ASDEX Upgrade Team, et al. The local nature of the plasma response to cold pulses with electron and ion heating at asdex upgrade. *Nuclear Fusion*, 59(10):106007, 2019. 55

[76] BA Carreras, D Newman, VE Lynch, and PH Diamond. A model realization of self-organized criticality for plasma confinement. *Physics of Plasmas*, 3(8):2903–2911, 1996. 56

[77] Xavier Garbet and Ronald E Waltz. Heat flux driven ion turbulence. *Physics of Plasmas*, 5(8):2836–2845, 1998. 56

[78] Y Sarazin and Ph Ghendrih. Intermittent particle transport in two-dimensional edge turbulence. *Physics of Plasmas*, 5(12):4214–4228, 1998. 56, 97, 127

[79] Yasuhiro Idomura, H Urano, Nobuyuki Aiba, and S Tokuda. Study of ion turbulent transport and profile formations using global gyrokinetic full-f vlasov simulation. *Nuclear Fusion*, 49(6):065029, 2009. 56

[80] Susan Ku, Choong-Seock Chang, and Patrick H Diamond. Full-f gyrokinetic particle simulation of centrally heated global itg turbulence from magnetic axis to edge pedestal top in a realistic tokamak geometry. *Nuclear Fusion*, 49(11):115021, 2009. 56

[81] Ben F McMillan, S Jolliet, TM Tran, L Villard, A Bottino, and P Angelino. Avalanchelike bursts in global gyrokinetic simulations. *Physics of Plasmas*, 16(2), 2009. 56

[82] Y Sarazin, V Grandgirard, J Abiteboul, S Allfrey, X Garbet, Ph Ghendrih, G Latu, A Strugarek, G Dif-Pradalier, Patrick H Diamond, et al. Predictions on heat transport and plasma rotation from global gyrokinetic simulations. *Nuclear Fusion*, 51(10):103023, 2011. 56

[83] Xavier Garbet, Yanick Sarazin, P Beyer, Ph Ghendrih, RE Waltz, M Ottaviani, and S Benkadda. Flux driven turbulence in tokamaks. *Nuclear Fusion*, 39(11Y):2063, 1999. 56

[84] Yanick Sarazin. *Confinement, Transport and Turbulence*. Draft lecture notes, Master level, 2024. 57, 124

[85] PA Politzer. Observation of avalanchelike phenomena in a magnetically confined plasma. *Physical review letters*, 84(6):1192, 2000. 57, 74, 163, 185

[86] PA Schneider, Pascale Hennequin, N Bonanomi, M Dunne, GD Conway, U Plank, ASDEX Upgrade Team, EUROfusion MST1 Team, et al. Overview of the isotope effects in the asdex upgrade tokamak. *Plasma Physics and Controlled Fusion*, 63(6):064006, 2021. 57, 74, 75, 169, 185, 198

[87] Steven M Tobias, Patrick H Diamond, and David W Hughes. β-plane magnetohydrodynamic turbulence in the solar tachocline. *The Astrophysical Journal*, 667(1):L113, 2007. 57

[88] K Miki, PH Diamond, Özgür D Gürcan, GR Tynan, T Estrada, L Schmitz, and GS Xu. Spatio-temporal evolution of the l$\rightarrow$ i$\rightarrow$ h transition. *Physics of Plasmas*, 19(9), 2012. 57

[89] P H Diamond, S-I Itoh, K Itoh, and T S Hahm. Zonal flows in plasma—a review. *Plasma Physics and Controlled Fusion*, 47(5):R35, apr 2005. 58, 81, 141, 152

[90] Akira Hasegawa, Carol G Maclennan, and Yuji Kodama. Nonlinear behavior and turbulence spectra of drift waves and rossby waves. *The Physics of Fluids*, 22(11):2122–2129, 1979. 58

[91] PH Diamond and Y-B Kim. Theory of mean poloidal flow generation by turbulence. *Physics of Fluids B: Plasma Physics*, 3(7):1626–1633, 1991. 58, 59, 141, 147, 155

[92] AI Smolyakov, PH Diamond, and MV Medvedev. Role of ion diamagnetic effects in the generation of large scale flows in toroidal ion temperature gradient mode turbulence. *Physics of Plasmas*, 7(10):3987–3992, 2000. 59, 141

[93] K Hallatschek. Turbulent saturation of tokamak-core zonal flows. *Physical review letters*, 93(6):065001, 2004. 59

[94] CJ McDevitt, PH Diamond, Özgür D Gürcan, and TS Hahm. Poloidal rotation and its relation to the potential vorticity flux. *Physics of Plasmas*, 17(11), 2010. 59

[95] Y Sarazin, Guilhem Dif-Pradalier, X Garbet, P Ghendrih, Anatole Berger, C Gillot, V Grandgirard, K Obrejan, R Varennes, L Vermare, et al. Key impact of phase dynamics and diamagnetic drive on reynolds stress in magnetic fusion plasmas. *Plasma Physics and Controlled Fusion*, 63(6):064007, 2021. 59, 141, 143, 152

[96] FL Hinton and MN Rosenbluth. Dynamics of axisymmetric and poloidal flows in tokamaks. *Plasma physics and controlled fusion*, 41(3A):A653, 1999. 60

[97] Garrard D Conway, Andrei I Smolyakov, and Takeshi Ido. Geodesic acoustic modes in magnetic confinement devices. *Nuclear Fusion*, 62(1):013001, 2021. 60, 70

[98] Niels Winsor, John L Johnson, and John M Dawson. Geodesic acoustic waves in hydromagnetic systems. *Physics of Fluids*, 11(11):2448–2450, 1968. 60

[99] L Schmitz, L Zeng, TL Rhodes, JC Hillesheim, EJ Doyle, RJ Groebner, WA Peebles, KH Burrell, and G Wang. Role of zonal flow predator-prey oscillations in triggering the transition to h-mode confinement. *Physical review letters*, 108(15):155002, 2012. 61, 95

[100] Pierre Morel, Ö D Gürcan, and Vincent Berionni. Characterization of predator–prey dynamics, using the evolution of free energy in plasma turbulence. *Plasma Physics and Controlled Fusion*, 56(1):015002, 2013. 61

[101] Sumire Kobayashi, Özgür D Gürcan, and Patrick H Diamond. Direct identification of predator-prey dynamics in gyrokinetic simulations. *Physics of Plasmas*, 22(9), 2015. 61

[102] K Miki and PH Diamond. Role of the geodesic acoustic mode shearing feedback loop in transport bifurcations and turbulence spreading. *Physics of Plasmas*, 17(3), 2010. 61, 81

[103] Zhihong Lin, Taik Soo Hahm, WW Lee, William M Tang, and Roscoe B White. Turbulent transport reduction by zonal flows: Massively parallel simulations. *Science*, 281(5384):1835–1837, 1998. 61, 155, 239

[104] Guilhem Dif-Pradalier, PH Diamond, Virginie Grandgirard, Yanick Sarazin, J Abiteboul, Xavier Garbet, Ph Ghendrih, A Strugarek, S Ku, and CS Chang. On the validity of the local diffusive paradigm in turbulent plasma transport. *Physical Review E—Statistical, Nonlinear, and Soft Matter Physics*, 82(2):025401, 2010. 62, 70, 198

[105] Guilhem Dif-Pradalier, Grégoire Hornung, Ph Ghendrih, Yanick Sarazin, F Clairet, L Vermare, PH Diamond, J Abiteboul, T Cartier-Michaud, C Ehrlacher, et al. Finding the elusive e× b staircase in magnetized plasmas. *Physical review letters*, 114(8):085004, 2015. 62, 70

[106] Guilhem Dif-Pradalier, G Hornung, X Garbet, Ph Ghendrih, V Grandgirard, G Latu, and Y Sarazin. The e× b staircase of magnetised plasmas. *Nuclear Fusion*, 57(6):066026, 2017. 62, 70, 129, 147, 148, 150, 155

[107] Grégoire Hornung, Guilhem Dif-Pradalier, F Clairet, Y Sarazin, R Sabot, Pascale Hennequin, and Geert Verdoolaege. staircases and barrier permeability in magnetised plasmas. *Nuclear Fusion*, 57(1):014006, 2016. 62, 76, 148, 150, 163, 165, 170

[108] Peter B Rhines. Waves and turbulence on a beta-plane. *Journal of Fluid Mechanics*, 69(3):417–443, 1975. 62

[109] Alain J Brizard and Taik Soo Hahm. Foundations of nonlinear gyrokinetic theory. *Reviews of modern physics*, 79(2):421–468, 2007. 64

[110] SI Braginskii. Transport processes in a plasma. *Reviews of plasma physics*, 1:205, 1965. 64

[111] Viktor Mikhaĭ Zhdanov. *Transport processes in multicomponent plasma*. 64

[112] GW Hammett, W Dorland, and FW Perkins. Fluid models of phase mixing, landau damping, and nonlinear gyrokinetic dynamics. *Physics of Fluids B: Plasma Physics*, 4(7):2052–2061, 1992. 64

[113] Y Sarazin, G Dif-Pradalier, D Zarzoso, Xavier Garbet, Ph Ghendrih, and V Grandgirard. Entropy production and collisionless fluid closure. *Plasma Physics and Controlled Fusion*, 51(11):115003, 2009. 64

[114] Xavier Garbet, P Donnel, Gianni L De, Z Qu, Y Melka, Y Sarazin, V Grandgirard, K Obrejan, E Bourne, and G Dif-Pradalier. Effect of shaping on trapped electron mode stability: an analytical model. 2024. 64, 123

[115] Virginie Grandgirard, Maura Brunetti, Pierre Bertrand, Nicolas Besse, Xavier Garbet, Philippe Ghendrih, Giovanni Manfredi, Yanick Sarazin, Olivier Sauter, Eric Sonnendrücker, et al. A drift-kinetic semi-lagrangian 4d code for ion turbulence simulation. *Journal of Computational Physics*, 217(2):395–423, 2006. 64

[116] Patrick Tamain, Hugo Bufferand, Guido Ciraolo, Clothilde Colin, Davide Galassi, Ph Ghendrih, Frédéric Schwander, and Eric Serre. The tokam3x code for edge turbulence fluid simulations of tokamak plasmas in versatile magnetic geometries. *Journal of Computational Physics*, 321:606–623, 2016. 64, 84

[117] Patrick H Diamond, Sanae-I Itoh, and Kimitaka Itoh. *Modern Plasma Physics: Volume 1, Physical Kinetics of Turbulent Plasmas*. Cambridge University Press, 2010. 65

[118] C Gillot, G Dif-Pradalier, Y Sarazin, C Bourdelle, A Bañón Navarro, Y Camenen, J Citrin, A Di Siena, X Garbet, Ph Ghendrih, et al. The problem of capturing marginality in model reductions of turbulence. *Plasma Physics and Controlled Fusion*, 65(5):055012, 2023. 65, 102

[119] JB Marston, GP Chini, and SM Tobias. Generalized quasilinear approximation: application to zonal jets. *Physical review letters*, 116(21):214501, 2016. 65, 67, 123

[120] Martin Greenwald, JL Terry, SM Wolfe, S Ejima, MG Bell, SM Kaye, and GH Neilson. A new look at density limits in tokamaks. *Nuclear Fusion*, 28(12):2199, 1988. 68

[121] Bruce D Scott. Drift wave versus interchange turbulence in tokamak geometry: Linear versus nonlinear mode structure. *Physics of Plasmas*, 12(6):062314, 2005. 68, 131, 133

[122] Thomas Eich, Peter Manz, ASDEX Upgrade Team, et al. The separatrix operational space of asdex upgrade due to interchange-drift-alfvén turbulence. *Nuclear Fusion*, 61(8):086017, 2021. 68, 69, 79, 96, 135

[123] M Giacomin, A Pau, P Ricci, O Sauter, T Eich, ASDEX Upgrade Team, JET Contributors, et al. First-principles density limit scaling in tokamaks based on edge turbulent transport and implications for iter. *Physical Review Letters*, 128(18):185003, 2022. 69

[124] Ryusuke Numata, Rowena Ball, and Robert L Dewar. Bifurcation in electrostatic resistive drift wave turbulence. *Physics of Plasmas*, 14(10), 2007. 69, 138, 139, 140, 150

[125] RJ Hajjar, PH Diamond, and MA Malkov. Dynamics of zonal shear collapse with hydrodynamic electrons. *Physics of Plasmas*, 25(6), 2018. 70, 140

[126] Minjun J Choi, Hogun Jhang, Jae-Min Kwon, Jinil Chung, Minho Woo, Lei Qi, Sehoon Ko, Taik-Soo Hahm, Hyeon K Park, Hyun-Seok Kim, et al. Experimental observation of the non-diffusive avalanche-like electron heat transport events and their dynamical interaction with the shear flow structure. *Nuclear Fusion*, 59(8):086027, 2019. 70

[127] Y. Kosuga, P. H. Diamond, G. Dif-Pradalier, and Ö. D. Gürcan. E × B shear pattern formation by radial propagation of heat flux waves. *Physics of Plasmas*, 21(5):055701, 04 2014. 70, 147, 149, 159

[128] JC Hillesheim, E Delabie, H Meyer, CF Maggi, L Meneses, E Poli, JET Contributors, EUROfusion Consortium, et al. Stationary zonal flows during the formation of the edge transport barrier in the jet tokamak. *Physical review letters*, 116(6):065002, 2016. 70, 75

[129] Akihide Fujisawa. A review of zonal flow experiments. *Nuclear Fusion*, 49(1):013001, 2008. 70

[130] L Schmitz, G Wang, JC Hillesheim, TL Rhodes, WA Peebles, AE White, L Zeng, TA Carter, and W Solomon. Detection of zonal flow spectra in diii-d by a dual-channel doppler backscattering system. *Review of Scientific Instruments*, 79(10), 2008. 72

[131] GD Conway, ASDEX Upgrade Team, et al. Amplitude behaviour of geodesic acoustic modes in the asdex upgrade tokamak. *Plasma Physics and Controlled Fusion*, 50(8):085005, 2008. 72

[132] GD Conway, C Tröster, B Scott, K Hallatschek, ASDEX Upgrade Team, et al. Frequency scaling and localization of geodesic acoustic modes in asdex upgrade. *Plasma Physics and Controlled Fusion*, 50(5):055009, 2008. 72

[133] A Storelli, Laure Vermare, Pascale Hennequin, Özgür D Gürcan, Guilhem Dif-Pradalier, Y Sarazin, X Garbet, T Görler, Rameswar Singh, Pierre Morel, et al. Comprehensive comparisons of geodesic acoustic mode characteristics and dynamics between tore supra experiments and gyrokinetic simulations. *Physics of Plasmas*, 22(6), 2015. 72, 176, 179, 180, 182

[134] Laure Vermare, Pascale Hennequin, Özgür D Gürcan, Tore Supra Team, et al. Detection of geodesic acoustic mode oscillations, using multiple signal classification analysis of doppler backscattering signal on tore supra. *Nuclear Fusion*, 52(6):063008, 2012. 72, 169, 176, 178, 182

[135] MA Pedrosa, C Silva, C Hidalgo, BA Carreras, RO Orozco, D Carralero, et al. Evidence of long-distance correlation of fluctuations during edge transitions to improved-confinement regimes in the tj-ii stellarator. *Physical review letters*, 100(21):215003, 2008. 73

[136] B Ph Van Milligen, I Voldiner, BA Carreras, L García, MA Ochando, et al. Rational surfaces, flows and radial structure in the tj-ii stellarator. *Nuclear Fusion*, 63(1):016027, 2022. 73, 151

[137] KJ Zhao, JQ Dong, LW Yan, WY Hong, A Fujisawa, CX Yu, Q Li, J Qian, J Cheng, T Lan, et al. Turbulence and zonal flows in edge plasmas of the hl-2a tokamak. *Plasma Physics and Controlled Fusion*, 52(12):124008, 2010. 73, 183

[138] GS Xu, BN Wan, M Song, and J Li. Direct measurement of poloidal long-wavelength e× b flows in the ht-7 tokamak. *Physical review letters*, 91(12):125001, 2003. 73

[139] A Fujisawa, K Itoh, H Iguchi, K Matsuoka, S Okamura, A Shimizu, T Minami, Y Yoshimura, K Nagaoka, C Takahashi, et al. Identification of zonal flows in a toroidal plasma. *Physical review letters*, 93(16):165002, 2004. 73

[140] DK Gupta, RJ Fonck, GR McKee, DJ Schlossberg, and MW Shafer. Detection of zero-mean-frequency zonal flows in the core of a high-temperature tokamak plasma. *Physical review letters*, 97(12):125002, 2006. 73, 183

[141] D Carralero, T Estrada, J.M. Garcia-Regana, E Sanchez, T Windisch, A Alonso, E Maragkoudakis, C Brandt, K.J. Brunner, C Gallego-Castillo, K Rahbarnia, H Thienpondt, and the Wedelstein 7-X team. First experimental observation of zonal flows in the optimized stellarator wendelstein 7-x. 73

[142] GR Tynan, C Holland, JH Yu, A James, D Nishijima, M Shimada, and N Taheri. Observation of turbulent-driven shear flow in a cylindrical laboratory plasma device. *Plasma physics and controlled fusion*, 48(4):S51, 2006. 73

[143] B Schmid, P Manz, M Ramisch, and U Stroth. Collisional scaling of the energy transfer in drift-wave zonal flow turbulence. *Physical Review Letters*, 118(5):055001, 2017. 73

[144] C Silva, ER Solano, JC Hillesheim, E Delabie, S Aleiferis, G Birkenmeier, L Gil, C Giroud, E Litherland-Smith, RB Morales, et al. Structure of the jet edge radial electric field in he and d plasmas. *Nuclear Fusion*, 61(12):126006, 2021. 75

[145] Olivier Panico, Yanick Sarazin, Hennequin Pascale, Roméo Bigué, Guilhem Dif-Pradalier, Xavier Garbet, Philippe Ghendrih, Ozgur Gurcan, Robin Varennes, and Laure Vermare. (sub) on the importance of flux-driven turbulence regime to address tokamak plasma edge dynamics. *Journal of plasma physics*, 2024. 80, 127, 129

[146] Laurent Chôné, Peter Beyer, Yanick Sarazin, Guillaume Fuhr, Clarisse Bourdelle, and Sadruddin Benkadda. Lh transition dynamics in fluid turbulence simulations with neoclassical force balance. *Physics of Plasmas*, 21(7), 2014. 82, 140

[147] PJ Catto, AM El Nadi, CS Liu, and MN Rosenbluth. Stability of a finite-β inhomogeneous plasma in a sheared magnetic field. *Nuclear Fusion*, 14(3):405, 1974. 82

[148] GQ Yu, SI Krasheninnikov, and PN Guzdar. Two-dimensional modelling of blob dynamics in tokamak edge plasmas. *Physics of Plasmas*, 13(4):042508, 2006. 84

[149] Justin R Angus and Maxim V Umansky. Modeling of large amplitude plasma blobs in three-dimensions. *Physics of Plasmas*, 21(1), 2014. 84

[150] Alexander Ross, Andreas Stegmeir, and David Coster. Effect of the boussinesq approximation: Turbulence studies with grillix in slab geometry. *Contributions to Plasma Physics*, 58(6-8):478–483, 2018. 84

[151] Benjamin Daniel Dudson and Jarrod Leddy. Hermes: global plasma edge fluid turbulence simulations. *Plasma Physics and Controlled Fusion*, 59(5):054010, 2017. 84

[152] Andreas Stegmeir, David Coster, Alexander Ross, Omar Maj, Karl Lackner, and Emanuele Poli. Grillix: a 3d turbulence code based on the flux-coordinate independent approach. *Plasma Physics and Controlled Fusion*, 60(3):035005, 2018. 84

[153] Philippe Ghendrih, Guilhem Dif-Pradalier, Olivier Panico, Yanick Sarazin, Hugo Bufferand, Guido Ciraolo, Peter Donnel, Nicolas Fedorczak, Xavier Garbet, Virginie Grandgirard, Pascale Hennequin, Eric Serre, and Patrick Tamain. Role of avalanche transport in competing drift wave and interchange turbulence. *Journal of Physics: Conference Series*, 2397(1):012018, dec 2022. 84, 113, 131

[154] Y Sarazin, X Garbet, Ph Ghendrih, and S Benkadda. Transport due to front propagation in tokamaks. *Physics of Plasmas*, 7(4):1085–1088, 2000. 87, 123, 159

[155] S Benkadda, P Beyer, N Bian, C Figarella, O Garcia, X Garbet, Ph Ghendrih, Y Sarazin, and PH Diamond. Bursty transport in tokamak turbulence: Role of zonal flows and internal transport barriers. *Nuclear fusion*, 41(8):995, 2001. 87

[156] N Bian, S Benkadda, OE Garcia, J-V Paulsen, and X Garbet. The quasilinear behavior of convective turbulence with sheared flows. *Physics of Plasmas*, 10(5):1382–1388, 2003. 87

[157] F. Ryter, F. Leuterer, G. Pereverzev, H.-U. Fahrbach, J. Stober, W. Suttrop, and ASDEX Upgrade Team. Experimental evidence for gradient length-driven electron transport in tokamaks. *Phys. Rev. Lett.*, 86:2325, 2000. 88

[158] RE Waltz and C Holland. Numerical experiments on the drift wave–zonal flow paradigm for nonlinear saturation. *Physics of Plasmas*, 15(12), 2008. 88

[159] N Mahdizadeh, F Greiner, T Happel, A Kendl, M Ramisch, BD Scott, and U Stroth. Investigation of the parallel dynamics of drift-wave turbulence in toroidal plasmas. *Plasma Physics and Controlled Fusion*, 49(7):1005, 2007. 88

[160] KH Burrell, SL Allen, G Bramson, NH Brooks, RW Callis, TN Carlstrom, MS Chu, AP Colleraine, D Content, JC DeBoo, et al. Confinement physics of h-mode discharges in diii-d. *Plasma Physics and Controlled Fusion*, 31(10):1649, 1989. 90, 96

[161] TA Gianakon, SE Kruger, and CC Hegna. Heuristic closures for numerical simulations of neoclassical tearing modes. *Physics of Plasmas*, 9(2):536–547, 2002. 90, 140

[162] L Chôné, P Beyer, Y Sarazin, G Fuhr, C Bourdelle, and S Benkadda. Mechanisms and dynamics of the external transport barrier formation in non-linear plasma edge simulations. *Nuclear Fusion*, 55(7):073010, 2015. 91, 140

[163] MA Malkov and PH Diamond. Bifurcation and scaling of drift wave turbulence intensity with collisional zonal flow damping. *Physics of Plasmas*, 8(9):3996–4009, 2001. 95

[164] Th Eich, RJ Goldston, A Kallenbach, B Sieglin, HJ Sun, JET Contributors, ASDEX Upgrade Team, et al. Correlation of the tokamak h-mode density limit with ballooning stability at the separatrix. *Nuclear Fusion*, 58(3):034001, 2018. 96

[165] X Garbet, L Laurent, J-P Roubin, and A Samain. A model for the turbulence in the scrape-off layer of tokamaks. *Nuclear Fusion*, 31(5):967, 1991. 97

[166] A Banón Navarro, T Happel, T Görler, F Jenko, J Abiteboul, A Bustos, H Doerk, D Told, ASDEX Upgrade Team, et al. Gyrokinetic studies of core turbulence features in asdex upgrade h-mode plasmas. *Physics of Plasmas*, 22(4), 2015. 102

[167] Masahiro Wakatani and Akira Hasegawa. A collisional drift wave description of plasma edge turbulence. *The Physics of fluids*, 27(3):611–618, 1984. 107

[168] H Bufferand, G Dif-Pradalier, P. Ghendrih, V Grandgirard, I Kudashev, Y Kunimoto, A Medvedeva Glasser, O Panico, Y Sarazin, and E Serre. K-epsilon modelling of turbulent transport in the edge-sol boundary layer. 2024. 113

[169] RE Waltz. Numerical simulation of electromagnetic turbulence in tokamaks. *The Physics of fluids*, 28(2):577–589, 1985. 123

[170] J Weiland, AB Jarmen, and H Nordman. Diffusive particle and heat pinch effects in toroidal plasmas. *Nuclear Fusion*, 29(10):1810, 1989. 123

[171] DE Newman, PW Terry, PH Diamond, Y-M Liang, GG Craddock, AE Koniges, and JA Crottinger. The dynamics of long wavelength electrostatic turbulence in tokamaks. *Physics of plasmas*, 1(5):1592–1600, 1994. 123

[172] Bruce D Scott. Tokamak edge turbulence: background theory and computation. *Plasma Physics and Controlled Fusion*, 49(7):S25, 2007. 123, 131

[173] B Scott. The geodesic transfer effect on zonal flows in tokamak edge turbulence. *Physics Letters A*, 320(1):53–62, 2003. 123

[174] A Kendl and BD Scott. Shear flow reduction by the geodesic transfer mechanism in tokamak edge turbulence. *Physics of plasmas*, 12(6), 2005. 123

[175] Y Camenen, A Pochelon, A Bottino, S Coda, F Ryter, O Sauter, R Behn, TP Goodman, MA Henderson, A Karpushov, et al. Electron heat transport in shaped tcv l-mode plasmas. *Plasma physics and controlled fusion*, 47(11):1971, 2005. 124

[176] X Garbet, Y Sarazin, Ph Ghendrih, S Benkadda, P Beyer, C Figarella, and I Voitsekhovitch. Turbulence simulations of transport barriers with toroidal velocity. *Physics of Plasmas*, 9(9):3893–3905, 2002. 124

[177] Mathieu Peret. *Pushing the physics of edge transport barriers towards the wall : how do boundary conditions impact confinement transitions in tokamaks?* PhD thesis, Institut polytechnique de Paris, 2022. 124

[178] Olivier Panico, Yanick Sarazin, Hennequin Pascale, Guilhem Dif-Pradalier, Xavier Garbet, Philippe Ghendrih, Ozgur Gurcan, and Robin Varennes. (in prep) zonal flows and staircase generation in competing drift-waves interchange turbulence. *Journal of plasma physics*, 2024. 127

[179] Özgür D. Gürcan. Internally driven β-plane plasma turbulence using the hasegawa-wakatani system. arXiv: https://arxiv.org/abs/2403.09911, 2024. 131

[180] Bruce D Scott, A Kendl, and T Ribeiro. Nonlinear dynamics in the tokamak edge. *Contributions to Plasma Physics*, 50(3-5):228–241, 2010. 131, 133

[181] G Grenfell, L Gil, C Silva, P Manz, J Adamek, D Brida, G.D. Conway, T Eich, M Faitsch, T Happel, M Spolaore, U Stroth, and E Wolfrum. Edge turbulence characterization of the eda h-mode in asdex upgrade. 133

[182] H Doerk, C Challis, J Citrin, J Garcia, T Görler, F Jenko, and JET Contributors. Gyrokinetic study of turbulence suppression in a jet-ilw power scan. *Plasma Physics and Controlled Fusion*, 58(11):115005, 2016. 133

[183] Norbert Wiener. Generalized harmonic analysis. *Acta mathematica*, 55(1):117–258, 1930. 136

[184] Alexander Khintchine. Korrelationstheorie der stationären stochastischen prozesse. *Mathematische Annalen*, 109(1):604–615, 1934. 136

[185] F Grander, FF Locker, and A Kendl. Hysteresis in the gyrofluid resistive drift wave turbulence to zonal flow transition. *Physics of Plasmas*, 31(5), 2024. 139, 150

[186] Y Xu, D Carralero, C Hidalgo, S Jachmich, P Manz, E Martines, B van Milligen, MA Pedrosa, M Ramisch, I Shesterikov, et al. Long-range correlations and edge transport bifurcation in fusion plasmas. *Nuclear fusion*, 51(6):063020, 2011. 140

[187] R Hong, GR Tynan, PH Diamond, L Nie, D Guo, T Long, R Ke, Y Wu, B Yuan, M Xu, et al. Edge shear flows and particle transport near the density limit of the hl-2a tokamak. *Nuclear Fusion*, 58(1):016041, 2017. 140

[188] Ting Long, PH Diamond, Min Xu, Rui Ke, L Nie, B Li, ZH Wang, JQ Xu, XR Duan, et al. Studies of reynolds stress and the turbulent generation of edge poloidal flows on the hl-2a tokamak. *Nuclear Fusion*, 59(10):106010, 2019. 140

[189] Rameswar Singh and PH Diamond. Zonal shear layer collapse and the power scaling of the density limit: old lh wine in new bottles. *Plasma Physics and Controlled Fusion*, 64(8):084004, 2022. 140

[190] Plamen G Ivanov, AA Schekochihin, W Dorland, AR Field, and FI Parra. Zonally dominated dynamics and dimits threshold in curvature-driven itg turbulence. *Journal of Plasma Physics*, 86(5):855860502, 2020. 141, 145, 146

[191] AM Dimits, BI Cohen, N Mattor, WM Nevins, DE Shumaker, SE Parker, and C Kim. Simulation of ion temperature gradient turbulence in tokamaks. *Nuclear fusion*, 40(3Y):661, 2000. 146

[192] Guilhem Dif-Pradalier, Virginie Grandgirard, Yanick Sarazin, Xavier Garbet, and Ph Ghendrih. Interplay between gyrokinetic turbulence, flows, and collisions: Perspectives on transport and poloidal rotation. *Physical Review Letters*, 103(6):065002, 2009. 146

[193] Jeffrey B Parker and John A Krommes. Zonal flow as pattern formation. *Physics of Plasmas*, 20(10), 2013. 150

[194] Andrew J Majda, Di Qi, and Antoine J Cerfon. A flux-balanced fluid model for collisional plasma edge turbulence: Model derivation and basic physical features. *Physics of Plasmas*, 25(10):102307, 2018. 150

[195] Xavier Garbet, O Panico, R Varennes, C Gillot, Guilhem Dif-Pradalier, Y Sarazin, V Grandgirard, P Ghendrih, and L Vermare. Wave trapping and e$\times$ b staircases. *Physics of Plasmas*, 28(4), 2021. 151

[196] ZB Guo and PH Diamond. Zonal flow patterns: How toroidal coupling induces phase jumps and shear layers. *Physical Review Letters*, 117(12):125002, 2016. 152

[197] Nicolas Fedorczak, James Paul Gunn, Ph Ghendrih, Pascale Monier-Garbet, and Alain Pocheau. Flow generation and intermittent transport in the scrape-off-layer of the tore supra tokamak. *Journal of Nuclear Materials*, 390:368–371, 2009. 155

[198] B Labit, I Furno, A Fasoli, A Diallo, SH Müller, G Plyushchev, M Podestà, and FM Poli. Universal statistical properties of drift-interchange turbulence in torpex plasmas. *Physical review letters*, 98(25):255002, 2007. 158

[199] Hongxuan Zhu, Yao Zhou, and IY Dodin. Theory of the tertiary instability and the dimits shift from reduced drift-wave models. *Physical Review Letters*, 124(5):055002, 2020. 159

[200] Y Kishimoto, T Tajima, W Horton, MJ LeBrun, and JY Kim. Theory of self-organized critical transport in tokamak plasmas. *Physics of Plasmas*, 3(4):1289–1307, 1996. 163

[201] E Mazzucato. Microwave reflectometry for magnetically confined plasmas. *Review of Scientific Instruments*, 69(6):2201–2217, 1998. 170, 172, 245

[202] Oleg Krutkin, Stephan Brunner, and Stefano Coda. A method for density fluctuation measurements using pulse reflectometry. *Nuclear Fusion*, 63(7):076012, 2023. 170

[203] M Hirsch, E Holzhauer, J Baldzuhn, B Kurzan, and B Scott. Doppler reflectometry for the investigation of propagating density perturbations. *Plasma physics and controlled fusion*, 43(12):1641, 2001. 170, 173

[204] GD Conway, J Schirmer, S Klenge, W Suttrop, E Holzhauer, ASDEX Upgrade Team, et al. Plasma rotation profile measurements using doppler reflectometry. *Plasma Physics and Controlled Fusion*, 46(6):951, 2004. 170, 173

[205] P Hennequin, C Honoré, A Truc, A Quéméneur, N Lemoine, J-M Chareau, and R Sabot. Doppler backscattering system for measuring fluctuations and their perpendicular velocity on tore supra. *Review of Scientific Instruments*, 75(10):3881–3883, 2004. 170, 176

[206] Cyrille Honoré. *Diffusion collective de la lumière par un milieu turbulent*. draft, 2013. 171

[207] C Honoré, P Hennequin, A Truc, and A Quéméneur. Quasi-optical gaussian beam tracing to evaluate doppler backscattering conditions. *Nuclear fusion*, 46(9):S809, 2006. 172

[208] Bruce D Scott. The mechanism of self-sustainment in collisional drift wave turbulence. *Physics of Fluids B: Plasma Physics*, 4(8):2468–2494, 1992. 173

[209] Peter Welch. The use of fast fourier transform for the estimation of power spectra: a method based on time averaging over short, modified periodograms. *IEEE Transactions on audio and electroacoustics*, 15(2):70–73, 1967. 173

[210] Pascale Hennequin and et al. Analysis of density fluctuation frequency spectra in tore supra as a tool for studying plasma motion and transport properties. In *26th EPS Conf. on Plasma Physics. Maastricht, 14 - 18 June 1999*, 1999. 174

[211] Elisée Trier. *Champ electrique radial dans les plasmas de tokamak non axi-symetrique, étude par réflectométrie Doppler*. PhD thesis, Ecole Polytechnique, 2010. 174

[212] Pascale Hennequin. Scaling laws of density fluctuations in tokamak plasmas. *Comptes Rendus Physique*, 7(6):670–678, 2006. 175

[213] Norden E Huang, Zheng Shen, Steven R Long, Manli C Wu, Hsing H Shih, Quanan Zheng, Nai-Chyuan Yen, Chi Chao Tung, and Henry H Liu. The empirical mode decomposition and the hilbert spectrum for nonlinear and non-stationary time series analysis. *Proceedings of the Royal Society of London. Series A: mathematical, physical and engineering sciences*, 454(1971):903–995, 1998. 179

[214] Gabriel Rilling and Patrick Flandrin. One or two frequencies? the empirical mode decomposition answers. *IEEE transactions on signal processing*, 56(1):85–95, 2007. 180, 181

[215] Ryan Deering and James F Kaiser. The use of a masking signal to improve empirical mode decomposition. In *Proceedings.(ICASSP'05). IEEE International Conference on Acoustics, Speech, and Signal Processing, 2005.*, volume 4, pages iv–485. IEEE, 2005. 181

[216] OB Fosso and M Molinas. Mode mixing separation in empirical mode decomposition of signals with spectral proximity. *arXiv*, (arXiv: 1709.05547 v2), 2019. 181

[217] B Kurzan, S de Peña Hempel, E Holzhauer, B Scott, F Serra, W Suttrop, A Zeiler, ASDEX Upgrade Team, et al. Measurement and scaling of the radial correlation lengths of turbulence at the plasma edge of asdex upgrade. *Plasma physics and controlled fusion*, 42(3):237, 2000. 185

[218] GR McKee, CC Petty, RE Waltz, C Fenzi, RJ Fonck, JE Kinsey, TC Luce, KH Burrell, DR Baker, EJ Doyle, et al. Non-dimensional scaling of turbulence characteristics and turbulent diffusivity. *Nuclear Fusion*, 41(9):1235, 2001. 185

[219] S Inagaki, T Tokuzawa, K Itoh, K Ida, S-I Itoh, N Tamura, S Sakakibara, N Kasuya, A Fujisawa, S Kubo, et al. Observation of long-distance radial correlation in toroidal plasma turbulence. *Physical review letters*, 107(11):115001, 2011. 185

[220] J Schirmer, GD Conway, E Holzhauer, W Suttrop, H Zohm, and ASDEX Upgrade Team. Radial correlation length measurements on asdex upgrade using correlation doppler reflectometry. *Plasma Physics and Controlled Fusion*, 49(7):1019–1039, 2007. 185, 191, 195

[221] Alexander N. Karpushov, Filippo Bagnato, Marcelo Baquero-Ruiz, Stefano Coda, Claudia Colandrea, Frédéric Dolizy, Jérémie Dubray, Basil P. Duval, Damien Fasel, Ambrogio Fasoli, Rémy Jacquier, Pierre Lavanchy, Blaise Marlétaz, Yves Martin, Lorenzo Martinelli, Dmytry Mykytchuk, Marta M. Pedrini, Jesús Poley, Holger Reimerdes, Umar Sheikh, Ugo Siravo, Matthieu Toussaint, and Matteo Vallar. Upgrade of the neutral beam heating system on the tcv tokamak – second high energy neutral beam. *Fusion Engineering and Design*, 187:113384, 2023. 185

[222] J Hawke, Y Andrebe, R Bertizzolo, P Blanchard, R Chavan, J Decker, B Duval, P Lavanchy, X Llobet, B Marlétaz, et al. Improving spatial and spectral resolution of tcv thomson scattering. *Journal of Instrumentation*, 12(12):C12005, 2017. 186

[223] RC Isler. An overview of charge-exchange spectroscopy as a plasma diagnostic. *Plasma Physics and Controlled Fusion*, 36(2):171, 1994. 186

[224] A Karpushov, Y Andrebe, BP Duval, and L Federspiel. Charge exchange recombination spectroscopy measurement of ion temperature, rotation and impurity density profiles on the tcv tokamak. In *39th EPS Conference & 16th Int. Congress on Plasma Physics*, pages O5–117. European Physical Society, 2012. 186

[225] P Molina Cabrera, S Coda, L Porte, N Offeddu, P Lavanchy, M Silva, M Toussaint, TCV Team, et al. V-band doppler backscattering diagnostic in the tcv tokamak. *Review of Scientific Instruments*, 89(8), 2018. 187, 191

[226] A Bottino, O Sauter, Y Camenen, and E Fable. Linear stability analysis of microinstabilities in electron internal transport barrier non-inductive discharges. *Plasma physics and controlled fusion*, 48(2):215, 2006. 189

[227] Y Camenen, A Pochelon, R Behn, A Bottino, A Bortolon, S Coda, A Karpushov, O Sauter, G Zhuang, et al. Impact of plasma triangularity and collisionality on electron heat transport in tcv l-mode plasmas. *Nuclear fusion*, 47(7):510, 2007. 189

[228] JR Pinzón, Teresa Estrada, T Happel, Pascale Hennequin, E Blanco, Ulrich Stroth, TJ-II Teams, et al. Measurement of the tilt angle of turbulent structures in magnetically confined plasmas using doppler reflectometry. *Plasma Physics and Controlled Fusion*, 61(10):105009, 2019. 191

[229] JR Pinzón, T Happel, Pascale Hennequin, Clemente Angioni, Teresa Estrada, Alexander Lebschy, Ulrich Stroth, ASDEX Upgrade Team, et al. Experimental investigation of the tilt angle of turbulent structures in the core of fusion plasmas. *Nuclear Fusion*, 59(7):074002, 2019. 191

[230] WA Peebles, TL Rhodes, JC Hillesheim, L Zeng, and C Wannberg. A novel, multichannel, comb-frequency doppler backscatter system. *Review of Scientific Instruments*, 81(10), 2010. 191

[231] T Estrada, J Sanchez, V Zhuravlev, E de la Luna, and B Branas. Turbulence and beam size effects on reflectometry measurements. *Physics of Plasmas*, 8(6):2657–2665, 2001. 195

[232] M Ugoletti, M Agostini, M La Matina, P Scarin, Y Wang, C Wüthrich, C Theiler, Y Andrebe, M Griener, M Zuin, et al. Role of radiation re-absorption in the thermal helium beam diagnostic. *Review of Scientific Instruments*, 95(8), 2024. 200

[233] G Fuchert, G Birkenmeier, D Carralero, T Lunt, P Manz, HW Müller, B Nold, M Ramisch, V Rohde, U Stroth, et al. Blob properties in l-and h-mode from gas-puff imaging in asdex upgrade. *Plasma Physics and Controlled Fusion*, 56(12):125001, 2014. 202

[234] N Offeddu, W Han, C Theiler, T Golfinopoulos, JL Terry, E Marmar, C Wüthrich, CK Tsui, H De Oliveira, BP Duval, et al. Cross-field and parallel dynamics of sol filaments in tcv. *Nuclear Fusion*, 62(9):096014, 2022. 202

[235] John Crank and Phyllis Nicolson. A practical method for numerical evaluation of solutions of partial differential equations of the heat-conduction type. In *Mathematical proceedings of the Cambridge philosophical society*, volume 43, pages 50–67. Cambridge University Press, 1947. 229

[236] Carl Runge. Über die numerische auflösung von differentialgleichungen. *Mathematische Annalen*, 46(2):167–178, 1895. 230

[237] Alessandro Casati, C Bourdelle, X Garbet, and F Imbeaux. Temperature ratio dependence of ion temperature gradient and trapped electron mode instability thresholds. *Physics of Plasmas*, 15(4), 2008. 237

[238] C Bourdelle, X Garbet, F Imbeaux, A Casati, N Dubuit, R Guirlet, and T Parisot. A new gyrokinetic quasilinear transport model applied to particle transport in tokamak plasmas. *Physics of Plasmas*, 14(11), 2007. 241

[239] Alessandro Casati. *A quasi-linear gyrokinetic transport model for tokamak plasmas*. PhD thesis, Aix-Marseille université, 2009. 241

[240] S. Rienäcker, P. Hennequin, L. Vermare, C. Honoré, S. Coda, O. Panico, and L. Frassinetti. Edge flows studies via doppler backscattering on the tcv tokamak. May 2024. 16th IRW, Greifswald. Oral contribution. 247

Appendix A: Introduction

A.1 The author & TCV

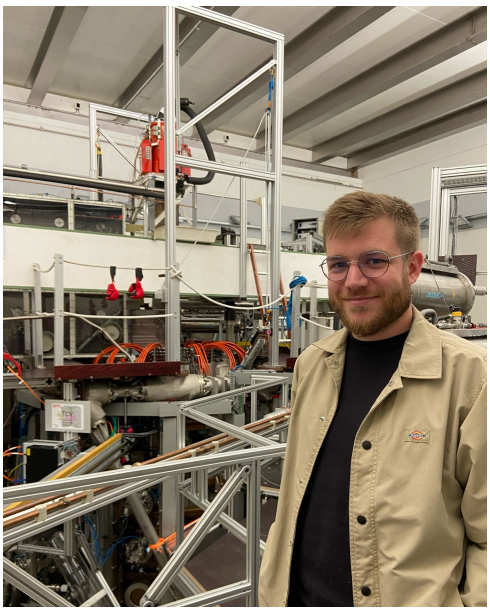

Figure A.1 – The author in front of the DBS launcher system at TCV.

A.2 Hot and magnetized plasma: typical length and time scales

The various processes taking place in a tokamak develop at different length and time scales which span a large number of orders of magnitudes. They are summarized in Figure A.2.
The spatial scale from smaller to larger:

- The **nucleus scale** ($\sim 10^{-15}\ m$): scale of the nuclear interaction, binding nuclei together.
- The **Landau distance** ($\Lambda_{Ls} \sim 10^{-13}\ m$): shortest distance of approach of thermal particles (in a plasma at about 10keV) that interact frontally.
- The **Debye length** ($\lambda_D \sim 10^{-4}$ m): characteristic distance at which the electric charge e_s of a given particle of species 's' can be considered screened by the charges of its neighbours. It is defined as:

$$\lambda_{D,s} = \sqrt{\frac{\varepsilon_0 T_s}{e_s^2 n_s}}$$

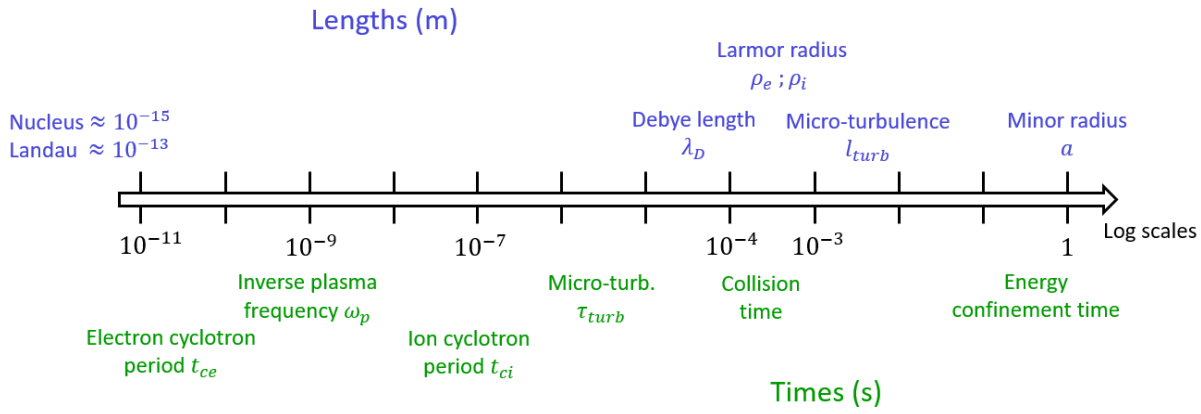

Figure A.2 – Typical length (top) and time (bottom) scales in a hot magnetized plasma.

With, ε_0 the permeability of free space, T_s and n_s the temperature and particle density of the species 's'. It ranges typically from $10^{-5}m$ for $(n,T) = (10^{19}\ m^{-3}, 300\ eV)$ to $10^{-4}m$ for $(n,T) = (10^{20}\ m^{-3}, 15\ keV)$ in a confined plasma. Above the Debye length, the plasma can be considered as quasi-neutral. Note that quasi-neutrality does not preclude the development of an electric potential and electric field in the plasma. It simply states that such a field exhibits large scale variations only.

- The **Larmor radii** ($\rho_e \sim 10^{-4}m$ for electrons and $\rho_i \sim 10^{-3}m$ for ions): it corresponds to the charged particle gyro-motion around a magnetic field line, detailed in Section 1.2.1. For single charged thermal particles, it is defined as,

$$\rho_s = \frac{v_{th,s}}{\omega_{c,s}} = \frac{\sqrt{m_s T_s}}{eB}$$

Where $v_{th,s} = \sqrt{T_s/m_s}$ is the thermal speed of species "s", ω_c the gyro-frequency and B the magnetic field strength.

- The **micro-turbulence correlation length** ($l_{turb} \sim 10\ \rho_i$): corresponds to the typical size of micro-turbulent structures responsible for the majority of cross-field transport.
- The **thermodynamic gradient lengths** ($L_P \sim 10^{-2} - 1$): typically of the order of a fraction of the machine minor radius. In practice, much smaller gradient lengths can develop in cases of staircases or High-confinement modes. Those situations are detailed in the following.
- The **particles mean-free path** ($\gtrsim 1$ km): typical distance between two collisions for electrons and ions.

The temporal scales:

- The **inverse plasma frequency** ($\omega_p^{-1} \sim 10^{-9}\ s$): characteristic time of plasma response

to a charge displacement. Defined as follows:

$$\omega_p = \sqrt{\frac{ne^2}{\varepsilon_0 m}}$$

- The **cyclotron-period** ($\omega_{ce}^{-1} \sim 10^{-11}s; \omega_{ci}^{-1} \sim 10^{-7}s$ for electrons and ions respectively): corresponds to the time associated with the gyro-motion and the Larmor radius.
- The **micro-turbulence auto-correlation time** ($\tau_{turb} \sim 1 - 100\ \mu s$): typical lifetime of a micro-turbulence structure.
- The **Coulomb collision time** or inverse collision frequency ($\nu^{-1} \sim 10^{-3} - 10^{-4}s$). It is defined as the time necessary for a particle to have its velocity vector deflected by about 90°.
- The **Energy confinement time** ($\tau_E \sim 0.1 - 1\ s$): time for which the energy stays confined in the plasma when external heating is removed.

s From this rapid overview, it appears that hot magnetized plasmas experience a large range of different lengths and time scales. The hierarchy has long advocated to address those processes on the basis of scale separation. Growing evidence shows, however, that plasma self-organization develops at intermediate - or meso - scales which fill the gap between micro-phenomena and the large machine scale.

Appendix B: Derivation Tokam1D

B.1 Tokam1D numerical implementation details

B.1.1 Tokam1D workflow and numerical stability

The $1D$-radial system of equations is written in FORTRAN90 and solved using a fourth order Runge-Kutta scheme in time and centered fourth order finite differences in space. The dissipation terms are treated to the second order using the semi-implicit Crank-Nicolson scheme [235]. A basic sketch of the workflow used in Tokam1D is given in Figure B.1. Details on the Runge-Kutta scheme and implementation of the diffusion can be found in the following sections.

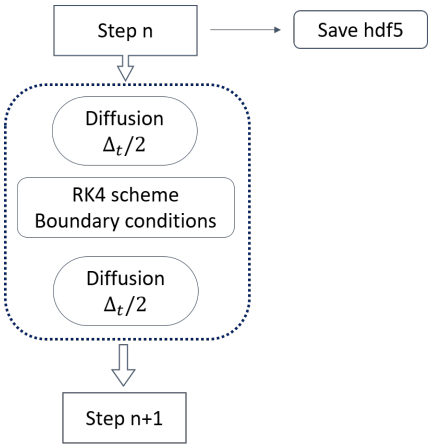

Figure B.1 – Tokam1D numerical workflow.

The numerical scheme is symmetric. Dissipation is applied 2 times on $\Delta t/2$, before and after the equation evolution. The arrays are saved every $X_d = 2\,dx$ and $T_d = 100\,dt$ points into HDF5 files. Neumann boundary conditions with vanishing gradients are used for the density at $x = 0$ and for the velocity at both ends. Dirichlet is used for the density imposed to $N_{eq} = 0.1$ at $x = L_x$ and the fluctuations set to zero at both boundaries. Finally, at the end of a restart, a file is written containing arrays, parameters and boundary conditions to the maximum accuracy. A subsequent simulation can then restart from this file.

The time step, dt, needs to be small with respect to the typical time involved in the system. In the case of Tokam1D, it should be compared to the growth rate γ and the real frequency ω of the instabilities. One needs to ensure that $\gamma dt \ll 1$ and $\omega dt \ll 1$. As shown in Figure 3.9, these inequalities are well fulfilled since the growth rate and frequencies are respectively of the order of 10^{-3} and 10^{-2} for typical values of the parameters. When the equilibrium density profile is

corrugated, it can locally develop large gradients, leading to larger values of γ. In most of the simulation performed, we used the conservative choice $dt = 0.1$. It leaves a comfortable margin to ensure proper convergence even in these large γ regions.

In addition, one can compute the Courant-Friedrichs-Lewy (CFL) condition of numerical stability:

$$v_{max} \leq \frac{dx}{dt}$$

Here v_{max} is the maximum characteristic speed of waves or information propagation in the simulation. In the reported simulations, the grid step size is $dx = 400/1024\ \rho_s$ and the time step is $\omega_{cs}dt = 0.1$, where ρ_s is the sound Larmor radius and ω_{cs} the ion cyclotron pulsation. The condition leads to $v_{max} < 4\ \rho_{cs}\omega_{cs} \approx 4v_{th}$, where v_{th} is the thermal velocity of the particles. In the framework of this reduced fluid model, we deal with drift velocities of the order of $\rho_\star v_{th} \ll v_{th}$ where $\rho_\star = \rho_s/a \ll 1$ is the sound Larmor radius normalized by the minor radius of the tokamak. Consequently, the CFL condition is well fulfilled with this time step $\omega_{cs}dt = 0.1$. Tests with smaller and larger time steps have shown that the simulations were actually well converged. For post-processing purposes, data are saved every 100 dt. The compromise is to have a sufficiently small diagnostic time step so that physical quantities exhibit a continuous dynamics, while not saving an unnecessary too large amount of data. The actual retained value ensures that the physical processes of interest are well captured even after this coarse-graining in time.

B.1.2 Fourth order Runge-Kutta scheme

The Runge-Kutta (RK) methods are a family of numerical methods used to solve differential equations with temporal discretization [236]. In this section, only explicit methods are described, as these are the ones used for Tokam1D. The first order, RK1 method is often known as "Euler scheme" is the simplest method to solve differential equation. Let us consider the following problem: $\partial_t y = f(t,y)$ with y the solved quantity and f the known fight-hand side equation. RK1 scheme then reads,

$$y_{n+1} = y_n + hf(t_n, y_n)$$

With y_n the solved quantity at time n and h the time step. It appears that taking more intermediate steps in between t_n and t_{n+1} leads to a higher order of accuracy. Fourth order RK4 schemes are particularly popular. The principle is similar to the first order but it makes use of estimations performed at the midpoint $t_{n+1/2}$. Its principle is detailed in Figure B.2, for an iteration. The resulting y_{n+1} is then a linear combination of the fourth intermediate steps k_1, k_2, k_3, k_4. The local truncation error is of the order of $O(h^5)$ while the total accumulated error is of the order of $O(h^4)$. Also note that the boundary conditions are applied in between each k_1, k_2 etc.

B.1.3 Second order dissipation

In fluid models, an ad-hoc dissipation is added to dissipate energy at small scales. These can be excited by non-linear coupling but cannot be solved due to the model finite spatial resolution. The introduction of a dissipation then prevents spurious numerical instabilities. The dissipation usually takes the form $\partial_t n = ... + D\nabla_\perp^\alpha n$, with D a constant dissipation coefficient and α the

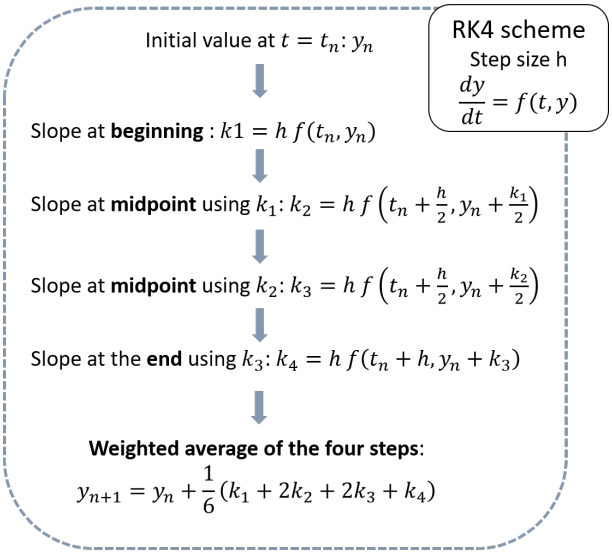

Figure B.2 – Iteration step detail of the 4th order Runge-Kutta numerical scheme.

dissipation order. Performing the spatial Fourier transform on the quantity n leads to $\partial_t n_k = ... + D((ik)^\alpha + \partial_x^\alpha) n_k$. For a dissipation to be an energy sink α has to be even so that $(ik)^\alpha < 0$. Often the choice is to take the standard $\alpha = 2$ dissipation. However, it can be wise to choose a hyper-dissipation $\alpha = (4,6)$, to focus the dissipation on the smaller scales and avoid interaction with physics at larger scales. A slightly more difficult task is to derive the dissipation when the coefficient D is not constant. In that case, the problem reads: $\partial_t n = ... + \nabla_\perp^{\alpha/2}\left(D\nabla_\perp^{\alpha/2} n\right)$.

Tokam1D provides options for second-order and fourth-order dissipation both treated with second order derivatives. It is also possible to use non-uniform second order dissipation. In this section is detailed the implementation of second-order dissipation treated to the second order. As a toy model, let us consider the diffusion-equation:

$$\partial_t u = \partial_x (D(x)\partial_x u)$$

The equation is discretized using finite differences at second order,

$$\partial_x (D(x)\partial_x u) = \frac{1}{\Delta x}\left[D_{i+1/2}\frac{u_{i+1} - u_i}{\Delta x} - D_{i-1/2}\frac{u_i - u_{i-1}}{\Delta x}\right]$$

With Δx the spatial step and i the current location. Since there is no information at location $i \pm 1/2$, the dissipation coefficient can be written as,

$$D_{i+1/2} = \frac{D_i + D_{i+1}}{2\Delta x}$$

The global equation is discretized using the Crank-Nicolson scheme,

$$\frac{u_i^{n+1} - u_i^n}{\Delta t} = \frac{1}{2}\left[[\partial_x (D(x)\partial_x u)]_i^{n+1} + [\partial_x (D(x)\partial_x u)]_i^n\right]$$

Putting everything together and gathering the $n+1$ terms on the left hand side, one can write

the equation with a tri-diagonal matrix such that,

$$AU^{n+1} = RU^n \tag{B.1}$$

With $U = (u_0, u_1, ..., u_i, u_{i+1}, ...)$ the discretized quantity and A the tridiagonal coefficient matrix. RU^n is the known right hand side at time n. By inverting the matrix A, one estimate the quantity at time $n+1$. The coefficients of A write,

$$\text{sub-diagonal} = \frac{\Delta t}{2\Delta x^2}(D_{i-1} + D_i) \tag{B.2}$$

$$\text{diagonal} = \left(1 + \frac{\Delta t}{2\Delta x^2}(2D_i + D_{i+1} + D_{i-1})\right) \tag{B.3}$$

$$\text{sur-diagonal} = \frac{\Delta t}{2\Delta x^2}(D_{i+1} + D_i) \tag{B.4}$$

Those coefficient can be readily implemented in an algorithm that inverse tri-diagonal matrices.

In the particular case of Tokam1D, the dissipation is applied both before and after the evolution of the system, each time using $\Delta t/2$. The case of a second-order dissipation treated at the fourth order and the case of a fourth-order dissipation treated to the second order lead to a penta-diagonal matrices that also need to be inverted.

B.2 Derivation of equilibrium and fluctuating Poisson brackets

This section derives useful mathematical expressions related to Poisson brackets. Those expression will be mainly used in chapter 3 to derive Tokam1D. The derivation is performed in a more general two dimensional case. The case of Tokam1D is then found by restricting the analysis to a single poloidal mode in the spirit of Equation 3.15. The problem at hand does not depend on the parallel direction, therefore we will consider a 2d problem in the radial (x) and poloidal (y) directions.

Let us consider two real quantities A and B that are decomposed into equilibrium and fluctuation parts: $A = A_{eq} + \widetilde{A}$. The equilibrium part is the average along the poloidal direction: $A_{eq} = \langle A \rangle_y$. The fluctuating component is Fourier transformed in the poloidal direction such that $\widetilde{A} = \sum_k \hat{A}_k e^{iky}$, with $\hat{A}_k$ the complex magnitude of the Fourier component k.

Remembering that Poisson brackets are defined as,

$$\{A, B\} = \partial_x A \partial_y B - \partial_y A \partial_x B = \partial_y (B \partial_x A) - \partial_x (B \partial_y A),$$

let us derive the flux-surface average:

$$\begin{aligned}
\langle \{A, B\} \rangle &= \langle \partial_y (B \partial_x A) - \partial_x (B \partial_y A) \rangle \\
&= -\partial_x \langle B \partial_y A \rangle \\
&= -\partial_x (B_{eq} \langle \partial_y A \rangle) - \partial_x \langle \widetilde{B} \partial_y \widetilde{A} \rangle
\end{aligned}$$

The first term is equal to zero since it is the flux-surface average of a poloidal derivative. The second term, labelled $\partial_x\Gamma$, is further decomposed in Fourier:

$$\begin{aligned}\Gamma \equiv -\langle\widetilde{B}\partial_y\widetilde{A}\rangle &= -\sum_k\sum_{k'}\hat{B}_k ik'\hat{A}_{k'}\langle e^{i(k+k')y}\rangle \\ &= -\sum_k ik'\hat{B}_k\hat{A}_{k'}\delta(k+k') \\ &= \sum_k ik\hat{B}_k\hat{A}_k^*\end{aligned}$$

A physicist knows that the manipulated flux-surface averaged quantities are real numbers. Therefore it directly results that $\sum_k \Re(k\hat{B}_k\hat{A}_k^*) = 0$ and $\Gamma = \sum_k(k\Im(B_kA_k^*))$. For the sake of scientific rigor we demonstrate it mathematically:

$$\begin{aligned}\sum_k k\Re(\hat{B}_k\hat{A}_k^*) &= \sum_{k>0} k\Re(\hat{B}_k\hat{A}_k^*) + \sum_{k<0} k\Re(\hat{B}_k\hat{A}_k^*) \\ &= \sum_{k>0} k\Re(\hat{B}_k\hat{A}_k^*) - \sum_{k'>0} k'\Re(\hat{B}_{k'}^*\hat{A}_{k'}) \\ &= 0 \\ \sum_k k\Im(\hat{B}_k\hat{A}_k^*) &= \sum_{k>0} k\Im(\hat{B}_k\hat{A}_k^*) - \sum_{k'>0} k'\Im(\hat{B}_{k'}^*\hat{A}_{k'}) \\ &= 2\sum_{k>0} k\Im(k\hat{B}_k\hat{A}_k^*)\end{aligned}$$

Therefore one have,

$$\boxed{\langle\{A,B\}\rangle = \partial_x\Gamma = 2\partial_x\sum_{k>0} k\Im(B_kA_k^*)} \tag{B.5}$$

The particular case of Tokam1D is found by choosing a single k mode. A slightly more complicated case can be derived using the same methods by noticing that $\langle\nabla_{\perp i}\{A,\nabla_{\perp i}B\}\rangle = \partial_x\langle\{A,\partial_xB\}\rangle$. Then one have,

$$\boxed{\partial_x\langle\{A,\partial_xB\}\rangle = -\partial_x^2\langle\partial_xB\partial_yA\rangle = 2\sum_{k>0} k\partial_x^2\left[\Im(A_k^*\partial_xB_k)\right]} \tag{B.6}$$

The two expressions Equation B.5 and B.6 are used to derive the equilibrium equations of the Tokam1D model.

The Poisson bracket fluctuating component is found by subtracting its equilibrium,

$$\{A,B\} - \langle\{A,B\}\rangle = \{\widetilde{A},B_{eq}\} + \{A_{eq},\widetilde{B}\} + \{\widetilde{A},\widetilde{B}\} - \langle\{\widetilde{A},\widetilde{B}\}\rangle$$

In the general case, the third and last terms need to be computed fully. We define $FT_k(A) =$

$A - \langle A \rangle$ the fluctuation term of the quantity A. Then, the third and fourth term can be written as:

$$FT_k\left(\{\widetilde{A},\widetilde{B}\}\right) \equiv \{\widetilde{A},\widetilde{B}\} - \langle\{\widetilde{A},\widetilde{B}\}\rangle = \partial_x\widetilde{A}\partial_y\widetilde{B} - \partial_y\widetilde{A}\partial_x\widetilde{B}$$
$$= \sum_k\sum_{k'}\left(\partial_x\hat{A}_k ik'\hat{B}_{k'} - ik\hat{A}_k\partial_x\hat{B}_{k'}\right)e^{i(k+k')y}$$

And the sum needs to be considered for every $k+k' = k_0$, with k_0 the Fourier mode that we want to solve. In the case of Tokam1D, since only a single k mode is retained, this term vanishes. As a result, one is left with,

$$\boxed{FT_k\left(\{A,B\}\right) = ik_y(B_k\partial_x A_{eq} - A_k\partial_x B_{eq})} \tag{B.7}$$

And similarly,

$$\boxed{\begin{aligned}FT_k\left[\nabla_{\perp i}\{A,\nabla_{\perp i}B\}\right] = ik_y[&\left(\partial_x^2 - k_y^2\right)B_k\partial_x A_{eq} + \partial_x B_k\partial_x^2 A_{eq}\\ &- \partial_x A_k\partial_x^2 B_{eq} - A_k\partial_x^3 B_{eq}]\end{aligned}} \tag{B.8}$$

B.3 Derivation of Tokam1D energy balance equation

To formulate the energy balance equation, we multiply Equation 3.12 and Equation 3.13 by $(1+\tau)N$ and $(\phi+\tau N)$ respectively. We then integrate by parts over the whole domain. Integration by parts leads to surface terms labelled ST that need to be considered carefully. The integration over the whole volume is written as $\langle ...\rangle = \int ...d\mathscr{V}$, with $\mathscr{V} = (x,y,z)$ the whole integration domain. The density energy equation can be written as,

$$\left\langle\frac{1}{2}\partial_t E_{dens}\right\rangle = g(1+\tau)\left\langle N\partial_y(\phi - N)\right\rangle + (1+\tau)\left\langle N\frac{\sigma_0}{n_\nu}\nabla_\parallel^2(N-\phi)\right\rangle$$
$$+ (1+\tau)D\left\langle N\nabla_\perp^2 N\right\rangle + (1+\tau)\left\langle NS_N\right\rangle$$

With $E_{dens} = (1+\tau)N^2$. The integration of the nonlinear advection term $\langle N\{\phi,N\}\rangle$ is equal to zero:

$$\langle N\{\phi,N\}\rangle = \left\langle N\left[\partial_y(N\partial_x\phi) - \partial_x(N\partial_y\phi)\right]\right\rangle$$
$$= \left\langle\frac{1}{2}\left[\partial_y(N^2)\partial_x\phi - \partial_x(N^2)\partial_y\phi\right]\right\rangle$$
$$= \left\langle\frac{1}{2}\left\{\phi,N^2\right\}\right\rangle$$

The Poisson bracket can be recast as $\left\{\phi,N^2\right\} = \partial_y(N^2\partial_x\phi) - \partial_x(N^2\partial_y\phi)$. The first term vanishes upon integration in the periodic direction. The second could possibly leads to surface terms due to the integration along x. In practice, the electric potential fluctuations are imposed at zero on both boundaries. It follows that $\partial_y\phi(L_x) = \partial_y\phi(0) = 0$ and the average of the Poisson bracket vanishes.

Integrating the density energy equation by parts leads to,

$$\begin{aligned}\left\langle \frac{1}{2}\partial_t E_{dens} \right\rangle =& g(1+\tau)\langle N\partial_y\phi\rangle + (1+\tau)\left\langle N\frac{\sigma_0}{n_v}\nabla_\parallel^2(N-\phi)\right\rangle \\ &+ ST_D - (1+\tau)D\left\langle(\nabla_\perp N)^2\right\rangle + (1+\tau)\left\langle NS_N\right\rangle\end{aligned} \tag{B.9}$$

With, $ST_D = [N\nabla_\perp N]_0^{L_x}$ the surface term linked to the integration by part of the diffusion term. The same work is done for the vorticity equation. First, we show that its nonlinear advection term vanishes. Writing $S \equiv \int(\phi+\tau N)\nabla_{\perp,i}\{\phi,\nabla_{\perp,i}(\phi+\tau N)\}d\mathscr{V}$,

$$\begin{aligned}S &= \int \nabla_{\perp,i}\left[(\phi+\tau N)\{\phi,\nabla_{\perp,i}(\phi+\tau N)\}\right] - \nabla_{\perp,i}(\phi+\tau N)\{\phi,\nabla_{\perp,i}(\phi+\tau N)\}d\mathscr{V} \\ &= -\int \nabla_{\perp,i}(\phi+\tau N)\{\phi,\nabla_{\perp,i}(\phi+\tau N)\}d\mathscr{V}\end{aligned}$$

Which is of the same form as $\langle N\{\phi,N\}\rangle$ leading to a vanishing integral. As a result, the vorticity energy equation can be written as,

$$\begin{aligned}\left\langle \frac{1}{2}\partial_t E_{vort} \right\rangle =& ST_\Omega + g(1+\tau)\left\langle\phi\partial_y N\right\rangle \\ &- \left\langle\frac{\sigma_0}{n_v}(\phi+\tau N)\nabla_\parallel^2(N-\phi)\right\rangle \\ &+ ST_\nu - \nu\left\langle\left(\nabla_\perp^2(\phi+\tau N)\right)^2\right\rangle\end{aligned} \tag{B.10}$$

With $E_{vort} = |\nabla_\perp(\phi+\tau N)|^2$. The vorticity and viscosity surface terms read respectively:

$$\begin{aligned}ST_\Omega &= [(\phi+\tau N)\partial_t\nabla_\perp(\phi+\tau N)]_0^{L_x} \\ ST_\nu &= \left[(\phi+\tau N)\nabla_\perp^3(\phi+\tau N)\right]_0^{L_x} - \left[\nabla_\perp(\phi+\tau N)\nabla_\perp^2(\phi+\tau N)\right]_0^{L_x}\end{aligned}$$

B.3.1 Global energy conservation equation

The global energy conservation equation is obtained by summing the two equations (B.9, B.10). First, terms linked to the constant g vanish are found to vanish:

$$(1+\tau)g\left\langle(N\partial_y\phi+\phi\partial_y N)\right\rangle = (1+\tau)g\left\langle\partial_y(N\phi)\right\rangle = 0$$

This is true provided that one keep the term linked to the divergence of the electric drift in the density equation Equation 3.4. The interchange terms are then only transfer terms in between density and vorticity energy. They do not lead to any source or sink of energy.

The drift wave terms can be further simplified if one considers that the conductivity σ is constant on flux surfaces and does not depend on the parallel coordinate. Then, it commutes with the $\nabla_\parallel$ operator and one can integrate by part on magnetic surfaces. The surface terms linked to the parallel current are all equal to zero due to the double periodicity of the torus.

Writting B_1 the current term of Equation B.9 and B_2 the current term of Equation B.10,

$$B_1 = (1+\tau)\sigma_0 \left\langle \frac{N}{n_\nu}\nabla_\parallel^2(N-\phi) \right\rangle \qquad = -(1+\tau)\sigma_0 \left\langle \frac{1}{n_\nu}\nabla_\parallel N \nabla_\parallel (N-\phi) \right\rangle$$
$$B_2 = -\sigma_0 \left\langle \frac{\phi+\tau N}{n_\nu}\nabla_\parallel^2(N-\phi) \right\rangle \qquad = +\sigma_0 \left\langle \frac{\nabla_\parallel(\phi+\tau N)}{n_\nu}\nabla_\parallel (N-\phi) \right\rangle$$

By summing the drift wave terms it readily appears that terms proportional to τ cancel each other. The others can be reorganized in the form of a parallel current $j_\parallel = \sigma n \nabla_\parallel (N-\phi)$ (where we recall that $\sigma = \sigma_0/n_\nu$):

$$B_1 + B_2 = -\left\langle \frac{\sigma_0}{n_\nu}\left[\nabla_\parallel(N-\phi)\right]^2 \right\rangle = -\left\langle \frac{1}{\sigma}\left(\frac{j_\parallel}{n}\right)^2 \right\rangle$$

Notice that this final result, already found in [62], directly results from $\sigma = \sigma_0/n_\nu$ being only dependent on the radial direction and time. The global conservation of energy, including surface terms then takes the following compact form:

$$\begin{aligned} \frac{d}{dt}\left\langle E_{dens} + E_{vort} \right\rangle = &+ (1+\tau)\left\langle N S_N \right\rangle - \left\langle \frac{\sigma_0}{n_\nu}\left[\nabla_\parallel(N-\phi)\right]^2 \right\rangle \\ &- D(1+\tau)\left\langle (\nabla_\perp N)^2 \right\rangle - \nu \left\langle \left[\nabla_\perp^2(\phi+\tau N)\right]^2 \right\rangle \\ &+ ST_\Omega + (1+\tau)DST_D + \nu ST_\nu \end{aligned} \tag{B.11}$$

Energy injection comes from the density source. All other terms contribute to energy dissipation, either due to the parallel resistivity or to the ad-hoc dissipative coefficients D and ν. Interestingly, the pressure energy has the form $(1+\tau)N^2$. One could expect the energy to be under the form of an electron and an ion energy, thus $(1+\tau^2)N^2$ or $(1+\tau)^2N^2$. This form of energy is also present in [62]. Also, note that the viscosity has to be written on the generalized vorticity instead of the electric potential. If not, the system does not conserve energy and spurious instabilities can appear.

B.3.2 From 3d to 1d

Replacing N and ϕ with their decomposition Equation 3.15 the pressure energy can be decomposed the following way:

$$\begin{aligned} (1+\tau)\left\langle N^2 \right\rangle &= (1+\tau)\left\langle \left(N_{eq} + N_k e^{i(k_y+k_\parallel)} + N_k^* e^{-i(k_y+k_\parallel)}\right)\left(N_{eq} + N_k e^{i(k_y+k_\parallel)} + N_k^* e^{-i(k_y+k_\parallel)}\right) \right\rangle \\ &= (1+\tau)\left\langle N_{eq}^2 + 2N_{eq}\left(N_k e^{(i(k_y+k_\parallel))} + N_k^* e^{-(i(k_y+k_\parallel))}\right) + N_k^2 e^{(i2(k_y+k_\parallel))} \right. \\ &\qquad \left. + N_k^{*2} e^{(-2i(k_y+k_\parallel))} + 2|N_k|^2 \right\rangle \\ &= (1+\tau)\left\langle N_{eq}^2 + 2|N_k|^2 \right\rangle \end{aligned}$$

Applying the same method to the vorticity yields:

$$\begin{aligned}\left\langle (\nabla_\perp(\phi+\tau N))^2 \right\rangle &= \left\langle (\partial_x(\phi+\tau N))^2 + (\partial_y(\phi+\tau N))^2 + 2\left(\partial_x(\phi+\tau N)\,\partial_y(\phi+\tau N)\right) \right\rangle \\ &= \langle \Big\{ \left(V_{eq}+\tau\partial_x N_{eq}\right)^2 + 2|\partial_x\phi_k|^2 + 4\tau\Re(\partial_x\phi_k\partial_x N_k^*) + 2|\tau\partial_x N_k|^2 \\ &\quad + 2k_y^2\left[|\phi_k|^2 + |\tau N_k|^2 + 2\tau\Re(\phi_k N_k^*)\right] \\ &\quad -2k_y\Im\left[\phi_k\partial_x\phi_k^* + \tau N_k\partial_x\phi_k^* + \tau\phi_k\partial_x N_k^* + \tau^2 N_k\partial_x N_k^*\right]\Big\}\rangle\end{aligned}$$

With this, one can then decompose the total energy into different channels, as indicated Equation 3.42 - 3.45.

B.4 Linear analysis: dual role of ion to electron temperature ratio

The role of the ion to electron temperature ratio, $\tau = T_i/T_e$, on the linear instabilities is studied in the framework of Tokam1D. A more complete contribution on the role of τ can be found in ref.[237] for ITG and TEM instabilities. The case of Tokam1D is peculiar: a single poloidal wavenumber k_y is chosen. Therefore, in the following we will treat both the case $k_y = cte$ and the case where k_x and k_y are chosen such that they maximize the growth rate, dubbed $k_y(\gamma_{max})$. We will show that τ can be either stabilizing or destabilizing depending on the instability at play. Also, it will appear that fixing a single k_y can lead to very different results as compared to the full $2D$ case.

First, let us study the case with both CDW and interchange instabilities. In Figure B.3a, we plot the growth rate as a function of τ for 4 different density gradients. The interchange parameter is fixed at $g = 2\times10^{-3}$ and the adiabatic parameter at $C = 10^{-3}$. The growth rate is shown for the case $k_y = 0.3$ in full lines and $k_y(\gamma_{max})$ in dotted lines. In Figure B.3b, the k_y leading to the maximal γ is indicated for each τ and gradient. The horizontal dotted line indicates $k_y = 0.3$, as chosen for Tokam1D.
For small τ, the effect on the growth rate is limited. The most prominent effect is visible for small density gradients where the growth rate increases from $\gamma\approx 0$ at $\tau = 10^{-3}$ to $\gamma = 2.5\times10^{-3}$ at $\tau\approx 6$. At larger τ, there is a large discrepancy between the cases at fixed k_y, and the cases $k_y(\gamma_{max})$. When several k_y are allowed, τ appears to be destabilizing whereas it is stabilizing in the fixed k_y case. This is a result of the ion to electron temperature ratio shifting the k_y of maximum growth rate from $k_y\approx 0.35$ to $k_y\approx 0.1$, see Figure B.3b. This highlights that Tokam1D is not suited to study the role of large ion to electron temperature ratios on the linear and non-linear dynamics since it requires several k_y to be described. For $\tau = 1$, the growth rate for the case at fixed k_y and $k_y(\gamma_{max})$ have been observed similar for most of the tested equilibrium parameters. It is considered relevant.

τ is stabilizing as it tends towards infinity. What happens between $\tau = 1$ and $\tau\longrightarrow+\infty$ depends on the instability at play. Displaying the same analysis as in Figure B.3, for the case interchange only and CDW only, one obtains the figures B.4.
For both CDW and interchange instabilities, τ is slightly destabilizing when small. Note that it can be enough to destabilize the system, see case drift waves at $1/L_N = 10^{-2}$ which displays

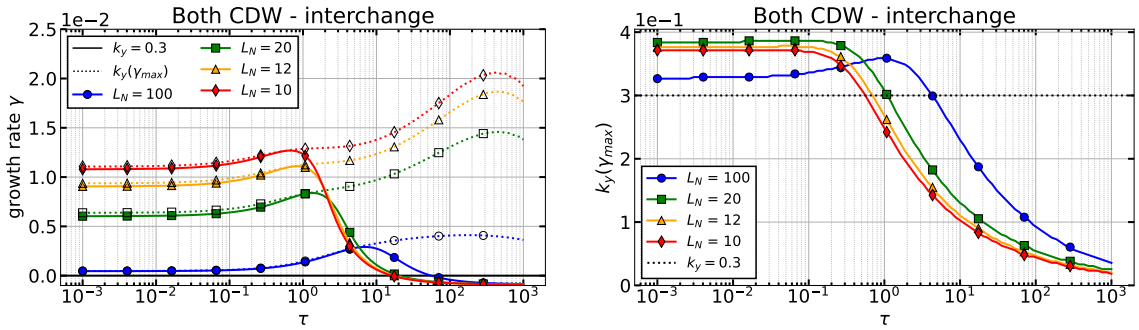

(a) (b)

Figure B.3 – (a) growth rate as a function of τ for different density gradients, $C = 10^{-3}$, $g = 2 \times 10^{-3}$. The case at fixed k_y is indicated in full lines. (b) k_y corresponding to the maximum growth rate (dotted lines in (a)). Other parameters: $D_1 = \nu_1 = 10^{-2}$ and $V_{eq} = V'_{eq} = N''_{eq} = 0$.

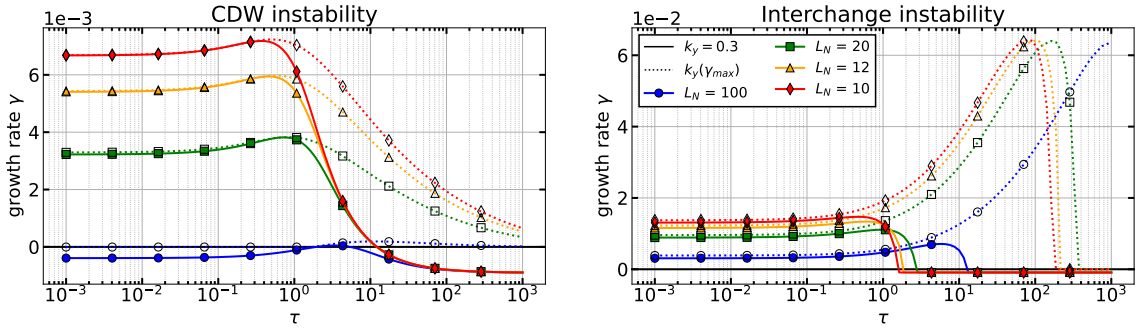

(a) (b)

Figure B.4 – (a) growth rate as a function of τ for different density gradients, $C = 10^{-3}$, $g = 0$. (b) Same as (a) with $C = 0$ and $g = 2.10^{-3}$. Other parameters: $D_1 = \nu_1 = 10^{-2}$ and $V_{eq} = V'_{eq} = N''_{eq} = 0$

a positive growth rate at $\tau = 3$. When larger, τ is always stabilizing for the Tokam1D case at fixed k_y but can be stabilizing or destabilizing depending on the instability at play for the general $k_y(\gamma_{max})$ case. At large τ, for the CDW case, in Figure B.4a, τ is stabilizing. For interchange, τ appears as destabilizing for the general case and stabilizing for the fixed k_y case. The behaviour of the general case with coupled instabilities displayed in Figure B.3 then depends on which instability is dominant.

We can conclude that τ exerts a dual effect on both the instabilities, depending on the dominant instability, density gradient and value of τ. More importantly, it is made clear that Tokam1D is not suited for the study of large τ since the growth rate exhibits a maximum at a poloidal wavenumber that significantly evolves with τ.

Appendix C: Details on simulations results

C.1 Artificially switching off ZFs

It has been clear that ZFs play a role in stabilizing the turbulence for more than 20 years now, [103]. Here we show that they are essential, even in the case where they are shown to be very small. We take a case with a low flows to turbulence energy ratio, at $C = 2\ 10^{-4}$ and $g = 10^{-4}$. In this simulation the flows account for ≈ 0.1 % of the turbulence energy. We show that by artificially suppressing them, the simulation diverges and a large radial mode fill in the simulation box. The results are shown in Figure C.1.

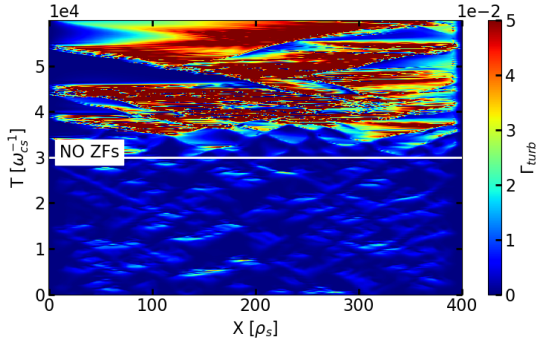

Figure C.1 – Turbulent flux Γ_{turb} as a function of time and radius. ZFs are artificially switched off at $T = 3\ 10^4$.

A large relaxation mode occurs when ZFs are switched off due to the gradient being large. The profile relaxes until it gets below the linear threshold. Then the system enters a periodic state where the gradient builds up, a large radial mode appears and the profile gets relaxed.

C.2 Larger dissipation leads to more structured flows

What lead to the radial structure of the flows? In the presented simulations, structured flows can appear both at low and large C, with no clear dependence on linear properties or turbulence parameters. Flows are shown to lose their structure when switching from flux driven to gradient driven simulations. The source and dissipation also appear as key player when it comes to the radial structure.

We take the case $(C, g) = (10^{-2}, 0)$ and we vary the dissipation coefficients on the fluctuation equations while keeping the source constant. Doing so, the linear threshold is modified as it depends directly on the dissipation. Since the source is kept constant, the distance to the linear

threshold is also modified. Two cases are performed, at $D_1 = \nu_1 = 2\ 10^{-2}$ and $D_1 = \nu_1 = 5\ 10^{-3}$. The results in terms of flows and density fluctuations are shown in Figure C.2.

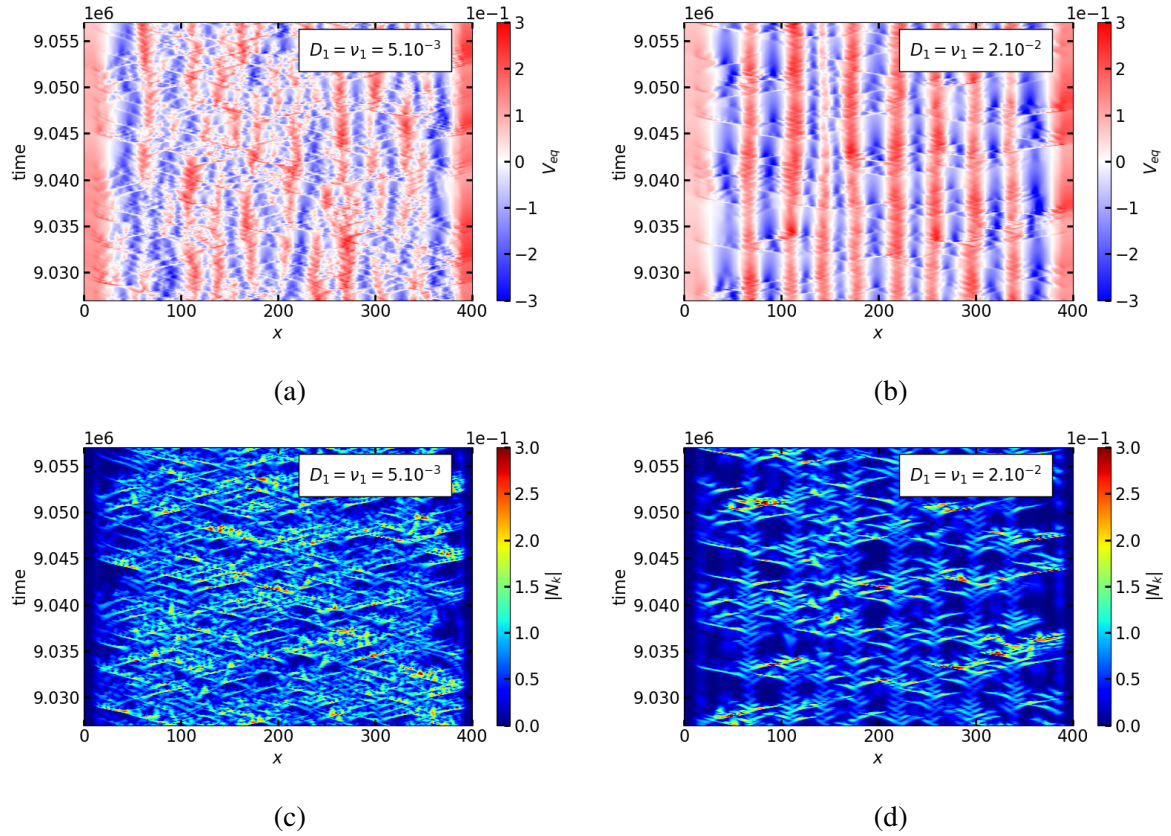

Figure C.2 – Variation of fluctuation dissipation coefficient D_1 and ν_1. (a,c) $D_1 = \nu_1 = 5\ 10^{-3}$. (b,d) $D_1 = \nu_1 = 2\ 10^{-2}$. The equilibrium velocity is displayed in (a) and (b) while the density fluctuation amplitude is shown in (c) and (d).

In Figure C.2a and C.2b are shown the equilibrium flows for both cases. Both ZFs have similar amplitude with the latter being more structured and stable in time. In Figure C.2c and C.2d are displayed the corresponding density fluctuation amplitudes. The low dissipation case leads to larger fluctuations. The size of the turbulent structures does not seem to vary much in between the two cases.

It is apparent that a larger dissipation leads to more stable flow structures. Distance to linear threshold seem to play a role, case $D_1 = \nu_1 = 2\ 10^{-2}$ evolves very close to its linear threshold, with its gradient being only 1.1 times the linear threshold. Case $D_1 = \nu_1 = 5\ 10^{-3}$ stands far from threshold with its gradient being 2.6 times the linear threshold. The underlying linear characteristics of the system are similar, for high dissipation case $\omega = 0.02$, $\gamma = 0.005$ and $\sin\Delta\varphi = -0.35$. For the low dissipation case, $\omega = 0.017$, $\gamma = 0.0044$ and $\sin\Delta\varphi = -0.3$. However it should be noted that these characteristics are computed with the smoothed steady-state gradient and do not take into account the corrugations. Possibly, the bifurcation occurs as a result of small scale effects. Link between corrugation, radial structure and stiffness of the system (in terms of variation of turbulent flux with density gradient) should also be explored.

C.3 Normalizing the turbulent flux of particles by a quasi-linear estimate

In this section, we normalize the turbulent flux of particles $\Gamma_{turb} = -2k_y\Im(N_k\phi_k^*)$ with its quasi-linear estimate Γ_{QL} using the linear relation F_{lin} (Equation 3.75). As the procedure contains several subtleties, it is wiser to approach the problem step by step. The example is provided for the scan of g (adapted source).

1. The linear relation between density and electric potential fluctuations is computed from the linear analysis with the steady-state rms gradient (Equation 4.2) at $V_{eq} = 0$ and $N_{eq}^{(2)} = 0$: $F_{lin}(k_x) = N_k/\phi_k$.

2. Since F_{lin} depends on k_x, the electric potential fluctuations are Fourier-transformed in both space and time, $\hat{\phi}_k(\omega, k_x)$ and further projected onto the ω corresponding to the linear estimation ω_{lin}.

3. Similarly to quasi-linear codes, such as QuaLiKiz [238], it is assumed that $\hat{\phi}_k(\omega, k_x)$ is not a dirac centered on ω_{lin} but that there is a frequency broadening in the form of a Lorentzian [239]. The electric potential results from the integral over frequencies as follows,

$$|\phi_k(k_x)|^2 = \int \frac{d\omega}{\pi} \frac{\alpha_k}{\alpha_k^2 + (\omega - \omega_{lin})^2} |\phi_k(\omega, k_x)|^2. \tag{C.1}$$

   With α_k the frequency broadening. The final result largely depends on the value taken for α_k as will be shown later on. A common choice is the linear growth rate: $\alpha_k = \gamma_{lin}$ [239] (p.43). It is important to ensure that the Lorentzian integral is close to unity, otherwise the electric potential fluctuation amplitude is underestimated. In practice, the signals have a finite time resolution which equally limits the integration bounds. Therefore, too large frequency broadening should be avoided since they would spread the lorentzian over large portion of ω. Describing the tails would then require very small time resolution (large ω).

4. The quasilinear flux is then computed by summing over k_x,

$$\Gamma_{QL} = -2k_y \sum_{k_x} \Im(F_{lin}(k_x)) |\phi_k(k_x)|^2. \tag{C.2}$$

In Figure C.3 are shown the electric potential and the quasi-linear flux as a function of k_x. The electric potential fluctuation function amplitude increases with g in agreement with the observed electric potential fluctuation amplitude Figure 4.6. Both the magnitude and the width of the function increase with g and two groups are distinguishable. At low g (in blue), the value of g barely affects the fluctuations or the quasi-linear flux. For $g > 10^{-3}$ the electric potential fluctuations are larger and increase with g. The first group corresponds to CDW dominated cases, while the second group is driven by interchange.
The behaviour of the quasi-linear flux is slightly different, it increases with g and starts to

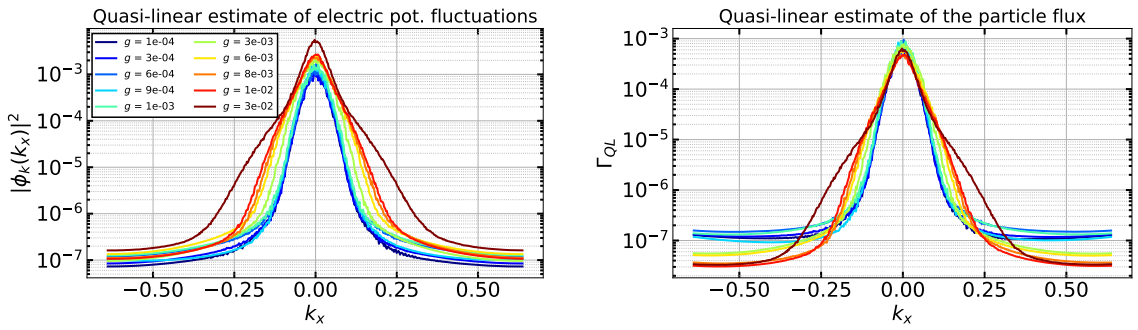

(a) (b)

Figure C.3 – (a) Quasi-linear estimate of the electric potential fluctuations as a function of k_x computed with a frequency broadening $\alpha_k = \gamma_{lin}$. (b) Corresponding quasi-linear flux of particles as a function of k_x. Both for the scan of the curvature parameter g performed with adapted sources.

decrease for very large values of g. The reduction of Γ_{QL} at large g is possibly caused by compressibility terms stabilizing the interchange instability.

Summing those two quantities over k_x, one can compare the first one to the rms-value of the electric potential and the second one to the turbulent flux of particles. The results are displayed in Figure C.4.

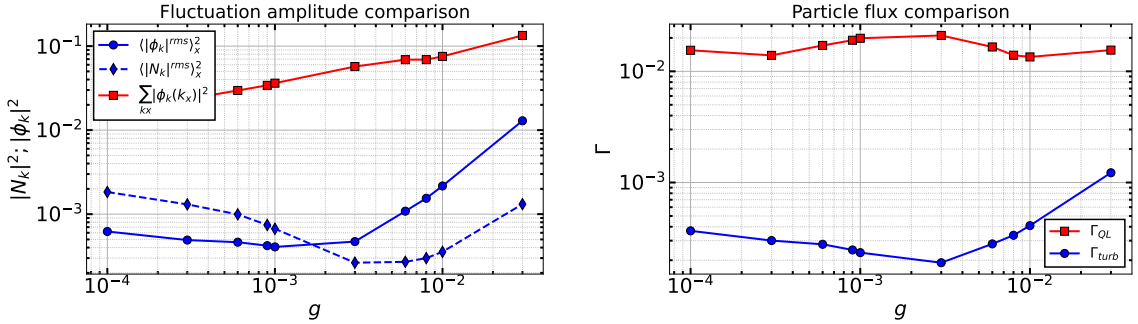

(a) (b)

Figure C.4 – Comparison between quasi-linear estimates and simulation results. (a) Quasi-linear electric potential fluctuations as a function of g compared with the rms-values of density and electric potential. (b) Quasi-linear flux compared to the turbulent flux of particles.

The estimate of the electric potential fluctuation amplitude is much larger than the rms-value of the electric potential. The resulting Γ_{QL} is much larger than the turbulent flux of particles. However, the quasi-linear computation at large g should be taken with caution because the frequency broadening is larger and leads to a reduced Lorentzian integral (≈ 0.68 at $g = 3 \times 10^{-2}$) and therefore a reduced estimated flux.

The influence of the frequency broadening on Γ_{QL} is illustrated Figure C.5 by choosing values of α_k between 10^{-4} and 10. The increasing widths are indicated with thin lines from purple

(small α_k) to yellow (large α_k). The case $\alpha_k = \gamma_{lin}$ is shown in red (squares) for reference.

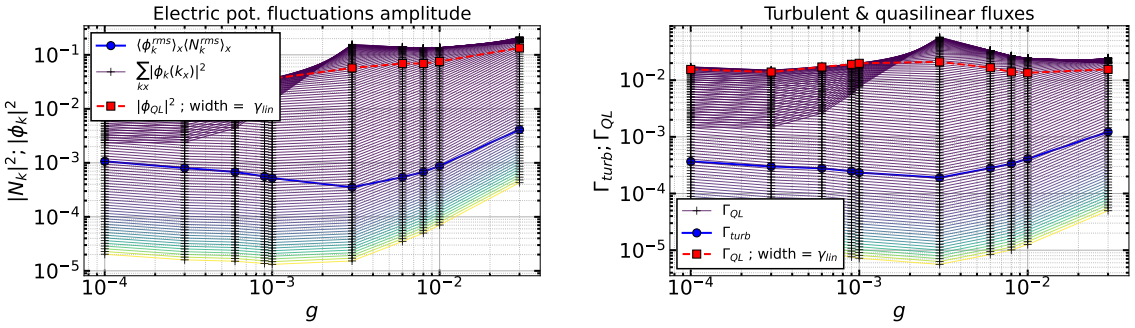

(a) (b)

Figure C.5 – Dependence of Figure C.4 on the chosen frequency broadening parameter α_k. Small frequency broadening ($\alpha_k = 10^{-4}$) is indicated in purple, large $\alpha_k = 10^{-1}$ is indicated in yellow. The case using the linear growth rate as the frequency broadening parameter is indicated in red (squares).

The normalization depends on the choice made for α_k in two ways. First, at low α_k, the behaviour of the electric potential fluctuations amplitude (left) as a function of g is inconsistent. It does not correspond to the rms-value of the electric potential it is supposed to estimate. Second, at large α_k both the behaviour of the quasi-linear flux and of the electric potential follow roughly the values taken from the simulations. However, due to the finite integration on frequencies, large values of α_k lead to an under estimation of $|\phi_k|^2$ leading to lower values of the quasi-linear flux. As a result, the normalization of Γ_{turb} by Γ_{QL} depends on α_k which is unsatisfactory. The normalization is shown Figure C.6.

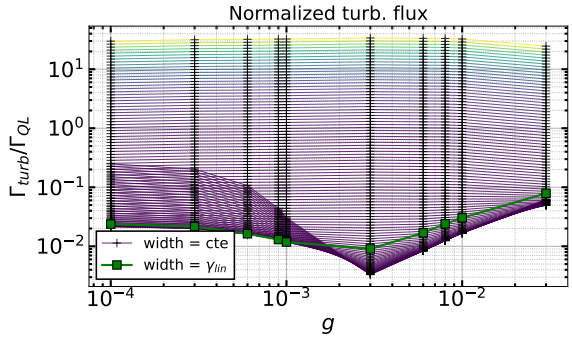

Figure C.6 – Normalization of Γ_{turb} with a quasi-linear estimate Γ_{QL} as a function of g and chosen frequency broadening α_k.

From this, it appears clearly that the normalization of the turbulent flux of particles with the quasi-linear estimate is not reliable since we lack the necessary time resolution to perform correctly the integration. Note that this is in terms of 'saved' points, not the real time resolution of the simulation. Therefore, we could do a restart and saving every time point but this would lead to very large arrays that are long to compute (especially for 120 simulations). Moreover,

the effect of ZFs and their radial structure still enters the estimate through the magnitude of ϕ_k. Consequently, no hasty conclusion will be drawn based on this normalization.

Appendix D: Doppler backscattering

D.1 Cut-off frequency estimation for reflectometry

The waves used for reflectometry are transverse waves propagating perpendicularly to the tokamak magnetic field, $\mathbf{k} \cdot \mathbf{B}_0 = 0$. Their properties, and in particular the cut-off layer, depend on their polarisation: ordinary, *O-mode*, or extraordinary, *X-mode*. For the former, the probing wave electric field is parallel to the macroscopic magnetic field: $\mathbf{E}_i^O \times \mathbf{B}_0 = 0$. As a result, the wave propagation is similar to a non-magnetized plasma and the refractive index depends only on the electron density n_e and the wave frequency ω:

$$N_O^2 = \frac{c^2 k^2}{\omega^2} = 1 - \frac{\omega_p}{\omega} \tag{D.1}$$

Where $\omega_p = \sqrt{n_e e^2 / m_e \varepsilon_0}$ is the plasma frequency. In *X-mode*, the wave electric field is perpendicular to the magnetic field $\mathbf{E}_i^X \cdot \mathbf{B}_0 = 0$. Now, the propagation depends also on the magnetic field. The refractive index reads,

$$N_X^2 = \frac{c^2 k^2}{\omega^2} = \frac{\omega^4 - \omega^2(\omega_{ce}^2 + 2\omega_p^2) + \omega_p^4}{\omega^2(\omega^2 - (\omega_{ce}^2 + \omega_p^2))} \tag{D.2}$$

With $\omega_{ce} = eB/m_e$ the electron cyclotron frequency. The details of this derivation can be found in ref. [201]. It follows that in O-mode, the iso-index surfaces correspond to magnetic surfaces, which is not the case in X-mode due to the magnetic field dependence.
The cut-off layer corresponds to the surface where $N = 0$. This condition gives three cut-off frequencies.

$$\omega = \omega_p \qquad \text{in O-mode} \tag{D.3}$$

$$\omega = \frac{|\omega_{ce} \pm \sqrt{\omega_{ce}^2 + 4\omega_p^2}|}{2} \qquad \text{in X-mode} \tag{D.4}$$

Knowing the cut-off frequencies as a function of density and magnetic field is essential because it will determine the local electron density where the signal will be reflected back from the plasma to the receiving antenna. Also, if one desires to make a local measurement the frequencies can be adjusted depending on the expected density profile. Two cut-off layers exist in X-mode but in practice it is the upper cut-off frequency that is mostly used in tokamaks. An example of the cut-off frequencies is shown Figure D.1 for a standard NBI-heated shot of TCV.

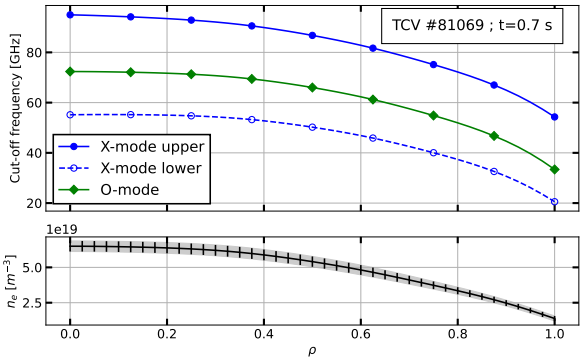

Figure D.1 – Cut-off frequencies in O and X mode for an example profile of density taken from #TCV81069 at $t = 0.7\ s$ averaged on 200 ms.

From this example note that different radial ranges are covered by O and X-mode. The mode is then chosen accordingly to the radio-frequency (RF) components capabilities, plasma parameters and desired measurement location. Here both O and X mode frequencies have similar shapes because of TCV low magnetic field ($B \approx 1.4\ T$). With strong magnetic field like Tore Supra the cut-off frequency can be a decreasing function of R, allowing to probe the core and high field side.

D.2 Hardware and heterodyne detection

The transmitted and received signals are processed by RF components represented in Figure D.2. The RF components are separated in two parts. The first is used to produce the signal sent into the plasma, at the right frequency. The second, is used to process the received signal, i.e. to separate the "plasma" signal from the carrier signal.

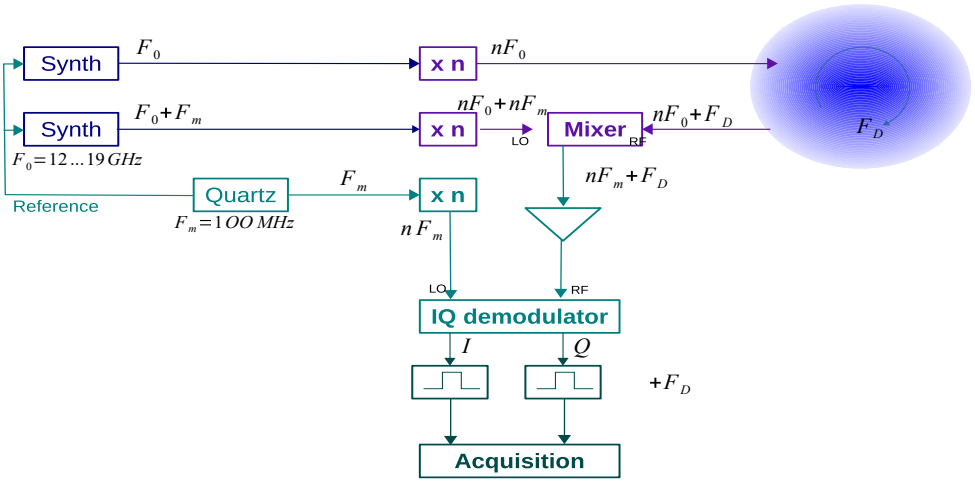

Figure D.2 – Schematic of the digital system used to process DBS signals at TCV, courtesy of P. Hennequin.

The micro-wave source is provided by two synthesizers producing signals of varying frequencies in the range $F_0 \in [12 - 19]\ GHz$. The first creates a signal at F_0 multiplied n times to reach

the cut-off frequencies appropriate for the given plasma conditions. It then reaches the antenna where it is polarized in O or X-mode before being sent into the plasma. The received signal contains the Doppler frequency information F_D of the order of 10^2 kHz. It is multiplied by a signal with a slight different frequency $F_0 + F_m$, with $F_m = 100$ MHz an added carrier frequency used for demodulation.
The signal is then demodulated two times to remove components carried by frequencies F_0 and F_m. The goal here is not to lose the phase which contains the Doppler shift information. This is done through an heterodyne detection with an IQ demodulator.

The principle of IQ demodulation is as follows. Consider a received signal of frequency $nF_m + F_D$:

$$s(t) = A\cos(2\pi(nF_m + F_D)t + \varphi_D) \tag{D.5}$$

A second signal is created by a local oscillator (LO) at a frequency nF_m. The demodulator multiplies s by two quadrature signals: $\cos(2\pi F_m t)$ and $\sin(2\pi F_m t)$ resulting in heterodynes signals:

$$x(t) = \frac{A}{2}\left[\cos(2\pi(2nF_m + F_D)t + \varphi_D) + \cos(F_D t + \varphi_D)\right] \tag{D.6}$$

$$y(t) = \frac{A}{2}\left[\sin(2\pi(2nF_m + F_D)t + \varphi_D) + \sin(F_D t + \varphi_D)\right] \tag{D.7}$$

Filtering out the high frequencies (hence choosing $F_m \gg F_D$) leads to a complex signal $z(t) = x(t) + iy(t)$ oscillating at the Doppler frequency F_D.

An upgrade from analog to digital I/Q demodulation has been performed recently for the TCV system. The final demodulation step can now be performed numerically. This allows to bypass the effect of a notch filter associated with the acquisition system. The filter causes the acquired signal to have a broad spectral gap ($\Delta F \sim 50$ kHz) around $F = 0$, making small F_D difficult to extract. When done numerically, the method ensures that the filter has no impact on relevant part of the spectrum. The details of the digital demodulation can be found in ref.[240].

D.3 Estimating the maximum of correlation on noisy signals

The goal of this appendix is to tackle the problem of the estimation of maximum of correlation when noise in the signal is important. Herafter, coherence refers to the cross-spectral density (cpsd) normalized by the power spectral densities (psd). It depends on frequencies. Correlation refers to the inverse Fourier transform (ifft) of the cpsd and depends on time delays. We emphasize that those two measurements are different even though they are giving an estimation of the correlation between two signals. The correlation function relates to the correlation between two signals when they are delayed with respect to each other. It is equivalent to a Pearson correlation estimation: degree of correlation given by plotting one signal as a function of the other and checking whether the scatter plot is close to a line. The spectral coherence separate this kind of analysis on different frequencies. Therefore, depending on the noise that affects the data, the two methods might not give the same result.

An easy way to see this effect is to perform the correlation / coherence on the same signal

adding synthetic noise. The chosen signal, $y(t)$, is taken from #81069 sweep 5, already assessed to have a low signal to noise ratio (SNR) in the main part of the thesis. A white noise of amplitude n_{amp} is added to the signal. The correlation is performed on the amplitude of $y(t)$ and $y(t) + n_{amp} \times noise$. A noise amplitude of $n_{amp} = 1$ corresponds to a noise of same amplitude as the signal $y(t)$. Examples of correlation and coherence functions are shown in Figure D.3 for different amplitudes of noise.

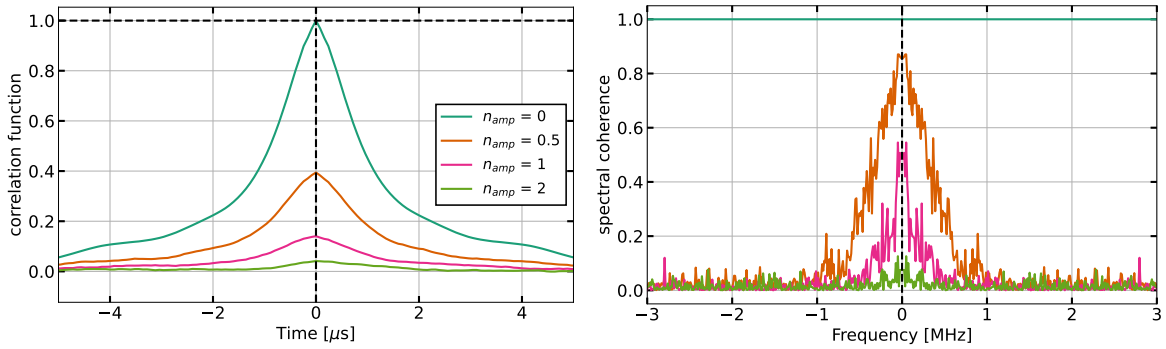

(a) (b)

Figure D.3 – Correlation (a) and coherence (b) functions of a signal $y(t)$ correlated with an artificial noise $y(t) + n_{amp} \times noise$.

The maximum of correlation drops quickly when noise is increased as opposed to the spectral coherence which stays relatively important at low frequencies. When probing to the core, the SNR is less important both because there is less turbulence and there are more perturbating effects along the beam path. As a result, radial correlation functions tend to flatten when estimated from the correlation function. See for example Figure 5.24. In that case, one can choose to work instead on the spectral coherence signal. However, this signal is also noisy and the estimation of the maximum can be tricky to perform in a systematic way.

Through trials and errors it appeared that the best way to estimate the maximum of coherence on the amplitude signal is with a Lorentzian fit. In some cases, when using the 'full' complex signal, it appeared better to use a Gaussian fit, but the difference in the estimation of the maximum is very small. Examples of fit are given in Figure D.4 for two noisy signals: #82607 sweep 3 at $\Delta = 0.25$ and 4.7 ρ_s respectively.
In both cases, the fits does a pretty well job at determining the maximum. This estimation is still tricky because the zero frequency component is removed from the signals through the normalizations. Therefore, the coherence functions tend to form a local minima at $f = 0$ with two peaks on the side. It is unclear, even for the experimentalist, to determine whether the maximum of correlation of the maximum of the fit is the best estimate. To be conservative, the choice is to take the fit because it tend to underestimates the maximum of correlation.

D.4 Mixed files technique for correlation noise estimation

In this appendix, we estimate the noise level in the correlation measurements, which is critical for determining the minimum correlation value considered significant. This is particularly important for avalanche measurements, where the secondary correlation slope may occur at low

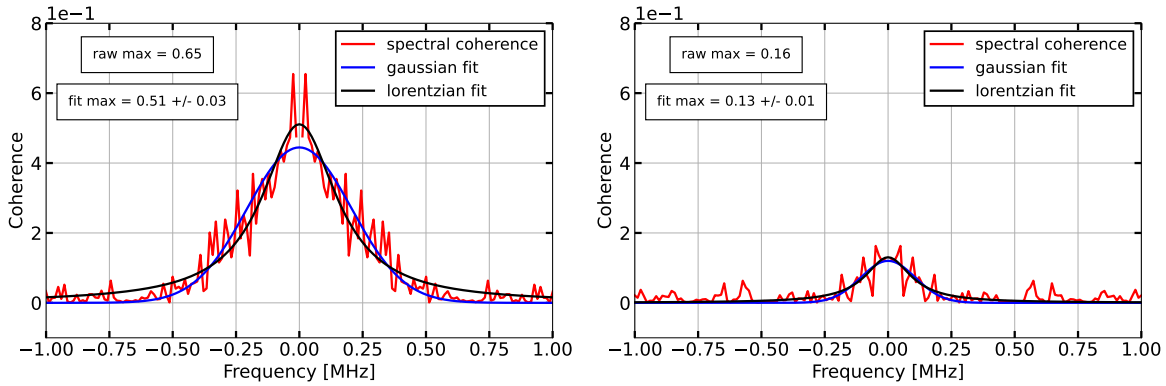

(a) (b)

Figure D.4 – Examples of gaussian and lorentzian fits on the spectral coherence function.

correlation values. In the literature, it is common practice to set the noise threshold at $\mathscr{C} = 0.1$. Here, we use the mixed files technique to estimate the noise level. The method consists in choosing two random pairs of signals from the performed Deuterium experiments at TCV (Table 5.2) and to perform their correlation. In Figure D.5 is shown an example of the obtained cross-spectral density together with the different estimations: correlation, spectral coherence and its Taylor fit. The correlation is obtained both through the inverse Fourier transform of the csd and through Pearson coefficient (in real space).

Both signals being the amplitude of the density fluctuations, their frequency maximum is not Doppler shifted and is located at $f = 0$. Since they are from different signals, their cross-spectral density (csd) is much lower than their power spectral densities (psd). This results in a small spectral coherence and in small correlation. Note that the fit is performed on the central part of the spectral coherence, where the signal have been set to zero for $|f| > 1$. Imposing a local maximum is done so that the Lorentzian fit converges towards a maximum close to the vanishing frequency. This overestimate the noise estimation. If the fit is done on the full frequency array, the maximum is below 10^{-2}.

To have a larger statistics, we repeat the above operation on random pairs of signals taken from the database Table 5.2. For each pair, we take the maximum of the spectral coherence, the maximum of correlation (ifft and Pearson) and the maximum of the Lorentzian fit. The result is shown in Figure D.6 for 100 pairs. The mean and standard deviation is shown for the spectral coherence as it gives the largest correlation.

For every method the correlation noise level is below $\mathscr{C} = 0.1$ with the worst case being the raw spectral coherence. This was expected, the spectral coherence being noisy. The Lorentzian fit of the coherence performs better because when the signal is too noisy, the fit tends to be flat and exhibits no large maximum. The same method has been applied at specific frequencies, for specific shots and for specific ρ_{ref}. Since the signals become more noisy as one get closer to the core of the plasma we could expect the correlation noise level to increase in a similar fashion. However in the cases tested no strong deviation from the above trend has been observed. When the signals are not correlated it does not matter whether the noise is important or not. This only reduces the maximum of correlation for signals that should exhibit a larger correlation.

From this estimation, we expect the correlation measurements to yields information below

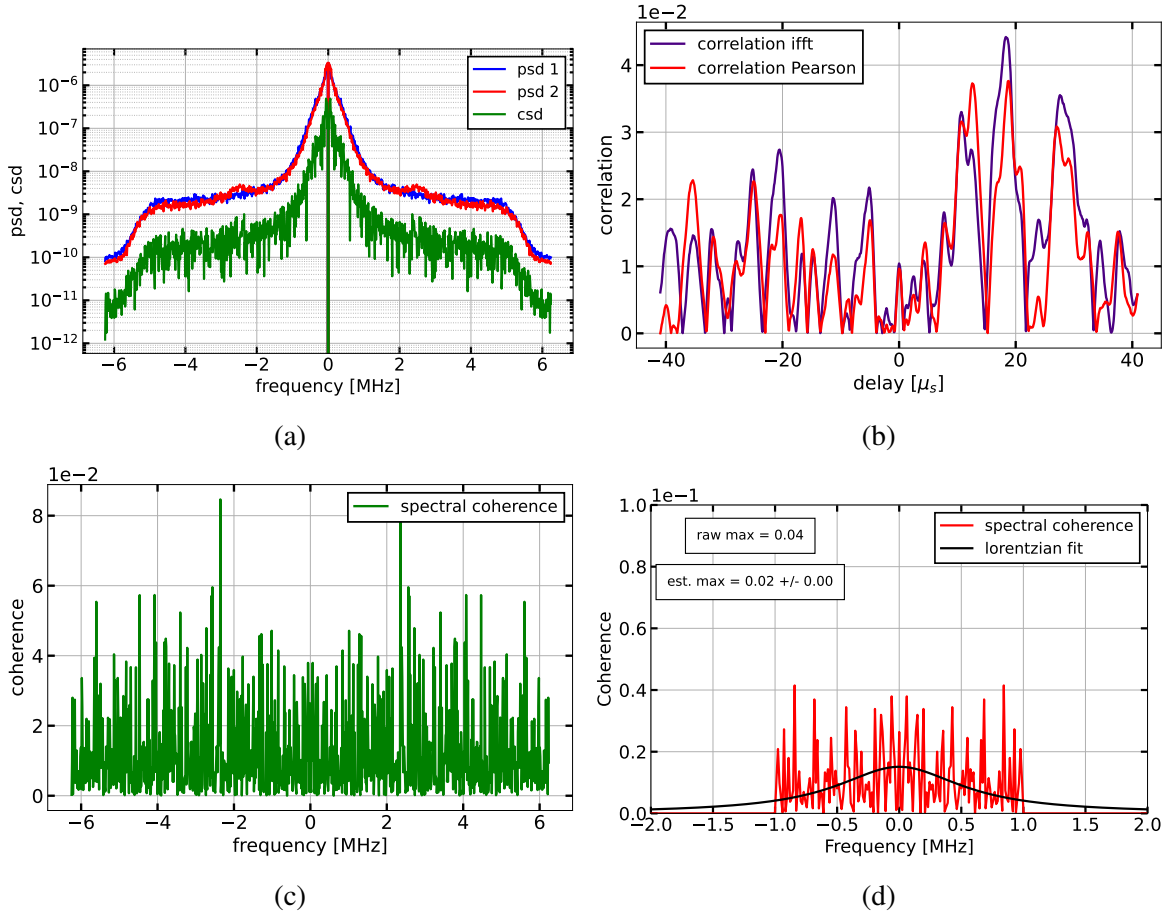

Figure D.5 – Correlation analysis of #81069 sweep 5 frequency 1 with #82607 sweep 3 frequency 7. (a) power spectral density (psd) and cross-spectral density (csd). (b) Correlation from inverse Fourier transform (ifft) and from Pearson. (c) Spectral coherence. (d) Lorentzian fit of the spectral coherence.

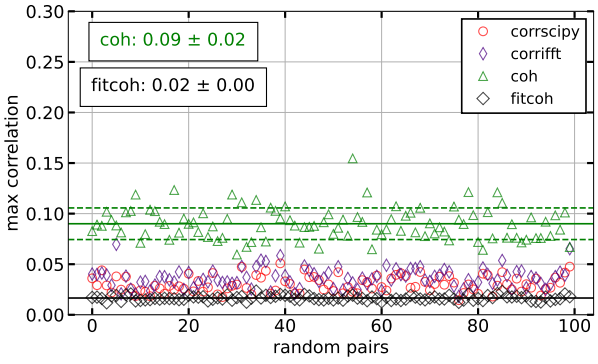

Figure D.6 – Mixed files technique for noise estimation on a 100 signal pairs taken from Table 5.2.

$\mathscr{C} = 0.1$ for the maximum of spectral coherence and below $\mathscr{C} = 0.05$ for the other estimation methods ($\mathscr{C} = 0.02$ for the Lorentzian fit). However, to be conservative, correlation below 0.1 are not given much weight.

D.5 Normalizing turbulence correlation lengths to ion Larmor radius

In this section, the normalization of the turbulence correlation length and avalanche extension is performed using the ion Larmor radius $\rho_i = \sqrt{m_i T_i} eB$ instead of the hybrid Larmor radius $\rho_s = \sqrt{m_i T_e} eB$. First, the ion Larmor radius as a function of ρ for the different experiments is shown in Figure D.7. This figure is to be compared with Figure 5.19.

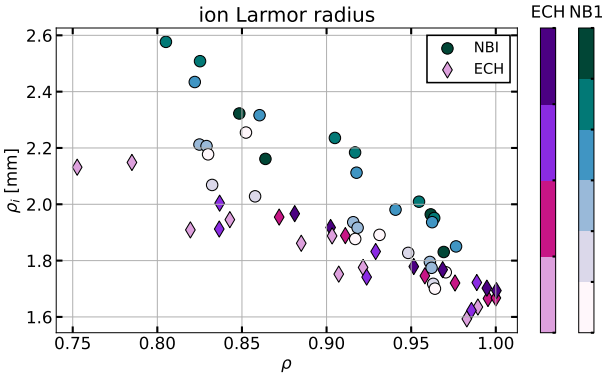

Figure D.7 – Larmor radius $\rho_i = \sqrt{m_i T_i})/(eB)$ as a function of ρ and heating for discharges in Table 5.2. ECH ranges from 590 to 1180 kW and NBI from 140 to 500 kW.

The ion Larmor radius varies from 1.6 to 2.6 mm with a larger variability as compared to the hybrid Larmor radius. This is caused by two effects. First, the CXRS diagnostic providing values for T_i is not as precise has the Thomson scattering system, especially in the edge. Second, the NBI cases tend to change the value of T_i much more than the value of T_e. It results that there is a heating dependence.

Using this new normalization, and similarly to Figure 5.27, the radial turbulence correlation length and avalanche extension normalized by ρ_i are shown in Figure D.8 as a function of ρ.

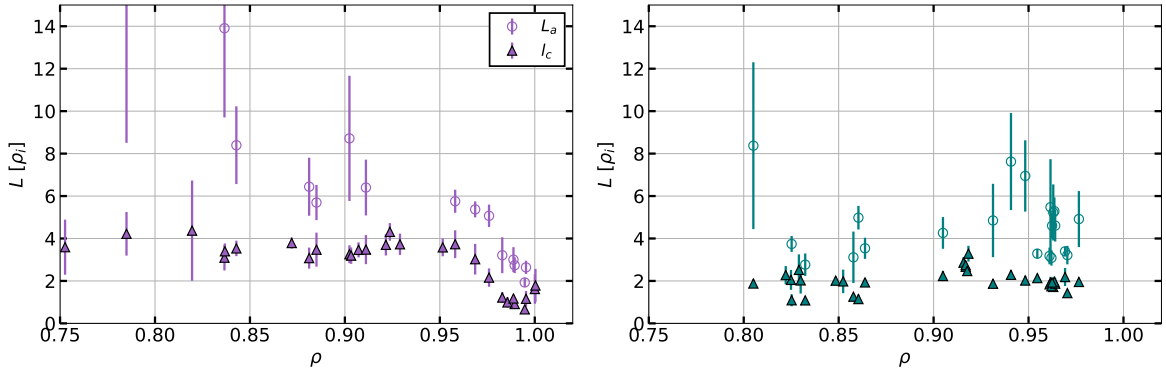

(a) (b)

Figure D.8 – Radial correlation length of the turbulent structures l_c and avalanches L_a for every ECH and NBH plasmas as a function of ρ_i.

The ECH cases, shown on the left hand side, display a constant radial correlation length at

$l_c \approx 3.5 - 4\ \rho_i$ for most of the studied domain. The correlation length reduces in the radial electric field well to $l_c \approx 1 - 1.5\ \rho_i$. The avalanche extension also reduces when getting closer to the edge. The NBI cases display a lower turbulence correlation length and comparatively less variability than when normalized to the hybrid Larmor radius (see Figure 5.27). However, no clear trend of the correlation length or avalanche extension has been observed as a function of the heating power.

DOCTORAL SCHOOL

Titre : Auto-Organisation de la turbulence de bord dans les plasmas de fusion

Mots clés : Plasma, Fusion, Turbulence, Tokamak, Ecoulements zonaux, Avalanches

Résumé : Ce travail de doctorat s'intéresse à la caractérisation de l'auto-organisation de la turbulence au bord des plasmas de tokamak, déterminante pour le transport et le confinement. Il a permis d'obtenir trois résultats principaux : l'identification des régimes de paramètres plasma propices à l'auto-organisation de la turbulence, l'élucidation de mécanismes physiques sous-jacents, l'obtention de preuves expérimentales de l'auto-organisation grâce à des mesures de rétrodiffusion Doppler (DBS).

Les tokamaks permettent le confinement de plasmas chauds à l'aide de champs magnétiques. Trois zones s'y distinguent : la zone de confinement du plasma, séparée de la zone externe où celui-ci interagit avec les matériaux par une zone de transition, dite "de bord". Dans le domaine opérationnel de fonctionnement des tokamaks, le transport perpendiculaire – et donc le confinement – est régi à l'échelle microscopique par la turbulence. Mieux connaître les mécanismes de saturation de la turbulence apparaît ainsi essentiel. Dans la zone de transition, la turbulence génère à la fois des événements de transport par avalanches, qui détériorent le confinement, et des écoulements zonaux (ZF) qui contribuent à la saturation de la turbulence. Ce travail cherche à comprendre et prédire l'auto-organisation, c'est-à-dire l'interaction auto-cohérente entre les ZF potentiellement structurés radialement, les profils moyennés sur les surfaces de flux et le transport turbulent, dans les différents régimes de paramètres des plasmas de bord des tokamaks. Pour cela, un modèle réduit non-linéaire Tokam1D a été développé. Il étudie l'évolution des profils moyens et des fluctuations de manière auto-cohérente dans un régime contrôlé par le flux. Pour permettre l'auto-organisation de la turbulence aux méso-échelles, aucune séparation d'échelle n'est présupposée. Le modèle inclut deux instabilités considérées comme dominantes : les ondes de dérive collisionnelles et l'interchange. Leurs paramètres de contrôle dépendent différemment des paramètres plasma, de sorte que différents régimes sont attendus dans les plasmas de bord des tokamaks. Le modèle est réduit à une dimension, en ne conservant qu'un seul mode parallèle et poloïdal pour les fluctuations, dans l'esprit d'une approche quasi-linéaire généralisée. Un large balayage des paramètres de contrôle des instabilités permet de cartographier le comportement du plasma de bord. Des régimes dominés par les écoulements sont prédits à faible collisionnalité ou à grande courbure magnétique. Cette dernière favorise la turbulence de type interchange, caractérisée par des événements de transport en avalanches et des ZF structurés radialement, conduisant à des profils de pression en escaliers appelés staircases. Les ZF sont générés par les composantes électrique et diamagnétique du tenseur de Reynolds. Leur corrélation et leur amplitude relative varient avec le régime de turbulence. La capacité du système à conserver de l'énergie dans le profil de pression comme dans les écoulements d'équilibre détermine l'existence des staircases, lesquels optimisent le confinement. Les avalanches sont caractérisées par une fonction de corrélation radiale à deux pentes : la première est attribuée à la turbulence à petite échelle, la seconde capture la longueur typique de l'avalanche. Des études expérimentales ont été réalisées sur Tore Supra (CEA) et TCV (EPFL) en utilisant deux systèmes DBS. Sur Tore Supra, des corrélations à longue distance sont observées en utilisant des DBS séparés poloïdalement et toroïdalement. En filtrant les modes géodésiques acoustiques, des signatures des ZF à basse fréquence sont identifiées. Sur TCV, des fonctions de corrélation radiale sont obtenues à l'aide d'un double système DBS. Deux longueurs typiques sont observées, comme dans les simulations. Ce résultat constitue une preuve indirecte supplémentaire de l'existence d'événements de type avalanche dans les plasmas de tokamaks, notoirement difficiles à observer.

Title : Edge turbulence self-organization in fusion plasmas

Keywords : Plasma, Fusion, Turbulence, Tokamak, Zonal flows, Avalanches

Abstract : This PhD work is a step forward in the characterisation of turbulence self-organization in edge tokamak plasmas, key player in transport and confinement. Three main results are obtained: the plasma parameter regimes prone to turbulence self-organization are identified, some of the underlying physical mechanisms at work are unravelled, and some experimental evidence of self-organization is obtained by means of Doppler Back-scattering (DBS) measurements in tokamak plasmas.

Tokamaks aim at confining hot plasmas by means of large magnetic fields. The last closed flux surface separates the confined inner region from the scrape-off layer where the plasma interacts with materials. In the tokamak operational regime, cross-field transport – hence confinement – is governed by micro-scale turbulence. Understanding the mechanisms of its saturation would open the route towards its possible control. Plasma conditions at the edge transition region are key. In this region, turbulence generates avalanche transport events, which deteriorates the confinement, and zonal flows that efficiently contribute to turbulence saturation. Understanding and predicting turbulence self-organization – i.e. the self-consistent interplay between potentially radially structured ZFs, flux-surface averaged profiles and turbulent transport – in the various parameter regimes of edge tokamak plasmas constitutes the backbone of this work. To this aim, the reduced non-linear model Tokam1D, developed on purpose, evolves the mean profiles and the fluctuations in a self-consistent manner in the flux-driven regime. Importantly, in view of studying turbulence self-organization at mesoscales, no scale separation is assumed. The model features two instabilities thought to be dominant at the edge, namely collisional drift waves CDW, originating from a finite phase shift between density and electric potential fluctuations, and interchange due to the magnetic field inhomogeneity (curvature). Their control parameters exhibit different dependencies with respect to plasma parameters, so that different regimes can be expected in edge tokamak plasmas. The model is reduced to 1-dimension by retaining a single parallel and poloidal mode for the fluctuations, in the spirit of a generalized quasilinear approach. A large scan of the instability control parameters, both at fixed source and fixed distance-to-threshold, allows one to pave the edge plasma parameter space. Large flow-to-turbulence energy ratios are predicted at low collisionality or large magnetic curvature. The latter favours interchange turbulence characterised by avalanche-like transport events and radially-structured ZFs leading to corrugated pressure profiles known as staircases. ZFs are driven by the electric and diamagnetic components of the Reynolds stress, whose phase alignment and relative amplitude vary with the turbulence regime. The system's freedom to store energy both in the pressure profile and mean flows is shown crucial to the staircase existence. Overall, the confinement is improved in regimes featuring staircases. Experimentally measurable signatures of avalanches are found in the form of a two slope radial correlation function, the smallest slope attributed to small-scale turbulent eddies, the largest capturing the avalanche typical propagation length. Experimental studies have been carried out on the Tore Supra (CEA Cadarache) and TCV (EPFL) tokamaks using a two-channel DBS for correlations. In Tore Supra long range correlations are observed when using poloidally and toroidally separated channels. When filtering out dominating geodesic acoustic modes, signatures of the elusive low frequency ZFs are found. In TCV, measurements using two co-located channels exhibit radial correlation functions with two slopes in certain regimes similarly to simulations. This result constitutes an additional indirect proof of the existence of avalanche events in tokamak plasmas, notoriously difficult to diagnose.

Institut Polytechnique de Paris
91120 Palaiseau, France